Nanomechanics-based thermodynamics : from molecules to mesoscopic phonons

Ilya Golokolenov

THÈSE

Pour obtenir le grade de

DOCTEUR DE L'UNIVERSITÉ GRENOBLE ALPES

École doctorale : PHYS - Physique
Spécialité : Nanophysique
Unité de recherche : Institut Néel

Thermodynamique basée sur la nanomécanique : des molécules aux phonons mésoscopiques

Nanomechanics-based thermodynamics: from molecules to mesoscopic phonons

Présentée par :

Ilya GOLOKOLENOV

Direction de thèse :

Eddy COLLIN — Directeur de thèse
DIRECTEUR DE RECHERCHE, Université Grenoble Alpes

Rapporteurs :

JUKKA PEKOLA
Professeur, AALTO Yliopisto
YURI PASHKIN
Professeur, Lancaster University

Thèse soutenue publiquement le **21 décembre 2022**, devant le jury composé de :

JUKKA PEKOLA Professeur, AALTO Yliopisto	Rapporteur
YURI PASHKIN Professeur, Lancaster University	Rapporteur
ANDREW ARMOUR Professeur, The University of Nottingham	Examinateur
LAURE MERCIER DE LEPINAY Professeur assistant, AALTO Yliopisto	Examinatrice
SIGNE SEIDELIN Maître de conférences HDR, UNIVERSITE GRENOBLE ALPES	Examinatrice
OLIVIER BOURGEOIS Directeur de recherche, CNRS DELEGATION ALPES	Président

Université Grenoble Alpes

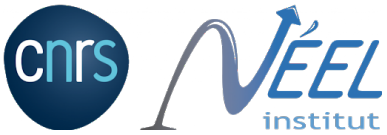

PhD in Physics

PhD Thesis

Nanomechanics-based Thermodynamics:
from molecules to mesoscopic phonons

Candidate
Ilya Golokolenov
Institut Néel

Advisor
Dr. Eddy Collin
Institut Néel - Univ. Grenoble Alpes

Academic Year 2022/2023

"Pourquoi faire simple
Quand on peut faire compliqué?"

— une devise Shadok

CONTENTS

LIST OF FIGURES

ACKNOWLEDGEMENTS

My supervisor is great. That's what he said. And I agreed, as without him all this work would have been impossible for too many reasons. In the first place, that's him, who gave me the job and the topic of research. He was a great teacher and boss all the way through. Finally, he edited this manuscript, and without that it would sound extremely naive and sometimes too straight-forward. Therefore Eddy Collin is the first and the most important person I would like to thank, particularly for his patience.

I would also like to thank my dear wife for being with me throughout my PhD, for supporting me, and feeding me when necessary.

I'm very grateful to all members of the Ultra Low Temperature group of the institute Néel, the former and current ones with whom I had the pleasure to work, for their comradeship and help. I would especially like to mention Dylan Cattiaux, Sumit Kumar, Rasul Gazizulin, and Andrew Fefferman.

I am obliged to Jean-Philippe Poizat and Benjamin Pigeau for their regular checks on how I was doing during the PhD, and our fruitful scientific discussions.

Besides, I'm beholden to all technical support members of our institute for their professionalism: cryogenics, nanofab and other departments. In particular James Butterworth, Sebastian Triqueneaux, Bruno Fernandez, Thierry Crozes, and Gwénaëlle Julie. And separately, for helping me to deal with endless French bureaucracy, I'm endlessly thankful to Elodie Ferrara.

I owe my appreciation to all our collaborators from Finland and United Kingdom; exceptionally to Mika Sillanpää for hosting me at Aalto university for a whole month.

A special shout-out to all members of my jury first of all for agreeing to be there, and moreover for reading and correcting this manuscript.

An extra reward for (almost) always being there for me goes to Café Fraica and its caffeine supply.

Golokolenov Ilya,
November 2022.

P.S.: Remerciements particuliers à Owen Molding pour la relecture et la correction du texte final.

INTRODUCTION

Nanotechnologies and cleanroom fabrication are the locomotive of modern solid state physics, as was foreseen by Richard P. Feynman in 1959 [1]. Their advancement changed our everyday life in a drastic way with the miniaturisation of devices and their extreme compactness. Besides, it opened new horizons for experimental science by pushing down the scale available to technologies: increasing the sensitivity up to the level of a single atom, and enabling the direct use of quantum phenomena: quantum bits, SQUIDs or single-electron transistors, all of which are fabricated within cleanroom facilities. The high manufacturing precision and variety of available materials open almost infinite possibilities for applications and investigations. These tools continue to improve constantly shifting the level of capabilities, increasing resolution, reproducibility, and adding new materials into action, which widens the already enormous potential for applications and investigations from fundamental to applied.

On Fig. 1 various devices from different laboratories are presented. The top left Scanning Electron Microscope (SEM) image shows two coupled qubits from Ref. [2], which was the first realisation of qubit coupling - a crucial brick for

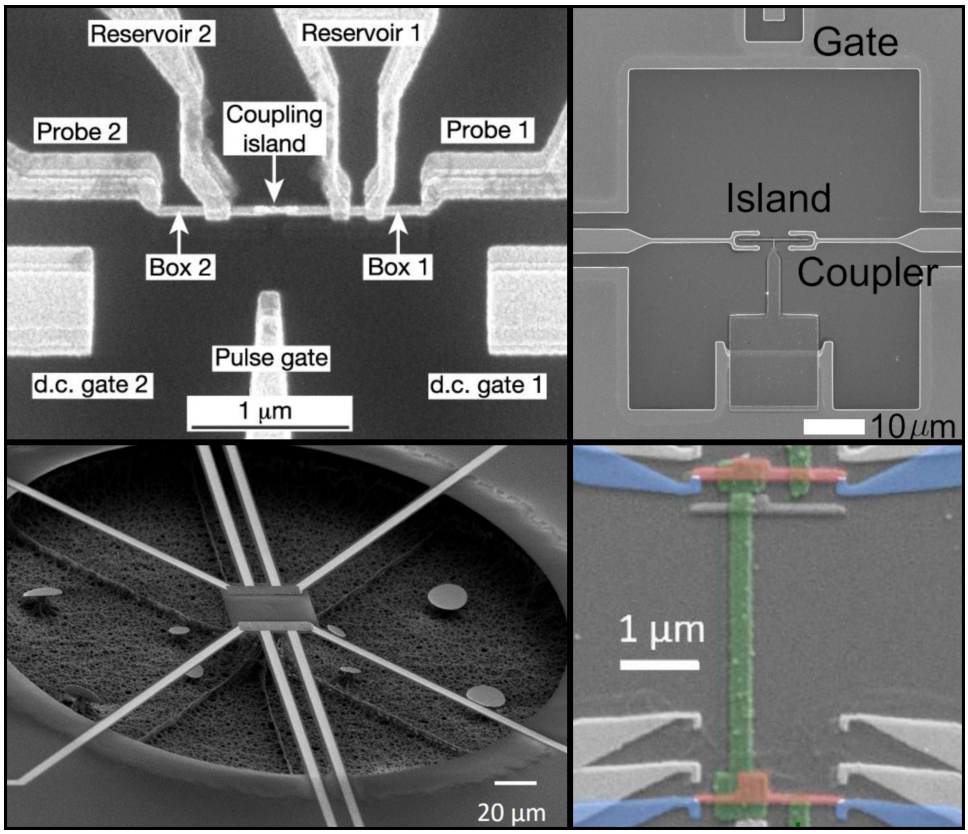

Figure 1: Examples of cleanroom devices from different laboratories

the building of quantum computers. The top right part shows a modern superconducting qubit from Ref. [3], used as a common coupling island between two superconducting coplanar waveguide resonators. This presents a potential use of qubits, here for quantum refrigeration.

The bottom left one demonstrates a suspended membrane-based zeptoJoule nanocalorimeter from Ref. [4], which has been used to measure specific heat of nanoscale objects and study thermal transport down to the nanoscale. Finally, the bottom right image shows a single electron transistor from Ref. [5], which was used to study thermodynamics at the nanoscale. All of these examples are linked to our topic: because of the ability to perform a measurement at the quantum level, of their focus on mesoscopic thermal properties, or mesoscopic thermodynamics. Nanofabrication, in the framework of our own devices, will be discussed in details in Ch. 1.

As was noticed by Michael Roukes and Keith Schwab: 'everything moves!' [6]. Motion is at the core of all phenomena around us, from electromagnetic waves and light to planets and stars. And the simplest and most direct way to investigate motion is with mechanical devices. It may look not that obvious in our modern world conquered by electronic systems, but we should remember that in the 18th century, mechanical systems allowed us to discover Coulomb's law [7] and to measure the gravitational constant [8]. Mechanical systems were and still are the most sensitive force/mass detectors. Nowadays, with the incomparable support of nanofabrication technologies, mechanical systems are having a Renaissance, which started around 20 years ago. Micro- and nano-mechanical systems (MEMS and NEMS) are widely used in ways somehow similar to the force detectors from the 18th century, but now with a much higher record-breaking sensitivity, achievable due to their miniature size. These systems are evolving with time by improving their characteristics and expanding their area of application: from the sensing of a single molecule 20 years ago [9], to capturing quantum vortices nowadays in a superfluid [10]. So far, all NEMS applications are within fundamental research, but who knows how it may turn in the future. Besides, moving objects are eventually behaving as quantum mechanics predicts [11], just as electrons or spins. This opens up unique capabilities based specifically on mechanics and quantum mechanics: a moving object is intrinsically different from an electron running in a SQUID loop, since it couples to fundamentally different baths. This had been pointed out also about 20 years ago by A.J. Leggett who discussed in a series of articles how little was experimentally known at that time on this topic [12].

Examples of nano-mechanical resonators can be seen on Fig. 2. The bottom part presents a suspended nano-beam device (300 nm wide and 300 μm long), from Ref. [13]. This device had been used as a model system, demonstrating how one can quantitatively measure decoherence within a mechanical mode. The top part shows a micrometer scale cantilever resonator (10 μm wide and 100 μm long) etched on the corner of a monocrystal, taken from Ref. [14]. This specific example shows how one can couple mechanics to other degrees of freedom: specifically here optical fields, building on the properties of a rare-earth doped crystal. The

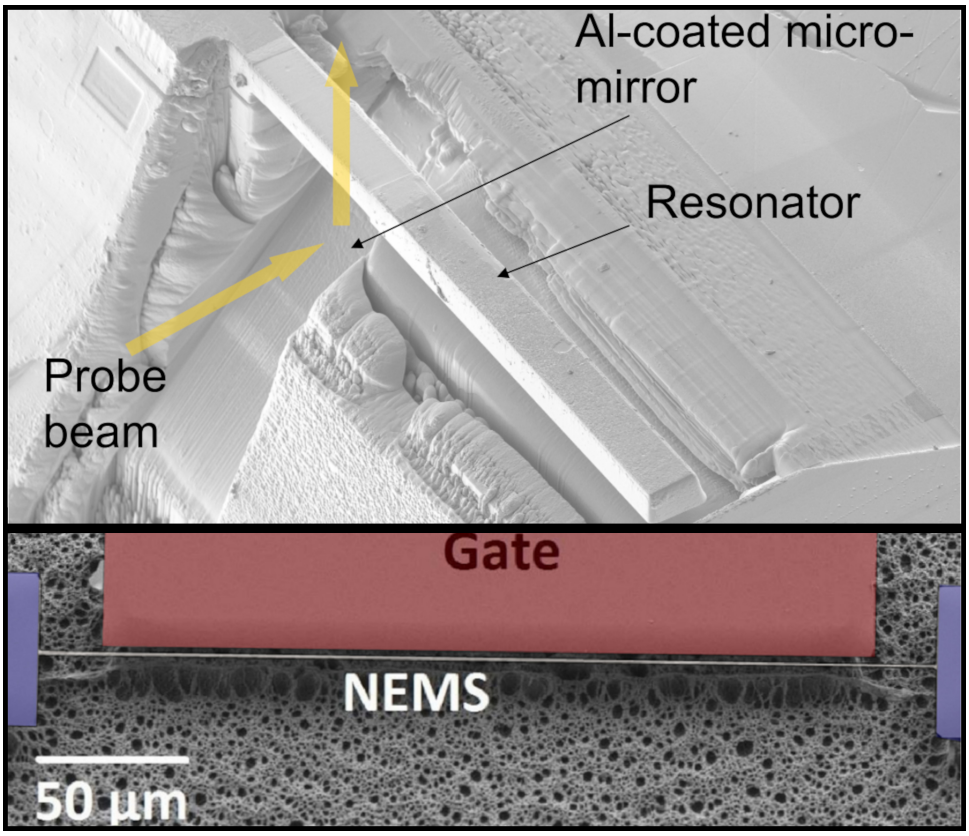

Figure 2: Examples of nano-mechanical resonators from different laboratories

characterisation of such beam nano-mechanical resonators will be explained in Ch. 4.

Indeed, the quantum limit in light detection ha already been achieved, so why not use it to bring sensing of mechanics to the same level? This idea is realised within the field of optomechanics, which couples mechanical motion to light. This coupling is realised through the radiation pressure force exerted by electromagnetic waves. This effect has been known since the 17th century and was formalised in the 19th. The original idea of observing radiation pressure forces on mechanical objects belongs to V. B. Braginsky [15] and was first realised using lasers [16]. These first measurements struggled with thermal noise and were far from the quantum limit and the observation of quantum effects. But it was already understood theoretically that such systems should be at the so-called Standard Quantum Limit (SQL) [15, 17]: the detection scheme enables in principle to measure motion to the best accuracy enabled by quantum mechanics and Heisenberg's principle, which belongs to a specific class of linear quantum amplifiers [18]. Today, systems based on optomechanical interactions are considered to be among the most sensitive instruments ever built, as illustrated by LIGO and VIRGO [19] which are able to detect gravitational waves. But gravitational waves are a classical field, i.e. a distortion of the space-time metric. With the quantum nature of mechanics and these unique sensing capabilities, one could think of probing quantum fields within optomechanical platforms [20]. The realisation of ultra-strong coupling

optomechanical systems, where the zero-point motion is enough to substantially shift the cavity frequency, stays one of the open challenges of the field [21].

Despite their impressive sensitivity and response time, even the best modern laser-based optomechanical systems suffer from a fundamental drawback: the presence of a powerful laser beam. This laser heats everything and makes working at low temperatures challenging, which are required to bring mechanical modes into their quantum ground state of motion [22]. This problem can be avoided by shifting optomechanics into the microwave domain by using superconducting materials and *RLC* circuits instead of lasers and mirrors. This is the field of microwave optomechanics [23]. It has been demonstrated recently that with microwave optomechanics and nuclear demagnetisation cryogenics, it is indeed possible to achieve ground state cooling of mechanical oscillators with pure brute-force cooling [24]. This means that today, mesoscopic mechanical objects with a mean population below a single quantum in their fundamental mode (and therefore, empty in all higher modes) can be probed and investigated with ultimate sensitivity.

Some examples of optomechanical systems are given in Fig. 2 and Fig. 3. In Fig. 2, the top image shows one of the simplest realisations of such a coupling, where a cantilever and a mirror form an optical cavity. On Fig 3, two examples of optomechanical systems are shown (separated by almost 20 years). In the left part, one of the pioneering optomechanical systems is presented, designed to be probed with a laser (from Ref. [25]). It consists of a suspended silicon disc, which possesses a breathing mechanical mode overlapping a whispering gallery optical mode. In the right panel, we present one of the most recent microwave lumped *LC* element optomechanical system (from Ref. [26]). The moving capacitor is the blue disc with square anchorings, while the inductor is the blue spiral. Optomechanics will be discussed particularly in Ch. 6.

One of the fields of interests for motion-sensitive devices is clearly to improve our understanding of motion itself. 'Everything moves', and this collective motion is at the core of our definition of heat with its specific energy quantum: the phonon. How energy is transferred and converted from work to heat is the domain of thermodynamics. Macroscopic (and classical) thermodynamics was created as an engineering tool to design steam-engines and other motors and cryogenic

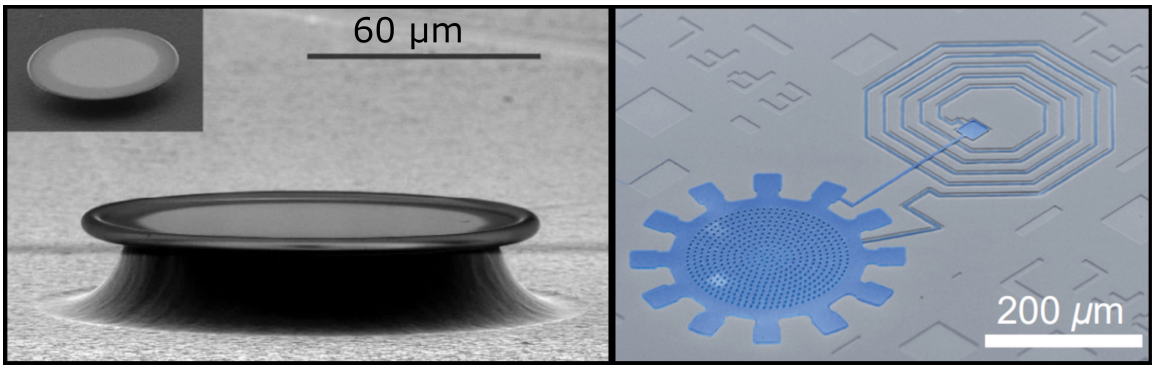

Figure 3: Examples of optomechanical systems from different laboratories

systems. Therefore, it cannot be applied to our small (and ground-state cooled) nano-mechanical systems. There is today a specific branch of thermodynamics, called stochastic thermodynamics, which tackles these fundamental issues. It takes into account the prominence of fluctuations, which can be as large as mean values [27], and brings some unorthodox results such as: apparent 'violations' of the second law of thermodynamics [5]; a blurred arrow of time; or the realisation of a 'Maxwell's demon' through feedback control and information processing [28]. All of these apparent paradoxes are solved within the new theory that takes into account the small size of the object, and the information, or entropy, that is channelled towards the bath. When quantum mechanics comes into play, the conceptual aspects of stochastic thermodynamics are even harder to interpret: this is the field of quantum thermodynamics, which has not yet been explored experimentally [29, 30].

Stochastic (classical) thermodynamics is broadly investigated experimentally today using various platforms [5, 31, 32, 33]. However in most of these experiments, there are 'mediating particles' which are transmitting heat/entropy, but which are not heat themselves in the sense that they are not atomic motion: an electron or a photon transmitting heat will eventually couple to a heat reservoir in which phonons will be created (or annihilated). This can be improved by introducing mechanics explicitly into these experiments. As such, mechanical model systems have already been used in realisations of stochastic thermodynamics, for example with trapped colloidal particles or cantilevers. In these experiments, the Landauer erasure principle has been experimentally verified [34, 35]: the erasing of a bit of information leads to a minimal production of heat of $k_B T \ln 2$. Fig. 4, taken from Ref. [35] demonstrates the dependence of the produced heat to the erasing rate.

All of these experiments are focused on thermodynamic cycles, which are at the core of engineering issues: systems driven to perform a particular action. Here, we are more interested in intrinsic and stationary properties: how the system equilibrates with a bath and fluctuates with no work produced. And with mechanical resonators, it becomes possible to probe the thermodynamics of motion itself. With brute-force cooling, intrinsic quantum fluctuations of the mechanical modes themselves should also become relevant, and potentially whichever fundamental bath Nature provides and couples to them, as proposed in recent collapse theories [36]. Thanks to what has been reported above about optomechanics and cryogenics, these aspects are within reach today [20]. Indeed, optomechanical systems as thermodynamic platforms are considered theoretically [37] but without much experimental realisation up to date.

The work of this thesis fits into this research area. Here, we will apply the high sensitivity of nano-mechanical and optomechanical systems to the sensing of basic stationary thermodynamic principles. In Ch. 7, we study the classical backaction of the optical field on the mechanics in an optomechanical platform by engineering artificially an effective high temperature cavity bath. In Ch. 8, we probe the thermodynamic equilibrium of a single mesoscopic mechanical mode, demonstrating all its specific classical signatures. Finally in Ch. 9, we characterise the (classical) interaction between a nano-beam and a rarefied gas, demonstrating

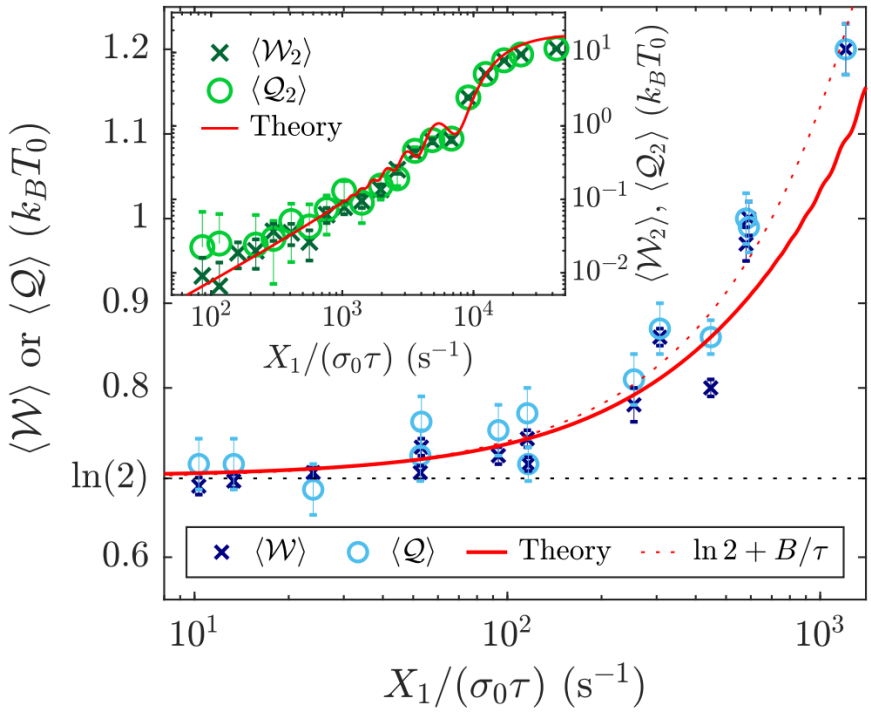

Figure 4: Demonstration of Landauer's erasure principle by ENS group from Lyon

that it can be understood in the framework of a rarefaction phenomenon occurring in the boundary (Knudsen) layer of the gas, when the particle mean-free-path becomes very large. We point out that all of these results are described in terms of classical physics, while a large part of the motivations were turned towards quantum physics. This is deliberate, and the link and analogies between classical and quantum approaches are underlined wherever appropriate. The key point here being that these classical results are a mandatory step, presenting benchmark results, before tackling a new field of physics which presents many exciting speculations. The manuscript is based on the publications which were made during the PhD: see following list.

LIST OF PUBLICATIONS DURING PHD

1. **Beyond Linear Coupling in Microwave Optomechanics**
   D. Cattiaux, S. Kumar, I. Golokolenov, R. R. Gazizulin, A. Luck, L. Mercier de Lépinay, M. Sillanpää, A. D. Armour, A. Fefferman and E. Collin;
   Physical Review Research **2** 033480 (2020)

2. **Microwave Single-tone Optomechanics in the Classical Regime**
   I. Golokolenov, D. Cattiaux, S. Kumar, M. Sillanpää, L. Mercier de Lépinay, A. Fefferman and E. Collin;
   New Journal of Physics **23** 053008 (2021)

3. **A Macroscopic Object Passively Cooled into its Quantum Ground State of Motion Beyond Single-mode Cooling**
   D. Cattiaux, I. Golokolenov, S. Kumar, M. Sillanpää, L. Mercier de Lépinay, R. R. Gazizulin, X. Zhou, A. D. Armour, O. Bourgeois, A. Fefferman and E. Collin;
   Nature Communications **12** 1-6 (2021)

4. **Fully Suspended Nano-beams for Quantum Fluids**
   I. Golokolenov, B. Alperin, B. Fernandez, A. Fefferman and E. Collin;
   Journal of Low Temperature Physics (2022)

5. **Superconducting Aluminum Heat Switch With** 3 $n\Omega$ **Equivalent Resistance**
   J. Butterworth, S. Triqueneaux, Š. Midlik, I. Golokolenov, A. Gerardin, T. Gandit, G. Donnier-Valentin, J. Goupy, M. K. Phuthi, D. Schmoranzer, E. Collin and A. Fefferman;
   Review of Scientific Instruments **93** 034901 (2022)

6. **Thermodynamics of a single mesoscopic phononic mode**
   I. Golokolenov, A. Ranadive, L. Planat, M. Esposito, N. Roch, X. Zhou, A. Fefferman and E. Collin;
   Physical Review Research **5** 013046 (2023)

7. **On the Link Between Mechanics and Thermal Properties: Mechanothermics**
   E. Collin, I. Golokolenov, O. Maillet, L. Saminadayar and O. Bourgeois;
   submitted arXiv:2211.15106

8. **Nano-beam Clamping Revisited**
   I. Golokolenov, S. Kumar, B. Alperin, B. Fernandez, A. Fefferman and E. Collin;
   submitted arXiv:2211.01617

Part I

INSTRUMENTS

In this part we will describe and discuss the main instruments which are crucial for our experiments.

Most aspects mentioned here are well-known or even could be found in textbooks. However, a basic understanding of them is compulsory for a clear view on different problems and questions which will be discussed in further chapters. Besides, some of these technologies have been developed within our group and/or institute. Therefore, they deserve a proper discussion in this thesis.

Out of all state-of-art technologies which were used, we will underline three main ones: Micro- and Nano- fabrication, Microwaves, and Cryogenics. These are keystones of all our investigations.

Micro- and Nano-fabrication, or clean-room fabrication, or NanoFab, is a set of technologies and devices used to create samples with the relevant dimensions of the order of or below a micron. We will briefly discuss methods which are important for basic understanding, show and explain the samples we used with their fabrication procedures and physical parameters. We shall also give a full detailed protocol for state-of-art mechanical nano-device fabrication.

Microwaves, and more specifically microwave detection techniques, have become almost unavoidable for quantum-limited readout of mesoscopic systems, let them be quantum bits or mechanical devices. We will demonstrate the schemes used for our measurements, explain their principle from the microwave's point of view and give a detailed description of their most important elements.

Cryogenics is a way to reach and control the temperature of the investigated media in the range of low and very low temperatures. The techniques required may vary a lot and depend on the needs of every particular experiment. But without a good understanding of thermal properties of materials at low temperatures, it is impossible to conduct any proper temperature-dependent measurements. We will explain methods used to reach, control, and measure temperatures, from about one Kelvin down to milli-Kelvins.

Dans cette partie, nous décrirons et discuterons les principaux instruments qui sont cruciaux pour nos expériences.

La plupart des aspects mentionnés ici sont bien connus ou pourraient même être trouvés dans des manuels. Cependant, une compréhension de base de ceux-ci est obligatoire pour une vision claire des différents problèmes et questions qui seront discutés dans les chapitres suivants. En outre, certaines de ces technologies ont été développées au sein de notre groupe et/ou institut. Par conséquent, ils méritent une discussion appropriée dans cette thèse.

De toutes les technologies de pointe qui ont été utilisées, nous en soulignerons trois principales : Micro- et Nano- fabrication, Micro-ondes et Cryogénie. Ce sont les clés de voûte de toutes nos investigations.

Micro- et Nano- fabrication, ou fabrication en salle blanche, ou NanoFab, est un ensemble de technologies et de dispositifs utilisés pour créer des échantillons avec des dimensions pertinentes de l'ordre, ou en dessous d'un micron. Nous discuterons brièvement des méthodes importantes pour la compréhension de base, montrerons et expliquerons les échantillons que nous avons utilisés avec leurs procédures de fabrication et leurs paramètres physiques. Nous donnerons également un protocole détaillé complet pour la fabrication de nano-dispositifs mécaniques de pointe.

Les micro-ondes, et plus spécifiquement les techniques de détection micro-ondes, sont devenues presque incontournables pour la lecture à la limite quantique de systèmes mésoscopiques, qu'il s'agisse de bits quantiques ou de dispositifs mécaniques. Nous allons démontrer les schémas utilisés pour nos mesures, expliquer leur principe du point de vue des micro-ondes, et donner une description détaillée de leurs éléments les plus importants.

La cryogénie est un moyen d'atteindre et de contrôler la température des milieux étudiés dans la plage des températures basses et très basses. Les techniques requises peuvent varier considérablement et dépendent des besoins de chaque expérience particulière. Mais sans une bonne compréhension des propriétés thermiques des matériaux à basse température, il est impossible d'effectuer des mesures appropriées en fonction de la température. Nous expliquerons les méthodes utilisées pour atteindre, contrôler et mesurer les températures, d'environ 1 Kelvin jusqu'aux milli-Kelvins.

1

MICRO- AND NANO-FABRICATION

1.1 WHAT IS IT ABOUT?

Micro- and Nano-fabrication are a complex set of procedures to design and manufacture various devices, which have their dimensions in a scale ranging from micrometers to nanometers respectively [38, 39]. They includes a broad range of technologies that could be very roughly divided into four categories: adding material on a chip, removing material from a chip, printing a pattern on a chip, and finally checking what you got. Though some of them may fall into more than one category.

Materials can be deposited through evaporation from a bulk source (Electron-Beam physical vapour Deposition [EBD], sputter deposition, Molecular-Beam Epitaxy [MBE]), through immersion of the chip into a solution (cooling crystallisation), or by direct infliction (spin-coating, dip pen nanolithography). If the desired device is developed mainly by one of these ways, it is usually called 'bottom-up' approach. Vice-versa, if the device is mainly fabricated by the removal of a material, it is called a 'top-down' approach. It can be done by chemical etching (wet or plasma) or mechanically (mechanical Scanning Probe Lithography [m-SPL]). Etching can also vary in selectivity: if it interacts with only one material, or with more than one but with different rates. It can vary with orientation as well: if the etching in one chosen direction is much faster than others, or if it etches in all directions at once.

However, these material manipulations are essentially homogeneous over an entire chip, while fabrication usually requires to create specific structures. This is why there is a need to make patterns on chip, which will work as masks for other methods (and specifically for the ones mentioned above). This can be done with different types of lithographies (photo- or electro-). As an alternative, scanning probe lithography also does patterns but it directly deposits the desired material onto the chip. With photo- or electro-litographies, one has to cover the chip first with the proper resist by spin-coating and baking, which then should be exposed by light (laser) or by electron-beam respectively at well-defined places, defining thus the regions which shall either be kept or removed. This choice depends on the type of resist used - positive or negative. Then, the exposed resist has to be developed in a suitable solution.

To check the obtained result, different kinds of microscopy are used: Scanning Electron Microscopy (SEM), Atomic Force Microscopy (AFM), or simply the optical one. Sometimes, to improve results and resolve details below the diffraction limit,

the intrinsic unscattered beam enabling the creation of the image can be excluded: this is called dark field microscopy and can be applied the same way to light and electron microscopy. Also, some chemical or X-ray analysing techniques are very useful to estimate the final quality of a produced device, giving some information about its constitution.

In this chapter we will describe all the kinds of samples used in the present work, we will briefly discuss their fabrication processes and will give their characteristics (Sec. 1.2,1.3,1.4). The sample (fully designed and fabricated by the author) will also have a complete fabrication protocol reported (Sec. 1.5).

1.2 A BEAM COUPLED TO A MICROWAVE CAVITY

For optomechanical investigations we need an optomechanical system, which consists of an optical cavity and a mechanical resonator, coupled to each other. In our case, we decided to take a small step away from classical optics and use a microwave-based setup. The simplest mechanical resonator in the nano-scale range is a doubly-clamped beam, which we shall describe first.

The sample demonstrated on Fig. 5 was fabricated in-house by Xin Zhou, and first used in Ref. [40]; it also appears in Refs. [41, 42]. It has a transmission line coupled to three microwave cavities. Each cavity is realised as a lumped-element resonator, where one end is capacitively coupled to a transmission line and the other end is grounded. A similar sample has been made, where the cavities are simply $\lambda/4$-resonators. Near each not-grounded end there is a metallised Nano-Mechanical beam, Electrically coupled to the microwave System (NEMS) trough a 100 nm gap forming a planar capacitor. The design of the chip allows to measure both in transmission and reflection due to its symmetry.

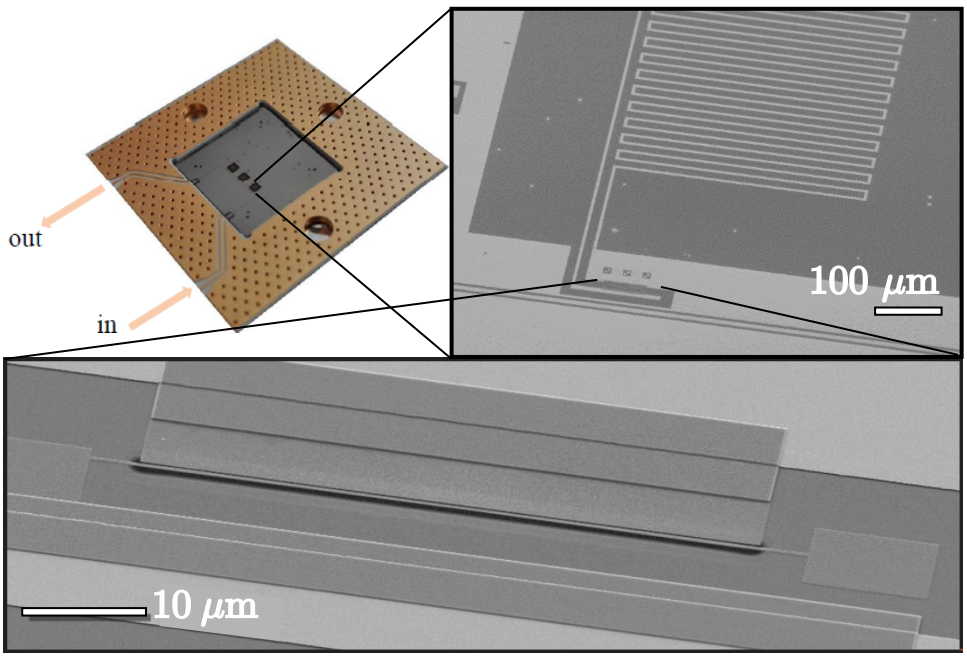

Figure 5: Photos of chip holder, cavity, and NEMS for the beam-based device

The cavities were patterned with laser lithography on a 120 nm thick layer of niobium (Nb), with the following RIE-etching. Typically, their fundamental resonances were at about 6 GHz with a total damping rate of about 150 kHz. The one we used was at 5.988 GHz with a linewidth of 190 kHz. Both parameters are slightly changing with temperature and applied microwave power.

The NEMS element is made from 80 nm thick high-stress silicon-nitride (SiN, 0.9 GPa), which covers the silicon (Si) wafer. It is covered by a 30 nm thick aluminium (Al) layer, which was patterned with e-beam lithography and then a lift-off. SiN was then etched-off with RIE, and the following selective anisotropic XeF_2 etching of Si released the beam. The typical mechanical resonance of such a 50 μm long beam is about 4 MHz with a damping rate of 10 Hz at 100 mK. The one we used was at 3.8 MHz and had an optomechanical coupling of 0.5 Hz.

Various experiments show a weird and unexpected behaviour of beam resonators at low temperatures, usually below 100 mK [40, 43, 44]. This phenomenon is called 'spikes' in the community, but it is not discussed much due to a lack of understanding and consistency between different samples. It is seen as a large out-of-equilibrium random excitation of the mechanical mode, which prevents any proper measurements to be conducted. This is why we will limit our results on beam devices to temperatures above 100 mK.

1.3 A DRUM COUPLED TO A MICROWAVE CAVITY

Beyond quasi-1D beam resonators, quasi-2D drum resonators can be realised and coupled to a microwave cavity. The main difference is that the coupling is realised through a parallel plate geometry, not a planar configuration. Such devices usually have much higher couplings, but smaller mechanical quality factors. Besides, they struggle less from the mentioned 'spikes' issue (for unknown reasons), but are significantly more challenging to fabricate.

We used two different drum samples in our experiments (see Fig. 6): one was presented in [45] (left), and the other one in [24, 46] (right). Both chips were obtained through a collaboration with Aalto University, fabricated by Laure Mercier de Lépinay, and designed for measurements performed in reflection mode.

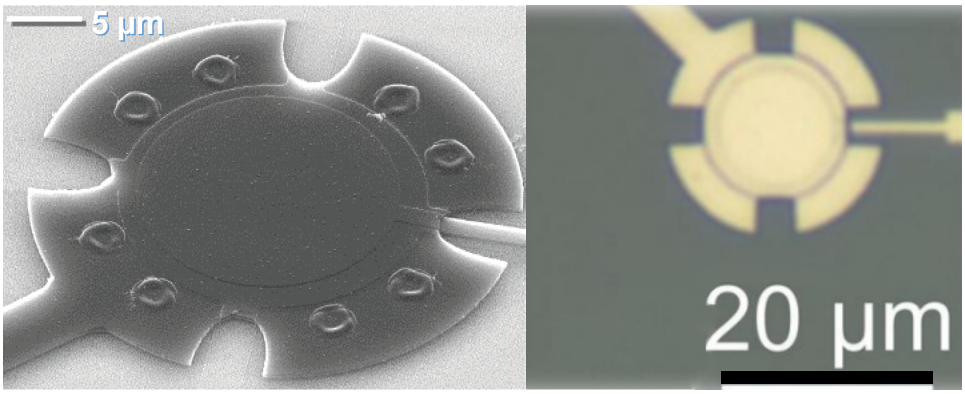

Figure 6: Photos of drumhead NEMS, from Aalto University, courtesy of L. Mercier de Lépinay and M. Sillanpää

They are made of pure Al, on top of a Sapphire or Quartz chips. The first one has a microwave cavity resonating at 6.8 GHz with a total damping rate of 4 MHz, with a 10 μm drum-head element which resonates at 6.7 MHz with a typical damping rate of 150 Hz at 50 mK in its first flexure. The single photon-phonon (optomechanical) coupling strength was measured to be 10 Hz. The other one has a cavity resonating at 5.15 GHz with a total damping rate of 230 kHz, with a 15 μm drum-head which resonates at 15.1 MHz with a total damping rate of 420 Hz at 100 mK. The optomechanical coupling was measured to be 220 Hz. This is an extremely high coupling for such devices, which makes this sample the most useful and promising for the lowest temperatures (since it requires less readout microwave power).

1.4 ARRAY OF BEAMS WITHOUT SUBSTRATE

Nano-mechanical beams which resonate in the MHz range can be used as non-invasive sensors for low temperature physics. An exemplary realisation of this is the study of quantum fluids with nano-mechanical probes, using the magneto-motive detection scheme that shall be discussed later on in the manuscript (see Ch. 5 and 9). When probing fluids, finite size effects should be addressed and can even play a dominant role when the mean-free-path of excitations exceeds the size of the experimental space [47]. However, fabrication of mechanical resonators which would be suspended at a distance larger than ≈ 1 μm from the underlying substrate is quite complex and demanding. For quantum fluids, this is a strong restriction which needs to be overcome. Here, we demonstrate the realisation of samples, which are freely suspended (no suspension trench), and give their typical characteristics. In the next section, we will detail the recipe to fabricate them.

We have made a series of samples with Al (40 nm thick) covered SiN (100 nm thick) beams stretched over a hollow window in Si. Each realised chip has 8 arrays of 5 beams over a square hole. These holes are of four lateral sizes: 100 μm, 200 μm, 300 μm and 400 μm. In an array, in order to make the beams' resonances not overlap in frequency, we varied their widths with a step of about factor of 2, having: 60 nm, 120 nm, 250 nm, 500 nm and 1 μm widths. This design allows to minimise any variations of resonators parameters between each other within a chip, except only for their width, which stays variable. In Fig. 7, one can see an example of final result for 400 μm long beams.

Resonance frequencies of such beams are inversely proportional to their lengths and slightly dependent on their widths, for example for 100 μm long beams these frequencies are: 906 kHz, 1006 kHz, 1089 kHz, 1189 kHz and 969 kHz respectively for 1 μm, 500 nm, 200 nm, 100 nm and 50 nm (we have 2 sets of identical lengths and widths in order to improve the success rate in fabrication). Quality factors vary a lot, but never drop below $3 \cdot 10^4$ and could be as big as $2 \cdot 10^5$. More results will be given in Ch. 4 and 5.

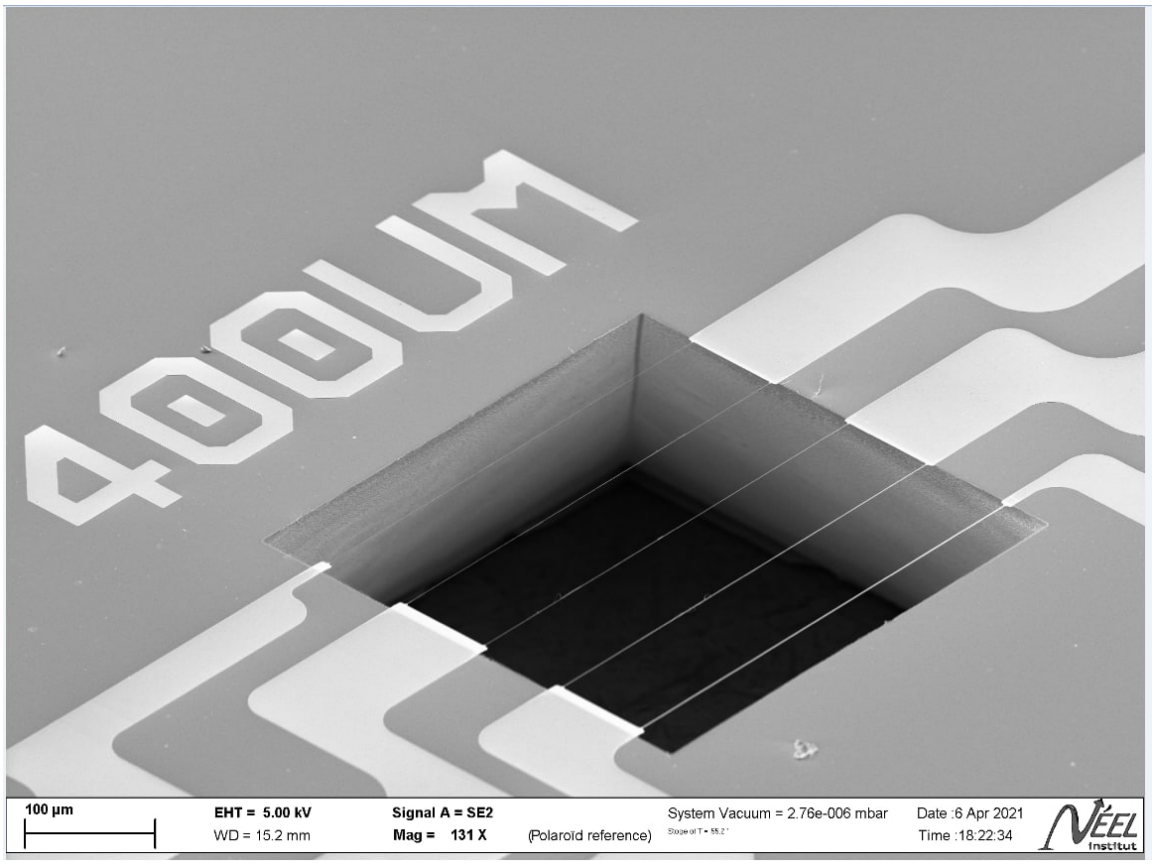

Figure 7: SEM of an array of fully suspended beams

1.5 FABRICATION PROTOCOL FOR FULLY SUSPENDED BEAMS

Required (used) equipment: laser lithography tool (Heidelberg Instruments DWL66$^+$), electron lithography tool (NanoBeam NB5), reactive ion etching machine (PLASSYS), e-beam evaporator (PLASSYS and SupraFAB), spin-coater, fume hood, thermostat, diamond scriber, tweezers, beakers.

Required chemicals: Deionized H_2O, Ethanol, Isopropanol (IPA), Acetone, KOH, photoresist S1805, Microposit Developer, electron-resist PMMA 3%, MIBK (Methyl-Isobutyl-Ketone), NMP (N-Methyl-2-Pyrrolidone), precurser HMDS.

Protective gear: Nitrile gloves, latex gloves, goggles, cleanroom overalls.

Recipe

Step 1: Cleave and clean (20 minutes)

- Take Silicon wafer covered with 100 nm SiN on both sides, mirror polished
- Mark squares 11 $\times$ 11 mm and scribe them with a diamond scriber
- Carefully cleave them without damaging the surface (use cleanroom paper)
- Clean obtained squares in acetone for 2 minutes, then rinse in ethanol, and dry with nitrogen

Step 2: Laser lithography for membranes making (40 minutes)

- Choose better side of the sample and spin resist S1805 at 6000 RPM for 30 s and bake for 1 min at 115° C
- Turn over sample and spin precursor HMDS at 6000 RPM for 30 s
- Spin resist S1805 over precursor at 6000 RPM for 30 s and bake for 1 min at 115° C
- Do laser lithography of squares with side of $x + 2 * 0.7 * d$, where x - planned size of membrane, and d - Silicon thickness, example in Fig. 8a

Step 3: Resist development and SiN etching (30 minutes)

- Develop resist in Microposit Developer : DI water (1 : 1) for 1 min and rinse in DI water, and dry with nitrogen
- Etch with Reactive Ion Etching (RIE) in SF_6 at 20 W for 3.5 min to remove SiN
- Clean sample in acetone for 2 minutes, then rinse in ethanol, dry with nitrogen, and turn over to better side

Step 4: KOH etching (13 hours)

- Put sample in KOH at 80° C for $\sim$ 11 hours to remove Si under removed SiN, arranging it vertically
- In all of the following steps put and remove sample in any liquid vertically, and before laying horizontally on cleanroom paper, touch it with sample corner to let it suck any liquid to protect membranes
- Rinse in DI water after KOH and with nitrogen at small flow
- Put sample in HNO_3 at 80° C for 1 hour to clean from any products of KOH etching

- Clean in ethanol for 1 min and dry with nitrogen at small flow

Step 5: Marks and labels (3 hours)

- Spin precursor HMDS at 6000 RPM for 30 s and spin resist S1805 over precursor at 6000 RPM for 30 s and bake for 1 min at 115° C
- Center coordinates in laser lithographer based on membranes position
- Do laser lithography of marks for e-beam lithography and necessary labels as in Fig. 8b
- Develop resist in Microposit Developer : DI water (1 : 1) for 1 min and rinse in DI water, dry with small flow of nitrogen
- Etch with RIE in O_2 at 10 W for 30 sec
- Using e-beam evaporator deposit 5 nm of Ti and 35 nm of Au with deposition rate $\sim$ 0.1 nm/s
- Lift-off in Acetone for 1 hour, use pipette to remove unnecessary metal, rinse in ethanol, dry with small flow of nitrogen

Step 6: E-beam Lithography (3 hours)

- Spin resist PMMA 3 % at 6000 RPM for 30 s and bake for 5 min at 180° C
- Do e-beam lithography of beams at 1 nA and of pads at 30 nA with dose of 300 μ C/cm^2 as in Fig. 8c and in Fig. 8d
- Develop resist in MIBK:IPA (1 : 3) for 35 sec, rinse quickly in IPA and for 1 min in another beaker of IPA
- Etch with RIE in O_2 at 10 W for 10 sec
- Using e-beam evaporator deposit 40 nm of Al with deposition rate $\sim$ 0.1 nm/s
- Lift-off in NMP for more than 5 hours, use pipette to remove unnecessary metal, rinse in IPA, and dry with small flow of nitrogen

Step 7: Membranes etch-off (15 minutes)

- Use RIE at 20 W with SF_6 without sample inside for 2.5 min
- Etch membrane off with RIE in SF_6 at 20 W for 3.5 min
- Control the result with optical microscope in a dark field, beams should be clearly visible

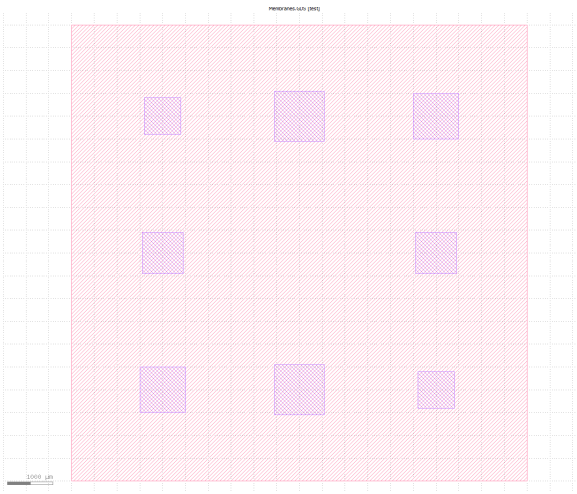

(a) Example of drawing to make membranes

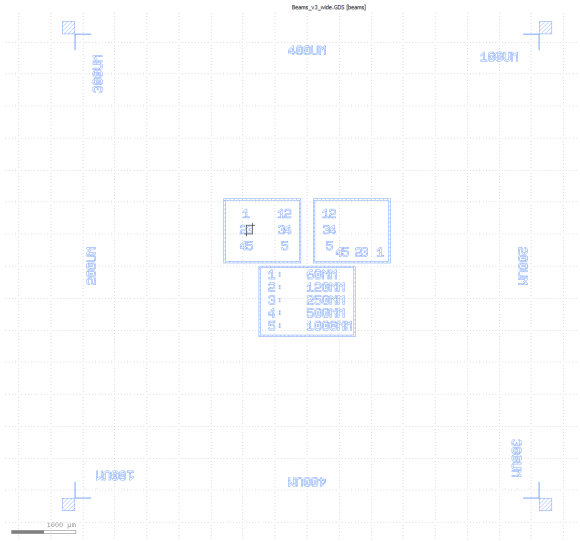

(b) Example of drawing to make marks and labels

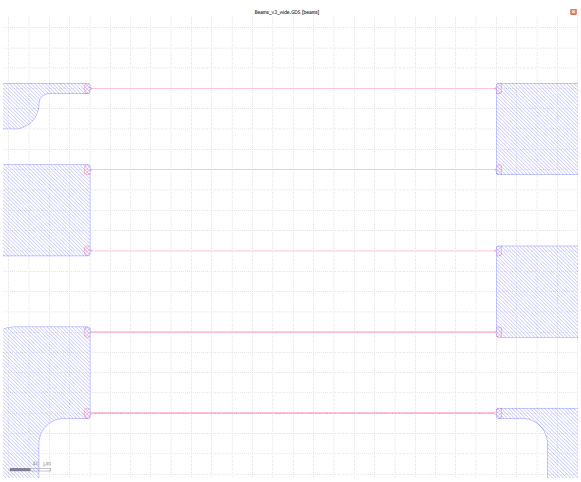

(c) Example of drawing of beams

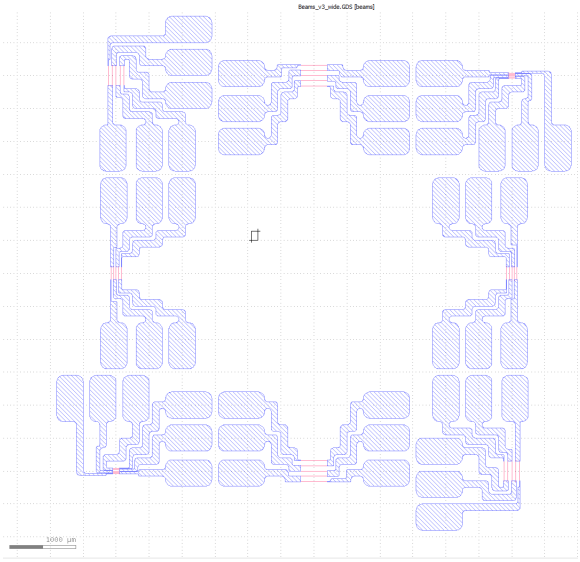

(d) Example of drawing of pads

Figure 8: Examples of drawings for the fabrication

2

MICROWAVES

2.1 WHY MICROWAVES?

Microwaves is the conventional name for alternating electric current (AC) or voltage in a range of frequencies ranging typically from 1 GHz to 30 GHz, but the precise definition of that range may vary in literature. It is part of the much larger family of radio frequency (RF) signals. Microwaves are widely used in communication, navigation, radio astronomy, and even simply to heat up some food. However, none of these applications are relevant to us: here, we are concerned with microwaves signals used for quantum-limited measurements. More specifically, we will describe their use for optomechanics, when a microwave pump tone excites a microwave cavity that is coupled to a MHz mechanical resonator.

As one could notice, all of our devices have cavities with resonance frequencies in the range from 5 GHz to 7 GHz. It appears to be so for several reasons. One is that the cavity frequency ω_c should be orders of magnitude larger than the frequency of the mechanical resonance Ω_M. Also, we want to have sideband-resolved measurements (see Ch. 6), which means that Ω_m should be bigger than the total damping rate of the cavity. This sets an upper limit on the cavity frequency, as with increasing ω_c we would have to increase the cavity quality factor proportionally, which is not always possible. Besides, the higher the frequency, the more complex, demanding, and expensive the measuring scheme is. At the same time, lower frequencies require physically longer coplanar waveguide resonators (as it should correspond to at least a quarter of the wavelength), which will take more of the precious space on a chip. Nonetheless, lower frequencies are beneficial to low temperature experiments, since each injected photon in the setup carries less energy and will cause less over-heating problems. This is why microwaves are more adapted than lasers for cryogenics measurements.

So, for the majority of our devices, microwaves are in the so-called golden middle [48]. This is not only a practical aspect, this is also mandatory if one wants to perform quantum-limited measurements: in this range, one can use all the resources developed for quantum technologies (high quality passive components, low-noise cryogenic amplifiers, and even quantum bits). In addition, some experiments which did not require quantum-limited schemes have been performed without microwave readout. These relied on a direct detection of the mechanical resonances in the MHz range by using the magnetomotive technique which shall be described in Ch. 5.

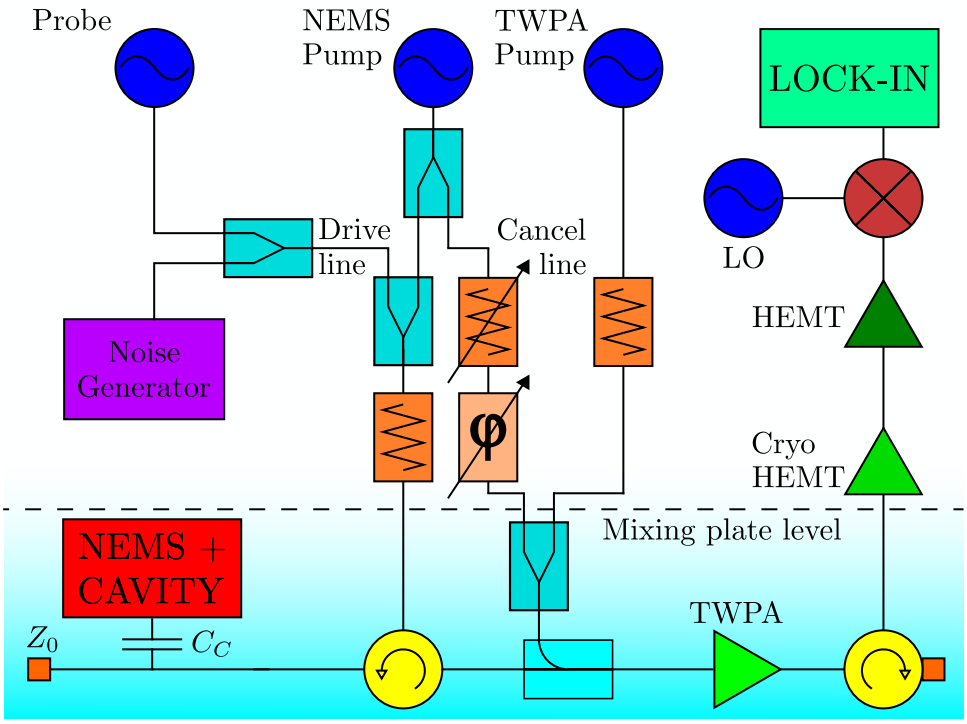

Figure 9: Generic microwave measuring scheme

2.2 CIRCUITRY AND CABLING

On Fig. 9, the most generic elements of our measuring schemes are shown. We will give an overall review of them, and in the following section will analyse each element more precisely. This scheme includes all elements ever used, but they are not necessarily needed for each independent experiment at hand.

All samples were measured in the reflection regime, but only the beam-based sample has a $Z_0 = 50\ \Omega$ load (orange square), because of its evanescent-coupling design to the measurement line (capacitor C_c). For drum devices, the line directly terminates onto the sample through the coupling element C_c.

The scheme divides into two main parts: injection and detection. The injection comes from different microwave generators: either as a monofrequency (pumps and probe - blue circles), or as a white random signal (noise generator - violet rectangle). These signals combine through power combiners (light blue rectangles) and all thermalise in the cryostat through a series of attenuators (orange rectangles). Attenuators are also required to protect the sample from room temperature noise, which they suppress. All optomechanics-related injected signals go to the sample (red box) through a circulator (yellow circle, on the left) - a specific passive microwave element with $3-4$ ports, which allows an electromagnetic wave to go from port 1 to port 2 without almost any losses, but any signal from port 2 to port 1 is suppressed by at least 20 dB (100 times in power; and likewise between ports 2 and 3, and 3 and 1). The arrow in the yellow circles depicts the allowed direction for microwaves. Thanks to this element, we can direct the microwave input signals towards the sample solely and send its output to the amplifier chain. Any noise

coming from this chain would be directed towards the input line, thus protecting the sample.

The signal from the sample goes to a chain of amplifiers (green triangles): a Travelling Wave Parametric Amplifier (TWPA), a low noise cryogenic High Electron Mobility Transistor (HEMT) amplifier, and room temperature HEMT amplifier. But before entering any of these amplifiers, the signal to be detected has to be combined with a 'cancellation signal' (also called 'opposition', Sec. 2.5) and a pump tone powering the TWPA. For this purpose we use a directional coupler instead of a power combiner, since it has negligible insertion losses for the main signal, while a power combiner is fully symmetric and has at least 3 dB losses for each port. The opposition line is required to cancel any leftover from the NEMS pump which could leak-out from the sample or sneak through the circulator. This is mandatory since injection signals may saturate the highly sensitive amplifiers we use. The second circulator is there to protect the TWPA from noise coming from the cryogenic HEMT.

After all the amplifiers, our NEMS signal comes to a mixer (maroon circle, see Sec. 2.3), which multiplies it with a Local Oscillator tone (LO, monofrequency generator). This enables us to shift our signal from the GHz range down to the MHz one and allows us to detect it with an ultra-sensitive lock-in (green rectangle, Sec. 2.4). The probe tone is needed for measuring the cavity in 'Vector Network Analyser (VNA) style', by sending a signal at a defined frequency and detecting it at the same frequency with the lock-in. This enables us to construct the microwave susceptibility curve of the cavity resonance, see e.g. Fig. 38 in Ch. 6. For precise quantitative measurements, one should measure the cavity while applying the microwave pump tone needed for the optomechanics experiments, since the cavity parameters may change with pump settings. This is particularly true of the Nb cavity used for the beam experiment, which has a very high Q; the Al cavities of the drum experiments are much more stable with respect to the pump parameters.

Most of the microwave equipment is commercial, except for the TWPA (see Sec. 2.7, soon to be commercialised), the NG (see Sec. 2.6), the sample holders, and cryostat wiring, which were all made in-house. To guarantee that all our measurements are precise in a quantitative sense, we have to calibrate our microwave circuitry with as high as possible precision. This is harder than it may seem, as each single element and junction has losses, even cables, and the gain characteristics of every amplifier is not perfectly flat as a function of frequency. We took special care to keep our absolute calibration error bars within ± 1 dB to ± 2 dB.

2.3 MIXER

We use a Marki® mixer to shift our signal from the GHz range to the MHz one. The mixing process of the signal from the sample V_s with demodulating frequency ω_d can be formally written as:

$$[\alpha V_s \times cos(\omega_d t)]_{\text{filter}} = V_d(t). \tag{1}$$

In Eq. 1: α is total losses and gains on the way from the sample to the mixer in the detection chain, and V_d is the demodulated signal after mixer, which can be written as:

$$V_d = \frac{\alpha}{2}\left[\left(\frac{V_{meas}(t)e^{-i(\overbrace{\omega_n-\omega_d}^{\Delta\omega})t} + V^*_{meas}(t)e^{+i(\overbrace{\omega_n-\omega_d}^{\Delta\omega})t}}{2}\right) + \left(\frac{V_{meas}(t)e^{-i(\omega_n+\omega_d)t} + V^*_{meas}(t)e^{+i(\omega_n+\omega_d)t}}{2}\right)\right]. \tag{2}$$

In Eq. 2: V_{meas} and ω_n are the magnitude and frequency of the GHz signal respectively, which is of interest to us. Indeed, mechanical motion imprints (in the sideband-resolved limit) clear peaks in the microwave spectrum at frequencies $\omega_n = \omega_c + n\,\Omega_M$ (where n is an integer). Depending on the scheme chosen (see Sec. 6.5), we shall measure at $n = 0, +1, -1$ typically. With the right choice of ω_d, the first term of Eq. 2 (which is shifted at $\Delta\omega = \omega_n - \omega_d$) can be within the MHz range, perfectly adapted to our lock-in detection. The second component (at $\omega_n + \omega_d$) remains in the GHz domain and is easily filtered by the lock-in.

However, we should not forget about the component of the signal at $\omega_{n'} = \omega_d - \Delta\omega = \omega_n - 2\Delta\omega$, as it is the same for the mixer as the one at ω_n. That basically implies that the background noise at these two frequencies will be summed: for us, it means that the noise just doubles if we compare a direct measurement in the GHz range to the MHz-shifted one (these frequencies are not too far from each other, so the noise amplitudes are reasonably identical and they are not correlated). Note that we should choose ω_d such that the signal will not mix with anything else; especially when a full comb of peaks is present (i.e. with self-oscillation experiments, Sec. 6.7), the components should not overlap. This is fairly easy to manage.

2.4 LOCK-IN

The cornerstone of our detection scheme is a high-quality lock-in. We use a Zurich Instruments® (ZI) UHFLI lock-in amplifier, which had at the time the highest operation frequency among all commercial lock-in amplifiers (with a frequency range from direct current (DC) to 600 MHz). It can run in two modes which are relevant to us: 'Scope' and 'Spectrum'.

A lock-in amplifier is primarily a type of amplifier dedicated to the extraction of a signal with a known carrier frequency from the noise. It uses heterodyne detection (the signal is compared to a given reference, which is used for demodulation), and filtering (only the slow demodulated component is kept). To do this reliably, it needs a strong and clean reference wave. The basic principle of an analog lock-in is the mixing of an input signal U_{in} with a reference at frequency ω_{ref}, averaging then over time τ:

$$U_{out}(t) = \frac{1}{\tau}\int_{t-\tau}^{t} \sin\left(\omega_{ref}x\right)\cdot U_{in}(x)\,dx = \frac{1}{2}V_{sig}(t)\cos(\theta), \tag{3}$$

with V_{sig} - magnitude of input signal at reference frequency and θ - its phase difference with input. This is basically the 'Scope' mode of the ZI.

With modern digital lock-ins, the variety of possibilities is far broader. With dedicated digital signal processors, they allow to extract in-phase and quandrature components of the signal at the same time and can process them further as complex numbers, for example applying complex Fast Fourier Transform (FFT) analysis. By demodulating input signals at a given frequency and processing them with FFTs, one can acquire the spectrum of the measured signal, shifted in frequency by the demodulating reference (just as with a mixer). The window of that spectrum and resolution can be tuned by data-acquisition settings within the lock-in. This is the 'Spectrum' mode of the ZI.

2.5 OPPOSITION LINE

The opposition line, as it was already mentioned, is required to cancel the remaining optomechanical pump signal in order to prevent any saturation of the amplifier . To do this, we split the optomechanics pump tone right after the generator, half of it being 'pump' and the other half being 'opposition'. On the latter half, we adjust the magnitude and phase to be exactly opposite to any pump leftover reaching the first amplifier stage. The very same concept is used nowadays in noise-cancellation headphones.

This cancellation is performed by a computer that periodically checks the pump amplitude on the output and adjusts a voltage-controlled attenuator and phase shifter on the opposition line (see realisation in Fig. 10). The computer performs a sort of dichotomy, trying to reach within a programmed loop a given remaining pump magnitude setting. We can suppress this pump leftover by at least 60 dB. At the smallest, it is mostly limited by the detection scheme sensitivity and we

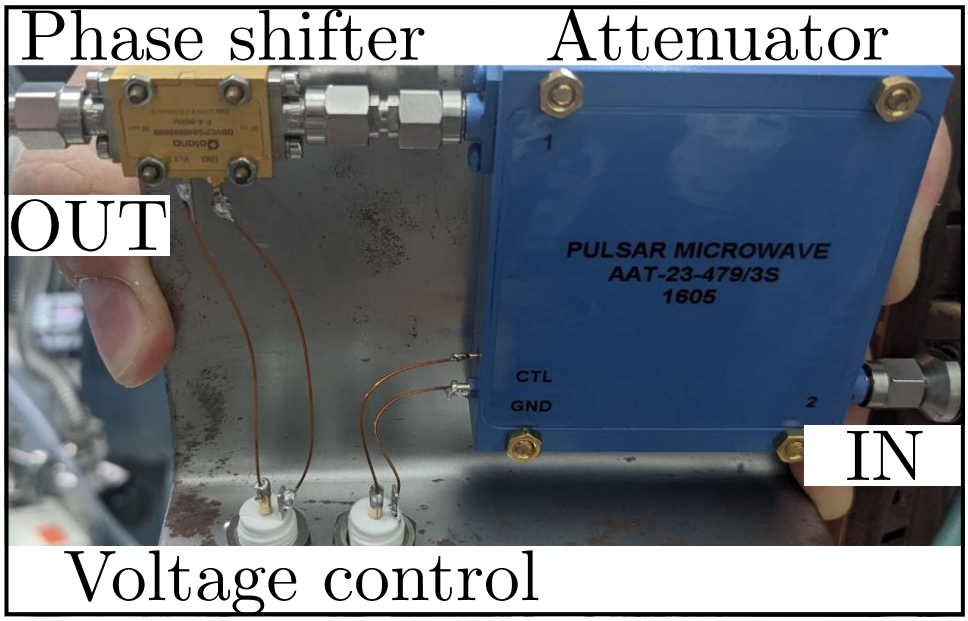

Figure 10: Voltage controlled opposition line

just cancel the pump signal to the level of the background noise. But at high powers, everything tends to drift significantly due to heating at different parts of the chain. This is why we can not measure for too long at relatively high powers, as the opposition settings will deteriorate quickly. It can be slightly prolonged towards even higher powers by extending the cancellation preparation time: tune it longer to compensate for drifts due to the heating of various elements. But it is still limited.

2.6 NOISE GENERATOR

The NG is used to apply an external noise to the microwave cavity in a controlled way, which allows to artificially tune its effective temperature from below 1 K up to about 300 K, while keeping it superconducting. This enables us to work with the microwave cavity mode in the classical regime while preserving good quality factors.

This NG is made of two HEMTs in series (total gain 64 dB), connected on one side to a 50 Ω load and on the other to a $4-8$ GHz filter, all at room temperature. At the frequency of the cavity ω_c, the applied microwave noise spectrum is essentially flat, with an amplitude E_{noise} that can be quantitatively expressed in terms of photon number $E_{noise}/\hbar\omega_c$ (in our case about 1000 photons). See Fig. 11 for the actual noise spectrum of NG; the inset shows a zoom on working frequencies around 5.15 GHz. The noise level is tuned by inserting fixed attenuators in the circuitry, which leads to an uncertainty (from screwing/unscrewing) of about ± 1 dB in noise level.

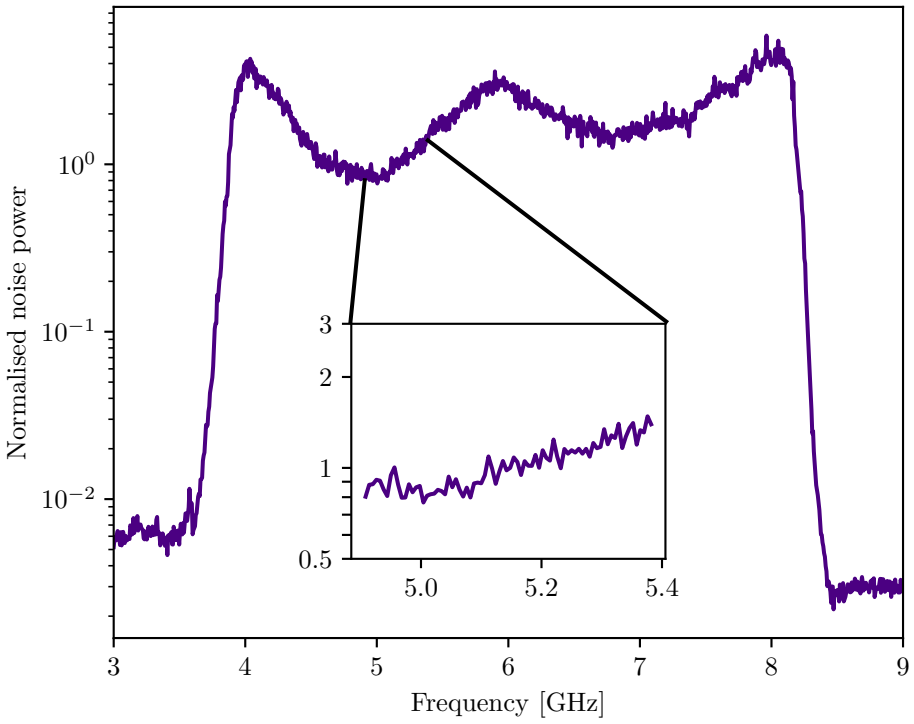

Figure 11: Normalised power spectrum of the NG by noise power at 5.15 GHz

On the detection side we have a cascade of amplifiers - TWPA, cryo-HEMT, and room temperature HEMT. All of them have two important parameters: gain at the working frequency and noise at the input. The cryogenic HEMT provides a gain of 40 dB while the room temperature one has 30 dB. The microwave noise background around 6 GHz, referenced at the input of the cryo-HEMT, is about 2.5 K; the noise of the room temperature apparatus is then negligible for us. This is what is obtained from measurements performed before the mixer with a spectrum analyser; when using the mixing technique, we obtain twice this background, as explained in Sec. 2.3.

Travelling Wave Parametric Amplifiers (TWPA) are the next step towards quantum limited detection. They are the latest evolution of Josephson Parametric Amplifiers (JPA). The important feature of parametric amplification is the absence of extra added noise to the signal by the amplification itself (beyond the quantum backaction), and JPAs already allow to have state-of-art quantum limited detection: ultimately, adding only one quantum $\hbar\omega$ for a detection at ω. However, JPAs have to be designed and made for each independent experiment, as they have a very narrow amplification bandwidth and very low saturation level, even though there have been great improvements in these directions [49, 50]. This is due to their resonant-based architecture. One of the solutions is to switch to a distributed non-linear based amplification, such as Kerr-nonlinearity based travelling wave tube amplifiers used in optics [51]. Transposed to superconducting circuits, this kind of device is precisely what a TWPA is. The idea behind its working principle is that a continuous non-linear medium, through which a signal wave travels along with a pump wave, enables to transfer energy from one to another all along the transmission. There are different realisations of that concept, from first demonstration based on the non-linearity of NbTiN films, to Superconducting QUantum Interference Devices (SQUID) based TWPAs [52], which is nearly quantum-limited. This is the one we have, provided by Silent Waves®.

At the lowest temperatures, the TWPA gain around 6 GHz is of order 10 dB, and up to $20-25$ dB around $4-5$ GHz. The insertion loss of 'TWPA+directional coupler+circulator' is about 4 dB at 6 GHz. The gain degrades quickly as we go above 300 mK, which corresponds approximately to $T_c/3$ for the Al superconducting transition. Besides, the intrinsic noise of the TWPA itself increases dramatically above this limit (because of free quasi-particles thermally excited in the Al layer, see Fig. 12). Typically, it can still be used up to 400 mK with some gain, and for higher temperature measurements it should be removed from the chain.

The measured noise of the full setup referenced to the input with the TWPA amplifier 'on' is shown in Fig. 12 (all gains are taken into account, TWPA plus the two HEMTs). As we increase the temperature T, we see a thermal increase in this noise (main graph, guide line below 350 mK). This contribution comes from the two 50 Ω loads (before and after the parametric amplifier, Fig. 9), but mostly from the TWPA itself. The $T \to 0$ noise amplitude is about 0.8 K: We obtain about 0.55 K from the TWPA plus 0.25 K which corresponds to the cryo-HEMT

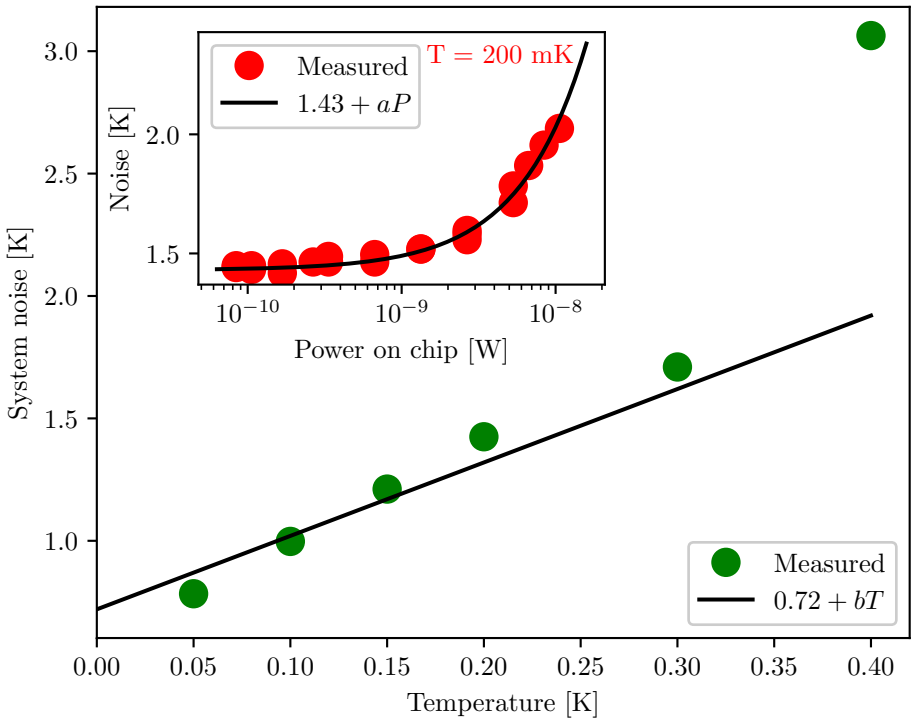

Figure 12: TWPA noise as a function of temperature (main) and power on chip (inset); Lines are linear guides for the eye

contribution; the total noise at $T = 0$ K is thus about 3 photons, which matches expectations [52]. This is by definition 3 times the Standard Quantum Limit (SQL).

In the inset of Fig. 12, we show the input power dependence of the measured noise: the background level increases with P_{in}. By measuring the cavity spectrum, we observe that this is actually due to an out-of-equilibrium photon population that increases with the pump power [40]. By using different microwave sources, or adding a notch filter, we can demonstrate that this noise is directly related to the quality of the pump signal (and not to a physical heating of an element of the circuitry). The actual power dependence seems to depend on the setup: it looks reasonably linear in Fig. 12 which is different from the findings of Ref. [40].

3

CRYOGENICS

3.1 WHAT IS CRYOGENICS?

Cryogenics (from *Greek* 'kryos' - cold, and 'genic' - to produce, to generate) - is a generic term that defines a complex set of devices and technologies used to achieve and sustain low, very-low, and ultra-low temperatures [53, 54]. The term can also be used as a name for the part of low temperature physics which investigates solid matter properties within the very/ultra-low temperature range, or as a name for the Science which develops and improves cryogenic technologies.

There is no precise international definition for low, very-low, and ultra-low temperatures due to disagreements between different fields of physics and techniques. This is why we shall call everything in the Kelvin range low temperatures, in the milli-Kelvin range very-low temperatures, and everything below: the ultra-low temperature domain (ULT). Nowadays, it is quite common to work at low and very-low temperatures because of a large variety of commercial solutions, such as BlueFors®, Oxford Instruments®, Leiden Cryogenics®, etc. However, there are no available options to reach ultra-low temperatures on the market yet. One requires a so-called nuclear demagnetization cryostat. There are propositions and a reasonably well-defined market for a ULT commercial solution in the future [55]. But these projects are still under development, and the ULT users are used to maintain homemade nuclear demagnetisation cryostats.

Table 1: Refrigeration techniques from Ref. [53]. The methods which dominate in the three temperature ranges are in bold. These methods will be explicitly described in further sections.

	Temperature range	Refrigeration technique	Available since	Typical T_{min}	Record T_{min}
I	Kelvin	Universe			2.73 K
		Helium-4 evaporation	1908	1.3 K	0.7 K
		Helium-3 evaporation	1950	0.3 K	0.23 K
II	Milli-Kelvin	**^{3}He - ^{4}He dilution**	1965	10 mK	2 mK
		Pomeranchuk cooling	1965	3 mK	2 mK
		Electronic magnetic refrigeration	1934	3 mK	1 mK
III	Micro-Kelvin	**Nuclear magnetic refrigeration**	1956	100 μK	1.5 μK

Besides, even with commercial setups, the question of having proper thermometry and good thermal contacts along with correct pressure measurements remain very important and deserves to be discussed in the present Chapter.

3.2 HELIUM-4 CRYOSTAT

Perhaps the simplest and the most wide-spread type of cryostats (at least before the quantum computing boom) is a Helium-4 cryostat. It basically consists of a helium dewar with a pump and a manometer connected to it. In our case we also include a superconducting magnet, an inner vacuum chamber (IVC) with pressure control, and a heater+thermometer, along with measuring wires. Schematics can be seen in Fig. 13. The source of the cooling power is liquid Helium-4 evaporation, with a boiling point at atmospheric pressure of 4.2 K. One can cool even lower by pumping Helium vapours down to $1.2 - 1.5$ K. The main drawback of that method is a large consumption of the cryoliquid, as it has to cool down the whole bath inside the dewar. This leads to an evaporation of more than 50% of the initial (full) amount of liquid. This problem can be solved by inserting a so called 1K-pot into the setup, but for our purposes it is excessive and shall not be done.

Despite its simplicity, our Helium-4 setup allows us to work at temperatures in the range of $1.5 - 30$ K with magnetic fields up to 2 T. We can also add gas to the IVC, with a pressure control in the range of $10^{-3} - 20$ Torr or keep the IVC under vacuum at approximately 10^{-6} Torr.

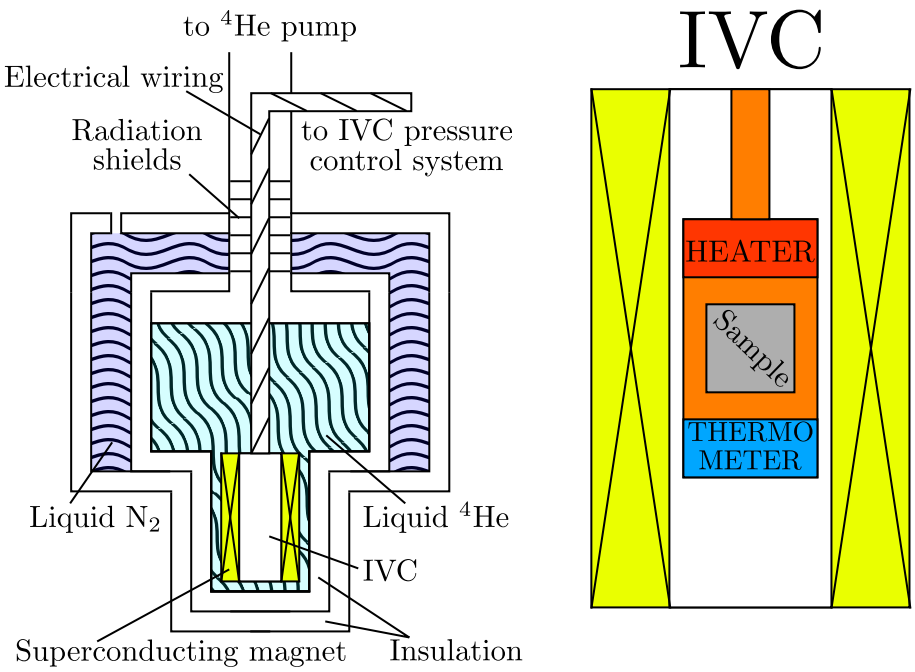

Figure 13: Schematic of Helium-4 cryostat (left) with zoom-in of IVC (right)

3.3 THERMOMOLECULAR PRESSURE DIFFERENCE

Due to the small size of our IVC and its location in liquid Helium-4, there is no possibility to easily add a pressure sensor inside this chamber. That is why usually in similar setups the pressure is measured with a room-temperature manometer, which is connected to the measured volume through a pipe or a capillary. However, when the measuring volume and the measured one are at different temperatures, the pressures in them (which is a little bit counter-intuitive) could be slightly different. This effect is usually called the thermomolecular effect or thermomolecular pressure difference.

The main criteria for its appearance is the characteristic size of the connecting capillary, along with the temperature difference, the pressure range and the kind of gas present in the chamber. As such, a thermomolecular pressure difference takes place if the two volumes are at different temperatures and are connected with a long capillary of a diameter $d \leq \lambda$, where $\lambda = k_B T/(\sqrt{\sigma} P)$ is the mean-free-path of gas molecules (T - temperature, σ - effective cross-section area for gas molecules, P - pressure). In that limit, the gas thermalises with the capillary walls and not within itself (through molecular shocks). This condition is also called the ballistic regime.

In equilibrium, the number of gas molecules $\dot{n}$ which are moving per unit time from the hot volume to the cold volume should be equal to the amount of gas molecules which are moving in the opposite direction. For the ballistic regime, this statement can be written as:

$$\dot{n} \propto nv = \frac{N}{V} \cdot \sqrt{\frac{2k_B T}{m}} \propto \frac{P}{T} \cdot \sqrt{T} = \frac{P}{\sqrt{T}}, \tag{4}$$

$$\frac{P_{cold}}{\sqrt{T_{cold}}} = \frac{P_{hot}}{\sqrt{T_{hot}}}. \tag{5}$$

Deeply in the ballistic limit, one could thus recalculate the cold point pressure from the room temperature measurement. However, for intermediate situations between conventional gas flow and the ballistic regime, the precise correction that should be applied is not trivial [56] and requires a good knowledge of the setup (pipe diameters, length). It is therefore easier to control the dimensions of our connecting tube and avoid $d \leq \lambda$. This is precisely why our IVC is connected to our manometer with a 1 cm diameter pipe. With such a size and Helium-4 as a gas, the thermomolecular pressure difference will start to appear at pressures below typically 10^{-2} Torr, which is anyway the lower limit of our manometer.

3.4 THERMOMETRY

To know well the temperature of a sample, it is quite simple on paper: one just needs to bring it into good thermal contact with any proper temperature sensor. Such a sensor has to have a clear and well-known temperature dependence of some measurable physical parameter. However, in the range of low and especially

ultra-low temperatures, both aspects (thermal contact and simple temperature-dependent law) become challenging.

All sensors are usually divided into two types: primary and secondary. With a primary sensor, one directly measures a property which follows a well-known physical law. In principle, this T-dependence should not depend on any calibration and would just give directly temperature in its working range: it can be used to construct the Kelvin temperature scale [57]. However, this definition can be reinterpreted with a bit of freedom, arguing that a single point calibration (leading to a scaling factor, essentially) is usually not an issue. These sensors are often referred to as semi-primary. In order to avoid terminology issues, we shall call all of these (primary and semi-primary) primary thermometers. In contrast, with secondary thermometers every sensor could have its own T-dependence for a given target physical quantity, which is why they require to be calibrated in the first place. Preferably, against a primary sensor (in order to avoid the propagation of errors); only then, can they be used in a reliable way.

The interest in using secondary thermometers is purely practical: these are usually cheap, easy to use, and install. For low and very-low temperatures, secondary sensors are commonly resistors of different kinds for different temperature ranges: platinum, RuO_2, carbon, etc. In our experiments, we are mostly using carbon resistors, home-calibrated. Resistors are very convenient and simple to measure, with specifically designed bridges that guarantee very low parasitic heatings. Our setups are equipped with the home-made TRMC2 equipment.

With primary thermometers, the situation is a bit more varied and complex: for different ranges, completely different working principles might be used. But for the whole domain encompassing low, very-low, and ultra-low temperatures, the properties of Helium can be helpful. For the Kelvin range, the simplest primary thermometer is the tabulated equilibrium vapour pressure of Helium-4 (from 1 K to 4 K), and similarly of Helium-3 (from 0.3 K to 3 K) [58]. For the milli-Kelvin range, the melting curve of Helium-3 can be used (from 1 mK to 2 K) [59]. And for the micro-Kelvin lowest temperatures, the Helium-3 viscosity (from 100 μK to 100 mK) is a reasonably simple option [60]. Besides, noise thermometry covers all these temperatures from essentially a few 100 μK up to a Kelvin.

Helium-3 viscosity thermometry, in both the normal state and the superfluid one, is implemented on our nuclear demagnetisation cryostat DN1 (see Sec. 3.6). It is measured in a dedicated double-wall cell with two quartz tuning forks (one in the outside part and the other one inside). The inside cell is in good thermal contact with the copper (Cu) nuclear stage by means of silver wires, while the outside one works as a thermal shield. As a mechanical resonator (as our tuning forks) is dragged within a viscous medium, its motion is affected by friction. By measuring this extra damping on our resonators, we can know the temperature from the tabulated Helium-3 viscosity [40]. It is also very convenient since Helium-3 goes through a phase transition at 0.95 mK (normal/BCS-superfluid at 0 bar), which gives us a fixed point in our thermometry: the friction is maximum there, leading to a maximum in the measured fork resonance linewidth.

Nowadays, our cryostats are also equipped with Magnicon® Magnetic Field Fluctuation Thermometers (MFFT), which are SQUID-based (Superconducting QUantum Interference Device) noise thermometers. It is a very handy modern solution, however with notable drawbacks: expensive, unreliable supply chain, prone to damage with cycling and electric shocks, and unsuitable in magnetic fields.

At ultra-low temperatures, knowing the temperature of the thermometer may not be enough to say anything reliable about the actual temperature of the sample: thermalisation becomes very challenging for various reasons, such as e.g. the Kapitza resistance (acoustic mismatch between materials) or the electron-phonon decoupling in thin films [61]. To be certain about the temperature of a mesoscopic device, it proves to be very useful to have on-chip thermometry. In our case, this can be performed via optomechancial means: the measurement of the mechanical frequency shift or the Brownian motion of a mode (Ch. 6) can be used as reliable and well-understood (if not primary) thermometers [40].

3.5 DILUTION REFRIGERATOR

The workhorse for reaching milli-Kelvin temperatures is the dilution refrigerator. In our experiments, we are using two variants of it: a commercial (BlueFors®) dry machine and a homemade ('DN1') wet machine, which possesses also a nuclear demagnetisation stage (see below). They are similar in their working principle, but use different ways of pre-cooling (or condensing) the mixture of Helium isotopes - Helium-3 and Helium-4.

In the homemade realisation, we have an 'old-school' 1K-pot, which is just a small volume connected through an impedance to the outside Helium-4 bath on one side, and is pumped from the other (it is basically a Helium-4 cryostat, as described before, in miniature). This volume is in thermal contact with the mixture, which enables its condensation. Usually, the temperature of the 1K-pot is largely below 2 K, which allows us to condensate mixture at atmospheric pressure or lower.

In the modern generation of dilution fridges, there is no 1K-pot and Helium-4 bath, which is why they are usually called 'dry fridges'. Instead, they use a pulse-tube cooler which pre-cools the mixture (and the rest of the cryostat). It is very convenient to use because of the absence of a Helium bath and the necessity to transfer cryoliquids regularly. The technical disadvantage of that approach on the first cool-down is the relatively high temperature of the pulse-tube (about 3 K), which is higher than the one of a 1K-pot. This requires us to use a compressor, to condense the mixture initially at a pressure higher than 1 bar. In the continuous running mode, heat exchange with the gas pumped from the 'still' (see below), which is at temperatures of the order of 1 K, enables then to stop the compressor.

As soon as there is condensed mixture, a finite cooling power can be achieved just by pumping on it. Naively, this should work just as Helium-3 evaporation, and stop at ≈ 0.3 K. However, at temperatures below 0.6 K the mixture splits into two phases in the so-called 'mixing chamber': a Helium-3 concentrated phase

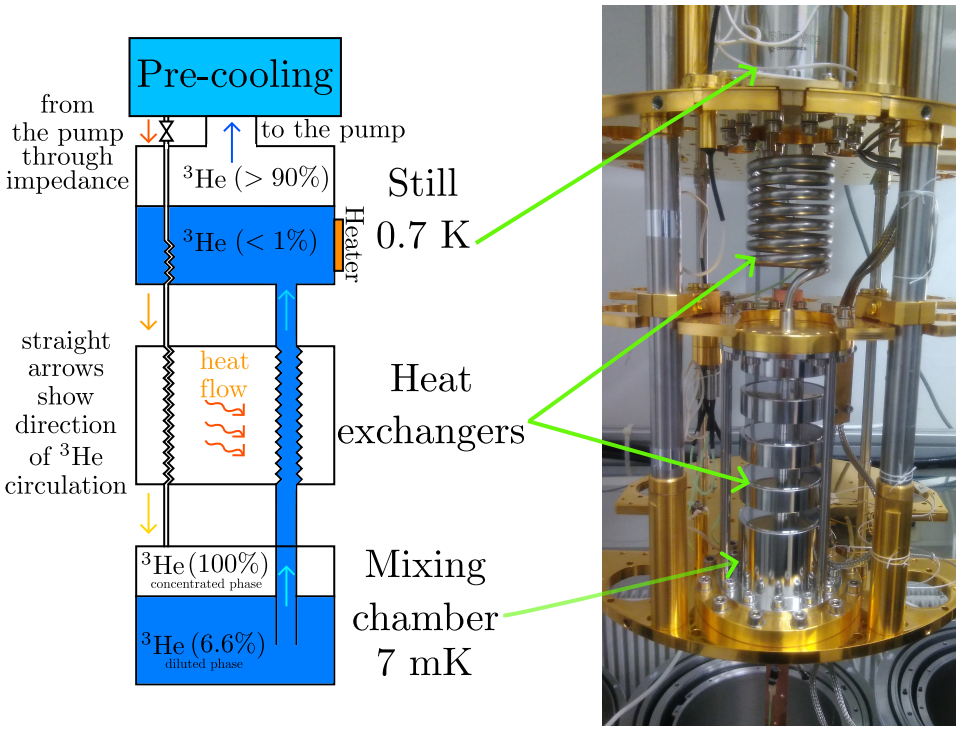

Figure 14: Scheme of a dilution refrigerator working principle (left) and photo of BlueFors® installation (right)

(lighter, making a top layer, 100% of ^{3}He at $T \to 0$) and a Helium-3 diluted phase (heavier, bottom layer, 6.6% of ^{3}He at $T \to 0$ within Helium-4). From now on, the cooling source is the dilution of Helium-3 from the top phase into the bottom one. To initiate the process, one just has to pump vapours on the so-called 'still', forcing by osmotic pressure the Helium-3 to flow through the interface. Because of the temperature at which the 'still' is maintained (about 0.7 K), the Helium-4 vapour pressure is orders of magnitude lower than that of Helium-3. This is why pumping mostly removes Helium-3, which triggers the dilution process. Maintaining the temperature of the 'still' around such a reasonably high temperature (with a heater) enables us to keep a reasonable Helium-3 vapour pressure: this is what sets the Helium-3 flow $\dot{n}_3$, which fixes the cooling power $\dot{Q}$:

$$\dot{Q} \propto \dot{n}_3 \cdot T^2. \tag{6}$$

This working principle is shown in Fig. 14.

Such a machine could work in single shot but is certainly more practical in continuous mode. To make it continuous, one has to return the pumped gas back to the 1K-pot injection port. However, since this gas got heated to room temperature in the process a simple return would lead to enormous heat-leaks. This is precisely why it is important to return it carefully, pre-cooling as much as possible at different stages of the cryostat. To achieve that goal, a series of heat exchangers are used, which are allowing the out-coming gas to pre-cool the in-coming one. Heat exchange within the 'still' had already been mentioned above. Single-shot dilution refrigerators could reach temperatures of about 2 mK, while

continuous are usually only capable of reaching temperatures down to about 7 mK.

3.6 NUCLEAR DEMAGNETISATION CRYOSTAT

Our nuclear demagnetisation cryostat (DN1, see Fig. 15) [62] consists of a homemade dilution unit (base temperature 10 mK), to which a demagnetisation stage is connected through a superconducting heat switch. The demagnetisation stage is a 1 kg stack of extremely high quality Cu sheets with silver wires between them. The superconducting heat switch is a piece of superconductor (an Al u-shaped block) with a small coil around it. Applying a small magnetic field with the coil (typically 15 mT), the superconductor can be switched into its normal state, where it conducts heat as a very good metal; comparatively in the superconducting state, its thermal conduction at 10 mK is vanishingly small.

The physics behind demagnetisation cooling is as follows: in an adiabatic transformation of a paramagnetic spin system (for us, the nuclear spins 3/2 carried by the Cu atoms), the ratio of magnetic field to temperature is constant. This means that an adiabatic field ramp $B_{init} \rightarrow B_{final}$ must satisfy:

$$\frac{B_{init}}{T_{init}} = \frac{B_{final}}{T_{final}}. \tag{7}$$

This law works down to the temperature/field corresponding to the spin-spin interaction energy. This means that to achieve the lowest temperatures, it is required to use a spin system with as small as possible spin-spin interactions. Therefore electronic systems (like Cerium Magnesium Nitrate, CMN) are not adapted for microkelvin temperatures, and the nuclear spins of $PrNi_5$ do not allow to cool below 400 μK (temperature at which they order). Cu is then a good choice, enabling to cool typically below 100 μK [53].

The cooling process includes two phases: magnetisation and demagnetisation. For the first phase, the heat switch is open and a magnetic field is applied onto the demagnetisation stage. Ramping up the magnetic field leads to heat generation in Cu (eddy currents), which has to be removed by the dilution refrigeration stage. As soon as the maximum target magnetic field B_{init} (about 8 T in our case) is reached and the temperature is back to base temperature (about 10 mK), the first phase is over. For the second phase the heat switch is closed, which means that the nuclear stage is isolated from the outside world: no heat transfer is possible anymore, so if any

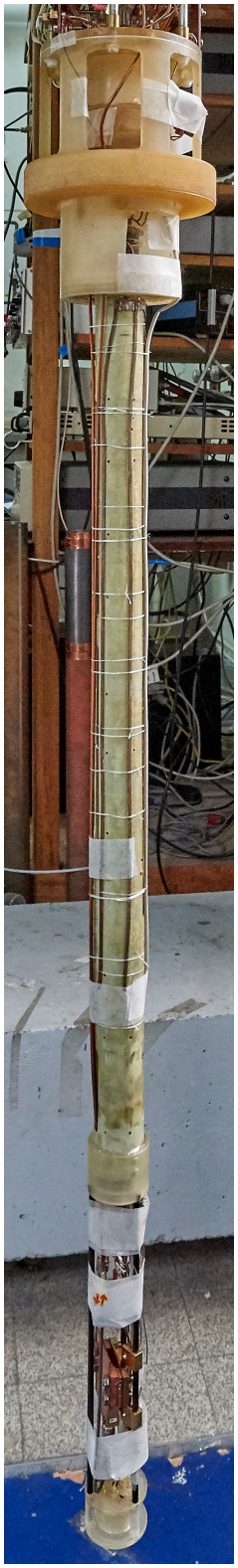

Figure 15: Photo of DN1

transformation applied to the spin system is preventing heat release as well, it shall be an adiabatic transformation. To do so, the magnetic field is slowly decreased down to the target value B_{final}, which is defined by the wanted temperature. Decreasing it down to 0 is not useful, since one would inevitably be limited by the internal spin-spin interaction field. Besides, one should point out that nuclear spins cool down the rest of the apparatus through their coupling to conduction electrons: this is the Korringa process. The Korringa constant, which characterises this interaction, is strongly magnetic field dependent [63]. It turns out that zero magnetic field is not optimal in the presence of an outside heat leak (see Sec. 6.4 of Ref. [54]). Finally, the lowest reachable temperature with nuclear demagnetisation refrigeration of Cu is 1.5 μK on the spins [53], and is typically about 100 μK for the experiment itself. In the case of DN1, the lowest temperature reached as of yet is about 400 μK, which seems to be due to the microwave coaxial wiring and the relatively big sample cell, which increases the heat load drastically.

In contrast with dilution refrigerators, demagnetisation cryostats work in a single shot regime: the two phases (magnetising, demagnetising) have to be repeated periodically, typically each one lasting about a week. There are different propositions and projects to make a continuous system based on a double-stage setup, but they have not yet been conclusive [55]. With the kg of Cu used as nuclear stage in DN1, one can indeed operate experiments at 400 μK for about a week, which is in most cases enough to realise one series of measurements.

3.7 SUPERCONDUCTING HEAT SWITCH

There are few realisations of demagnetisation refrigeration in dry fridges, but they all suffer from a relatively small hold time at the coldest temperatures (about $1-2$ days), along with other issues [64, 65, 66, 67]. It appears to be not that simple for multiple reasons: the lack of cooling power from the pulse tube, the low level of vacuum in the large vacuum can of commercial fridges, and the excessive heat leak due to vibrations. A simple strategy circumventing these problems can be chosen by making the stage as large as possible to increase the hold time. However, this also increases the pre-cooling time, which can make the duty-cycle of the cryostat's operation rather poor [67]. Another strategy is to design a double-stage system that can hold permanently a temperature below 1 mK

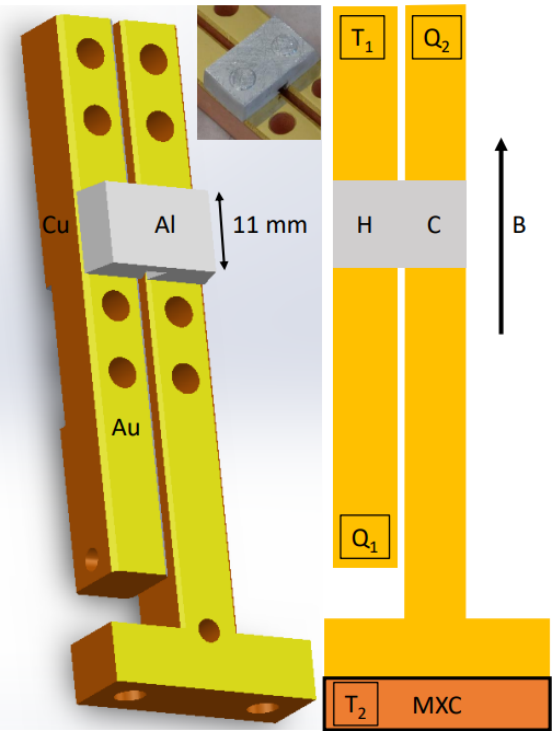

Figure 16: Schemes and photo of the new heat switch

[55, 68]. This makes the whole setup much more complex, with two superconducting magnets and 3-4 heat switches. Indeed, two designs are possible with different heat switch requirements: one with stages in parallel, and the other one with stages in series [69]. In the latter case, it turns out that the normal state heat conduction of the switches is a key limiting factor. For this reason, better heat switches had to be developed, and we describe them in the following paragraphs.

In our institute, a high quality Al heat switch has been constructed. Its design is significantly different from previous heat switches (see Fig. 16). It is bolted in the cryostat through large pieces of high quality Cu, to which the Al is attached. The whole system is immersed in a small coil. In order to join the Al to Cu with low contact resistance, the Al was plasma etched to remove its oxide layer and then immediately Au was deposited on it without breaking the vacuum of the e-beam evaporator. In the normal state of the heat switch, the thermal conductance was measured to be $8T$ W/K^2, which is equivalent to an electrical resistance of 3 nΩ according to the Wiedemann-Franz law. This is a remarkable result. In the superconducting state, the thermal conductance falls down $2 \cdot 10^6$ times lower than that of the normal state at 50 mK.

On Fig. 16, which is taken from Ref. [70], one has on the left: the heat switch which consists of two Au-plated Cu legs joined to an Au-plated Al piece. Inset: photo of the Al element and part of the Au-plated Cu legs. Right: for the thermal conductance measurements, the positions of the heaters (Q1, Q2), the thermometers (T1, T2), and the direction of the magnetic field B are indicated. The hot and cold sides of the heat switch are labelled "H" and "C", respectively, and the mixing chamber plate is labelled "MXC".

Part II

THEORY

In this part of the manuscript, we will give a generic theoretical review of the different topics which are relevant to our experiments. It is mostly concentrated on textbooks and articles results, with some specific developments related to our work (clamping, mechanical view of heat transport). These extensions of basic theory are directly relevant to some of our experiments, or are simply pushing forward the intimate analytic description of the devices' characteristics.

We will focus on three topics: Nano-mechanical dynamics, Magnetomotive (classical) drive/detection and finally Optomechanics, with both the classical and the quantum-limited approach.

Nano-mechanical resonators are the main sensitive element in all of our experiments. We already discussed in Ch. 1 how such devices are fabricated in modern cleanroom facilities. In **Nano-mechanical dynamics**, we will focus on the theoretical definition of the characteristics required to design them, and the way they depend on device parameters, e.g. geometry and material properties.

In **Magnetomotive dynamics**, we will describe a simple way to probe mechanical resonators using a small magnetic field and a small AC current. We will demonstrate some experimental results, including the (classical) backaction of the method on the outcome and how to account for it.

In **Optomechanics**, we will give the theoretical background relevant to optomechanical systems and explain how to interact with them. Two theoretical approaches will be discussed, the standard quantum one and a purely classical one based on electric circuit theory. The reasoning and predictions of both methods will be given and compared. Non-linearities of such systems will be also mentioned, with their impact on measurements and a method to characterise them.

Dans cette partie du manuscrit, nous donnerons une revue théorique générique des différents sujets qui sont pertinents pour nos expériences. Elle est majoritairement concentrée sur les résultats de manuels et d'articles, avec quelques développements spécifiques liés à nos travaux (ancrages des nano-poutres, vision mécanique du transport de chaleur). Ces extensions de la théorie de base sont directement pertinentes pour certaines de nos expériences, ou poussent simplement vers l'avant la description analytique intime des caractéristiques de nos dispositifs.

Nous nous concentrerons sur trois sujets : la dynamique nano-mécanique, la commande/détection magnétomotrice (classique) et enfin l'optomécanique, avec à la fois l'approche classique et l'approche quantiquement-limitée.

Les résonateurs nano-mécaniques sont le principal élément sensible de toutes nos expériences. Nous avons déjà discuté en Ch. 1 la façon dont de tels dispositifs sont fabriqués dans les salles blanches modernes. Dans **Dynamique nanomécanique**, nous nous concentrerons sur la définition théorique des caractéristiques nécessaires à leur conception et sur la manière dont elles dépendent des paramètres des dispositifs, par ex. géométrie et propriétés des matériaux.

Dans **Dynamique magnétomotrice**, nous décrirons une manière simple de sonder des résonateurs mécaniques en utilisant un petit champ magnétique et un petit courant alternatif. Nous démontrons quelques résultats expérimentaux, y compris l'action-en-retour (classique) de la méthode sur les mesures et comment en rendre compte.

Dans **Optomécanique**, nous donnerons le contexte théorique relatif aux systèmes optomécaniques et expliquerons comment interagir avec eux. Deux approches théoriques seront discutées, l'une quantique standard et l'autre purement classique basée sur la théorie des circuits électriques. Le raisonnement et les prédictions des deux méthodes seront donnés et comparés. Les non-linéarités de tels systèmes seront également évoquées, avec leur impact sur les mesures et une méthode pour les caractériser.

4

NANO-MECHANICAL DYNAMICS

4.1 FROM GENERAL BEHAVIOUR OF SOLIDS TO MECHANICAL RESONATORS

From a practical point of view, the most important parameters of any mechanical resonator are the resonance frequencies of its modes and their corresponding quality factors. With the knowledge of all geometrical and material properties, these parameters can be found from basic principles, which arise from the classic theory of the atomic lattice (microscopically) or the continuum theory of solids (macroscopically) [39, 71]. But in the vast majority of cases, this is an impossible task analytically because the devices are too complex, and then it can only be done with numerical simulations. Even though this is a very powerful modern technique, it does not provide any insight into the nature of the parameters' dependencies, as it can only give a numeric answer for each particular simulated case.

But the need for a mathematical description of mechanical objects existed before numerical technologies, and the analytic tools developed in the past remain extremely useful when it is about understanding how mechanical properties depend on other parameters. Such a model for beams was created by J. Bernoulli and L. Euler in the 18th century. A similar theory has been developed for drums, which is basically an extension of the Euler-Bernoulli one in two dimensions. It is called Kirchhoff–Love plate theory after the people who developed it, G. Kirchhoff and A. E. Love in the 19th century. Here we will introduce and justify the beam theory and will only give the final results for plate theory in Sec. 4.4.

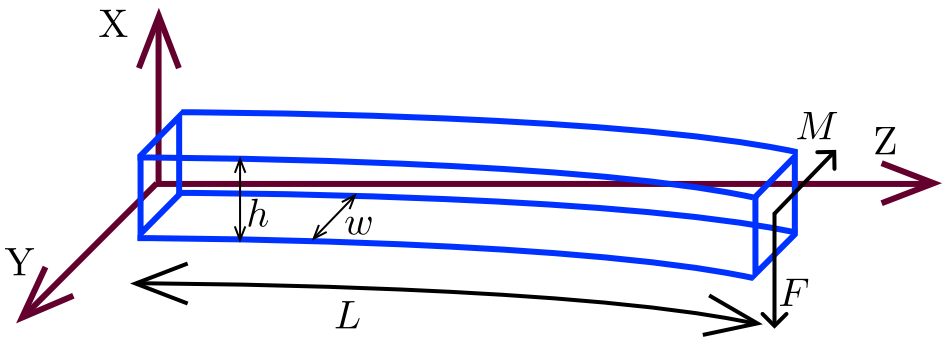

Figure 17: Beam under torque with fixed left end

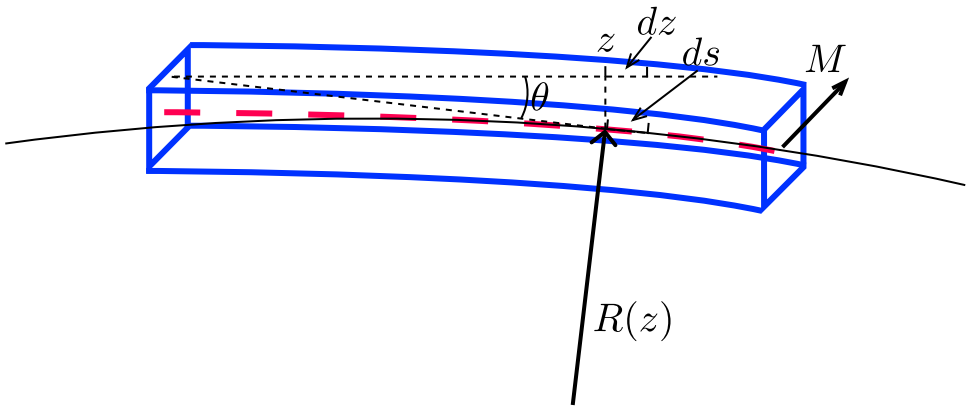

Figure 18: Radius of curvature of the beam under torque

Let us consider an isotropic and homogeneous piece of matter. For a long and thin beam with rectangular cross-section (see Fig. 17), under an applied torque M a bending (radius of curvature R) appears that can be expressed as:

$$R = \frac{E_z I_z}{M}, \tag{8}$$

where E_z is Young's modulus and I_z - the polar bending moment of inertia, which in the case of a rectangular beam of length L, width w and thickness h is $wh^3/12$ when displaced along $\vec{x}$ (for motion along $\vec{y}$ swap $w \leftrightarrow h$). Consider the shape function $f(z)$ (red dashed line in Fig. 18) which corresponds to the so-called 'neutral axis', the line located at the centre of the beam which does neither stretch nor squeeze. The radius of curvature can be expressed at point z as:

$$\frac{1}{R(z)} = \frac{d\theta(z)}{ds} = \frac{d^2 f(z)}{dz^2} = \frac{M(z)}{E_z I_z}, \tag{9}$$

taking into account local variations of torque and radius of curvature.

The torque balance written at position z, for the small element dz leads to:

$$\frac{dM(z)}{dz} = -F(z), \tag{10}$$

having introduced the applied force $F(z)$ (along $\vec{x}$, the torque being along $\vec{y}$). Writing now the balance of forces on the same element, we obtain:

$$\frac{dF(z)}{dz} = \rho A_z \frac{\partial^2 f(z)}{\partial t^2}, \tag{11}$$

where we introduced the inertia of the element dz, with cross section $A_z = w\,h$ (ρ is mass density). If the beam is stretched by a force $S_z = \sigma_0 A_z$ (σ_0 being an axial in-built stress), one has to replace $F \to F - S_z \frac{\partial f(z)}{\partial z}$. Taking Eq. 9, and using Eqs. 10 and 11, one obtains the so-called Euler-Bernoulli equation:

$$E_z I_z \frac{\partial^4 f(z,t)}{\partial z^4} + S_z \frac{\partial^2 f(z,t)}{\partial z^2} = -\rho A_z \frac{\partial^2 f(z,t)}{\partial t^2}, \tag{12}$$

where the time dependence is explicitly written. With this writing, the stored stress is $S_z < 0$ if it is tensile. Here, we essentially neglected torsional and shearing forces along with rotational inertia of each small element dz of the beam. We also assumed all displacements and angles to be small. In a doubly-clamped situation, the neutral axis does stretch with motion and the axial load S_z is deformation dependent: this leads to the Duffing effect presented in Sec. 5.3, which is neglected for now.

The solution of Eq. 12 for small displacements can be separated into spatial and temporal terms as follows (with $n \in \mathbb{N}_0$):

$$f_n(z,t) = \psi_n(z)x_n(t). \tag{13}$$

The temporal part can always be solved as $x_n(t) = x_A \cos(\omega t + \phi)$, where x_A is an amplitude, which shall be non-zero only around $\omega = \omega_n$ - the resonance frequency; ϕ is a phase, which depends on the starting conditions. To solve the spatial part $\psi_n(z)$, the mode shape of mode n, for every situation, it is necessary to define the boundary conditions associated to Eq. 12.

To define the quality factor of the nano-mechanical resonators, we will assume here that the main cause of energy dissipation is the strain caused by the bending in the bulk material, following the theory for nanobeams presented in Ref. [72]. Contributions to damping from other sources stay negligibly small as, e.g. gas damping (see Ch. 9), radiation damping in the clamps (see Sec. 4.3), or thermoelastic relaxation [73] (conversion of strain changes into heat through the thermal expansion effect). The latter remains a very small damping contribution at low temperatures, because the thermal expansion coefficient becomes extremely small. We present below a continuum mechanics approach to friction which goes beyond the standard one found in articles [74]. The link to the phenomenological conventional writing is given at the end of this Section.

According to Hooke's law, strain $\varepsilon = \delta L/L$ and stress $\sigma = F/A_z$ in a bar are linked through a constant called the Young's modulus $E_z = \sigma/\varepsilon$. More generally speaking, in an isotropic continuum one should take into account another constant that characterises by how much the bar shrinks laterally when it is pulled upon: Poisson's ratio ν. Then, for a motion of the beam with mode shape $f_n(z,t)$ and a distortion in the $\vec{x}$ direction, the strain 6-vector can be written as [39]:

$$\varepsilon = (\nu x f'', \nu x f'', -x f'', 0, 0, \nu x f''). \tag{14}$$

This expression essentially assumes that planes orthogonal to the neutral axis remain orthogonal to the displaced neutral axis (Euler-Bernoulli approximation), while it guarantees no lateral stresses (see σ_{el} below).

Then the linear response for the stress is:

$$\sigma_{el} = (0, 0, -E_z x f'', 0, 0, \frac{E_z \nu}{2(1+\nu)} x f''), \tag{15}$$

where we have both Young's E_z and Poisson's ratio ν (from elasticity theory). We assume linearity to apply, such that this stress adds up to the in-built load σ_0 (purely along $\vec{z}$).

Likewise, the same linear hypothesis can be made for the local friction stress, which at the macroscopic scale will produce the friction force (proportional to velocity $\dot{x_n}$). But in order to match Zener's low frequency limit [75] and reproduce a standard viscous friction mechanism, this friction component shall be proportional to the time rate of change of strain $\dot{\varepsilon}$. For the friction component we thus similarly introduce:

$$\sigma_{fr} = E_p \cdot \left(\frac{\nu - \nu_p}{(1+\nu_p)(1-2\nu_p)}, \frac{\nu - \nu_p}{(1+\nu_p)(1-2\nu_p)}, - \frac{1-\nu_p-2\nu\nu_p}{(1+\nu_p)(1-2\nu_p)}, 0, 0, \frac{\nu}{2(1+\nu_p)} \right) \cdot x\dot{f}'', \tag{16}$$

with two parameters describing friction, $E_p(\omega)$ and $\nu_p(\omega)$, producing a similar linear response parametrisation as for stress-strain. The frequency-dependence of these parameters arises from materials properties [75].

Then the power lost through friction writes:

$$\begin{aligned} P_{fr} &= \iiint_V \sigma_{fr} \cdot \dot{\varepsilon} \, dxdydz \\ &= \iiint_V E_p \left[1 + o(\nu, \nu_p)\right] x^2 \omega^2 \left(\frac{\partial^2 f_n(z,t)}{\partial z^2} \right)^2 dxdydz, \end{aligned} \tag{17}$$

the small parameter being $o(\nu, \nu_p) = (\nu^2(5-2\nu_p) - 8\nu\nu_p + 4\nu_p^2)/(2(1+\nu_p)(1-2\nu_p))$. By integration over a cross-section $x^2 \to I_z$, and we can write:

$$P_{fr} = E_p \left[1 + o(\nu, \nu_p)\right] I_z \omega^2 x_n(t)^2 \int_0^L \left(\frac{\partial^2 \psi_n(z)}{\partial z^2} \right)^2 dz = \Lambda_n \dot{x}_n^2, \tag{18}$$

where $-\Lambda_n \dot{x}_n$ represents an effective friction force, acting on mode n. By definition, the damping parameter is then $\Delta\omega_n = \Lambda_n / m_n$. The effective mass m_n of the mode can be defined from the kinetic energy as:

$$E_{kin} = \int_0^L \frac{\rho A_z}{2} \left(\frac{\partial f_n(z,t)}{\partial t} \right)^2 dz = \frac{\rho A_z}{2} \omega^2 x_n(t)^2 \int_0^L \psi_n^2(z) dz = \frac{m_n \dot{x}_n^2}{2}. \tag{19}$$

In the literature, dissipation is phenomenologically modelled by introducing a complex Young's modulus $E_z(\omega) = E_1(\omega) + iE_2(\omega)$. E_1 is the purely elastic component, and E_2 models dissipation; both are frequency-dependent. This is strictly equivalent to our approach provided $E_2 \to \omega E_p \left[1 + o(\nu, \nu_p)\right]$. For a high-$Q$ mode, we can make the approximation $\omega \approx \omega_n$ and from Eq. 18 and Eq. 19 we obtain:

$$Q_n = \frac{\omega_n}{\Delta\omega_n} = \frac{\rho A_z \omega_n^2}{I_z E_2} \frac{\int_0^L \psi_n^2(z) dz}{\int_0^L \left(\frac{\partial^2 \psi_n(z)}{\partial z^2} \right)^2 dz}, \tag{20}$$

which matches Ref. [72]. It turns out that experimentally, E_2 is found to be almost frequency-independent by these authors.

One can take the bi-layer structure into account simply by replacing the density $\rho \to \bar{\rho}$ by the mean density, and also the Young's modulus $E_z \to \bar{E}_z$ by an averaged modulus over the layer's inertia integrals [76]. E_2 remains a fit parameter.

Eq. 12 is generic as it describes all configurations with different boundary conditions, which from now on have to be defined. For us, the only important case is the one of a doubly-clamped beam in the high-stress limit. The high-stress limit, also called string limit, means that the contribution of bending is much smaller than the one from the stored stress: $E_z I_z \frac{\partial^4 f(z,t)}{\partial z^4} \ll S_z \frac{\partial^2 f(z,t)}{\partial z^2}$. Eq. 12 is then rewritten as:

$$S_z \frac{\partial^2 f(z,t)}{\partial z^2} = -\rho A_z \frac{\partial^2 f(z,t)}{\partial t^2}, \tag{21}$$

$$f(z,t)|_{z=[0,L]} = 0, \tag{22}$$

with the two ideal clamping conditions: Eq. 22 corresponds to the absence of clamp motion at the two ends of the beam. Relaxed clamping conditions will be considered in Sec. 4.3. Eq. 21 can be solved in the Fourier domain for the spatial part of f_n as:

$$\psi_n(z) = C_1 \sin(\lambda_n \frac{z}{L}) + C_2 \cos(\lambda_n \frac{z}{L}), \tag{23}$$

with a linear dispersion relation:

$$\omega_n = \frac{\lambda_n}{L}\sqrt{\frac{|S_z|}{\rho A_z}} = \frac{(n+1)\pi}{L}\sqrt{\frac{|\sigma_0|}{\rho}}. \tag{24}$$

The boundary conditions Eq. 22 then imply $C_2 = 0$; we can then take $C_1 = 1$ without loss of generality. The mode shape $\psi_n(z)$ is then normalised to 1 at its maximum. The final solution then is:

$$f_n(z,t) = x_A \cdot \cos(\sqrt{\frac{|S_z|}{\rho A_z}}\frac{(n+1)\pi}{L} \cdot t + \phi) \cdot \sin(\frac{(n+1)\pi}{L} \cdot z). \tag{25}$$

The corresponding modes quality factors can be obtained by injecting Eq. 24 and Eq. 25 into Eq. 20:

$$Q_n = \frac{12|\sigma_0|L^2}{h^2 E_2 ((n+1)\pi)^2}. \tag{26}$$

Although the mechanical frequencies ω_n reproduce quite well the experimental results, the quality factor Q_n does not match: one expects a linear scaling with L [72]. The reason for this is that most of the dissipation occurs where the bending is the strongest, which is near the anchoring points. This is precisely what has been neglected in the high-stress modelling. We will now consider accurately what happens at the clamps in Sec. 4.3.

4.3 CLAMP'S EFFECT

Beyond internal damping, the anchoring points appear to play a very important role in beam dynamics. The vibration of the mechanical modes irradiates acoustic waves in the supports, which limits the Q. This radiation damping has been

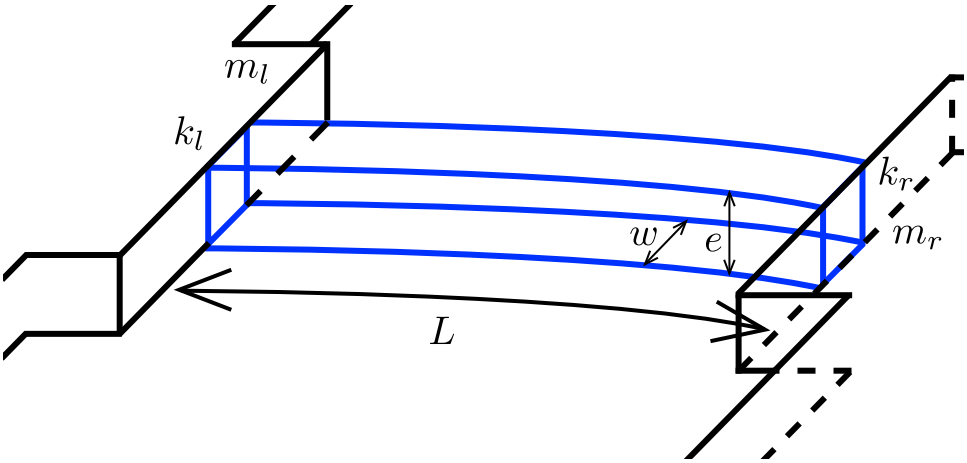

Figure 19: Model of imperfect clamps

modelled in particular for thin supports [77, 78, 79, 80], which is typically the geometry obtained when the fabrication process under-etches the clamps (so-called undercut). The actual limiting Q-value depends on the precise geometry of the beam (particularly its width w and length L) and of the anchor. Experimentally, for the first flexure ($n = 1$) of millimetre length low-stress structures resonating at sub-MHz frequencies, radiation loss seems irrelevant for widths $w < 3$ μm [81], which is the case for all our devices. But the anchoring does more than enabling irradiation into the bulk: it defines the precise bending shape at the clamping point. It had been realised about a decade ago that most of the friction occurs near the beam's ends, where the bending is the most dramatic [81, 82]. As such, structuring the clamps can have a rather interesting effect: it can reduce this bending and mitigate the losses, which is named 'soft clamping' [83, 84, 85].

After fabricating and measuring samples presented in Sec. 1.4 (see Fig. 7), we discovered that the frequency spacing between the first out of plane mode resonances of beams of the same length and different widths is significant, while according to Eq. 24 there should be none. A similar unexpected dependence was observed for quality factors as a function of beam width: according to Eq. 26 and Ref. [72], it should be width independent for out of plane modes, while it appeared that the quality factors grow with increasing width. It is therefore rather natural to wonder if a 'soft clamping' effect could account for both the frequency shift and the Q factor increase. As a matter of fact, a precise quantitative modelling is also an important tool for design purposes: being able to predict the frequency spacing of resonances for multiplexing purposes [86], and predicting the quality factors.

Beyond the ideal clamping discussed in Sec. 4.1 and Sec. 4.2, we present here an improved model in which we add the effect of the finite forces and torques that the anchors apply on the end of a beam. These results have been discussed in Ref. [74]. The new boundary conditions that define the mode's shape $\psi_n(z)$ are

thus a force $F_{l,r}$ and a torque $M_{l,r}$ (l, r for left and right). We model these relaxed boundary conditions as a spring constant $k_{l,r}$ and an inertia $m_{l,r}$ (see Fig. 19):

$$\begin{aligned} F_l =& + E_z I_z \frac{\partial^3 f(z=0,t)}{\partial z^3} - S_z \frac{\partial f(z=0,t)}{\partial z} = -k_l f(z=0,t) + m_l \frac{\partial^2 f(z=0,t)}{\partial t^2} \\ =& - \left(k_l + m_l \omega^2\right) f(z=0,t) = -k_l^* f(z=0,t), \end{aligned} \tag{27}$$

$$\begin{aligned} F_r =& - E_z I_z \frac{\partial^3 f(z=L,t)}{\partial z^3} + S_z \frac{\partial f(z=L,t)}{\partial z} = -k_r f(z=L,t) + m_r \frac{\partial^2 f(z=L,t)}{\partial t^2} \\ =& - \left(k_r + m_r \omega^2\right) f(z=L,t) = -k_r^* f(z=L,t), \end{aligned} \tag{28}$$

And for torques:

$$\begin{aligned} M_l =& - E_z I_z \frac{\partial^2 f(z=0,t)}{\partial z^2} = -\Gamma_l \frac{\partial f(z=0,t)}{\partial z} + \mathcal{M}_l \frac{\partial^3 f(z=0,t)}{\partial t^2 \partial z} \\ =& - \left(\Gamma_l + \mathcal{M}_l \omega^2\right) \frac{\partial f(z=0,t)}{\partial z} = -\Gamma_l^* \frac{\partial f(z=0,t)}{\partial z}, \end{aligned} \tag{29}$$

$$\begin{aligned} M_r =& + E_z I_z \frac{\partial^2 f(z=L,t)}{\partial z^2} = -\Gamma_r \frac{\partial f(z=L,t)}{\partial z} + \mathcal{M}_r \frac{\partial^3 f(z=L,t)}{\partial t^2 \partial z} \\ =& - \left(\Gamma_r + \mathcal{M}_r \omega^2\right) \frac{\partial f(z=L,t)}{\partial z} = -\Gamma_r^* \frac{\partial f(z=0,t)}{\partial z}, \end{aligned} \tag{30}$$

with similarly torsional spring $\Gamma_{l,r}$ and inertia $\mathcal{M}_{l,r}$. In the above, spring and inertia are regrouped in effective parameters named with an asterisk *.

The general solution of Eq. 12, which we take to be normalised at 1 for $z = z_{max}$ at maximum displacement, writes as:

$$\begin{aligned} \psi_n(z) =& \, C_{n,1} \sin\left(\lambda_{n+} \, z/L\right) + C_{n,2} \cos\left(\lambda_{n+} \, z/L\right) \\ &+ C_{n,3} \sinh\left(\lambda_{n-} \, z/L\right) + C_{n,4} \cosh\left(\lambda_{n-} \, z/L\right), \end{aligned} \tag{31}$$

where λ_{n+} and λ_{n-} are deduced from $\lambda_n(a)$ (which was introduced in the previous Section), and can all be written as Taylor expansions of a small parameter $a = \sqrt{E_z I_z / (S_z L^2)} \ll 1$, which in the case of the string-limit brings:

$$\lambda_n(a) = \lambda_n(0) + \lambda_n'(0) \cdot a + (1/2)\lambda_n''(0) \cdot a^2 + \ldots \tag{32}$$

$$\lambda_{n+}(a) = \lambda_n(0) + \lambda_n'(0) \cdot a + (1/2)[\lambda_n''(0) - \lambda_n^3(0)] \cdot a^2 + \ldots \tag{33}$$

$$\lambda_{n-}(a) = 1/a + (1/2)\lambda_n^2(0) \cdot a + [\lambda_n(0)\lambda_n'(0)] \cdot a^2 + \ldots, \tag{34}$$

with the dispersion law:

$$\omega_n = \frac{\lambda_n(a)}{L} \sqrt{\frac{|\sigma_0|}{\rho}}, \tag{35}$$

similarly to Eq. 24. To generate the Taylor expansion, we made use of an 'exponential approximation': terms of the type $exp[-o(1)/a]$ appearing because of the cosh and sinh functions have been set to zero. We simplify the writing down to 2 unitless parameters, defining:

$$\alpha_{r,l} = \frac{L}{S_z} k_{r,l}^*. \tag{36}$$

$$\gamma_{r,l} = \frac{\Gamma_{r,l}^*}{SL}. \tag{37}$$

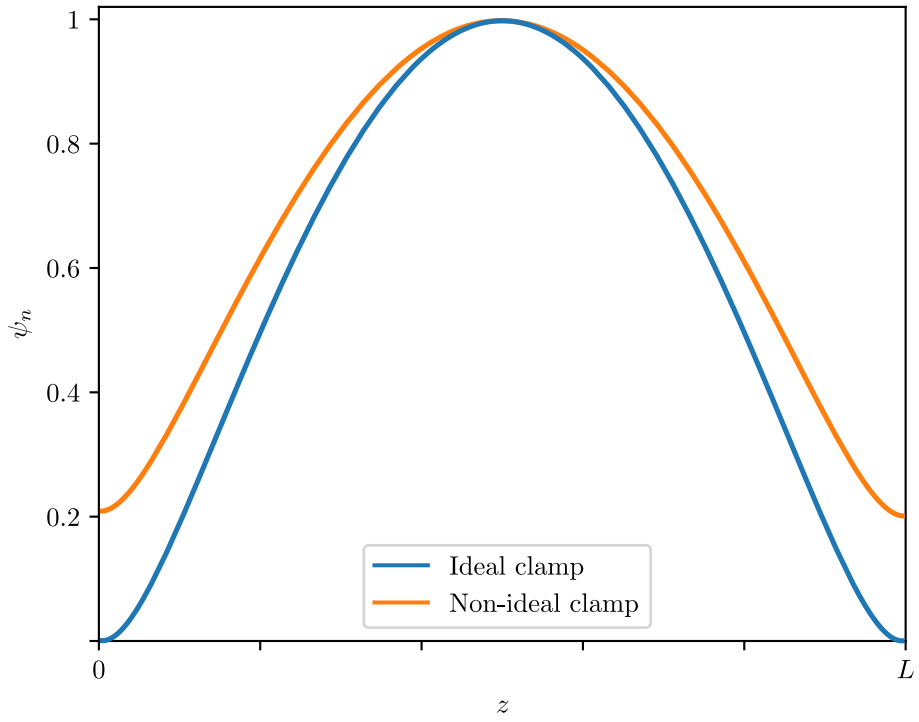

Figure 20: Mode shape with ideal and non-ideal clamps

Then, the solution for the mode shape $\psi_n(z)$ is found by defining the $C_{n,i}$ and z_{max} as a function of $\lambda_n(0)$, $\lambda_n'(0)$, and $\lambda_n''(0)$. The writing of these expressions is extremely tedious, so we do not reproduce them here. The λ_n Taylor coefficients are finally obtained as a function of the clamp parameters $\alpha_{r,l}, \gamma_{r,l}$. To illustrate this, we show an example of computed solutions on Fig. 20 for ideal, and non-ideal clamp with parameters $\alpha_r = \alpha_l = 15$ and $\gamma_r = \gamma l = 1$. For non-ideal clamps, the ends of the beam are displaced, which should explain why the resonance frequency ω_n decreases (increasing the effective mass). Also, the overall shape is less curved, which means that the beam bends less and dissipates less energy, increasing the quality factor Q_n.

We measured $f_n = \omega_n/2\pi$ and Q_n of the samples presented in Sec. 1.4 using the magnetomotive method described in Ch. 5. The clamps of these devices, as seen in pictures like Fig. 7, are all reasonably symmetric and similar: their suspended length is about 10 μm and their width is at least 20 times wider than w. We shall thus assume $\alpha_r = \alpha_l = \alpha$ and $\gamma_r = \gamma_l = \gamma$. Besides, it turns out that the pulling force dominates over the bending torque: we thus consider only α, and take $1/\gamma = 0$. For any mode n, the resonance frequency then writes [74]:

$$f_n(a, \alpha) = f_{n,0}\, P_f(n, a, \alpha), \tag{38}$$

with $f_{n,0}$ obtained from Eq. 35, and the quality factor Q_n is:

$$Q_n(a, \alpha) = Q_{n,0}\, \frac{P_f(n, a, \alpha)^2}{P_Q(n, a, \alpha)}, \tag{39}$$

with $Q_{n,0}$ given by Eq. 20. The functions P_f and P_Q are corrections obtained as second order expansions in both a and α:

$$P_f(n,a,\alpha) = 1 - \frac{2}{\alpha} + \frac{4}{\alpha^2} + a\left(2 - \frac{8}{\alpha} + \frac{2(12 - n^2\pi^2)}{\alpha^2}\right) + \frac{1}{2}a^2\left(8 + n^2\pi^2 - \frac{2(24 + 5n^2\pi^2)}{\alpha} + \frac{24(8 + n^2\pi^2)}{\alpha^2}\right), \quad (40)$$

$$P_Q(n,a,\alpha) = 1 - \frac{6}{\alpha} + \frac{24 - n^2\pi^2}{\alpha^2} + a\left(6 + \frac{1}{2}n^2\pi^2 - \frac{48 + 6n^2\pi^2}{\alpha} + \frac{144 - 8n^2\pi^2}{\alpha^2}\right). \quad (41)$$

More generic expressions can be found in Ref. [74] Supplementary Material.

The resonance frequency dependence to the width w is shown in Fig. 21. The data is normalised to the expected ideal clamp value, which means infinitely stiff $k_{r,l} \to \infty$. Different markers correspond to different chips with similar samples, while different colours correspond to different lengths. A very good analytic fit is obtained with a simple ansatz for the clamp parameter: $\alpha \propto n\pi/w$. Discrepancies can be justified by the nano-fabrication imperfect reproducibility.

Similar results for the normalised quality factor Q_n are shown on the Fig. 22. There the agreement is not as good. But one should keep in mind that (for simplicity) we only took into account the effect of the parameter α, and completely neglected γ. Including it into calculations does improve the agreement between expected and measured parameters, but it also significantly increases the complex-

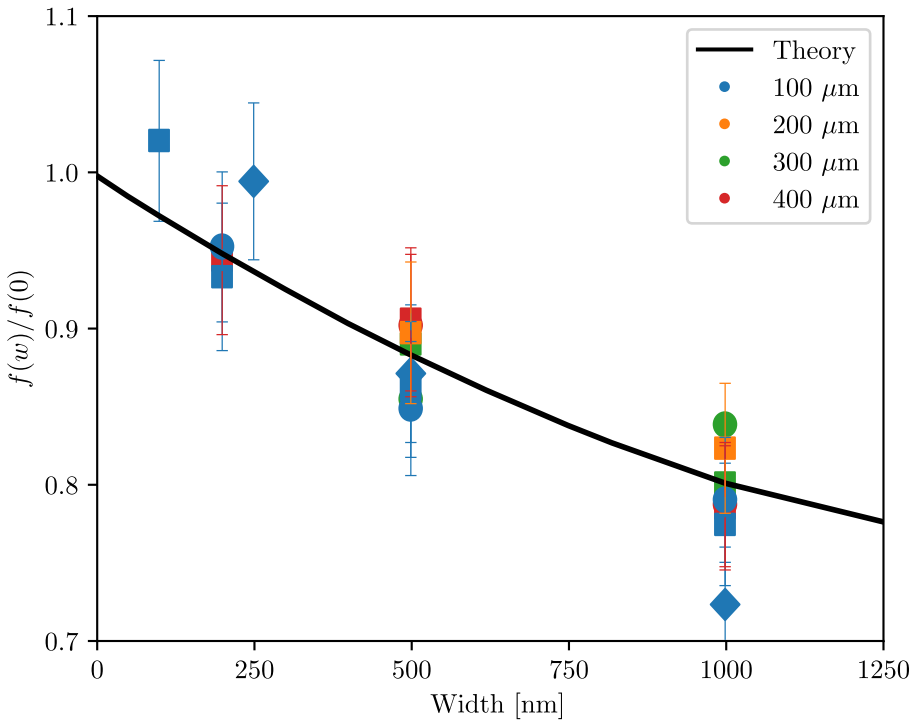

Figure 21: Normalised resonance frequency as a function of beam width

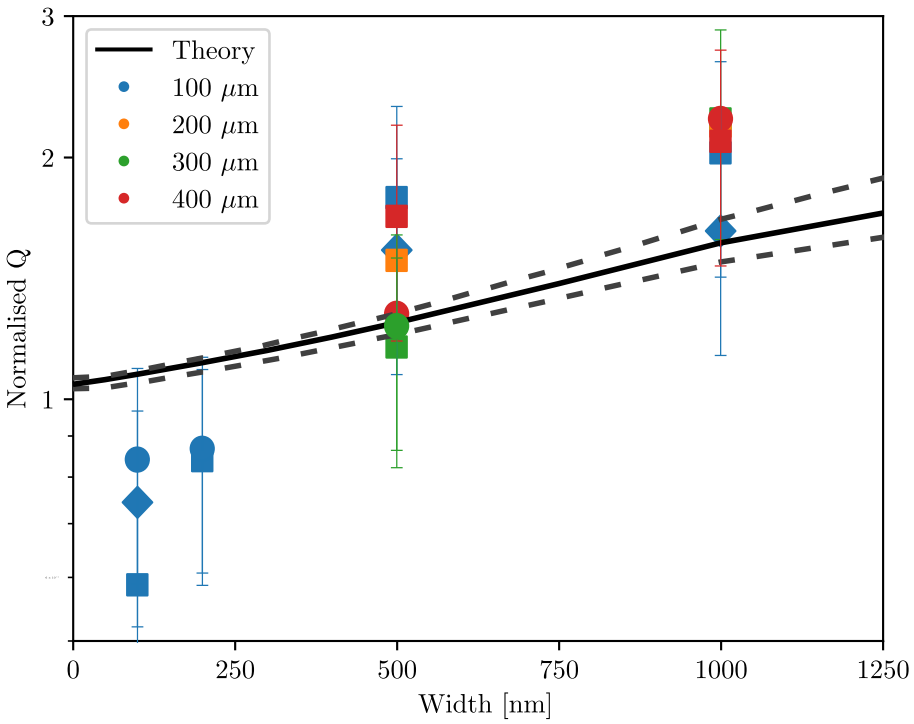

Figure 22: Normalised quality factor as a function of beam width

ity of the problem. For quantitative fits, Eq. 20 has a single material-dependent fit parameter - E_2 (ρ, E_z and σ being known from resonance frequency fits). The extracted numerical values are in agreement with the literature, see Supplementary Material of Ref. [74] (together with all other fit numbers).

To conclude the Section, we demonstrate that suspended anchoring points of the beams act as an 'easy soft clamping': it is responsible for both a downward resonance frequency shift and an increase in quality factor. It turns out that the effective clamp spring constants $k_{l,r}$ are the dominant ingredient. For symmetric devices with similar clamps, $k_{l,r} \approx k$ is found to be $k \propto f/w$, with f frequency and w beam width. For the frequency shift, following Ref. [87], this can be recast into an effective lengthening $L \to L + \Delta L$ with $\Delta L \propto w/f$ at lowest order (and clamp-parameter dependent). For the quality factor, the fit is reasonably good but could be improved with a torque spring parameter $\Gamma_{l,r}$. To do so, the theory would need to be improved; likewise, it could be extended to the case of beams with no (or very little) axial stress and even to cantilevers. The problem addressed here is extremely widespread, and beams with a 'natural' clamp undercut (i.e. due to the fabrication process) are extensively used. Our results are relevant to nano-mechanical design: for both defining precisely resonance frequencies (mandatory when multiplexing is at hand) and quality factors.

Similarly to the Euler-Bernoulli beam theory, the Kirchhoff–Love plate theory for thin drums can be obtained with similar arguments. Using polar symmetry we write:

$$D_r \Delta^2 f(r,\theta,t) + T_r \Delta f(r,\theta,t) = -\rho h \frac{\partial^2 f(r,\theta,t)}{\partial t^2}, \tag{42}$$

where $\Delta\cdot = \frac{1}{r}\partial_r(r\partial_r\cdot) + \frac{1}{r^2}\partial_\theta^2\cdot$ is the usual Laplacian operator in polar coordinates, $D_r = E_r h^3 / \left(12(1-\nu_r^2)\right)$ is the flexural rigidity with ν_r Poisson's ratio and E_r Young's modulus of the material, and $T_r = h\,\sigma_0$ is the stored tension per unit length inside the drum. We define h the thickness and R the radius of the drum.

With a similar approach as in the 1D case, we can write down boundary conditions and solve Eq. 42 in the high-stress limit (i.e. the membrane limit), assuming small displacements and by separating temporal, spatial, and angular parts of the displacement function $f(r,\theta,t)$:

$$f_{n,m}(r,\theta,t) = \psi_{n,m}(r)\cos(n\theta)x_{n,m}(t), \tag{43}$$

having now introduced two indexes for the modes (azimuthal and radial $n, m \in \mathbb{N}^2$). The motion amplitude is $x_{n,m}(t) = x_A \cos(\omega_{n,m}t + \phi)$ with $\omega_{n,m}$ the mode resonance frequency. The problem to solve is then:

$$T_r \Delta f(r,\theta,t) = -\rho h \frac{\partial^2 f(r,\theta,t)}{\partial t^2}, \tag{44}$$

$$f(r,\theta,t)|_{r=R} = 0. \tag{45}$$

This can be solved in terms of Bessel functions of the first kind J_n as:

$$\psi_{n,m}(r) = \frac{J_n(\frac{\lambda_{n,m} r}{R})}{J_n(\frac{\lambda_{n,m} r_{n,m}}{R})}, \tag{46}$$

with a linear dispersion relation:

$$\omega_{n,m} = \sqrt{\frac{|T_r|}{\rho h}}\left(\frac{\lambda_{n,m}}{R}\right) = \frac{\lambda_{n,m}}{R}\sqrt{\frac{|\sigma_0|}{\rho}}, \tag{47}$$

where $r_{n,m}$ is the radial position of the maximum amplitude, which depends on n, m and will be reached at a given angle θ (with $r_{0,m} = 0$). With this choice, the mode function is normalised to 1 at its maximum, as for beams.

Frequencies $\omega_{m,n}$ are well described by the high-stress model, provided measured devices are within this limit. But as for beams, the $Q_{n,m}$ quality factors require a more subtle modeling taking into account the bending near the clamp [88]. Also, a non-linear theory can be built that takes into account the stretching under motion, which leads to a similar Duffing effect as the one obtained for beams [89]. For all our measurements on drum-NEMS, we only used the first mode $\psi_{0,0}$ as it has the lowest frequency and the highest coupling to the cavity in optomechanical systems.

All solid matter consists of atoms, which are kept together by internal forces. When one atom moves, it leads to motion of all the neighbours. This motion can thus be described as a (microscopic) collective mode of elementary oscillation, a so-called phonon, from which all bulk thermal properties such as the specific heat C_v or the thermal conductivity κ can be constructed. On the other hand, one builds elastic theory from the very same grounds, namely the inter-atomic interaction, and from this one creates the (macroscopic) collective modes: the motions described in Secs. 4.2, 4.4. It is therefore natural to point out that thermal properties should be describable in terms of elasticity theory as a whole. This means that it should be possible to derive the macroscopic bulk properties C_v, κ from continuum mechanics as well as by phonons, leading obviously to the same results. Here, we will try to give a short insight into the theoretical synthesis of macroscopic thermal properties from the linear superposition of the mechanical modes Brownian motion. The conclusion of this analysis is that heat transport is not performed by the mechanical modes themselves but by their 2-wave mixing. The clamp plays a very specific role in the problem, generating cross-correlations between these modes. As a result, the macroscopic size of the clamping region is related to a microscopic lengthscale: the phononic mean-free-path. More details, and the complete mathematical treatment can be found in Ref. [90].

For simplicity, let us consider the case of an electrically insulating cylindrical rod connected to two infinite thermal reservoirs ('hot' and 'cold') all in vacuum (see Fig. 23). Let this rod have a length L, and a cross-section radius R (inset of Fig. 23 with radial axis linked to it), with the z-axis along the rod. Let the cold bath be at the temperature T_c and the hot one at the temperature T_h; the cold end of the homogeneous rod at $T_{c,+}$ and the hot one at $T_{h,-}$. The link between the baths and the rod is the clamp region of length $\varepsilon \ll L$, which plays the role of transition zone. A heat flow $\dot{Q}$ is going from the hot bath to the cold one through the rod, which creates a linear temperature gradient along the z-axis, with the origin at the cold end of the homogeneous rod.

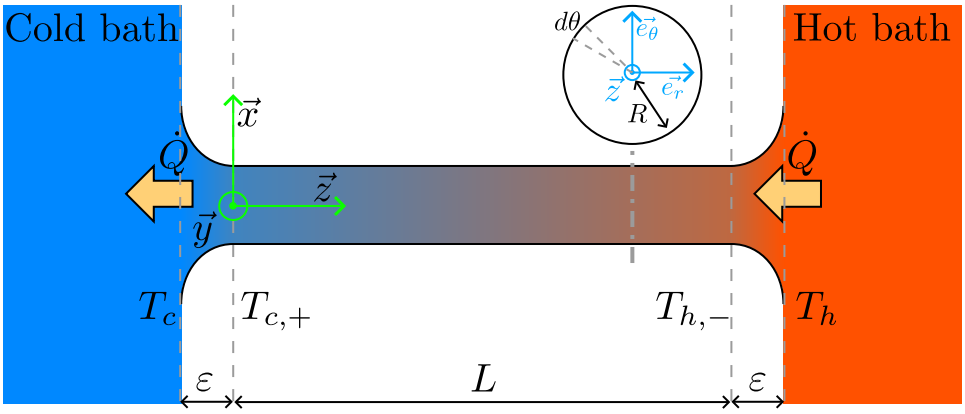

Figure 23: Schematic of the thermal transport problem

Considering a small thermal gradient, the classical solution for the heat flow $\dot{Q}$ using Fourier's law is:

$$\dot{Q} = -\frac{\kappa(T_{avg})\pi R^2}{L}\Delta T, \tag{48}$$

and the specific heat in the classical Dulong-Petit limit is:

$$C_v = 3\frac{N}{V}k_B, \tag{49}$$

with N the number of atoms and $V = L\pi R^2$ the rod's volume. The energy stored E_{tot} therefore leads to the linear energy density:

$$\frac{dE_{tot}(z)}{dz} = \frac{3N}{L}k_B T(z), \tag{50}$$

where in the above the mean temperature $T_{avg} = (T_h + T_c)/2 \gg \Delta T = T_h - T_c$ (temperature difference), and the local temperature $T(z) = T_{avg} + \Delta T\left(\frac{z}{L} - \frac{1}{2}\right)$. The phonon theory links thermal conductivity and specific heat through the excitations mean-free-path λ_{mfp}: $\kappa = \frac{1}{3}C_v\bar{c}\lambda_{mfp}$, having introduced the average speed of sound $\bar{c}$.

These are the basics of thermal properties at the macroscopic level. Now, let us consider the rod in terms of continuum mechanics. The distortion of solid matter is described by the displacement field $\vec{u}(\vec{r}, t)$, for which the fundamental equation of motion in the absence of external forces is written [39]:

$$\rho\frac{\partial^2\vec{u}}{\partial t^2} = \frac{E_z}{2(1+\nu)(1-2\nu)}\vec{\text{grad}}(\text{div}[\vec{u}]) + \frac{E_z}{2(1+\nu)}\vec{\Delta}\vec{u}, \tag{51}$$

where we introduced Young's modulus of the material E_z, Poisson ratio ν, the material's mass density ρ, and the Laplacian vector operator $\vec{\Delta}$. In the limit $L \gg R$, variables (in cylindrical coordinates) can be separated and a solution can be obtained as:

$$\begin{aligned} u_r(r,\theta,z,t) &= \phi_{r\{\eta\}}(r,\theta)U_{\{\eta\}}(z,t), \\ u_\theta(r,\theta,z,t) &= \phi_{\theta\{\eta\}}(r,\theta)U_{\{\eta\}}(z,t), \\ u_z(r,\theta,z,t) &= \phi_{z\{\eta\}}(r,\theta)R\frac{\partial U_{\{\eta\}}}{\partial z}(z,t). \end{aligned} \tag{52}$$

$U_{\{\eta\}}$ represents a propagating solution along z, while $\phi_{i\{\eta\}}$ describe the shape of the distortion within each sector. $\{\eta\}$ corresponds to a set of parameters that will distinguish different existing solutions: the rod's mechanical modes.

Solutions for $U_{\{\eta\}}(z,t)$ can be classified as follows:

$$\begin{aligned} \text{Travelling} : U_{\{\eta\},0}(z,t) &= U_0\cos(\pm k_p z - \omega t), \\ \text{or } U_{\{\eta\},\pi/2}(z,t) &= U_0\sin(\pm k_p z - \omega t), \end{aligned} \tag{53}$$

$$\begin{aligned} \text{Evanescent} : U_{\{\eta\},0}(z,t) &= U_0\exp(\pm k_e z)\cos(\omega t), \\ \text{or } U_{\{\eta\},\pi/2}(z,t) &= U_0\exp(\pm k_e z)\sin(\omega t), \end{aligned} \tag{54}$$

$$\begin{aligned} \text{Mixed} : U_{\{\eta\},0}(z,t) &= U_0\exp(\pm k_e z)\cos(\pm k_p z - \omega t), \\ \text{or } U_{\{\eta\},\pi/2}(z,t) &= U_0\exp(\pm k_e z)\sin(\pm k_p z - \omega t). \end{aligned} \tag{55}$$

Solutions of Eq. 51 for $\phi_{r\{\eta\}}$, $\phi_{\theta\{\eta\}}$, and $\phi_{z\{\eta\}}$ are known as Pochhammer-Chree waves [91], and can be regrouped in 3 families: torsional (T), longitudinal (L), and flexural (F). Torsional and longitudinal waves can be defined by a single index, while flexural ones require two. The choice of a family, of an index within it, and of the type of wave (travelling, evanescent, or mixed) defines a branch of solutions with a dispersion relation $\omega(k_p, k_e)$.

The Pochhammer-Chree waves dispersion relations, and their shapes, are very complex: we shall not comment on this and refer the reader to specialised articles [90, 91]. For each family, only the first branch has a dispersion relation that goes all the way to $\omega \to 0$ when the wave-vector $k_p, k_e \to 0$. These are the conventional modes described in beam theory, e.g. for flexure the Euler-Bernoulli equation Eq. 12, Sec. 4.1. Within these, only flexural modes possess an evanescent branch: the first branch T and L waves are only propagating.

The next step requires us to define the normal modes in the rod as standing waves by fixing the boundary conditions for each family of solutions. Then, we define the mechanical energy stored in the rod and the dissipated power through friction, with both a bulk and a clamp contribution. All these are functionals of the displacement field $\vec{u}$, and can therefore be analytically written down. Formulas are tedious, so we do not reproduce them here: see Ref. [90] for all of these expressions.

The key to the analysis is linear response theory. The total displacement field $\vec{u}$ is written as:

$$\vec{u}(r, \theta, z, t) = \sum_{\{\eta\}} \vec{u}_{\{\eta\}}(r, \theta, z, t), \tag{56}$$

a superposition of all modes. From the motion amplitudes U_0 of Eqs. 53-55, one defines the Brownian motion amplitudes of each mode, in units of temperature. Since all energetics functionals are quadratic with respect to the displacement field, they generate terms $\sim \vec{u}_{\{\eta\}} \cdot \vec{u}_{\{\eta'\}}$ in the energy densities (or similarly products of spatial/temporal derivatives, which then need to be integrated over a rod's slice to obtain linear energy densities along z). When $\eta = \eta'$, one obtains a term leading to the definition of $T_{\{\eta\}}$, the mean temperature of the mode. From this, one recovers the canonical results of the Fluctuation Dissipation Theorem (FDT). The terms $\eta \neq \eta'$ correspond to cross-correlations between modes $T_{\{\eta,\eta'\}}$, which are discussed below.

The point is that the energy density functional obtained from continuum mechanics should match the conventional result Eq. 50. As a result, the cross-correlation terms $T_{\{\eta,\eta'\}}$ appear as a sort of Fourier-transform amplitudes of the linear shape $T(z)$ of the thermal gradient. Explicitly, after performing all calculations we obtain:

$$\dot{Q} \approx +3Nk_B \frac{E_z}{\bar{\Lambda}_c} \frac{\varepsilon}{L} \sum_{\substack{\Delta q=-\infty \\ \Delta q \neq 0}}^{+\infty} T_{avg,\Delta q}, \tag{57}$$

where $\bar{\Lambda}_c$ is an average clamping loss parameter and $\Delta q = q' - q$ - the difference between mode numbers within the same branch. In Eq. 57, the subscript avg refers to an average over all branches $\{\eta\}$.

The average cross-correlation temperature is obtained as:

$$T_{avg,\Delta q} = -\frac{[1-(-1)^{\Delta q}]}{\pi^2(\Delta q)^2}\Delta T. \tag{58}$$

These correlations fall off very quickly with the mode distance Δq: it appears that only neighbouring modes of the same branch are relevant, which comes from a mode orthogonality property [90]. The heat flow can then be recast into:

$$\dot{Q} \approx -\frac{\pi R^2}{L}\left[\frac{3}{2}\frac{(N/V)k_B E_z}{\bar{\Lambda}_c}(\varepsilon L)\right]\Delta T. \tag{59}$$

We stated earlier that the clamp parameter $\varepsilon \ll L$. We see now, that for the solution Eq. 59 to be finite, the product εL should exist. Therefore, we introduce a new parameter $l^2 = \varepsilon L \neq 0$, which will characterise the anchoring zone of the rod. By equalising now Eq. 59 with Eq. 48, we can identify the thermal conductance κ and the phonon mean free path λ_{mfp}:

$$\kappa = \frac{3}{2}\frac{(N/V)k_B E_z l^2}{\bar{\Lambda}_c} = \frac{1}{3}C_v\bar{c}\left[\frac{3}{2}\frac{E_z l^2}{\bar{c}\bar{\Lambda}_c}\right] \tag{60}$$

$$\lambda_{mfp} = \frac{3}{2}\frac{E_z l^2}{\bar{c}\bar{\Lambda}_c}. \tag{61}$$

This final result demonstrates the link between continuum mechanics and macroscopic thermal transport properties. It shows that thermal transport appears due to cross-correlations between nearest modes of the same family, which in principle should be measurable. This actually means that energy flow is not carried by the modes themselves, but by their 2-wave mixing. Moreover we discovered a new length-scale l, which defines the size of the clamp as being related to a microscopic lengthscale: the mean-free-path of phonons. The clamping zone is a key element of the modelling: this is where correlations between modes are created, leading to the transport of energy through their 2-wave mixing. The full model is a linear theory, even though nonlinear processes within the clamps are key.

5

MAGNETOMOTIVE DETECTION

5.1 GENERAL DESCRIPTION

One of the simplest ways to measure the characteristic parameters of a nanomechanical beam is by means of the so-called magnetomotive technique. One detects the voltage induced by the motion of the beam in a magnetic field, while it is driven by a current flowing through it and generating a Lorentz force [92].

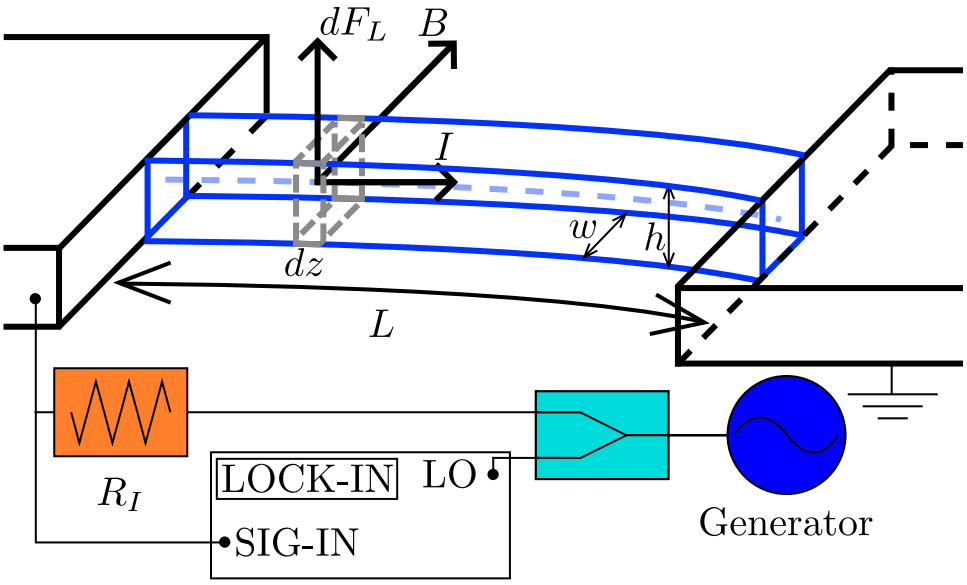

Figure 24: Magnetomotive measuring scheme

The electric current $I(t)$ flowing through the beam's segment dz placed in a static magnetic field B creates a Lorentz force $dF_L(t)$ acting on this segment (see Fig. 24):

$$dF_L(t) = BI(t)dz. \tag{62}$$

Let us consider one mode n. The force can be projected onto this mode, leading to an effective dynamics equation for its motion amplitude $x_n(t)$:

$$m_n \frac{d^2x_n(t)}{dt^2} + \gamma_n m_n \frac{dx_n(t)}{dt} + k_n x_n(t) = F_n(t) = B\,\zeta_n L\, I(t) \tag{63}$$

where γ_n is the damping coefficient, m_n the effective mass affected to the mode, and k_n the corresponding effective spring constant.

At the same time, the motion of the conductor in the magnetic field generates an electromotive force (EMF):

$$\mathcal{E}(t) = -\frac{d}{dt}\Phi(t) = -\int_0^L B\frac{\partial f(z,t)}{\partial t}dz = -\zeta_n L\, B\frac{dx_n(t)}{dt}, \tag{64}$$

where ζ_n in Eqs. 63, 64 is a constant based on the mode shape which was discussed in Ch. 4, and is defined as $\zeta_n = \int_0^L \psi_n(z)dz/L$.

In the limit of a circuit with infinite impedance, the EMF voltage in frequency domain is given as (in complex form):

$$V_{\text{EMF}}(\omega) = \frac{i\omega\,\zeta_n^2 L^2 B^2/m_n}{\omega_n^2 - \omega^2 + i\omega\omega_n/Q_n} I(\omega), \tag{65}$$

where $Q_n = \omega_n/\gamma_n$ is the intrinsic quality factor of the mechanical resonator, and ω_n the intrinsic resonance frequency.

When the impedance of the circuit is not infinite, the measured characteristics are not the intrinsic ones but are altered by the (extrinsic) measurement setup. This magnetically-coupled electromechanical resonator can be treated as an equivalent combination of a resistor R_m, inductor L_m, and capacitor C_m connected in parallel with the external electric circuit. The equivalent values would be as follows (for mode n):

$$\begin{aligned} C_m &= \frac{m_n}{\zeta_n^2 L^2 B^2}, \\ L_m &= \frac{\zeta_n^2 L^2 B^2}{\omega_n^2 m_n}, \\ R_m &= \frac{\zeta_n^2 L^2 B^2}{\omega_n m_n} Q_n. \end{aligned} \tag{66}$$

The finite impedance of the circuit is connected in parallel with the mechanical resonator's equivalent RLC elements: it leads to a change in observed parameters as compared to the intrinsic ones, an effect called loading. Assuming a high value for the intrinsic quality factor $Q_n \gg 1$, the external impedance of the electric circuit can be treated as frequency-independent: $Z_{ext} \approx R_{ext} + iX_{ext}$. Then the observed voltage across the total circuit is written as:

$$\begin{aligned} V_T &= \left[\frac{\omega_n^2 - \omega^2 + i\omega\omega_n/Q_n}{i\omega/C_m} + \frac{1}{R_{ext} + iX_{ext}}\right]^{-1} I(\omega) \\ &= \frac{i\omega/C_m}{(\omega_n^2 + \omega\omega_n Z_c X_{ext}/|Z_{ext}|^2) - \omega^2 + i\omega\omega_n(1/Q_n + Z_c R_{ext}/|Z_{ext}|^2)} I(\omega), \end{aligned} \tag{67}$$

where $Z_c = \sqrt{L_m/C_m} = \zeta_n^2 L^2 B^2/(\omega_n m_n)$ is the characteristic impedance corresponding to mode n.

From Eq. 67 it follows that the effective frequency and quality factor of the mechanical resonator in the presence of a magnetic field will be different from its intrinsic values. For the limit of a high external impedance $Z_{ext} \gg Z_c$, the loaded value for the resonance frequency ω_L will be:

$$\omega_L = \omega_n\sqrt{1 + \frac{Z_c X_{ext}}{|Z_{ext}|^2}} \approx \omega_n\left(1 + \frac{\zeta_n^2 L^2 B^2 X_{ext}}{2\omega_n m_n |Z_{ext}|^2}\right), \tag{68}$$

and likewise for the loaded quality factor Q_L (or loaded damping γ_L):

$$\begin{aligned}\frac{1}{Q_L} &= \frac{1}{Q_n} + \frac{Z_c R_{ext}}{|Z_{ext}|^2} = \frac{1}{Q_n} + \frac{\zeta_n^2 L^2 B^2 R_{ext}}{\omega_n m_n |Z_{ext}|^2}, \\ \gamma_L &= \gamma_n + \frac{Z_c R_{ext} \omega_n}{|Z_{ext}|^2} = \gamma_n + \frac{\zeta_n^2 L^2 B^2 R_{ext}}{m_n |Z_{ext}|^2}.\end{aligned} \tag{69}$$

A quadratic correction $\propto B^2$ has therefore to be applied to experimental data, in order to extract the proper γ_n value.

5.2 LINEAR RESPONSE

From the experimental point of view, the actual measurement scheme is depicted in Fig. 24: a probing voltage tone at a known frequency is sent from the generator to the sample through a resistor R_I, thus generating a drive current $I(t)$, and the detected voltage is demodulated by a lock-in with a Local Oscillator (LO) at the same frequency. The impedance R_I for the probing tone is required to be in the high-impedance limit $R_I \gg Z_c$. Then, the generator's frequency is swept to scan the system's response at different frequencies. The first scan is usually done without magnetic field to define the background of the setup. This scan can be subtracted later on to improve the quality of the actual device measurements. The response of one of the devices discussed in Sec. 1.4 with subtracted background is shown in Fig. 25. This is a multi-beam setup (Fig. 7), for which we connected

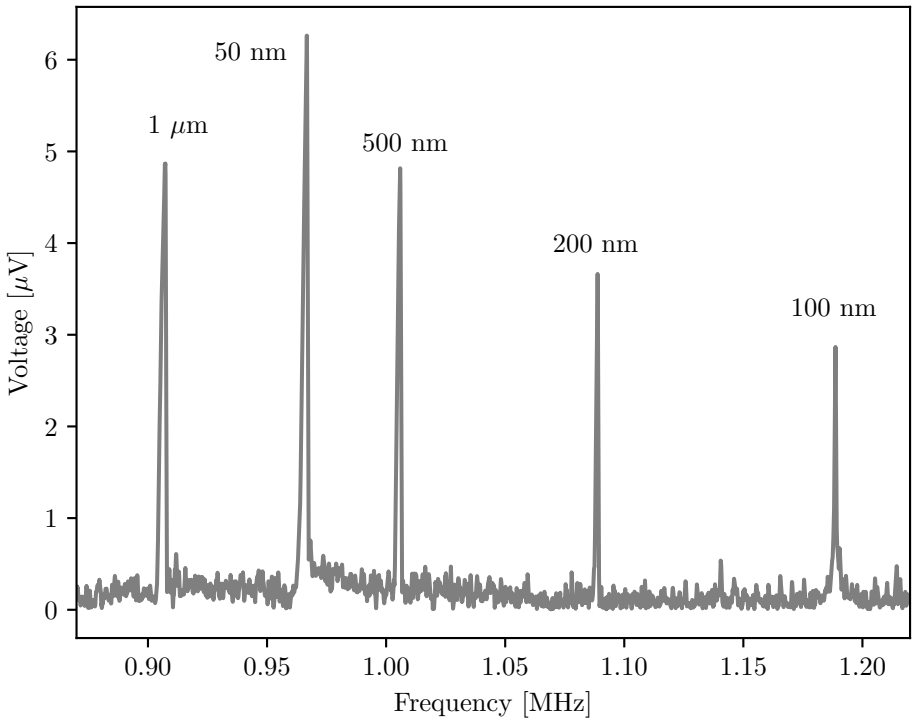

Figure 25: Magnetomotive measurements of the fully suspended beams

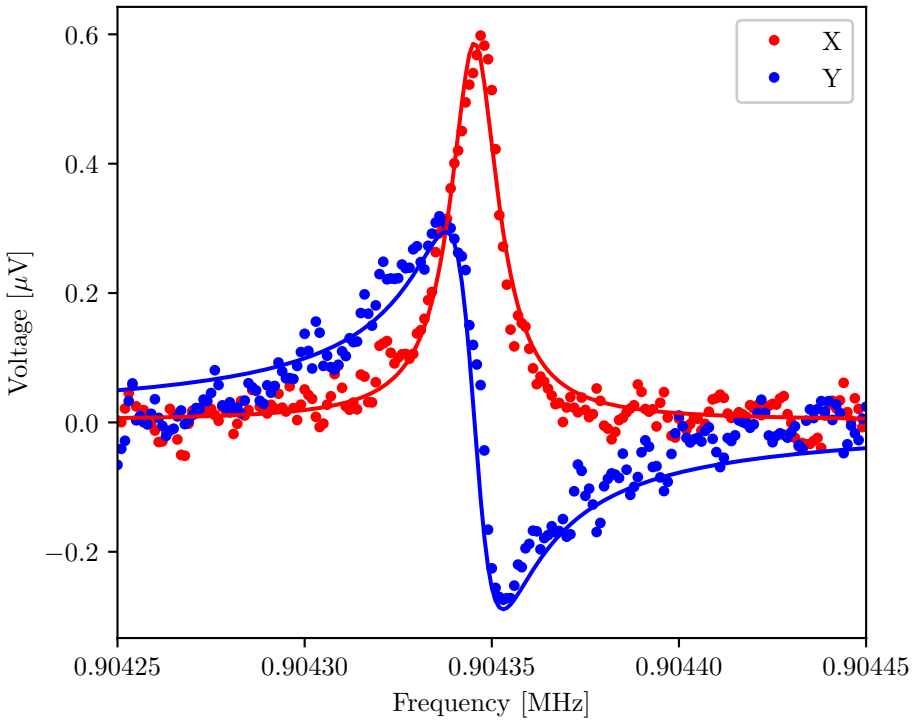

Figure 26: Typical linear response curve

all beams in series. Note that the data presented in this Chapter is published in Ref. [86].

The lock-in demodulation leads to two quadratures of the voltage signal $X(\omega)\cos(\omega t) + Y(\omega)\sin(\omega t)$, taking as phase definition for the current $I(t) = I_{max}\cos(\omega t)$. In Fig. 25, we plot the magnitude $R(f) = \sqrt{X(f)^2 + Y(f)^2}$. This sample has beams of lengths $L = 100$ μm. The trace shown was measured at 4.2 K in a cryostat, with a magnetic field B of about 1.8 T and a drive current I_{max} of 60 nA. All five beams were also connected independently, in order to define which beam corresponds to which resonance frequency (their corresponding widths w are written on the Fig. 25). The peaks measured correspond to the first flexures $n = 0$ of the beams, which have been multiplexed through the series electric connection. The resonance frequencies and amplitudes change monotonically with w, together with their damping rate (peak width), in agreement with the clamp effect discussed in Sec. 4.3. This is true for all beams excluding the 50 nm wide one which behaves differently. We tend to link this to the fact that at that scale, the size of aluminium grains ($\approx$ 20 nm) become comparable to the width w, which leads to a large irreproducibility in the fabrication quality.

We further demonstrate the application of the magnetomotive technique for characterisation of nano-mechanical devices, using as an example the 1 μm wide and 100 μm long beam measured at 4.2 K in vacuum. A detailed scan of the first $n = 0$ flexural mode of that beam can be seen on Fig. 26, measured with 0.2 T and 0.5 nA. Points correspond to actual data, while solid lines show a Lorentzian fit (see Eq. 70), which allows to define the effective damping (width $\Delta f_L = \gamma_L/2\pi$),

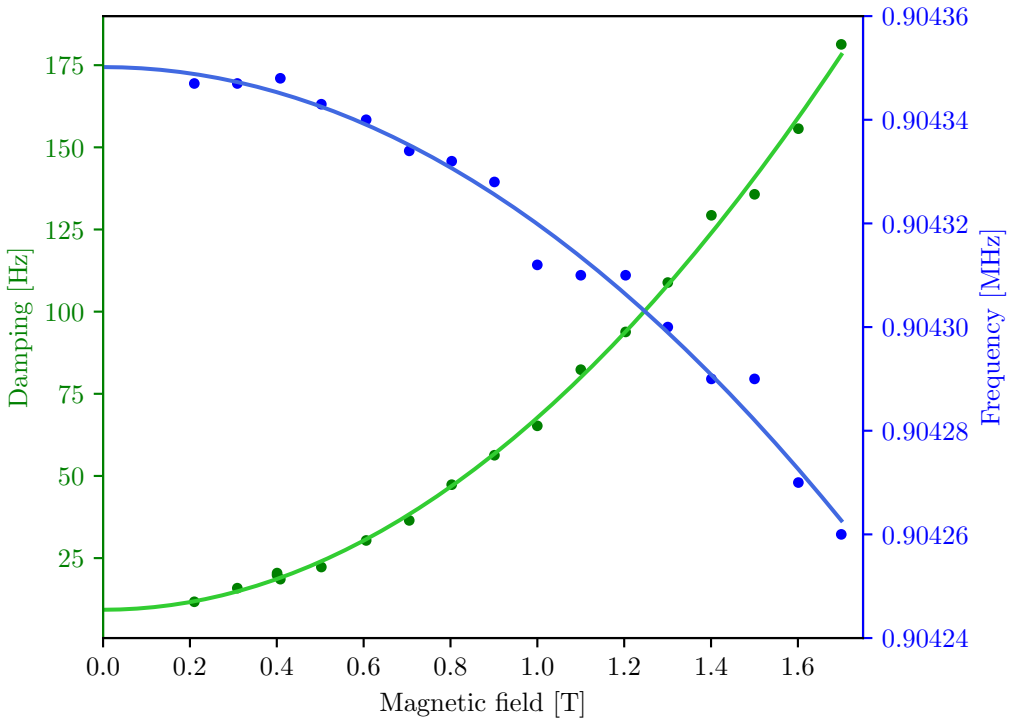

Figure 27: Extracted linewidth and resonance frequency as a function of magnetic field

maximum displacement of the resonator (from the fit height X_m) and the resonance frequency (central position $f_L = \omega_L/2\pi$):

$$X(f) = \frac{X_m \Delta f_L^2}{\Delta f_L^2 + (f - f_L)^2},$$
$$Y(f) = \frac{X_m (f - f_L) \Delta f_L}{\Delta f_L^2 + (f - f_L)^2}. \tag{70}$$

We will determine all mentioned parameters from the fit of the in-phase signal X.

Such a linear response can be measured at different magnetic fields in order to define the intrinsic resonance frequency and damping along with the characteristic impedance of the system. The result of these measurements for the 1 μm wide beam $n = 0$ mode is shown in Fig. 27. The linear response was measured with a fixed drive current, which was small enough to avoid Duffing nonlinearities (see Sec. 5.3). Data is demonstrated with points, while solid lines show quadratic fits of damping $\gamma_0/2\pi + \beta_r B^2$ and resonance frequency $f_0 + \beta_i B^2$. From these fits, we find $\gamma_0/2\pi = 9.3$ Hz and $f_0 = 904350$ Hz which correspond to an intrinsic quality factor for the beam of $Q_0 = 10^5$ (reasonably high value for such devices). From the quadratic components of these fits, by using Eq. 68 and Eq. 69 we can find the parameters of our external circuit: $R_{ext} = 280\ \Omega$, which proves that our setup is indeed high impedance ($R_{ext} \gg 50\ \Omega$), which is necessary to minimise the loading effect on damping. Besides, we can notice from the fit of the observed resonance frequency that $X_{ext} < 0$, which means that our setup is slightly capacitive at MHz frequencies. The reason behind these R_{ext} and X_{ext} values is the impedance

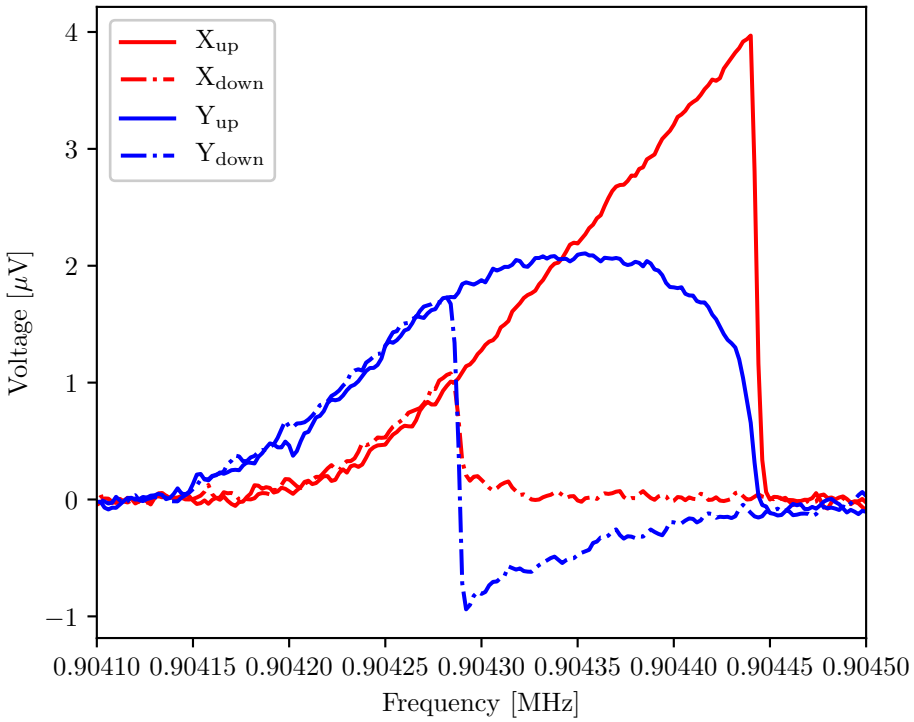

Figure 28: Typical nonlinear response curve

mismatch of our circuit: a high-impedance environment comes at the cost of a disadapted setup, which leads to parasitic reflections and resonances in the lines. This is why $R_{ext} \neq R_I$ and $X_{ext} \neq 0$; which have to be calibrated *in situ*.

5.3 NONLINEAR RESPONSE

When the amplitude of motion becomes large enough, the response curve changes shape and stops being Lorentzian. Due to the large displacement from the equilibrium position, the material of the beam starts to stretch which leads to its stiffening and then an increase of the effective spring constant of the resonator. This increase makes the resonance frequency shift upward. Such a response is usually called a Duffing resonance [93], and the phenomenon is called Duffing nonlinearity. It can be described by an extra positive fit parameter (see Eq. 72). There are exotic cases where a Duffing-like nonlinearity leads to an effective softening, and a shift of the resonance frequency downward. This is described as a negative Duffing constant. In the magnetomotive detection, the nonlinear response can be observed when the driving current is large enough. An example of a strongly nonlinear response is demonstrated on Fig. 28, for the same device as for Fig. 26.

These curves are measured at a relatively small magnetic field of 0.4 T (to minimise damping due to the loading), and at a high drive current of 2.5 nA. The red lines correspond to the in-phase signal X and the blue ones to the quadrature Y. The solid lines show a scan 'up' - where the drive frequency was slowly increased,

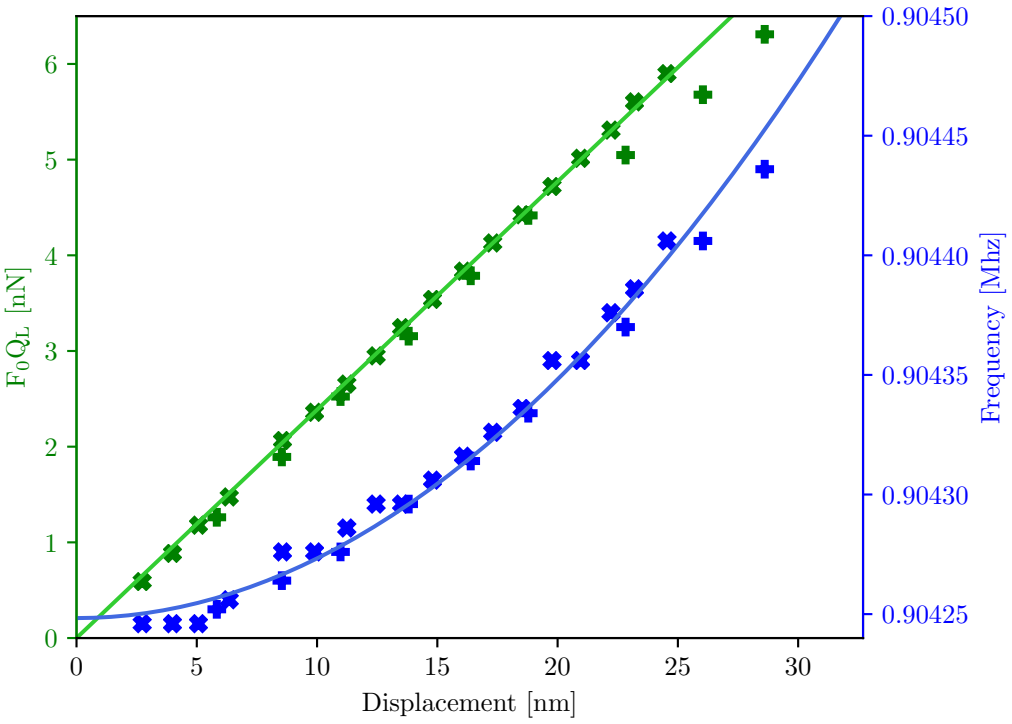

Figure 29: Combined plot of force-displacement and frequency-displacement dependencies

and the semi-dashed lines - scan 'down'. The hysteresis between 'up' and 'down' sweeps is one the fingerprints of the Duffing effect. A region in frequency opens up where the system is bistable: two mechanical states coexist, one with a very large amplitude and the other one which is barely moving.

From such curves we can extract the frequency f_r of the maximum value of the detected voltage and its magnitude X_m on the X_{up} sweep (solid red line on Fig. 28), as a function of drive amplitude F_0. The width of the peak is not related anymore unambiguously to the damping parameter: to extract the latter, one needs a proper numerical fit of the line shape.

The magnitude X_m (here in μV) corresponds to the maximum displacement of the mode $x_n(t)$ from its equilibrium, which means that it can be recalculated in proper units of motion: meters. This displacement grows linearly with the Lorentz force, which is proportional to the drive current, according to Eq. 63. On Fig. 29, the measured dependence of the displacement to the driving force is demonstrated (green axis), along with the frequency versus displacement one (blue axis) for two different magnetic fields: 0.4 T (straight crosses/pluses) and 1.6 T (tilted crosses). The two sets of data overlap well, having taken into account the loading corrections from Fig. 27. The value $F_0 Q_L$ can be clearly fit linearly, according to:

$$k_0 \, X_m = F_0 \, Q_L, \tag{71}$$

which directly gives the spring constant $k_0 = 0.65$ N/m of the measured mode (with X_m expressed in meters). The mode mass can then be obtained simply as $m_0 = k_0/(2\pi f_0)^2 = 20$ pg, which agrees well with geometric expectations.

As well, the frequency shift versus displacement can be fit as:

$$f_r = f_0 + D_0 X_m^2, \tag{72}$$

where $D_0 = 2.5 \cdot 10^{17}$ Hz/m^2 is the Duffing parameter (of mode $n = 0$).

The described set of measurements allows to calibrate nano-mechanical devices along with RF lines in a very sensitive and self-consistent way. This is a pre-requisite for comparison with theory, as performed in Sec. 4.3.

6

OPTOMECHANICS

6.1 OPTICAL ORIGIN

An example of optomechanical system in the optical domain is represented in Fig. 30 (adapted from Ref. [94]). It is basically a Fabry-Pérot interferometer, which consists of two mirrors spaced by a distance L one of which is attached to a spring. This mirror on a spring can move and creates a mechanical resonator with an effective mode resonance at frequency Ω_M. The Fabry-Pérot interferometer on the other hand consists of a cavity located between its mirrors with a frequency ω_c that is fully defined by the length L.

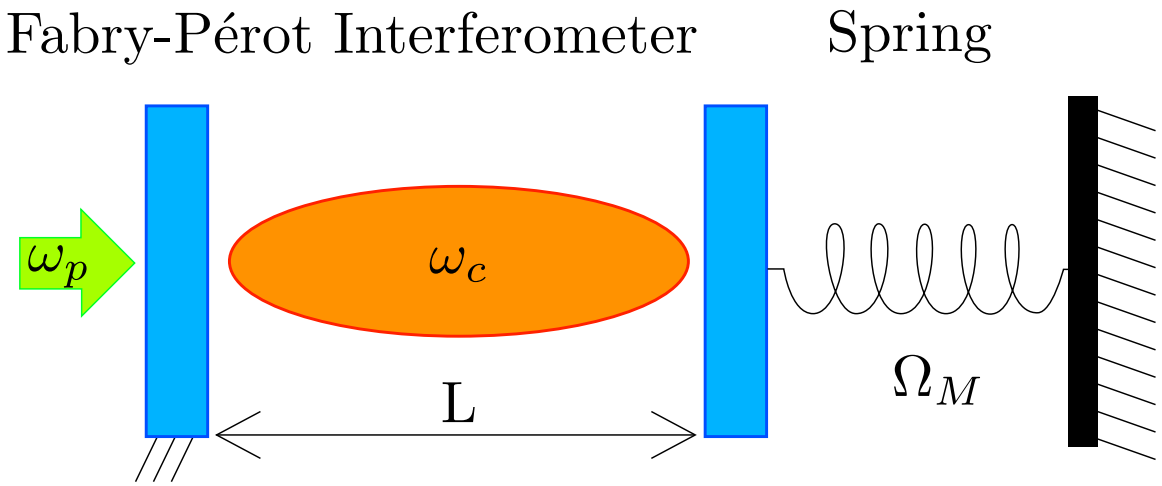

Figure 30: General scheme of an optomechanical system

As soon as there is light in the cavity (fed in through one semi-transparent mirror with a pump at frequency ω_p), it creates a radiation pressure on both mirrors. This pressure makes the mirror on the spring move as a mechanical resonator. This motion changes the gap L between mirrors, which leads to a variation in the interferometer's cavity frequency. This process results in modulations of the cavity frequency ω_c at the frequency of the mechanical resonator Ω_M. This is the optomechanical coupling, which allows to couple mechanical and optical degrees of freedom both ways: enabling us to detect mechanical motion with optics, and vice-versa.

The concept of coupling electromagnetic waves with mechanical motion was foreseen in the 80s by V. Braginsky and C. Caves [15, 17], who demonstrated

that it is potentially a quantum limited detection scheme for motion and defined that quantum limit. These authors had proposed to use the extreme sensitivity to motion/force for gravitational wave detection: which has been achieved by LIGO and VIRGO recently [19]. These are macroscopic optomechanical setups; microscopic ones based on NEMS are also unique force/motion sensors: an example of which being the interaction between a microscale whispering-gallery-mode resonator and a superfluid Helium-4 film [95].

6.2 QUANTUM FORMALISM

As optomechanics originates from experiments in optics using lasers, it is conventionally described in terms of a quantum-mechanical formalism. The most generic Hamiltonian can be written as follows [94, 96]:

$$\begin{aligned}\hat{H} =& \hat{H}_0 + \hat{H}_{0,int} + \hat{H}_{Mec,Duffing} + \hat{H}_{Opt,Kerr} + \\ & \hat{H}_{MecBath} + \hat{H}_{MecBath,int} + \hat{H}_{OptBath} + \hat{H}_{OptBath,int} \ ,\end{aligned} \tag{73}$$

where essentially all relevant ingredients are included: the quantum harmonic oscillators Hamiltonians $\hat{H}_0$ for photonic and phononic modes; the coupling interaction Hamiltonian $\hat{H}_{0,int}$ representing the interaction between them; Hamiltonians for nonlinearities in mechanics $\hat{H}_{Mec,Duffing}$ and optics $\hat{H}_{Opt,Kerr}$; Hamiltonians for optical $\hat{H}_{OptBath}$ and mechanical $\hat{H}_{MecBath}$ baths and interactions with them $\hat{H}_{OptBath,int}$, $\hat{H}_{MecBath,int}$. The applied optical drive (pump) $\hat{H}_D$ can be included in the optical bath $\hat{H}_{OptBath}$ and its interaction $\hat{H}_{OptBath,int}$, i.e. one of the bath modes being populated by a well-defined (classical) amplitude, as described below. A full mathematical derivation can be found in Ref. [96]; here we will only give the linearised Hamiltonian in the semi-classical limit and its main basic implications which are required for the understanding of our experiments.

The Hamiltonian of the optomechanical system with an applied driving tone of power $P_{in} = \hbar\omega_p \langle \hat{A}_p^\dagger \hat{A}_p \rangle$ at frequency ω_p can be written as, without the baths and nonlinear terms:

$$\hat{H} = \hbar(\omega_c(0) - G\hat{x})\hat{a}^\dagger\hat{a} + \hbar\Omega_M \hat{b}^\dagger\hat{b} - i\hbar K_p(\hat{a}^\dagger\hat{A}_p - \hat{A}_p^\dagger\hat{a}) + \ldots, \tag{74}$$

where $\hat{a}$ and $\hat{b}$ are photon and phonon annihilation operators, $G = -\partial\omega_c/\partial x = g_0/x_{zpf}$ is the frequency shift per displacement, g_0 is the optomechanical single-photon coupling rate, and $\hat{x} = x_{zpf}(\hat{b}^\dagger + \hat{b})$ is the displacement operator with x_{zpf} - the zero-point fluctuations amplitude. The constant K_p is related to the coupling rate κ_{ext} of the cavity to the incoming/outgoing laser mode (we consider a single-port setup), and by definition $\hat{A}_p$ represents a traveling wave operator (in units of $\sqrt{\text{Rad/s}}$). This comes from the definitions used in the input-output formalism [97].

First, we will describe the cavity response and the related parameters in the absence of the mechanics. From the Heisenberg equations of motion and making

use of the input-output relations, after a Rotating Wave Transform (RWT) the time evolution of the field $\hat{a}$ inside the cavity is:

$$\dot{\hat{a}} = -\frac{\kappa_{tot}}{2}\hat{a} + i\Delta\hat{a} - \sqrt{\kappa_{ext}}\langle\hat{A}_p\rangle - \sqrt{\kappa_{in}}\hat{f}_{in} - \sqrt{\kappa_{ext}}\hat{f}_{ext}, \tag{75}$$

where $\Delta = \omega_p - \omega_c$ is the detuning of the drive from the cavity, $\kappa_{tot} = \kappa_{ext} + \kappa_{in}$ is the total cavity loss rate which includes the one due to the coupling to the outside κ_{ext}, and the internal cavity loss rate κ_{in}. The term $\hat{f}_{in}$ represents the bosonic operator associated to the cavity internal bath, while $\hat{f}_{ext}$ represents the one of the laser mode. $\langle\hat{A}_p\rangle$ is the classical field amplitude of the incoming laser.

For the Fabry-Pérot resonator and according to the input-output theory, the reflected field writes:

$$\hat{a}_{ref} = \hat{f}_{ext} + \sqrt{\kappa_{ext}}\,\hat{a}, \tag{76}$$

which links what is measured to the intra-cavity field. The mean cavity photon population $\bar{n}_{cav}$, by solving Eq. 75 for the steady-state amplitude (neglecting quantum noise from $\hat{f}_{in}, \hat{f}_{ext}$), can then be written as:

$$\bar{n}_{cav} = \langle\hat{a}^\dagger\hat{a}\rangle = \left|\frac{\sqrt{\kappa_{ext}}\langle\hat{A}_p\rangle}{\kappa_{tot}/2 - i\Delta}\right|^2 = \frac{\kappa_{ext}P_{in}}{[\Delta^2 + (\kappa_{tot}/2)^2]\hbar\omega_p}. \tag{77}$$

For the incoming field, we neglect quantum fluctuations and treat it as a classical field since its amplitude is always much larger than 1: $\langle\hat{A}_p^\dagger\hat{A}_p\rangle = |\langle\hat{A}_p\rangle|^2$. Here, we can make the link between this result and the in-cavity field at the Fourier frequency ω around 0 in the rotating frame (drive ω_p in laboratory frame), which is obtained from the optical susceptibility χ_{opt}:

$$\chi_{opt}(\omega) = \frac{1}{\kappa_{tot}/2 - i(\omega + \Delta)}\,, \tag{78}$$

which is directly derived by Fourier-transforming Eq. 75. We obtain $\bar{n}_{cav} = |\chi_{opt}(0)|^2\,\kappa_{ext}P_{in}/(\hbar\omega_p)$.

After having described the cavity alone, let us now return to the coupling mechanism between mechanical and optical fields. The radiation pressure force can be expressed as:

$$\hat{F}_{rad} = -\frac{d\hat{H}_{0,int}}{d\hat{x}} = -\frac{d(-\hbar G\hat{x}\,\hat{a}^\dagger\hat{a})}{d\hat{x}} = hG\hat{a}^\dagger\hat{a} = \hbar\frac{g_0}{x_{zpf}}\hat{a}^\dagger\hat{a}. \tag{79}$$

The cavity field $\hat{a}$ can be separated into the mean coherent amplitude $\bar{\alpha}$ (arising from the pump) and a fluctuating part $\delta\hat{a}$ (linked to the optomechanical coupling) as $\hat{a} = \bar{\alpha} + \delta\hat{a}$. This brings $\bar{n}_{cav} = |\bar{\alpha}|^2 + \langle\delta\hat{a}^\dagger\delta\hat{a}\rangle$, which can be simplified for large intra-cavity fields when $|\bar{\alpha}|^2 \gg \langle\delta\hat{a}^\dagger\delta\hat{a}\rangle$. The interaction part of the Hamiltonian $\hat{H}_{0,int}$ can then be expressed in terms of the mean field population in the cavity as:

$$\hat{H}_{0,int} = -\hbar g_0(\bar{\alpha} + \delta\hat{a})^\dagger(\bar{\alpha} + \delta\hat{a})(\hat{b} + \hat{b}^\dagger) \approx -\hbar g_0\sqrt{\bar{n}_{cav}}(\delta\hat{a}^\dagger + \delta\hat{a})(\hat{b} + \hat{b}^\dagger), \tag{80}$$

assuming implicitly $\bar{\alpha} > 0$ with no loss of generality and neglecting again $\delta\hat{a}^\dagger\delta\hat{a}$ (limit of $\bar{\alpha} \gg 1$). The different terms $\delta\hat{a}^\dagger\hat{b}^\dagger$, $\delta\hat{a}^\dagger\hat{b}$, $\delta\hat{a}\hat{b}^\dagger$, $\delta\hat{a}\hat{b}$ correspond to the

simultaneous creation or destruction of corresponding quanta, within the two fields.

We then can write down from the input-output formalism the motion equations including the coupling part, for both the cavity field $\delta\hat{a}$ and the phonon field in the mechanical resonator $\hat{b}$:

$$\begin{aligned}\delta\dot{\hat{a}} &= \left(-\frac{\kappa_{tot}}{2} + i\Delta\right)\delta\hat{a} + ig_0\sqrt{\bar{n}_{cav}}(\hat{b}^\dagger + \hat{b}) - \sqrt{\kappa_{in}}\hat{f}_{in} - \sqrt{\kappa_{ext}}\hat{f}_{ext}\ , \\ \dot{\hat{b}} &= \left(-\frac{\Gamma_m}{2} - i\Omega_m\right)\hat{b} + ig_0\sqrt{\bar{n}_{cav}}(\delta\hat{a}^\dagger + \delta\hat{a}) - \sqrt{\Gamma_m}\hat{f}_m\ ,\end{aligned} \tag{81}$$

with $\hat{f}_m$ representing the mechanical bath boson field. Note the symmetry between these two equations; the drive amplitude $\langle\hat{A}_p\rangle$ has now formally disappeared since it is implicitly contained in $\sqrt{\bar{n}_{cav}}$.

These coupled equations can be solved in Fourier space. Remembering the rule $\hat{X}(\omega)^\dagger = \hat{X}^\dagger(-\omega)$, we obtain:

$$\begin{aligned}\delta\hat{a}(\omega)\left[\frac{\kappa_{tot}}{2} - i(\Delta+\omega)\right] &= +ig_0\sqrt{\bar{n}_{cav}}\left[\hat{b}^\dagger(\omega) + \hat{b}(\omega)\right] \quad -\sqrt{\kappa_{in}}\hat{f}_{in}(\omega) \\ &\qquad -\sqrt{\kappa_{ext}}\hat{f}_{ext}(\omega), \end{aligned} \tag{82}$$

$$\begin{aligned}\delta\hat{a}^\dagger(\omega)\left[\frac{\kappa_{tot}}{2} + i(\Delta-\omega)\right] &= -ig_0\sqrt{\bar{n}_{cav}}\left[\hat{b}^\dagger(\omega) + \hat{b}(\omega)\right] \quad -\sqrt{\kappa_{in}}\hat{f}^\dagger_{in}(\omega) \\ &\qquad -\sqrt{\kappa_{ext}}\hat{f}^\dagger_{ext}(\omega), \end{aligned} \tag{83}$$

$$\hat{b}(\omega)\left[\frac{\Gamma_m}{2} + i(\Omega_m-\omega)\right] = +ig_0\sqrt{\bar{n}_{cav}}\left[\delta\hat{a}^\dagger(\omega) + \delta\hat{a}(\omega)\right] - \sqrt{\Gamma_m}\hat{f}_m(\omega), \tag{84}$$

$$\hat{b}^\dagger(\omega)\left[\frac{\Gamma_m}{2} - i(\Omega_m+\omega)\right] = -ig_0\sqrt{\bar{n}_{cav}}\left[\delta\hat{a}^\dagger(\omega) + \delta\hat{a}(\omega)\right] - \sqrt{\Gamma_m}\hat{f}^\dagger_m(\omega). \tag{85}$$

Adding-up two by two these equations, re-injecting $\delta\hat{a}^\dagger(\omega) + \delta\hat{a}(\omega)$ into $\hat{b}^\dagger(\omega) + \hat{b}(\omega)$, and remembering that $\hat{x}(\omega) = x_{zpf}[\hat{b}^\dagger(\omega) + \hat{b}(\omega)]$, we obtain the compact writing that will be described below:

$$\delta\hat{a}^\dagger(\omega) + \delta\hat{a}(\omega) = +i\frac{g_0\sqrt{\bar{n}_{cav}}}{x_{zpf}}\hat{x}(\omega)\left[\chi_{opt}(\omega) - \chi_{opt}(-\omega)^*\right] + \hat{F}_{opt}\ , \tag{86}$$

$$\left[\chi_m(\omega)^{-1} + \Sigma(\omega)\right]\hat{x}(\omega) = \hat{F}_m\ . \tag{87}$$

We introduced the two effective baths forces acting respectively onto the optical degree of freedom and the mechanical one:

$$\hat{F}_{ext} = \hat{f}_{ext}(\omega) + \hat{f}^\dagger_{ext}(\omega), \tag{88}$$

$$\begin{aligned}\hat{F}_{opt} = &-\left[\sqrt{\kappa_{in}}\hat{f}_{in}(\omega) + \sqrt{\kappa_{ext}}\hat{f}_{ext}(\omega)\right]\chi_{opt}(\omega) \\ &-\left[\sqrt{\kappa_{in}}\hat{f}^\dagger_{in}(\omega) + \sqrt{\kappa_{ext}}\hat{f}^\dagger_{ext}(\omega)\right]\chi_{opt}(-\omega)^*, \end{aligned} \tag{89}$$

$$\begin{aligned}\hat{F}_m = m_{eff}x_{zpf}\Bigg[&-\sqrt{\Gamma_m}\hat{f}_m(\omega)\left[\frac{\Gamma_m}{2} - i(\Omega_m+\omega)\right] \\ &-\sqrt{\Gamma_m}\hat{f}^\dagger_m(\omega)\left[\frac{\Gamma_m}{2} + i(\Omega_m-\omega)\right] + 2g_0\sqrt{\bar{n}_{cav}}\Omega_m\,\hat{F}_{opt}\Bigg], \end{aligned} \tag{90}$$

together with the output field noise $\hat{F}_{ext}$. These are constructed from the original bosonic fields $\hat{f}_{in}, \hat{f}_{ext}$, and $\hat{f}_m$ (which have units of $\sqrt{\text{Rad/s}}$). The term m_{eff} is the effective mass of the mechanical mode represented by $\hat{b}$, which for the first flexural mode of a nanostructure will be simply m_0 (see Ch. 4). The zero-point fluctuations are then defined as $x_{zpf} = \sqrt{\hbar/(2m_{eff}\Omega_m)}$. Note the presence of $\hat{F}_{opt}$ in Eq. 90, which demonstrates how the noisy input optical fields influence the mechanics: this is called the stochastic backaction component.

Eq. 86 tells us how the motion $\hat{x}(\omega)$ impacts the optical field, while Eq. 87 simply states that the mechanical susceptibility $\chi_m(\omega)$ is modified through the interaction with light by a term $\Sigma(\omega)$ called the optical self-energy:

$$\begin{aligned}\chi_m(\omega) =& \frac{1}{m_{eff}\left[(\Gamma_m/2)^2 + \Omega_m^2 - \omega^2 - i\omega\Gamma_m\right]} \\ \approx& \frac{1}{2m_{eff}\Omega_m\left[(\Omega_m - \omega) - i\Gamma_m/2\right]}, \qquad (91)\\ \Sigma(\omega) =& 2m_{eff}\Omega_m g_0^2 \bar{n}_{cav}\left[\frac{1}{(\Delta+\omega) + i\kappa_{tot}/2} + \frac{1}{(\Delta-\omega) - i\kappa_{tot}/2}\right], \qquad (92)\end{aligned}$$

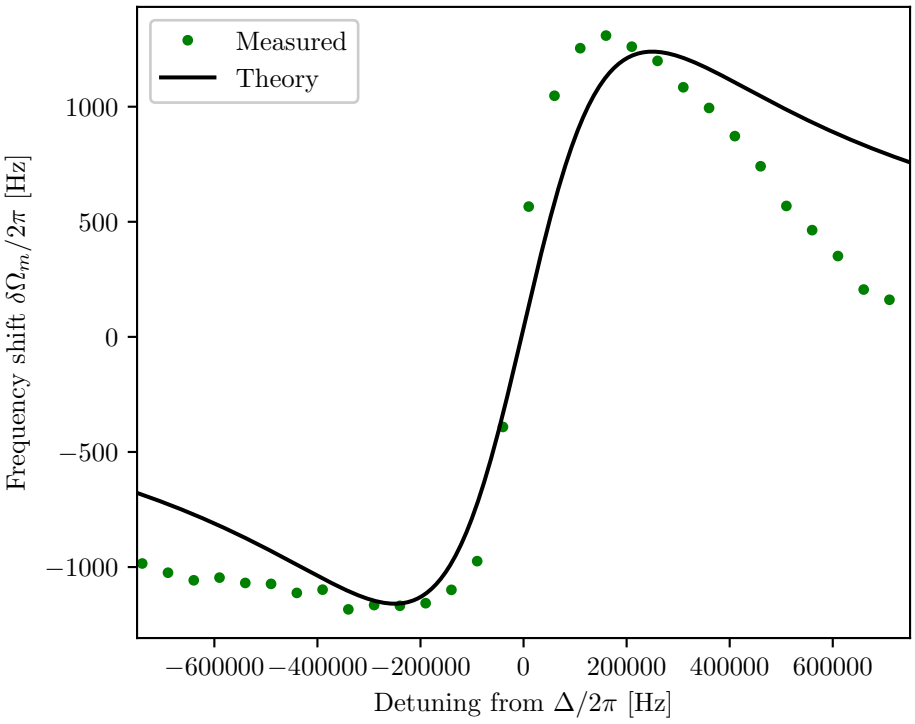

Figure 31: Optical spring measured with the pump tone in the cavity, $\Delta = 0$

where we used $\Gamma_m/2 \ll \Omega_m$ and $\omega \approx \Omega_m$ in Eq. 91 (high Q approximation). Eq. 92 can be recast into $\delta\Omega_m(\omega) - i\Gamma_{opt}(\omega)/2$ by taking real and imaginary parts:

$$\delta\Omega_m = g_0^2 \bar{n}_{cav} \left[\frac{\Delta + \Omega_m}{(\Delta + \Omega_m)^2 + \kappa_{tot}^2/4} + \frac{\Delta - \Omega_m}{(\Delta - \Omega_m)^2 + \kappa_{tot}^2/4} \right], \tag{93}$$

$$\Gamma_{opt} = g_0^2 \bar{n}_{cav} \left[\frac{\kappa_{tot}}{(\Delta + \Omega_m)^2 + \kappa_{tot}^2/4} - \frac{\kappa_{tot}}{(\Delta - \Omega_m)^2 + \kappa_{tot}^2/4} \right], \tag{94}$$

in which we made the approximation $\omega \approx \Omega_m$ since $\Omega_m \gg \kappa_{tot}/2$ (sideband resolved limit).

The meaning of Eqs. 93, 94 is now rather obvious: the former corresponds to a mechanical frequency shift (so-called optical spring) and the latter to a friction term (optical damping). The two contributions are called dynamic backaction of the light field on the mechanical mode. We then write $\Omega_{eff} = \Omega_m + \delta\Omega_m$ and $\Gamma_{eff} = \Gamma_m + \Gamma_{opt}$. These terms depend on the pump strength (with $\bar{n}_{cav}$), but also on the drive detuning Δ. With a pump placed at the cavity frequency ($\Delta = 0$, so-called 'green' scheme), the damping effect is zero while the frequency does shift with pump detuning, see Fig. 31 (measured with a highly coupled optomechanical drum system from Sec. 1.3, using a pump power of 0.1 nW at 10 mK). On the other hand, this damping can be both positive or negative, depending on the sign of the drive tone detuning $\Delta \neq 0$. This is shown in Sec. 6.4; further implications of the measuring scheme are explicitly discussed in Sec. 6.5. For now, we shall come to the mathematical description of the measurement that is specific to our scheme: microwave optomechanics.

6.3 MICROWAVE ANALOGUE

Any optomechanical system consists of three main elements: a cavity, a mechanical resonator, and a means to couple them. This coupling is the key ingredient of such systems, both for their theoretical description and their physical implications. In the original optomechanical configuration described earlier, the coupling happens due to the radiation pressure exerted by light onto a mirror. But radiation pressure originates from electromagnetic interactions, which means that to create an optomechanical-like system there is no need to use lasers, complex optical setups or single-photon counters. A similar effect should exist if one uses lower frequency signals while relying only on electric circuits.

The question that arises is then: how low can the photon's frequency be? From a purely theoretical perspective, the answer should be that it does not matter. However, for practical reasons it is clear that there are limitations. These were discussed in Ch. 2, and the frequency range for the electric signals to use happens to be the microwave domain. As such, the electrical approach to radiation pressure implementation is called microwave optomechanics [23]. Indeed, the microwave range is a good trade-off between low frequencies (down to DC) which are very noisy ($1/f$ noise mainly), and higher frequencies (including light) which are extremely energetic and invasive. Besides, nowadays microwave technologies are on the rise because of the quantum computing boom: amplifiers reach the quantum

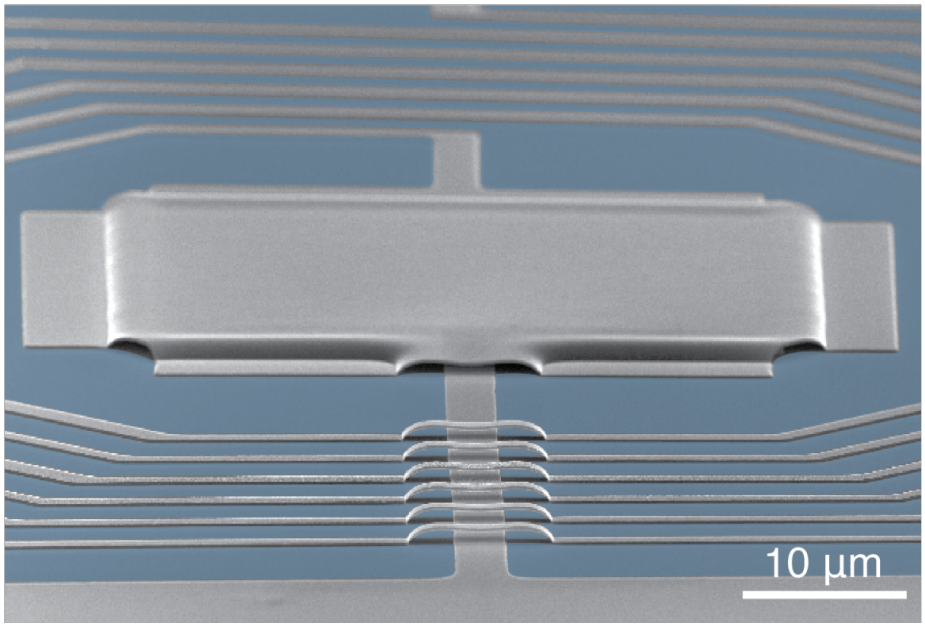

Figure 32: SEM image from literature of a drumhead device in a lumped element type microwave cavity

limit and quantum bits can be interfaced to produce specific schemes. Interestingly, the reverse is also true: since optomechanical systems are quantum-limited by construction and extremely sensitive [15, 17], microwave optomechanical systems can also be thought of as new quantum devices for quantum electronics [98].

The role of the cavity in the microwave domain is taken by superconducting resonators, which are usually realised by coplanar waveguides or microstrips of length $\lambda/2$ (no grounding) or $\lambda/4$ (grounded on one end). Alternatively, the microwave cavity can be realised as a lumped element with a specific design that has to be numerically simulated. This is shown in Fig. 5 of Ch. 1 and in Fig. 32 - image taken from Ref. [99]. The microwave cavity, whatever its design, is just an equivalent RLC circuit in the GHz domain.

This microwave cavity is then coupled to a metalised nano-mechanical resonator, usually capacitively. For better coupling, it is located next to the highest electric field in the cavity: in the case of $\lambda/4$ resonators, it is opposite to the grounding end, while for $\lambda/2$ - it is any of the ends. The motion of the device then modulates the capacitance of the cavity, i.e. $C(x)$. This is the scheme we will describe further. But the coupling can also be realised inductively [100], e.g. through the inductance of a SQUID, which partially consists of a mechanical beam resonator.

For a microwave setup, the actual measured value by the experimentalist is the observable voltage $\hat{V}_{ref} \propto \hat{O}_{ref} = \hat{a}^{\dagger}_{ref} + \hat{a}_{ref}$, which travels in a coaxial cable away from the microwave cavity. Measuring with a spectrum analyser of input impedance Z_0, one obtains the power spectral density, $\mathcal{S}_{\hat{V}_{ref}}(\omega)/Z_0$ (in Joules). From the input-output relation Eq. 76, and using $\hat{a} = \bar{\alpha} + \delta\hat{a}$, one can then link $\hat{O}_{ref}$ to the intra-cavity field observable $\hat{O} = \delta\hat{a}^{\dagger} + \delta\hat{a}$. The spectrum $\hbar\omega\mathcal{S}_{\hat{O}_{ref}}(\omega)$ is

thus this detected power leaving the experiment, which can be formally obtained from (in the laboratory frame):

$$\mathcal{S}_{\hat{O}_{ref}}(\omega) = \mathcal{S}_{\hat{F}_{ext}}(\omega) + \kappa_{ext}\left[\mathcal{S}_{\hat{O}}(\omega) + \bar{n}_{cav}(\omega)\right] + \sqrt{\kappa_{ext}}\mathcal{S}_{\hat{O},\hat{F}_{ext}}(\omega), \tag{95}$$

with $\bar{n}_{cav}(\omega)$ representing the pump tone (symmetric Dirac peaks at $\pm\omega_p$). This is precisely the term that one has to cancel to avoid saturation of amplifiers, see Ch. 2. The term $\mathcal{S}_{\hat{F}_{ext}}(\omega)$ corresponds to the background noise of the travelling wave modelled by $\hat{F}_{ext}$, Eq. 88. $\mathcal{S}_{\hat{O}}(\omega)$ is the spectrum of the cavity, and interestingly $\mathcal{S}_{\hat{O},\hat{F}_{ext}}(\omega)$ corresponds to the spectrum of cross-correlations between $\hat{F}_{ext}$ and $\delta\hat{a}$: these are nonzero by construction since $\hat{f}_{ext}$ appears in both the optical bath driving field $\hat{F}_{opt}$, Eq. 89, and the mechanical driving field $\hat{F}_m$, Eq. 90. Such correlations are also hidden within the definition of $\mathcal{S}_{\hat{O}}(\omega)$; we can express them as:

$$\mathcal{S}_{\hat{O},\hat{F}_{ext}}(\omega) = \mathcal{S}_{\hat{F}_{opt},\hat{F}_{ext}}(\omega) + \frac{g_0\sqrt{\bar{n}_{cav}}}{x_{zpf}}\mathcal{S}_{\chi_{opt}\hat{x},i\hat{F}_{ext}}(\omega), \tag{96}$$

$$\mathcal{S}_{\hat{O}}(\omega) = \mathcal{S}_{\hat{F}_{opt}}(\omega) + \frac{g_0^2\bar{n}_{cav}}{x_{zpf}^2}\frac{\mathcal{S}_{\hat{x}}(\omega \pm \omega_p)}{\kappa_{tot}^2/4 + (\omega \pm \omega_c)^2} + \frac{g_0\sqrt{\bar{n}_{cav}}}{x_{zpf}}\mathcal{S}_{\chi_{opt}\hat{x},i\hat{F}_{opt}}(\omega). \tag{97}$$

Note the argument $\omega \pm \omega_p$ in the mechanical motion's spectrum, which stipulates that it has been translated in frequency space to the pump tone position. We shall not write down explicitly the cross-correlation terms, which is extremely tedious. Neither will we explicitly express the final measured spectra (which are symmetrised expressions). We refer the interested reader to Ref. [96]. Reinjecting these expressions into Eq. 95, one finally writes:

$$\begin{aligned}\frac{\mathcal{S}_{\hat{V}_{ref}}(\omega)}{Z_0} = \hbar\omega\mathcal{S}_{\hat{O}_{ref}}(\omega) =& \hbar\omega\left[\mathcal{S}_{\hat{F}_{ext}}(\omega) + \kappa_{ext}\mathcal{S}_{\hat{F}_{opt}}(\omega) + \sqrt{\kappa_{ext}}\mathcal{S}_{\hat{F}_{opt},\hat{F}_{ext}}(\omega)\right] \\ &+ \hbar\omega\,\kappa_{ext}\frac{g_0^2\bar{n}_{cav}}{x_{zpf}^2}\frac{\mathcal{S}_{\hat{x}}(\omega \pm \omega_p)}{\kappa_{tot}^2/4 + (\omega \pm \omega_c)^2} \\ &+ \frac{g_0\sqrt{\bar{n}_{cav}}}{x_{zpf}}\left[\kappa_{ext}\mathcal{S}_{\chi_{opt}\hat{x},i\hat{F}_{opt}}(\omega) + \sqrt{\kappa_{ext}}\mathcal{S}_{\chi_{opt}\hat{x},i\hat{F}_{extt}}(\omega)\right].\end{aligned} \tag{98}$$

The first line of this equation corresponds to the total background noise: the microwave coaxial line field, the cavity field that leaks out plus their cross-correlations. The latter ensures that the cavity will be visible in the background signal only if its population differs from the travelling wave one (which is possible only if the internal bath is not at the same temperature as the external one). The second term is what is of interest to us: a contribution proportional to the mechanical motion spectrum $\mathcal{S}_{\hat{x}}(\omega)$ visible around the pump tone. However, the last term is rather intriguing: it is due to the backaction of the optical field which drives the mechanics. This leads to the famous effect called sideband asymmetry, that will be discussed further in Sec. 6.4 and Ch. 7. Interestingly, the dynamic backaction effect Eqs. 93, 94 and the formal structure of the detected spectrum Eq. 98 are not specific to quantum mechanics, even though we derived them within this formalism. We will demonstrate it by finding their classical analogue in the next Section.

The microwave optomechanical system could be simplified down to an *RLC*-circuit, where the capacitor has one electrode connected to a spring. Obviously, there is not always a physical lumped element capacitor or inductor, but there can be instead a distributed capacitance and inductance which is in the vicinity of ω_c behave as lumped elements. Then, the equivalent scheme of the microwave optomechanical setup can be drawn as, Fig. 33:

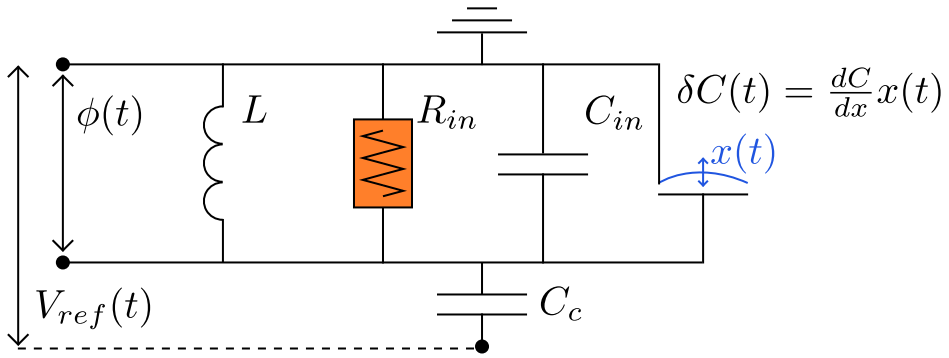

Figure 33: Electric circuit corresponding to a microwave optomechanical system

Having such an electrical scheme implies that the behaviour of this system does not need to be described in terms of quantum mechanics, unless it is in its ground state or very close to it. The vast majority of experiments with microwaves are performed at temperatures in the range from 10 mK to 500 mK, which corresponds to a 4 MHz mechanical resonator's phonon population n_{th} of $60 - 3000$ phonons. This is well within the classical regime $n_{th} \gg 1$. However for the optical part, a microwave mode at 4 GHz has a very low population for temperatures below 1 K. Nonetheless, if there is noise at these frequencies, one can easily obtain photon populations greater than 1. This then corresponds to effective temperatures much larger than 1 K, where the electric circuit behaves classically. And it is obviously possible to perform microwave optomechanics at room temperature: one simply loses resolution because of the noise and the poor microwave quality factors of normal-conducting circuits [101]. Therefore, there is no real need for the quantum formalism in this limit, and it should be possible to describe everything classically with a conventional electric circuit model. Such a model has been recently developed in Ref. [102], and here we will give a quick review of its main results.

The dynamics of the electric circuit on Fig. 33 can be written in terms of classical electric theory as:

$$\frac{d}{dt}\left([C_c + C_{in}(x)]\frac{d\phi}{dt}\right) + \left(\frac{1}{R_{in}} + \frac{1}{R_{ex}}\right)\frac{d\phi}{dt} + \frac{1}{L} = I_{dr} + I_{noise} \tag{99}$$

where $C_{in} = C_{in}(0) + \delta C(t) = C_{in}(0) + dC/dx \cdot x(t)$. I_{dr} corresponds to the pump tone drive, and I_{noise} to the current noise present in the circuit. This

equation can be simplified by introducing the coupling parameter $G = d\omega_c/dx = (d\omega_c/dC)\cdot(dC/dx)$ as:

$$\left(1+\frac{2G}{\omega_c}x\right)\frac{d^2\phi}{dt^2}+\left(\kappa_{tot}+\frac{2G}{\omega_c}\frac{dx}{dt}\right)\frac{d\phi}{dt}+\omega_c^2\phi=\frac{I_{dr}+I_{noise}}{C} \tag{100}$$

with the total capacitance $C = C_c + C_{in}$, the cavity frequency $\omega_c = 1/\sqrt{LC}$, and the loss rate $\kappa_{tot} = \kappa_{ext} + \kappa_{in} = 1/(R_{ext}C) + 1/(R_{in}C) = 1/(RC)$. The external loss $R_{ext}^{-1} = (\omega_c C_c)^2 Z_0$ corresponds to the absorption of the outgoing voltage wave V_{ref} by the circuit load Z_0 (see end of Section) and eventually the input of an amplifier (Sec. 2.2).

The drive current (analogue of the pump tone in Sec. 6.2) can be written as $I_{dr} = \frac{1}{2}I_p \exp(-i\omega_p t) + c.c.$ and the mechanical displacement can be expressed as $x(t) = \frac{1}{2}x_0 \exp(-i\Omega_m t) + c.c.$, with I_p and x_0 the corresponding complex amplitudes. I_p is defined by the pump generator, while x_0 is a stochastic variable, usually the Brownian motion of the mechanical resonator thermalised at the temperature T_m. As already introduced in the previous Section, this motion can also be affected by the backaction from the circuit. The terms in Eq. 100 where motion $x(t)$ multiplies the potential $\phi(t)$ create a nonlinear mixing, which results in harmonics at $\omega_n = \omega_p + n\Omega_m$. The exact solution can be written as:

$$\phi(t) = \sum_{n=-\infty}^{+\infty}\phi_n(t) = \sum_{n=-\infty}^{+\infty}\frac{1}{2}\mu_n(t)\exp(-i\omega_n t) + c.c. \tag{101}$$

By injecting Eq. 101 in Eq. 100, and decomposing also the noise in terms of ω_n as $I_{noise} = \sum_n \frac{1}{2}\delta I_n(t)\exp(-i\omega_n t) + c.c.$, a system of coupled equations for $\mu_n(t)$ can be created. In practice, only solutions which are close to the cavity frequency are relevant, as the amplitudes of these components fall off rapidly with the distance from the cavity position in the sideband-resolved limit $\kappa_{tot} \ll \Omega_m$. Therefore, we will only keep components corresponding to $n = -1, 0, 1$ and will call these components l low, p pump, and h high respectively. For them, the solutions can be found by a rotating wave approximation with the assumption $\Omega_m \ll \omega_c$, as:

$$\begin{aligned}
\mu_p(t) &= +\frac{i}{2}\left(\frac{I_p}{\omega_c C}+\frac{\delta I_p(t)}{\omega_c C}\right)\chi_p,\\
\mu_l(t) &= +\frac{i}{2}\left(G x_0^*(t)\mu_p(t)+\frac{\delta I_l(t)}{\omega_c C}\right)\chi_l,\\
\mu_h(t) &= +\frac{i}{2}\left(G x_0(t)\mu_p(t)+\frac{\delta I_h(t)}{\omega_c C}\right)\chi_h,
\end{aligned} \tag{102}$$

where the cavity susceptibility for each spectral component is:

$$\begin{aligned}
\chi_p &= \frac{1}{-i\Delta+\kappa_{tot}/2},\\
\chi_l &= \frac{1}{-i(\Delta-\Omega_m)+\kappa_{tot}/2},\\
\chi_h &= \frac{1}{-i(\Delta+\Omega_m)+\kappa_{tot}/2}.
\end{aligned} \tag{103}$$

The backaction force on the mechanics due to the capacitor's voltage bias is defined as the gradient of the electromagnetic energy:

$$F_{ba} = +\frac{d}{dx}\left(\frac{1}{2}C(x)\left(\frac{d\phi(t)}{dt}\right)^2\right). \tag{104}$$

We are only interested in the component of this force which affects the mechanics, i.e. the $F_0(t)$ component of it corresponding to an excitation at the mechanical frequency Ω_m: $F_{ba}(t) \approx \frac{1}{2}F_0(t)\exp(-i\Omega_m t) + c.c.$. It can be expressed in the limit of small motion as:

$$F_0(t) \approx +i\frac{G^2}{\omega_c}\left(\frac{C\omega_c^2|\mu_p|^2}{2}\right)(\chi_h - \chi_l^*)\,x_0(t) + i\frac{G}{2}\left(\delta I_h(t)\mu_p^*\chi_h - \delta I_l^*(t)\mu_p\chi_l^*\right), \tag{105}$$

where the first term is the dynamic component proportional to x_0, while the second one is the stochastic component which we will call $\delta F_0(t)$.

The mechanical motion dynamics equation of $x_0(t)$ can be written:

$$-2i\dot{x}_0(t) - i\Gamma_m x_0(t) = \frac{L_0(t) + F_0(t)}{m_{eff}\Omega_m} \tag{106}$$

where L_0 is the Langevin force component acting at Ω_m on an object of effective mass m_{eff}. The solution for x_0 in the rotating frame at Ω_m can be written as:

$$x_0(\omega) = \chi_m(\omega)\left[L_0(\omega) + \delta F_0(\omega)\right], \tag{107}$$

where we defined the mechanical susceptibility $\chi_m(\omega)$ modified by the presence of the optomechanical coupling, in a full analogy with the expressions of the quantum formalism Eqs. 91, 92:

$$\begin{aligned}\chi_m(\omega) &= \left(2m_{eff}\Omega_m(-i\Gamma_m/2 - \omega) + \Sigma(\omega)\right)^{-1},\\ \Sigma(\omega) &= -i\frac{G^2}{\omega_c}\left(\frac{C\omega_c^2|\mu_p|^2}{2}\right)(\chi_h - \chi_l^*),\end{aligned} \tag{108}$$

with $\Sigma(\omega)$ the optomechanical self-energy.

From Eq. 108 we can again define the optical spring effect and the optical damping:

$$\delta\Omega_m = \frac{G^2}{2m_{eff}\Omega_m\omega_c}\frac{C\omega_c^2|\mu_p|^2}{2}\left(\frac{\Delta + \Omega_m}{(\Delta + \Omega_m)^2 + \kappa_{tot}^2/4} + \frac{\Delta - \Omega_m}{(\Delta - \Omega_m)^2 + \kappa_{tot}^2/4}\right), \tag{109}$$

$$\Gamma_{opt} = \frac{G^2}{2m_{eff}\Omega_m\omega_c}\frac{C\omega_c^2|\mu_p|^2}{2}\left(\frac{\kappa_{tot}}{(\Delta + \Omega_m)^2 + \kappa_{tot}^2/4} - \frac{\kappa_{tot}}{(\Delta - \Omega_m)^2 + \kappa_{tot}^2/4}\right). \tag{110}$$

We can notice that the energy stored in the cavity E_c is equal to:

$$E_c = \frac{C\omega_c^2|\mu_p|^2}{2} = P_{in}\kappa_{ext}|\chi_p|^2 = \hbar\omega_c n_{cav}, \tag{111}$$

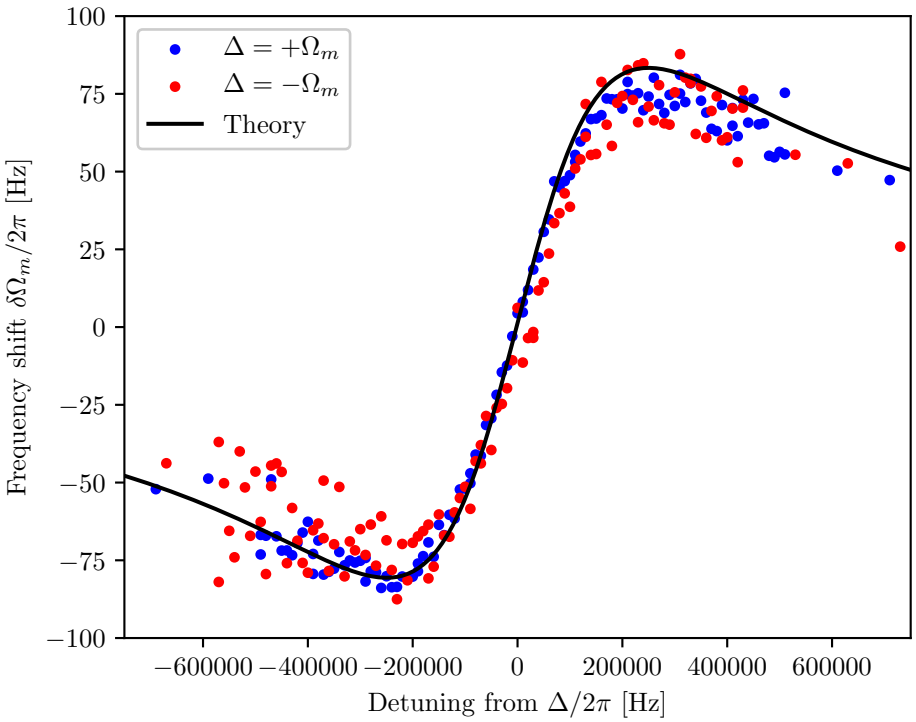

Figure 34: Optical spring measured with the pump tone detuned from the cavity by $\Delta = \pm\Omega_m$

having reproduced also the quantum expression. Also, the first term in Eqs. 109, 110 can be rewritten as, having introduced the x_{zpf} definition:

$$\frac{G^2}{2m_{eff}\Omega_m\omega_c} = \frac{g_0^2}{\hbar\omega_c}. \tag{112}$$

Injecting these two results into the above equations shows that Eq. 109 and Eq. 110 are full analogues to Eq. 93 and Eq. 94. An example of an optical spring is shown in Fig. 34, for 'blue' $\Delta = +\Omega_m$ and 'red' $\Delta = -\Omega_m$ detuning schemes, measured on the same device as for the 'green' case shown in Fig. 31, but here with a pump power $P_{in} = 0.02$ nW at 200 mK.

The measured quantity, from the experimental point of view, is the Power Spectral Density (PSD) of the voltage V_{ref}, which is defined classically as $S_{PSD}(\omega) = 2S_{V_{ref}}(\omega > 0)/Z_0$. It is written as [102]:

$$\begin{aligned} S_{V_{ref}}(\omega) =& S_{V_{noise}} + \omega_c^4 (C_c Z_0)^2 \sum_{n=-\infty}^{+\infty} \left[\frac{S_{\mu_n}(\omega - \omega_n)}{4} + \frac{S_{\mu_n}(\omega + \omega_n)}{4} \right] \\ & - \omega_c^2 (C_c Z_0) \sum_{n=-\infty}^{+\infty} \left[\frac{S_{\mu_n,\delta V_n}(\omega - \omega_n)}{4} + \frac{S_{\mu_n,\delta V_n}(\omega + \omega_n)}{4} \right], \end{aligned} \tag{113}$$

where the first term is the spectrum of the noise on the detector $V_{noise}(t)$ (which is assumed to be due to I_{noise} solely) the second is the sum of the n components of the flux $\phi(t)$, and the third is the sum of the cross-correlations between that flux

and the voltage noise components δV_n (directly linked to δI_n). This subdivision in three terms is formally equivalent to the quantum expression Eq. 98. But in the latter, we had immediately simplified the multi-component structure of the signal (peaks at ω_n); it nonetheless has to be considered when dealing with the self-oscillating state, see Sec. 6.7.

Thus we focus only on terms corresponding to $n = -1, 0, +1$ (l, p, h). The components of the flux $\phi(t)$ introduced above are written:

$$\begin{aligned}
S_{\mu_p}(\omega) =& |\mu_p|^2 2\pi\delta_0(\omega) && + \frac{RS_{\delta I_n}}{4}\frac{\kappa_{tot}}{C\omega_c^2}|\chi_p|^2, \\
S_{\mu_l}(\omega) =& |\mu_p|^2 G^2 \frac{S_{x_0}(\omega)}{4}|\chi_l|^2 && + \frac{RS_{\delta I_n}}{4}\frac{\kappa_{tot}}{C\omega_c^2}|\chi_l|^2 \\
& && + \frac{|\mu_p|^2 G^2 \kappa_{tot}}{2\omega_c}\left[i(\chi_m^*\chi_l - \chi_m\chi_l^*)\right]\frac{RS_{\delta I_n}}{4}|\chi_l|^2, \\
S_{\mu_h}(\omega) =& |\mu_p|^2 G^2 \frac{S_{x_0}(\omega)}{4}|\chi_h|^2 && + \frac{RS_{\delta I_n}}{4}\frac{\kappa_{tot}}{C\omega_c^2}|\chi_h|^2 \\
& && + \frac{|\mu_p|^2 G^2 \kappa_{tot}}{2\omega_c}\left[i(\chi_m\chi_h - \chi_m^*\chi_h^*)\right]\frac{RS_{\delta I_n}}{4}|\chi_h|^2,
\end{aligned} \tag{114}$$

where $\delta_0(\omega)$ is the Dirac function and $S_{x_0}(\omega) = |\chi_m(\omega)|^2(S_{L_0} + S_{\delta F_0})$ is the displacement spectrum (according to Eq. 107), which is nothing but a Lorentzian peak. Similarly, the cross-correlations are:

$$\begin{aligned}
S_{\mu_p,\delta V_p}(\omega) =& + \frac{2(\omega_c C_c Z_0)}{\omega_c C}\left[\chi_p + \chi_p^*\right]\frac{R_{ext}S_{\delta I_n}}{4}, \\
S_{\mu_l,\delta V_l}(\omega) =& + \frac{2(\omega_c C_c Z_0)}{\omega_c C}\left[\chi_l + \chi_l^*\right]\frac{R_{ext}S_{\delta I_n}}{4} \\
& + |\mu_p|^2 G^2(\omega_c C_c Z_0)\left[i(\chi_l^2\chi_m^* - \chi_l^{*2}\chi_m)\right]\frac{R_{ext}S_{\delta I_n}}{4}, \\
S_{\mu_h,\delta V_h}(\omega) =& + \frac{2(\omega_c C_c Z_0)}{\omega_c C}\left[\chi_h + \chi_h^*\right]\frac{R_{ext}S_{\delta I_n}}{4} \\
& + |\mu_p|^2 G^2(\omega_c C_c Z_0)\left[i(\chi_h^2\chi_m - \chi_h^{*2}\chi_m^*)\right]\frac{R_{ext}S_{\delta I_n}}{4}.
\end{aligned} \tag{115}$$

Finally, the resulting spectrum on the lock-in in 'Spectrum' mode (see Sec. 2.4) can be written in a compact form:

$$\begin{aligned}
S_{PSD}(\omega) =& 2k_B T_{ext} + P_{dr}2\pi\delta_0(\omega - \omega_p) \\
& + \kappa_{ext}k_B(T_{cav} - T_{ext})\kappa_{tot}|\chi_p|^2\Pi(\omega - \omega_p) \\
& + \kappa_{ext}\frac{g_0^2 n_{cav}}{\hbar\omega_c}\frac{S_x^-(\omega - \omega_p)}{x_{zpf}^2}|\chi_l|^2 + \kappa_{ext}k_B(T_{cav} - T_{ext})\kappa_{tot}|\chi_l|^2\Pi(\omega - \omega_l) \\
& + \kappa_{ext}\frac{g_0^2 n_{cav}}{\hbar\omega_c}\frac{S_x^+(\omega - \omega_p)}{x_{zpf}^2}|\chi_h|^2 + \kappa_{ext}k_B(T_{cav} - T_{ext})\kappa_{tot}|\chi_h|^2\Pi(\omega - \omega_h),
\end{aligned} \tag{116}$$

where $\Pi(\omega)$ represents a door function (in this case of width Ω_m), remembering that each cavity component is defined around a precise angular frequency $\omega_n =$

$\omega_p + n\Omega_m$. In this expression, we injected the external temperature defined as $k_B T_{ext} = R_{ext} S_{I_{noise}} = R_{ext} S_{\delta I_n}/4$, and the cavity temperature as $2k_B T_c = R S_{I_{noise}} = R S_{\delta I_n}/4$ (defined for each specific n). As already mentioned in the quantum Section, if $T_{cav} = T_{ext}$ the cavity peak becomes invisible: one needs a photon flux in (dip, $T_{cav} < T_{ext}$) or out (peak, $T_{cav} > T_{ext}$) to see it. The term P_{dr} is the power of the drive microwave pump, which leaks out of the cavity: this is precisely the term that the opposition line compensates, see Sec. 2.5. All cross-correlations terms are included into the spectra of negative ($n = -1$) and positive ($n = +1$) sidebands as:

$$S_x^-(\omega) = S_x(\omega) + |\chi_m(\omega - \Omega_m)|^2 S_{\delta F_{ext,l}}, \tag{117}$$

$$S_x^+(\omega) = S_x(\omega) + |\chi_m(\omega + \Omega_m)|^2 S_{\delta F_{ext,h}}. \tag{118}$$

$S_{\delta F_{ext,l}}$ and $S_{\delta F_{ext,h}}$ mimic an extra-noise force, which depends on the sideband. Note that these exist only in the measured signal, because of cross-correlations, and do not correspond to a real force on the device: this is the essence of sideband asymmetry.

As already stated, Eq. 116 basically represents the same result as Eq. 98. Beyond the sideband asymmetry effect, the dynamic and stochastic backaction terms are already included into $S_x(\omega)$, according to Eqs. 107 and 108. These results will be experimentally realised in Ch. 7, using our three basic single-tone measuring schemes presented below in Sec. 6.5. The key is that all the basic optomechanical features have been derived here in a completely classical treatment with no quantum nature. Mimicking a high temperature cavity environment will thus require the use of our Noise Generator (NG), see Sec. 2.6.

6.5 MAIN MEASURING SCHEMES

We shall from now on make the link experimentally between the quantum and the classical approaches. In this thesis, we essentially used only single-tone measurements: applying a pump microwave signal at a given detuning Δ from the cavity frequency ω_c, while measuring the sideband peak seen in the spectrum at the proper frequency (depending on the scheme). This peak can be fit with a Lorentzian expression (Eq. 119):

$$R[f] = \frac{a(\gamma/2)^2}{(\gamma/2)^2 + (f - f_0)^2}, \tag{119}$$

$$A = \pi a(\gamma/2). \tag{120}$$

The signal A (in photons/s) is acquired as the area of that Lorentzian fit as Eq. 120. The Lorentzian expression also includes γ as the full width of the peak (in Hz), a as its height (in photons), and f_0 as the central frequency position (in Hz).

There are 3 main measuring schemes to probe the optomechanical system with an applied pump: in-cavity ('green'), Stokes ('blue'), and anti-Stokes pumping ('red').

We demonstrate sideband peaks of the highly coupled drum device (see Sec. 6, all examples of measurements in this Section were acquired with it), measured

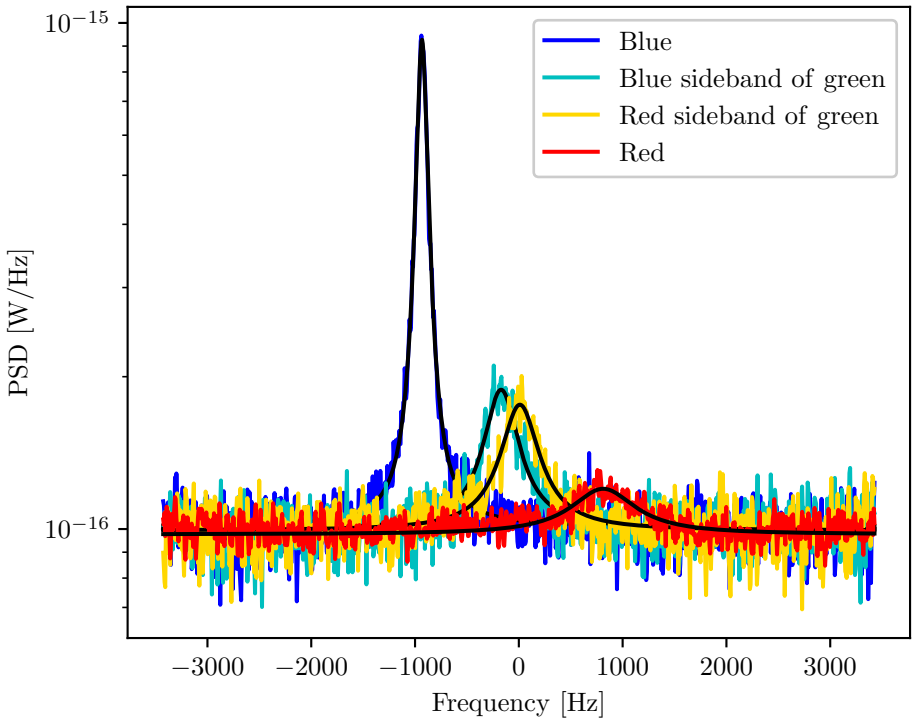

Figure 35: Signals of the optomechanical response as seen on the lock-in with a background translated to 10^{-16} W/Hz, and corresponding Lorentzian fits on top

at 100 mK with a pump power $P_{in} = 0.02$ nW with 3 measuring schemes on the Fig. 35 with corresponding fits. With in-cavity (or 'green') pumping, the signal from the pump has a frequency equal to the resonance frequency of the cavity, $\omega_p = \omega_c$ (equivalently detuning $\Delta = 0$). The sidebands to be measured appear at frequencies $\omega_c \pm \omega_m$, where ω_m is the frequency of the mechanical resonator. The signal at $\omega_c - \omega_m$ will be further called 'redside' signal (Fig. 35, yellow line), and the one at $\omega_c + \omega_m$ the 'blueside' one (Fig. 35, cyan line). The two peaks are Lorentzian with a width given by the intrinsic mechanical damping rate Γ_m. There is no optomechanical damping effect, and the two peaks have essentially the same height.

For Stokes pumping (or 'blue amplification'), the pump signal frequency $\omega_p = \omega_c + \Delta$ is detuned from the cavity by $\Delta = +\Omega_m$. The signal is then observed inside the cavity at ω_c (Fig. 35, blue line), the sideband at $\omega_c + 2\Omega_m$ being strongly suppressed. This scheme is remarkable since it leads to parametric amplification of the Brownian motion: the linewidth of the peak narrows as $\Gamma_{eff} = \Gamma_m - |\Gamma_{opt}|$, while its amplitude grows with applied pump power P_{in}. This effect is called dynamic backaction [94, 102].

With anti-Stokes pumping (or 'red cooling'), the pump signal is detuned from the cavity by $\Delta = -\Omega_m$, and the sideband is also observed in the cavity (Fig. 35, red line), as the other one is again suppressed. The remarkable feature of this scheme is that this time the dynamic backaction makesthe damping increase as

$\Gamma_{eff} = \Gamma_m + |\Gamma_{opt}|$ with pump power P_{in}, leading to de-amplification (or cooling) of the mode.

The generic expression for the signal dependence to applied pump power on chip in all three measuring schemes can be summarised as, in the classical limit:

$$A = \frac{k_B T}{\hbar \Omega_m} g_0^2 n_{cav} \frac{\kappa_{ext}}{(|\Delta| - \Omega_m)^2 + (\kappa_{tot}/2)^2} \frac{\Gamma_m}{\Gamma_m - |\Gamma_{opt}| \cdot sign(\Delta)}, \tag{121}$$

where:

$$n_{cav} = \frac{\kappa_{ext} P_{in}}{[\Delta^2 + (\kappa_{tot}/2)^2]\hbar\omega_c}, \tag{122}$$

$$|\Gamma_{opt}| = \frac{4 g_0^2 n_{cav}}{\kappa_{tot}}, \tag{123}$$

with the function $sign(\Delta) = -1, 1$, and 0 for negative, positive, and zero Δ values respectively. Note the new definition $|\Gamma_{opt}|$ that we adopt now on for simplicity, independently of the scheme. Data measured at 100 mK are shown in Fig. 36 for the three schemes. Lines are fits (see discussion below).

The effect of the measuring scheme and applied pump power P_{in} on the effective mechanical damping rate can be summed-up as:

$$\Gamma_{eff} = \Gamma_m - sign(\Delta)|\Gamma_{opt}| = \Gamma_m - sign(\Delta)\frac{4 g_0^2}{\kappa_{tot}} \frac{\kappa_{ext} P_{in}}{[\Delta^2 + (\kappa_{tot}/2)^2]\hbar\omega_c}. \tag{124}$$

Measured data of effective damping Γ_{eff} obtained simultaneously with the previous graph are shown in Fig. 37, with fits (small correction for the 'technical heating' is included, see Ch. 7).

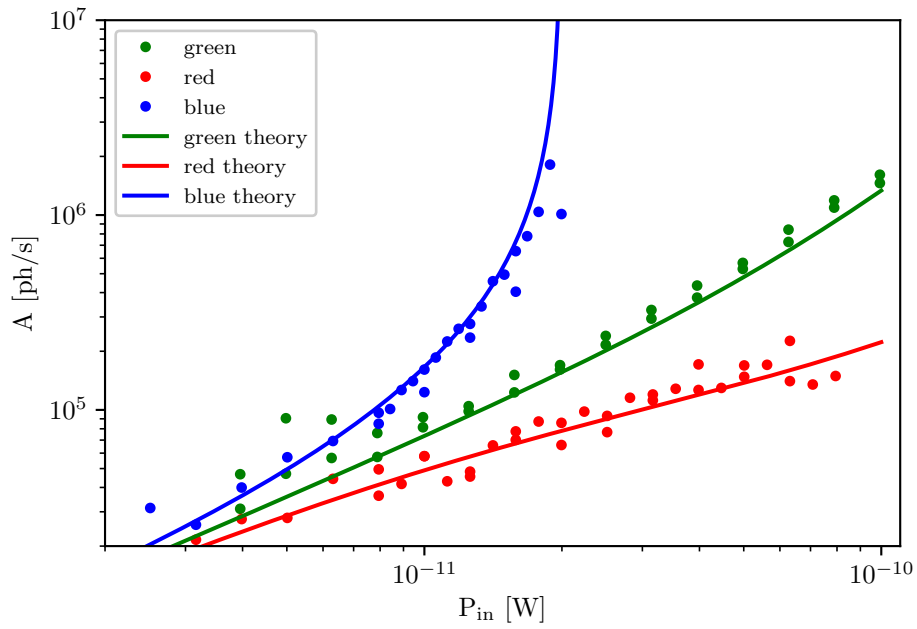

Figure 36: Typical measured signal using different pumping schemes: theory and experiment

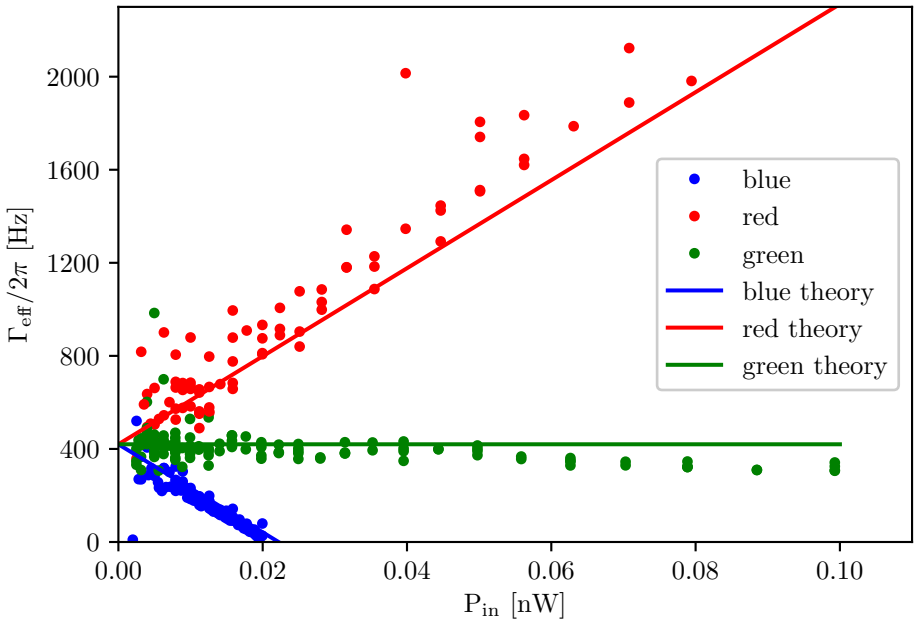

Figure 37: Damping power dependence for different measuring schemes

The measurements demonstrated in Fig. 36 and Fig. 37 are used to define the value of g_0 according to Eq. 121 and Eq. 124. As far as $k_B T \gg \hbar\Omega_m$, the classical expressions and quantum expressions of the previous Sections are equivalent: Eq. 121 essentially leads to the mode temperature extraction T, which will be further discussed with our experimental results in the Ch. 7.

One can note that Eqs. 122, 123 directly depend on the damping rates of the microwave cavity $\kappa_{ext}, \kappa_{tot} = \kappa_{in} + \kappa_{ext}$: for a quantitative fitting, one should in the first place measure these parameters together with the cavity frequency ω_c. The microwave cavity resonance can be characterised with a standard linear response procedure by applying a small probe tone (at frequency $f = \omega/2\pi$, and fixed power P_{probe}) and measuring the output signal P_{out} at the same frequency. Their ratio leads to the definition of the parameter $S_{11}[\omega] = P_{out}[\omega]/P_{probe}[\omega]$ which is the reflection component of the scattering matrix, also called 'S-matrix'. It can be done with a Vector Network Analyser (VNA), or with a synchronised generator and lock-in through our mixing technique (see Sec. 2.3). This measurement can be fit by the expression from Ref. [103]:

$$S_{11}[\omega]_{dB} = 20\,log\left|\frac{(Q_{ext} + iQ_{im} - 2Q)(Q_{ext} + iQ_{im})^{-1} + 2iQ\frac{\omega-\omega_c}{\omega_c}}{1 + 2iQ\frac{\omega-\omega_c}{\omega_c}}\right|. \qquad (125)$$

In this expression Q_{im} captures the phase-dependent background that is hidden in a global amplitude measurement. Such a fit is shown in Fig. 38 as solid black line on our data at 100 mK. From the fit of Q_{ext}, Q we define the damping rates as $\kappa_{tot} = \omega_c/Q$ and $\kappa_{ext} = \omega_c/Q_{ext}$. These cavity characterisations are done with a probe power as low as possible, such that the S_{11} measurement is not affected by it. On the other hand, they are performed at various temperatures and applied

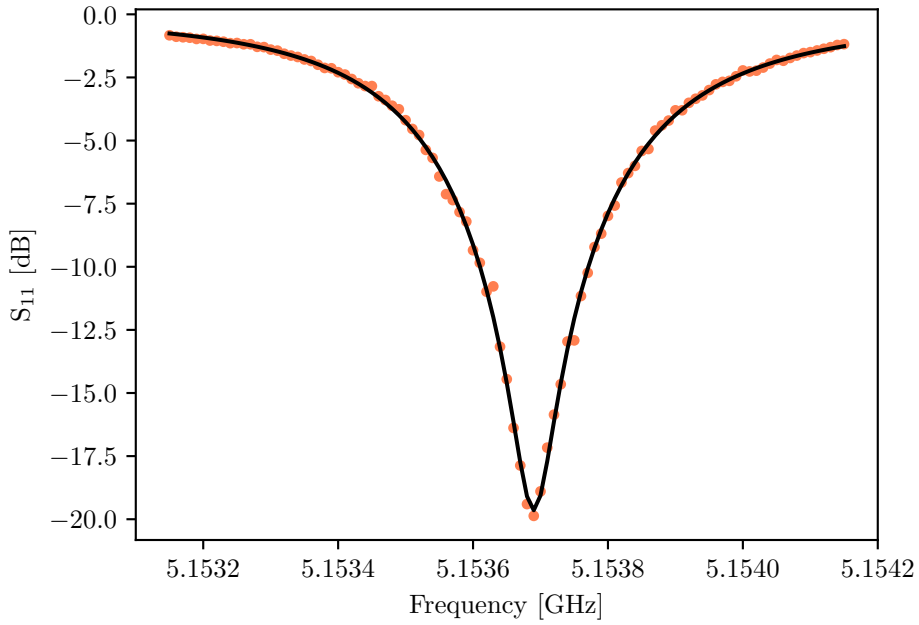

Figure 38: Linear response of a typical cavity measured with a probe tone

pump powers in order to track the cavity properties corresponding to our specific optomechanical settings.

6.6 FROM ENERGY SPECTRA TO LANGEVIN FORCE

Experimentally, we measure the energy stored in a mechanical mode $\propto T$ (classical limit). This comes from the Brownian motion $x(t)$ that this mode encounters, which is described as being due to a stochastic driving force exerted by the thermal bath, the Langevin force. There should thus be a direct link between the energetic description and the mechanical description.

We will here reconstruct the energetic description of a mode from its motion, at least in the so-called high-Q limit [42]. Consider the dynamics equation of a harmonic oscillator:

$$\ddot{x} + \Gamma_m \dot{x} + \Omega_m^2 x = L_m / m_{eff}, \tag{126}$$

with $L_m(t)$ the Langevin force linked to the damping Γ_m through the fluctuation-dissipation theorem. Both originate from a thermal bath at temperature T, and the stochastic force is by definition described by a centred ($\langle L_m \rangle = 0$) Gaussian probability distribution with correlator:

$$C_{L_m}(\tau) = \langle L_m(t) L_m(t-\tau) \rangle = 2 m_{eff} \Gamma_m k_B T \, \delta_0(\tau). \tag{127}$$

The presence in the above equation of the Dirac distribution simply means that there is no finite correlation time characterising the bath (the associated spectrum is white). This obviously poses a mathematical problem for our definitions: the variance of this noise which defines the width of the Gaussian probability distribution is infinite (since it is related to the integral of the fluctuation spectrum).

It shall not impact the final result of the modelling, which is cut-off at high frequencies by the mechanical relaxation rate. One should therefore clarify that L_m fluctuations are Gaussian for any bandwidth $\Delta\omega$ cut in the white noise spectrum around any frequency ω_0.

Let us now transpose the dynamics into the Rotating Frame associated to the mode (at frequency Ω_m):

$$L_m(t) = L_X(t)\cos(\Omega_m t) + L_Y(t)\sin(\Omega_m t), \tag{128}$$

$$x(t) = X(t)\cos(\Omega_m t) + Y(t)\sin(\Omega_m t), \tag{129}$$

having introduced the two quadratures of force and motion. The complex Langevin force introduced in Sec. 6.4 therefore writes $L_0(t) = L_X(t) + iL_Y(t)$. Eq. 126 can be rewritten in matrix form:

$$\begin{pmatrix} 1 & +\frac{1}{2Q} \\ -\frac{1}{2Q} & 1 \end{pmatrix} \begin{pmatrix} -\dot{X} \\ +\dot{Y} \end{pmatrix} = -\frac{\Gamma_m}{2} \begin{pmatrix} 1 & 0 \\ 0 & 1 \end{pmatrix} \begin{pmatrix} -X \\ +Y \end{pmatrix} + \frac{\Omega_m}{2k_{eff}} \begin{pmatrix} L_Y \\ L_X \end{pmatrix},$$

with $Q = \Omega_m/\Gamma_m$ the quality factor, having neglected the slow components $\ddot{X}, \ddot{Y}$ (Rotating Wave Approximation, valid for $Q \gg 1$). The effective spring constant is simply $k_{eff} = \Omega_m^2 m_{eff}$. Similarly, we write:

$$\dot{x}(t) \;=\; \Omega_m \left[-X(t)\sin(\Omega_m t) + Y(t)\cos(\Omega_m t)\right], \tag{130}$$

for the velocity, neglecting $\dot{X}, \dot{Y}$. From the definitions of kinetic energy $E_c = m_{eff}\dot{x}^2/2$ and potential energy $E_p = k_{eff}x^2/2$, we simply obtain for the total energy $E_m = E_c + E_p$:

$$E_m(t) = k_{eff}\frac{X(t)^2 + Y(t)^2}{2}. \tag{131}$$

Let us take the limit $Q \to +\infty$ in Eq. 130; the X and Y equations then separate. Multiplying the first one by $k_{eff}X$, and the second one by $k_{eff}Y$ we write:

$$\begin{cases} k_{eff}X\,\dot{X} = -\dfrac{\Gamma_m}{2}k_{eff}X^2 - \dfrac{\Omega_m}{2}X\,L_Y, \\ k_{eff}Y\,\dot{Y} = -\dfrac{\Gamma_m}{2}k_{eff}Y^2 + \dfrac{\Omega_m}{2}Y\,L_X, \end{cases} \tag{132}$$

which after adding-up leads to the result:

$$\frac{dE_m}{dt} = -\Gamma_m E_m + \frac{\Omega_m}{2}\left[Y\,L_X - X\,L_Y\right]. \tag{133}$$

Introducing the energy difference $\Delta E(t) = E_m(t) - \langle E_m\rangle$ and the bath stochastic energy flow $R_m(t)$:

$$R_m(t) = \frac{\Omega_m}{2}\left[Y(t)L_X(t) - X(t)L_Y(t)\right] - \Gamma_m\langle E_m\rangle, \tag{134}$$

obtained here in the high-Q limit, this equation can be recast into the form of:

$$\frac{d\Delta E(t)}{dt} = -\Gamma_m\Delta E(t) + R_m(t). \tag{135}$$

A more generic discussion can be found in Ref. [104]. The mean energy can be inferred from the equipartition result (see thereafter): $\langle E_m \rangle = k_B T$. Eq. 135 is finally easily solved in frequency-space as:

$$S_{\Delta E}(\omega) = \frac{S_{R_m}(\omega)}{\Gamma_m^2 + \omega^2}, \tag{136}$$

with S_{R_m} the spectrum associated to R_m. We should now construct the statistical properties of this variable from the initial properties of L_m.

To do so, Eq. 134 is rewritten as:

$$R_m(t) = R_X(t) + R_Y(t) - \Gamma_m \langle E_m \rangle, \tag{137}$$

$$R_X(t) = \frac{\Omega_m}{2}(\chi * L_X)(t) L_X(t), \tag{138}$$

$$R_Y(t) = \frac{\Omega_m}{2}(\chi * L_Y)(t) L_Y(t), \tag{139}$$

where we introduced the mechanical susceptibility $\chi(t)$ Fourier Transform (in the rotating frame), and $*$ designates the convolution product [$(f * g)(t) = \int_{-\infty}^{+\infty} f(t - x) g(x) dx$]. We have:

$$\chi(t) = \frac{\Omega_m}{2k_{eff}} e^{-\frac{\Gamma_m}{2} t} \Theta(t), \tag{140}$$

$$\langle L_X(t) L_X(t - \tau) \rangle = 4 m_{eff} \Gamma_m k_B T \, \delta_0(\tau), \tag{141}$$

$$\langle L_Y(t) L_Y(t - \tau) \rangle = \langle L_X(t) L_X(t - \tau) \rangle, \tag{142}$$

$$\langle L_X(t) L_Y(t - \tau) \rangle = 0, \tag{143}$$

with $\Theta(t)$ the Heaviside step-function (0 for $t < 0$ and 1 for $t > 0$; for the time being, we only require $\Theta(0)$ to be finite). The relations Eqs. 142, 143 simply state that the phase of the random force is irrelevant, which would not be the case in the presence of a squeezed noise. Eq. 140 solves Eq. 130 in the limit $1/Q \approx 0$, while Eq. 141 is deduced from Eqs. 127, 128 (note the extra factor of 2 in the rotating frame noise amplitude). L_X and L_Y have by construction the same probability distribution as L_m (namely Gaussian). The mean values satisfy:

$$\langle R_X \rangle = \langle R_Y \rangle = \Gamma_m k_B T \int_{-\infty}^{+\infty} e^{-\frac{\Gamma_m}{2}(t-x)} \Theta(t - x) \delta_0(x - t) dx = \Gamma_m k_B T \, \Theta(0), \tag{144}$$

which introduces the value $\Theta(0)$ which has not been defined yet. In order to impose $\langle R_m \rangle = 0$, we have to take $\Theta(0) = 1/2$.

Consider now the correlation functions of the type:

$$\langle R_A(t) R_B(t') \rangle = \left(\frac{\Omega_m^2}{4k_{eff}} \right)^2 \times \int_{-\infty}^{+\infty} \int_{-\infty}^{+\infty} e^{-\frac{\Gamma_m}{2}(t-x)} \Theta(t - x) \, e^{-\frac{\Gamma_m}{2}(t'-x')} \Theta(t' - x') \langle F_A(x) F_A(t) F_B(x') F_B(t') \rangle dx dx', \tag{145}$$

with $A, B = X, Y$ in all possible combinations. The second order force correlator can be decomposed using Wick's theorem:

$$\langle F_A(x) F_A(t) F_B(x') F_B(t') \rangle = \langle F_A(x) F_A(t) \rangle \langle F_B(x') F_B(t') \rangle + \langle F_A(x) F_B(x') \rangle \langle F_A(t) F_B(t') \rangle + \langle F_A(x) F_B(t') \rangle \langle F_B(x') F_A(t) \rangle. \tag{146}$$

Reinjecting this result into Eq. 145, one obtains:

$$\langle R_X(t)R_X(t')\rangle = \langle R_Y(t)R_Y(t')\rangle = (\Gamma_m k_B T)^2\,\Theta(0)^2 + \Gamma_m\,(k_B T)^2\left[\delta_0(t-t') + \Gamma_m\Theta(t-t')\Theta(t'-t)\right], \tag{147}$$

$$\langle R_X(t)R_Y(t')\rangle = \langle R_Y(t)R_X(t')\rangle = (\Gamma_m k_B T)^2\,\Theta(0)^2. \tag{148}$$

In Eq. 147, the product $\Theta(t-t')\Theta(t'-t)$ can obviously be dropped when compared to the $\delta_0(t-t')$ term. Finally, making use of all of these findings, we deduce from Eq. 137:

$$\langle R_m(t)R_m(t')\rangle = 2\Gamma_m(k_B T)^2\delta_0(t-t'), \tag{149}$$

which leads to the corresponding (white) spectrum $S_{R_m}(\omega) = 2\Gamma_m(k_B T)^2$; Eq. 136 therefore produces an energy power spectrum typical of an Ornstein-Uhlenbeck process [105, 106]. This is precisely what is measured for the thermodynamics component in Ch. 8, having taken into account the optical bath as well.

To conclude this Section, let us focus on the distributions of the random variables. Since the forces L_X, L_Y are Gaussian distributed, their corresponding motions X, Y are also Gaussian (linear response). Their Probability Distribution Functions (PDF) are written as:

$$p(X) = \frac{1}{\sqrt{2\pi\sigma_X^2}} e^{-\frac{X^2}{2\sigma_X^2}}, \tag{150}$$

$$p(Y) = \frac{1}{\sqrt{2\pi\sigma_Y^2}} e^{-\frac{Y^2}{2\sigma_Y^2}}, \tag{151}$$

with σ_X^2, σ_Y^2 the corresponding variances, which are defined as:

$$\sigma_X^2 = \sigma_Y^2 = \frac{1}{2\pi}\int_{-\infty}^{+\infty} |\chi(\omega)|^2 S_{L_X}(\omega)\,d\omega = \frac{k_B T}{k_{eff}}, \tag{152}$$

in which we introduced:

$$\chi(\omega) = \frac{\Omega_m}{2k_{eff}}\frac{1}{\Gamma_m/2 + i\omega}, \tag{153}$$

$$S_{L_X}(\omega) = 4m_{eff}\Gamma_m k_B T, \tag{154}$$

the mechanical susceptibility $\chi(\omega)$ in frequency-space and the force noise spectrum $S_{L_X}(\omega)$. The variances are finite, as they should.

Eq. 131 tells us that energy is the sum of two uncorrelated squared Gaussian variables: this is known as a $(\chi_2)^2$ law. It results in an exponential distribution function:

$$p(E_m) = \frac{1}{\sigma_E} e^{-\frac{E_m}{\sigma_E}}\,\Theta(E_m), \tag{155}$$

which satisfies $\langle E_m\rangle = \sigma_E$ and $\langle E_m^2\rangle = 2\sigma_E^2$ and leads to an energy variance of σ_E^2. Since $\langle E_m\rangle = k_{eff}(\sigma_X^2 + \sigma_Y^2)/2$, one infers immediately that $\sigma_E = k_B T$ which matches the well-known equipartition result.

Eq. 155 is nothing but the classical version of the Boltzmann distribution. This is indeed the statistics we measure in Ch. 8 for a single mechanical mesoscopic mode. The final message is then that an exponential energy distribution is equivalent to a Gaussian motion distribution with the magnitudes of the associated white spectrum related to T, the bath characteristic temperature.

6.7 SELF-OSCILLATIONS AND NON-LINEARITIES OF THE HAMILTONIAN

When using a 'blue detuned' pumping, the effective mechanical damping linearly decreases while increasing pump power, as seen from Eq. 124 and Fig. 37. In fact, the mechanical system switches into a different dynamical state as soon as the pump power corresponds to $\Gamma_{opt} \geq \Gamma_m$. This state is called a self-oscillation state, or a self-sustained oscillation state, and is characterised by an enormous amplitude of both the mechanical motion and the corresponding optical signal (see Fig. 39 for a comparison of signals on the lock-in in the self-oscillating state and our maximally amplified 'blue' signal, right before the switch). The power $P_{in} = P_{thr}$ where $\Gamma_{opt} = \Gamma_m$ is called the threshold to self-sustained motion. Note that what limits the maximum gain in the 'blue-detuned' scheme is actually the stability of the system, especially in pump power and mechanical damping rate. When we are very close to the threshold, a tiny fluctuation in these parameters is enough to make the system switch to self-sustained motion.

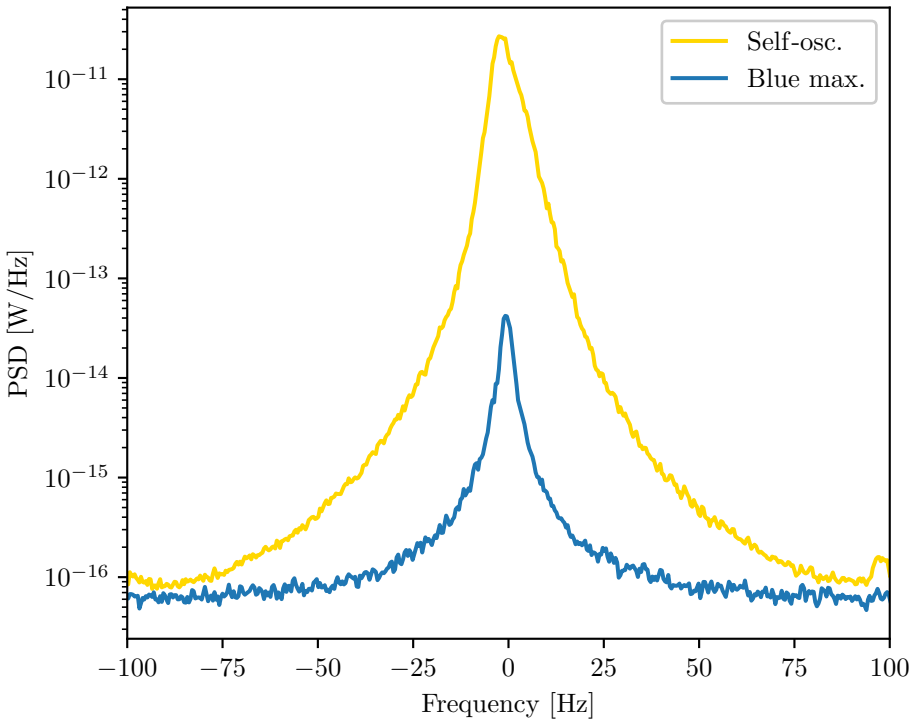

Figure 39: Comparison of the self-oscillating state signal with the one right before the instability

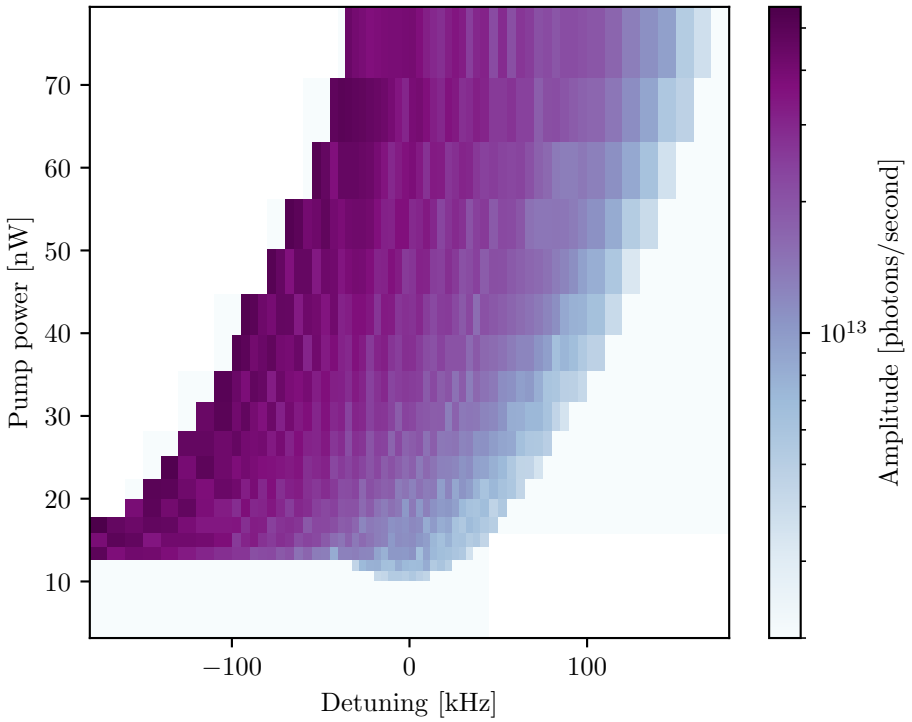

Figure 40: Colourmap of a beam setup self-oscillation photon magnitude

The optomechanical coupled dynamics can be computed from equations similar to Eqs. 81 rewritten in the semi-classical approach with $\langle \hat{a} \rangle \approx \alpha(t)$, $\langle \hat{b} \rangle \approx \beta(t)$:

$$\dot{\alpha} = (i\Delta - \kappa_{tot}/2)\,\alpha + ig_0(\beta + \beta^*)\alpha - \sqrt{\kappa_{ext}}\langle \hat{A}_p \rangle, \tag{156}$$

$$\dot{\beta} = -(i\Omega_m + \Gamma_m/2)\,\beta + ig_0|\alpha|^2. \tag{157}$$

By doing so, one essentially neglects classical and quantum fluctuations: $\alpha(t)$ is not a mean population anymore (which was directly imposed by the pump tone amplitude $\langle \hat{A}_p \rangle$ in the previous Sections), but it now depends explicitly on time t. These equations can be solved by means of a simple ansatz for $\beta(t)$:

$$\beta(t) = \beta_c + Be^{-i\phi}e^{-i\omega t}, \tag{158}$$

and the use of the Jacobi-Anger transformation $\alpha = \tilde{\alpha}e^{i\Theta}$, with a wisely chosen Θ [107]. The term β_c is related to a static deflection of the mode, while $Be^{-i\phi}$ corresponds to the (complex valued) coherent motion. The solution for the optical field is then obtained as $|\alpha|^2 = \sum_{q\in\mathbb{Z}} e^{-iq\omega t}\eta_q$, with:

$$\eta_q = \kappa_{ext}|\langle \hat{A}_p \rangle|^2 \left[\sum_{n\in\mathbb{Z}} \frac{f_n f_{n+q}}{h_n h^*_{n+q}}\right] e^{-iq\phi}, \tag{159}$$

$$f_n = J_n\left(-\frac{2g_0 B}{\omega}\right), \tag{160}$$

$$h_n = i(n\omega - \Delta') + \kappa_{tot}/2, \tag{161}$$

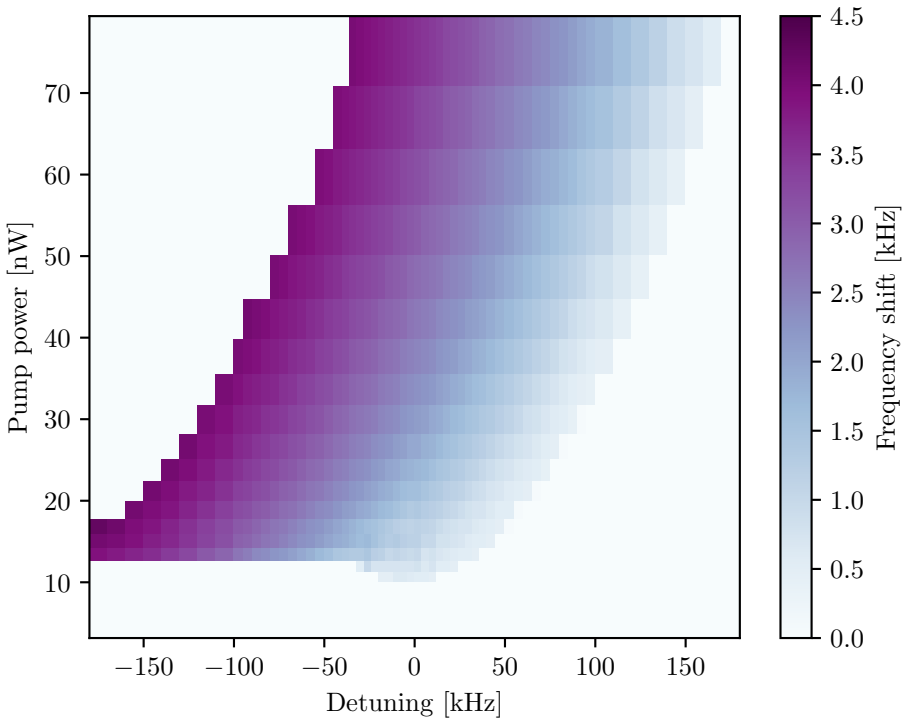

Figure 41: Colourmap of a beam self-oscillation mechanical frequency

with $\Delta' = \Delta + 2g_0 Re[\beta_c]$. The effect of the large motion amplitude is thus to imprint a comb in the optical spectrum, of peak intensities η_q. Injecting Eq. 159 into Eq. 157 leads to the set of self-consistent equations for the mechanics:

$$\omega = \Omega_m + \delta\Omega_m, \tag{162}$$

$$\Gamma_m + \Gamma_{opt} = 0, \tag{163}$$

with $\delta\Omega_m = -Im[\mathcal{X}]$, $\Gamma_{opt} = -2Re[\mathcal{X}]$ and:

$$\mathcal{X} = i\kappa_{ext}|\langle \hat{A}_p \rangle|^2 \frac{g_0}{B} \sum_{n\in\mathbb{Z}} \frac{f_n f_{n+1}}{h_n h^*_{n+1}}. \tag{164}$$

This theoretical prediction resembles very much what can be measured on drum devices, but it is not enough to obtain a quantitative agreement between experiment and theory. The reason for this is the very large amplitudes of motion (and of the photon field); because of this, the non-linearities of the Hamiltonian, which have been neglected up to now, have to play a role [45]. Note that the situation in optics is very different from microwaves: because of the large powers at stake, the devices heat up a lot and the dominant nonliearities are of thermo-optical origin [108].

With microwave setups, heating effects are small and only cause drifts in system parameters that can be calibrated for. The relevant nonlinearities are then the Duffing effect for the mechanics, the equivalent Kerr effect for the optical cavity, and the nonlinearities in the optomechanical coupling. In Ref. [45], it has been shown that the latter are the dominant ones which impact directly the

amplitude of the measured photon field. The Kerr effect of this drum Al device was negligible, and the Duffing effect only responsible for mechanical frequency shifts. A quantitative fit then enabled the extraction of non-linear parameters g_1, g_2 of the optomechanical coupling originating from the Taylor expansion of the capacitance $\delta C(x)$ [45].

However, the same approach does not work with a beam setup, which presents a rather different behaviour. Preliminary measurements are shown on Figs. 40 and 41 for our beam device measured at 425 mK. We show signal amplitude and frequency shift in colour plots as a function of microwave power P_{in} and detuning Δ. Surprisingly, a large triangular-shaped region appears on the left of the graph (towards the cavity frequency), which is not present for the drum. This zone even appears to be meta-stable. The reason for this remains unknown and deserves further study. But clearly, one ingredient is missing in the modelling: one possibility might be the Kerr effect, which we neglected for the drums. Since the beam device requires much higher pump powers (because the g_0 coupling is very small) and has a much higher cavity Q factor, it might be that in this case the Kerr effect does play a role in the dynamics.

Part III

THERMODYNAMICS

In this part, we will present our experimental results on probing different thermodynamic concepts with mechanical resonators at low temperatures. What is meant by thermodynamic concept are the properties of the mesoscopic mechanical mode that are linked to its interaction with thermodynamic reservoirs. These baths can be artificial or can be a real thermal equilibrium. We study the mean properties of the mechanics, and more interestingly its flucutations as a function of bath properties.

In **Noise in the Bath**, we engineer an external noise that mimics an optical bath temperature. We then analyse quantitatively the impact of this 'effective temperature' in the different optomechanical single-tone schemes and demonstrate fundamental concepts that are usually experienced in the quantum limit. Here, the whole analysis is performed in the classical domain.

In **Statistics of a Single Mechanical Mode**, we measure the phononic population fluctuations of a single mechanical mode and introduce the concept of in-equilibrium mesoscopic phonon thermodynamics. We will explain all technologies developed for the population's fluctuations probing in a wide range of frequencies (from 10^{-5} Hz to about 10 Hz). Part of the measured fluctuation spectrum is clearly of thermodynamic origin, but we discovered a very slow ($1/f$ type) contribution of unknown origin.

In the **Knudsen Layer** Chapter, we will discuss the influence of boundaries on an ideal gas thermodynamic properties. The influence of the presence of an infinite wall and the finite size of the probe immersed in the gas are demonstrated experimentally by measuring gas damping onto a NEMS device. A theoretical description of that effect has been developed and is also provided.

Dans cette partie, nous présenterons nos résultats expérimentaux sur le sondage de différents concepts thermodynamiques avec des résonateurs mécaniques à basse température. Par concept thermodynamique, on entend les propriétés du mode mécanique mésoscopique liées à son interaction avec les réservoirs thermodynamiques : ces bains peuvent être artificiels, ou être un véritable équilibre thermique. Nous étudions les propriétés moyennes de la mécanique, mais aussi ses fluctuations en fonction des propriétés du bain.

Dans **Bruit dans le Bain** nous créons un bruit externe qui imite la température d'un bain optique. Nous analysons ensuite quantitativement l'impact de cette 'température effective' dans les différents schémas optomécaniques à un seul ton, démontrant des concepts fondamentaux qui sont généralement expérimentés dans la limite quantique. Ici, toute l'analyse est effectuée dans le domaine classique.

Dans **Statistique d'un mode mécanique unique**, nous mesurons les fluctuations de population phononique d'un mode mécanique unique et introduisons le concept de thermodynamique mésoscopique des phonons en équilibre. Nous expliquerons toutes les technologies développées pour sonder les fluctuations de la population, dans une large gamme de fréquences (de 10^{-5} Hz à environ 10 Hz). Une partie du spectre de fluctuations mesuré est clairement d'origine thermodynamique, mais nous avons découvert une contribution très lente (type $1/f$) d'origine inconnue.

Dans le chapitre **Couche de Knudsen**, nous discuterons de l'influence des bords sur les propriétés thermodynamiques d'un gaz parfait. L'influence de la présence d'une paroi infinie et de la taille finie de la sonde immergée dans le gaz est démontrée expérimentalement, en mesurant l'amortissement du gaz sur un dispositif NEMS. Une description théorique de cet effet a été développée et est également fournie.

7

NOISE IN THE BATH

7.1 CONTEXT

In Ref. [102], a fully classical model of single-tone optomechanics has been derived. The point is to reproduce experimentally all of its predictions and fit them quantitatively. To do so, we are using one of the optomechanical systems presented in Sec. 1.3 (the highly coupled drum), realised in Aalto by Laure Mercier de Lépinay. The idea is to artificially create a large cavity population, such that it can be viewed as a high-temperature bath. This can be done by injecting microwave noise in the setup. Beyond the validity of the classical approach of microwave optomechanical systems, this will also allow us to comprehend the classical phenomena which are analogous to quantum features: like sideband asymmetry and backaction noise without referring to the quantum operator formalism (see Sec. 6.4).

Cryogenic microwave technologies are widely used in applications dealing with superconducting quantum bits and quantum computing [109, 110], which are today investigated in a continuously expanding number of laboratories. The development of scalable and robust quantum computing systems may find applications in very different fields from numerical (quantum) simulations to cryptography. Microwave nano-electro-mechanical systems (NEMS) are promising devices for such applications in quantum data processing [111, 112]. Such elements, which are based on the coupling of electro-magnetic waves with mechanical motion [113], are proposed as new (quantum-limited) electric components [98] or new (quantum-limited) sensors [114] as was mentioned in Sec. 6.1.

Besides quantum electronics, microwave optomechanics can also lead to new components for conventional electronics, and experiments have already demonstrated the feasibility of room temperature devices [101]. In that case, the setups are fully classical and the tedious quantum formalism should not be required for their theoretical description. For electronics engineers, the classical electric circuit modelling has thus been derived [102], which gives them the required tools for basic understanding and modelling of optomechanics.

To be in a fully classical limit, it is required to have both the population of the cavity and of the mechanical resonator $\gg 1$. It is relatively easy for the mechanical population, as for the device we use $\hbar\Omega_m/k_B = 0.72$ mK and at a cryostat temperature of $T_{cryo} = 100$ mK the effective phonon population of the resonator is still $140 \gg 1$. However, to bring the cavity population to the classical limit, the system has to be at a relatively high temperature such that the cryostat

satisfies $T_{cryo} \gg \hbar\omega_c/k_B = 0.24$ K. But our microwave optomechanics are based on superconducting circuits, and it essentially does not work anymore above about $1/3$ of the critical temperature T_c of the material in use: the microwave cavity becomes over-damped by quasi-particles. For us, it is Al with a bulk superconducting transition critical temperature of $T_c = 1.19$ K. It is therefore impossible to heat the system high enough to be in the classical limit. We therefore decided to mimic a cavity high temperature by populating it with white microwave noise from a home-made Noise Generator (NG, see Sec. 2.6).

The cavity susceptibility at full applied noise from NG has been measured with our lock-in (in scope mode with FFT applied, see Sec. 2.4), and recalculated in photons, see Fig. 42. It shows an effective cavity population of about $1200 \gg 1$ photons, which is equivalent to a temperature of 300 K, while the temperature of the cryostat stays fixed at 100 mK through all experiments in this Chapter. Single pumping tone optomechanical measurements have been performed with the setup shown on Fig. 9 in Sec. 2.2 using the lock-in in Spectrum mode with our mixing technique (see Sec. 2.3 and Sec. 2.4). The three pumping schemes described in Sec. 6.5 have been implemented ('Blue', 'Green' and 'Red' detuned), and with different amounts of noise in the bath. The detected signal coming from the mechanics was fitted with Lorentzian functions from Eq. 119, and the signal area A is recalculated in photons/s.

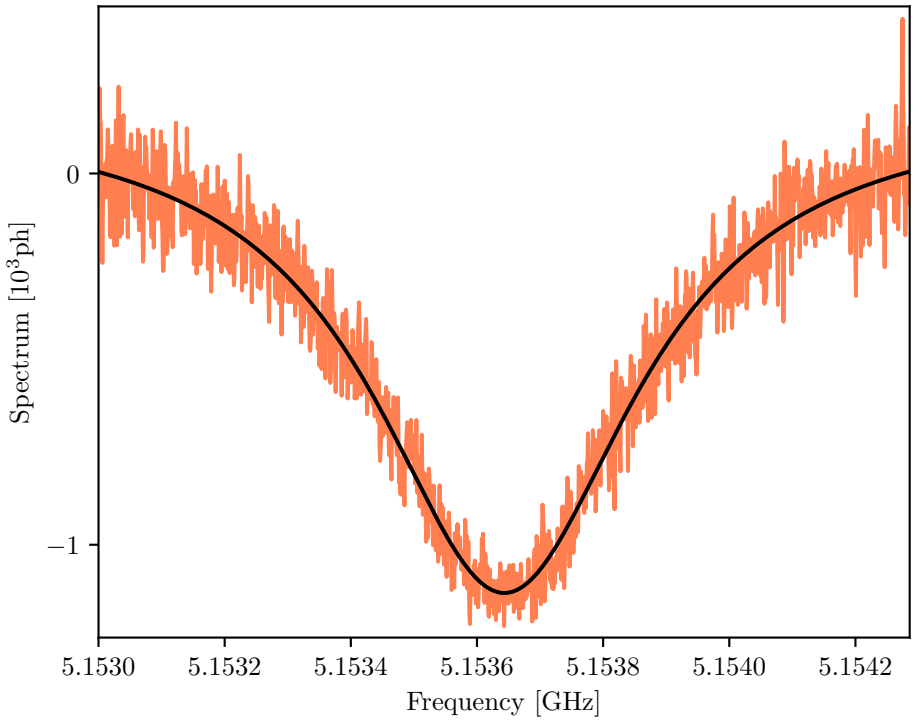

Figure 42: Cavity measurement with full noise

We first start with the influence of the bath on the optomechanical response generated by in-cavity ('green') pumping. The pump power P_{in} dependence of the signal $|A|$ without added noise is shown in Fig. 43 as a solid green line (corresponding to data from Fig. 36), which goes according to Eq. 121. It is a single line, since both sidebands (the redside and blueside ones) give the same value within error-bars. However, the presence of the added noise modifies the observed temperature T in Eq. 121 differently for those two sidebands: their measurement of $|A|$ (in dots) at full noise power from NG are shown in different colours (yellow and cyan respectively) on Fig. 43. Solid lines are theoretical curves with no fitting parameters (all variables being measured independently). Note that for the blueside sideband, the peak in the measured spectrum actually transforms into a dip at low P_{in}, which means a negative area A: this is called the 'squashing region' (grey zone on Fig. 43). This is why we used an absolute value in our logarithmic plot. The dotted magenta lines show powers at which 'noise cuts' were made (measurements at fixed P_{in} but different NG amplitudes), which will be discussed below. The dashed black line indicates the quadratic asymptotic curve associated to the backaction contribution.

Fig. 43 demonstrates the three effects discussed in Sec. 6.4: 'sideband asymmetry' - a distinguishable difference between sidebands; 'noise squashing' - when the blueside sideband peak becomes a dip, which suppresses the background noise

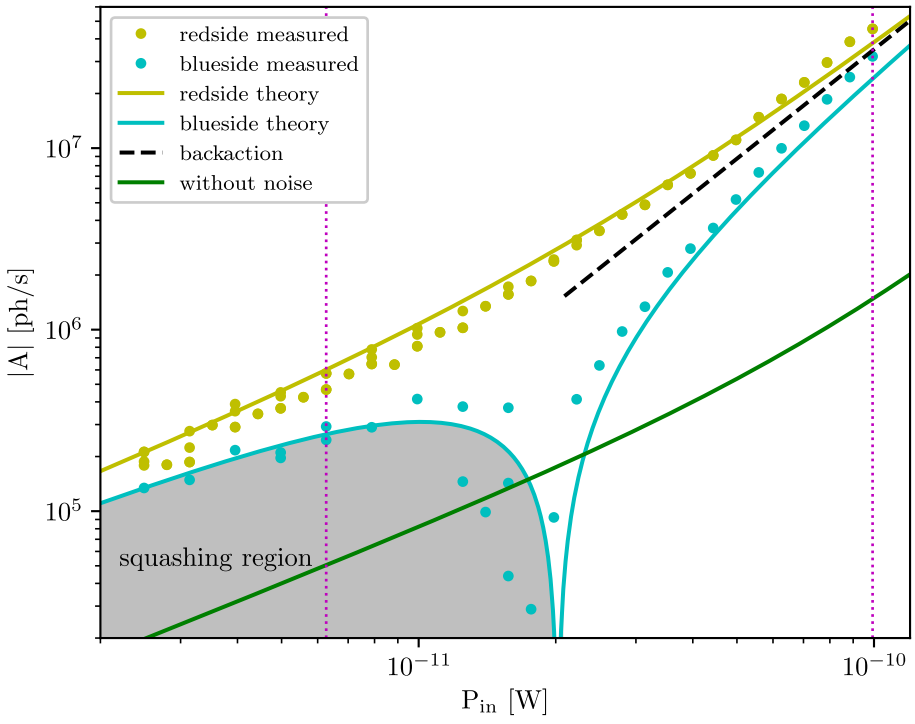

Figure 43: Power dependence of signal with in-cavity pump

and 'backaction' - visible as a change of power law dependence from linear to quadratic at large pumping powers.

The observed temperature T can be written in a completely generic way as:

$$T = T_{cryo} + T_{heat} + T_{sa} + T_{backaction}. \tag{165}$$

T_{cryo} is the already mentioned temperature of the cryostat, and T_{heat} is the so called 'technical heating', which appears at relatively high values of pump power and is responsible for the deviation from linearity of the solid green line in Figs. 36, 43. It is usually associated with a small 'out-of-equilibrium heating' contribution due to the phase noise of the generator, but its actual origin remains mysterious; we come back to this issue in Chapter 8. We fit it here to be $T_{heat} = 9 \cdot 10^{11} P_{in}^{1.3}$ (in K for P_{in} in W), similarly to Ref. [40]. These two components are always present, with or without added noise. The other two terms however are due to the cavity affecting the mechanics and can be related to its effective mode temperature.

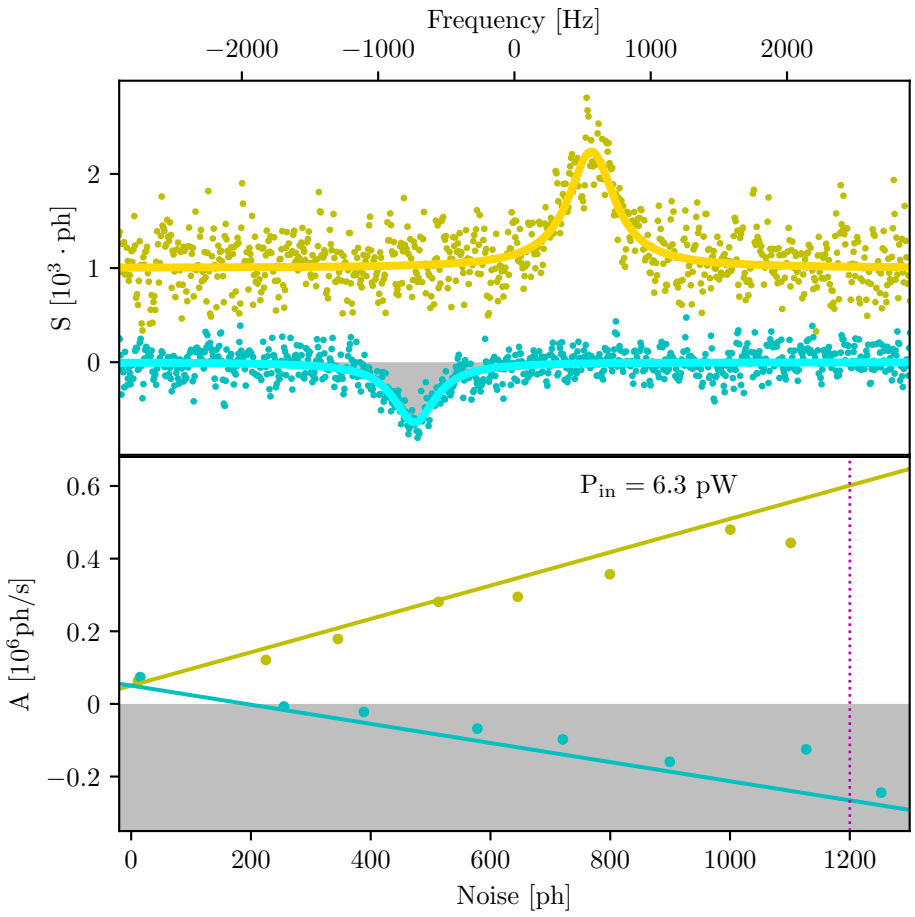

Figure 44: Noise cut at low power with in-cavity pump

The contribution T_{sa} depends on the measured sideband and is derived from the spectra of Sec. 6.4:

$$T_{sa} = +\frac{\Omega_m}{\omega_c} T_{noise} - \text{for 'redside'}, \tag{166}$$

$$T_{sa} = -\frac{\Omega_m}{\omega_c} T_{noise} - \text{for 'blueside'}, \tag{167}$$

where $T_{noise} = E_{noise}/k_B$ is the noise energy stored in the cavity, recalculated in temperature units (Kelvin). The sign difference is what creates the 'sideband asymmetry' effect. When the negative contribution is very large, it can even surpass the other contributions: this is what changes the sign of the sideband signal, transforming the peak into a dip, the so-called 'noise squashing' effect.

Sideband asymmetry is most relevant at low pump powers, as T_{sa} is P_{in}-independent while $T_{backaction}$ depends on it (see below). To demonstrate its influence, we made a 'noise cut': measurements of the optomechanical response A on both sidebands at fixed, relatively small pump power $P_{in} = 6.3$ pW (left dotted magenta line on Fig. 43), with different amounts of noise in the cavity (Fig. 44, lower panel). The top part of Fig. 44 demonstrates the actual measured spectra for both sidebands (using their respective colours as dots), with their Lorentzian fits as solid lines at maximum noise from NG (corresponding to the magenta dotted line in the bottom part of the same figure).

The resonance frequencies appear slightly shifted because of the small residual "optical spring" effect due to imperfect pump tuning. Yellow points and curve are shifted up by 10^3 photons for clarity. The bottom graph shows values of signal A at different noise amplitudes in the cavity for both redside and blueside sidebands in yellow and cyan dots respectively. The solid lines are theoretical predictions without fitting parameters. The grey filling colour marks again the noise squashing zone, as in Fig. 43, where the signal becomes negative.

As mentioned above, the contribution $T_{backaction}$ is pump power dependent (through $\propto |\Gamma_{opt}|$ defined as Eq. 123) and corresponds to the noise from the cavity fed back into the mechanical mode by backaction:

$$T_{backaction} = T_{cav} \frac{\Omega_m}{\omega_c} \frac{\kappa_{tot}^2}{2\Omega_m^2} \frac{|\Gamma_{opt}|}{\Gamma_m}, \tag{168}$$

where the effective cavity temperature can be written as:

$$T_{cav} = \frac{T_{noise}\,\kappa_{ext} + T_{cryo}\,\kappa_{int}}{\kappa_{tot}}, \tag{169}$$

the mean between the different baths to which it is connected (see also Ch. 8). This 'backaction' term is effectively observed as a change in the signal A dependence to power P_{in} from linear to quadratic (see dashed black line Fig. 43), as $T_{backaction} \propto P_{in}$. Its contribution is thus more relevant at higher powers, and we demonstrate it through a 'noise cut' taken at $P_{in} = 0.1$ nW (shown on Fig. 43 as magenta dashes), similarly to Fig. 44. The top part of Fig. 45 presents actual measured spectra for both sidebands as dots using their respective colours with their Lorentzian

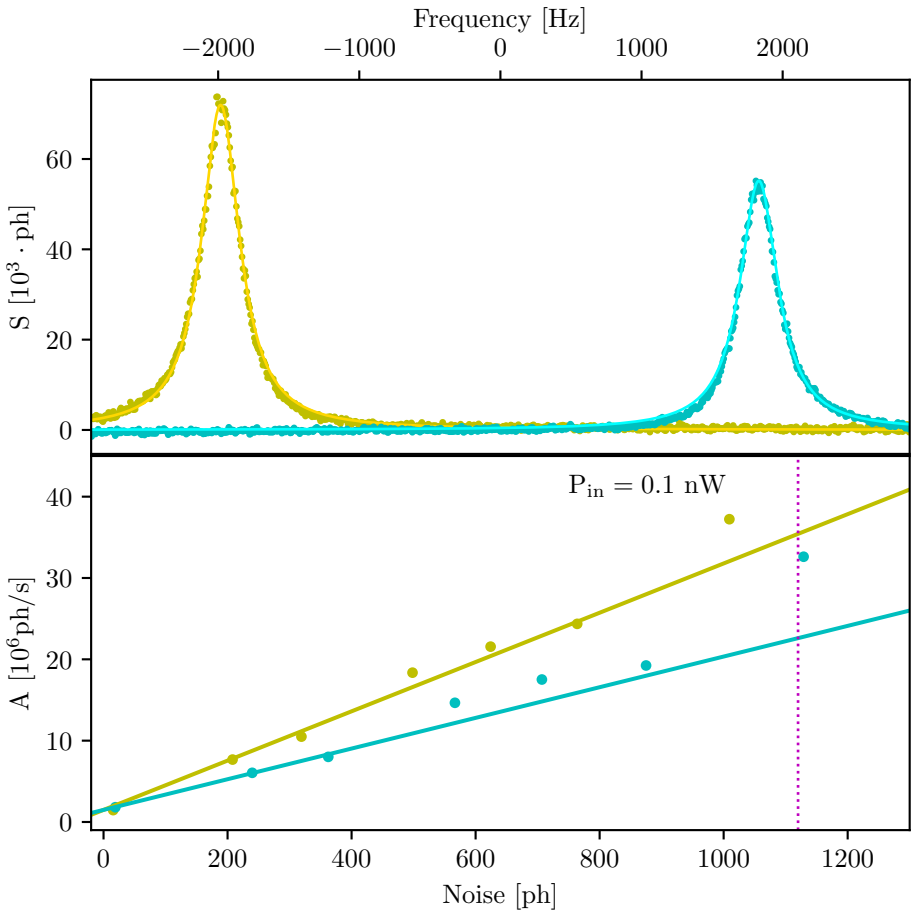

Figure 45: Noise cut at high power with in-cavity pump

fits as solid lines. It corresponds to the maximum noise from NG (the magenta dotted line in the bottom panel). Again, the resonance frequencies appear slightly shifted because of the small residual "optical spring" effect due to the imperfect pump tuning; this shift is bigger than on Fig. 44 as it is proportional to applied pump power, according to Eq. 93. Here, the area of the two peaks becomes very similar, as opposed to Fig. 44, but a slight difference is still visible since the term T_{sa} remains relevant. The bottom part of the graph shows values of signal A at different noise power levels in the cavity, for both the redside and blueside sidebands in yellow and cyan dots respectively. The solid lines are theoretical predictions without fitting parameters.

The same experiment can be conducted using 'blue' or 'red' sideband pumping schemes. For 'blue' and 'red' the equations are quite similar but with slightly different sideband asymmetry and backaction temperatures. The theoretical expressions are written as:

$$
\begin{aligned}
T_{sa} &= \frac{\Omega_m}{\omega_c}(2T_{cav} - T_{noise}) \; - \text{for 'blue'}, \\
T_{sa} &= \frac{\Omega_m}{\omega_c}(T_{noise} - 2T_{cav}) \; - \text{for 'red'}, \\
T_{backaction} &= T_{cav}\frac{\Omega_m}{\omega_c}\frac{|\Gamma_{opt}|}{\Gamma_m}.
\end{aligned} \tag{170}
$$

These expressions are plotted on experimental data in Fig. 46 and Fig. 47, similarly to the case of in-cavity pumping. The agreement is again very good with no free parameters.

Fig. 46 shows the photon flux A dependence on pump power with 'blue' and 'red' pumping schemes and maximum noise applied from NG. Dots are the data and solid lines are theoretical predictions with no fitting parameters. Dashed red and blue lines mark the references measured without external noise from Fig. 36, similarly to the solid green line in Fig. 43. The dotted magenta lines mark the powers at which 'noise cuts' presented in Fig. 47 are done. The noise cut at small pump power $P_{in} = 6.3$ pW (left dotted magenta line on Fig. 46) aims at demonstrating the sideband asymmetry component T_{sa}, as seen on the left part of Fig. 47. Noise cuts performed for high pump powers aim at demonstrating the backaction component $T_{backaction}$: they were made at different powers for 'red' and 'blue' pumping, as the higher the power the more clear the effect is, but for 'blue' pumping there is a threshold (to self-oscillation, see Sec. 6.7) that limits us. For 'blue' pumping the pump power for the noise cut was chosen to be slightly

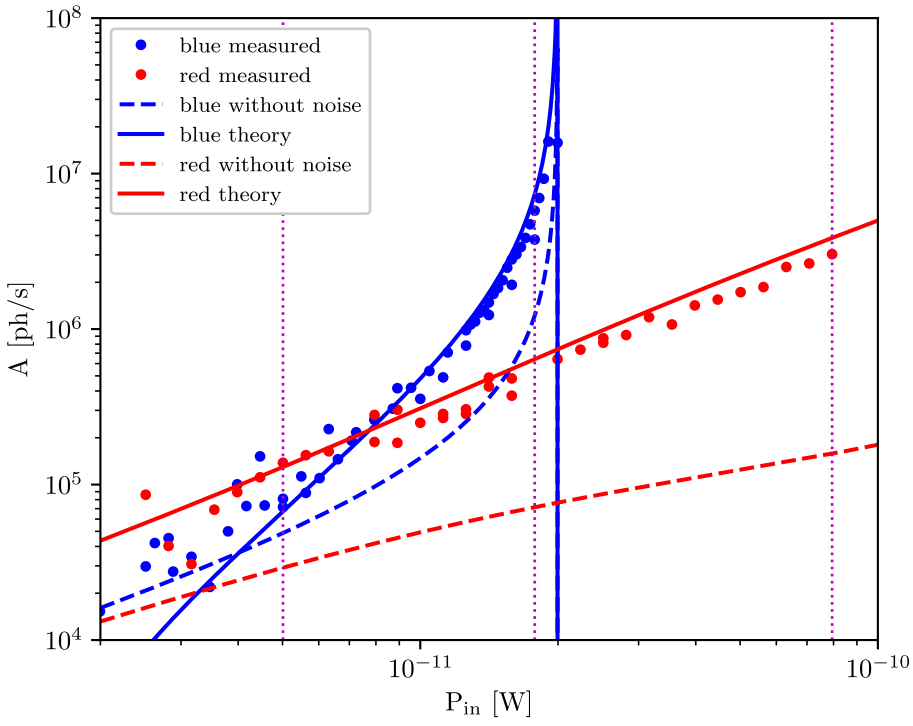

Figure 46: Power dependence of signal with Stokes/anti-Stokes pump

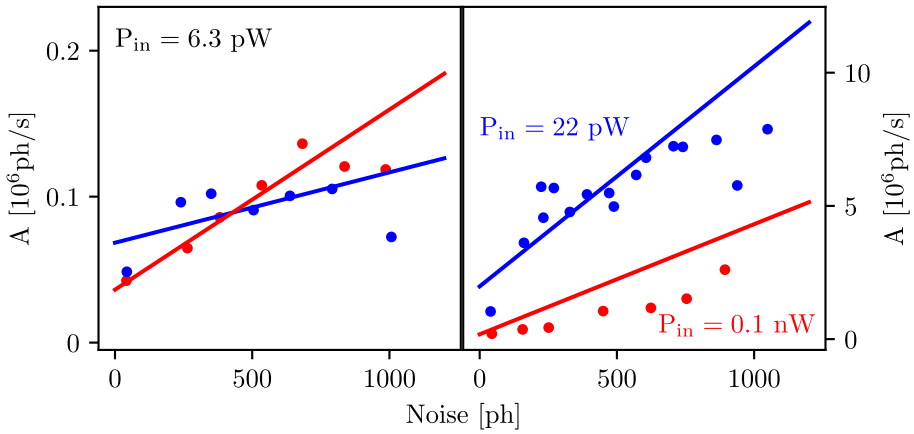

Figure 47: Noise cuts with Stokes/anti-Stokes pump

smaller than the threshold value, $P_{in} = 22$ pW (middle dotted magenta line on Fig. 46), while for the 'red' scheme that value is the highest we could attain in our setup, $P_{in} = 0.1$ nW (right dotted magenta line on Fig. 46, the same as for the 'green' high power noise cut).

'Blue' and 'red' schemes had been used in the past to demonstrate 'sideband asymmetry' and 'squashing' in microwave devices [99, 115, 116], but to our knowledge Fig. 43 is the first demonstration of these effects using the 'green' pumping. Furthermore, our data is acquired within a genuine single-tone scheme: there is no 'cooling tone' applied to bring the NEMS mode close to its ground state, since we want to keep it classical, in strong contrast with the previous references. Note the difference in the expressions Eq. 170 of T_{sa} for the different schemes. One can see that for 'blue' and 'red' $T_{sa} \sim T_{noise}(2\kappa_{ext}/\kappa_{tot} - 1)$, which makes it very sensitive to $\kappa_{ext}/\kappa_{tot}$ (it even vanishes for $\kappa_{ext}/\kappa_{tot} = 1/2$ very close to our situation here), while this is not the case for 'green'. This shall be explicitly addressed in the Discussion section below.

7.3 DISCUSSION

The experiment is in good agreement with the classical electric circuit theory [102], with no free parameters: all terms are measured independently with methods explained in Sec. 6.5. This demonstrates the validity of the modeling and validates its use as a new tool for engineers willing to develop classical applications of microwave optomechanics. Besides, building on the formalism of Ref. [102] our work illustrates classical analogues of 'sideband asymmetry', 'noise squashing', and 'backaction force noise'. These effects, which are in the literature discussed in terms of quantum operators, can be easily understood by electronics engineers with purely classical concepts, as presented in Sec. 6.4.

Classical mechanics tells us that when the temperature of the measuring device, that is the microwave cavity T_{cav}, T_{heat} and the microwave line T_{noise}, goes to zero, then $T_{obs} = T_{cryo}$: the NEMS temperature observed is exactly the cryostat

temperature. However, quantum mechanics tells us that this is impossible: an ultimate bound to backaction is imposed by the zero-point fluctuations of the microwave mode. They will start to be relevant at low temperatures when the photon population in the cavity becomes close to 1: this is the natural limit of validity of the classical approach. Strictly speaking, the measured temperature T_{obs} can never be exactly T_{cryo}: there will always be some addendum, no matter how small it might be. The precise definition of it constitutes the so-called standard quantum limit. A closer look to the boundary between the classical electric circuit model and the quantum formalism can be found in Ref. [102].

Moreover, we can build on our results a method for measuring the $\kappa_{ext}/\kappa_{tot}$ ratio independently of the usual microwave cavity calibrations. It is based on the high sensitivity of T_{sa} for 'blue' and 'red' pumping to that ratio, while for 'green' it is almost insensitive to it. Only when $T_{cav} = T_{noise}$ the T_{sa} value is the same for the sideband signals measured in the different schemes; the methodology requires thus to send a large microwave noise to the device, ensuring $T_{cav} \neq T_{noise}$. In this case, measuring the sidebands with the 'green' scheme at small pump power one can calibrate T_{noise} from the 'sideband asymmetry'. Measuring then the sidebands obtained using both 'blue' and 'red' pumping, again at low powers, one can define T_{cav} and therefore $\kappa_{ext}/\kappa_{tot}$. The backaction dominated range at large pump powers is then a self-consistency check ensuring that the fits are correct. The method is fairly sensitive, since a 5 % change in $\kappa_{ext}/\kappa_{tot}$ leads to a clearly visible change in our fits. This scheme is rather straightforward, and essentially only limited by the maximum power that the NG can afford.

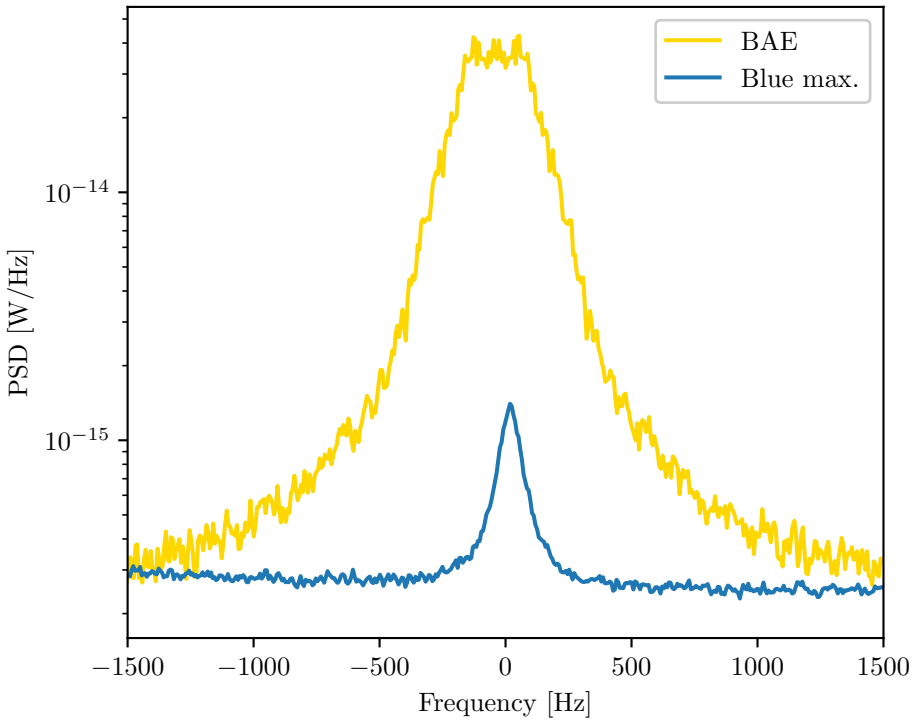

Figure 48: Signal with BAE pump compared to 'blue' pump

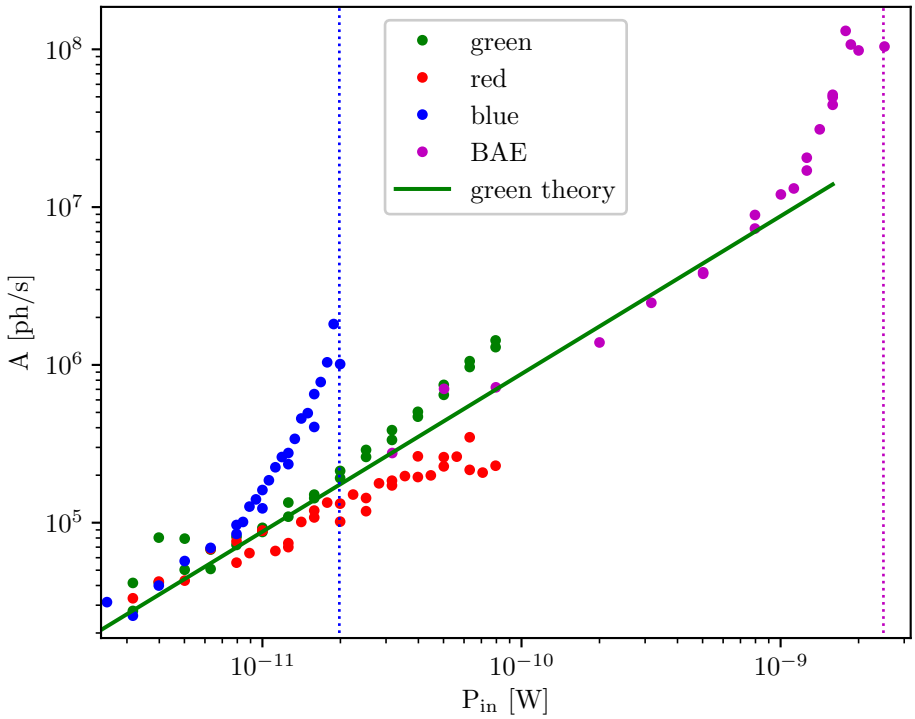

Figure 49: BAE measurements at different powers

The methods and measurements discussed in this Chapter can be expanded from the simplest case of a single pumping tone applied to the system to the more general situation of multiple tones. Such pumping schemes are widely used for different purposes: a 'red' pump of very high amplitude can be applied to a system constantly, in order to effectively 'cool' the mechanical mode into its ground state while it is further probed by other signals [117, 118]. Complex schemes with many tones can be used to entangle the modes of two distinct mechanical objects to create an 'effective resonator' with specific quantum properties: the one of a mode behaving as if evading the backaction laws of quantum mechanics [11]. One of the simplest of such schemes is called 'backaction evading' (BAE), and requires two simultaneous, synchronised and well-tuned 'blue' and 'red' pumps. If their amplitudes are strictly equal, the dynamic backaction is cancelled, and all the stochastic contribution can be fed into only one quadrature, leaving the other one 'noise-free' [116, 119]. This result can lead to a dramatic increase in motion sensitivity, see Fig. 48 and related discussion below. However, an instability similar to the blue self-oscillation threshold is observed [120]. The fine tuning of this technique is therefore rather difficult. Besides, its classical limit has not been addressed so far, which is the point of this final comment.

Investigations in this direction are currently in progress. There are no conclusive results yet, but some preliminary qualitative features were already demonstrated. An example of measurements using the BAE scheme is shown on Fig. 48, with a comparison to the same device measured with a standard 'blue' pump. The power of the 'blue' pump is chosen here slightly below the threshold to self-oscillation,

while the power of each pump for the BAE scheme is more than 20 dB higher (see Fig. 49, dashed verticals). It is clear from this figure that the signal with BAE pumping (which we will nickname 'Purple' pump) can be orders of magnitude higher than any other signal reachable with a standard single-tone measuring scheme (as the 'blue' pump ones are the largest possible, see Fig. 35). On the other hand, such signals cannot be well fitted with Lorentzians (Fig. 48), but experiments show that they can be reasonably well fitted with two Lorentzians having the same width, which are slightly displaced from each other. We believe that this is due to a small mismatch in the 'blue' and 'red' pumping optical springs, which leads to a splitting of the resonance peak. The actual reason for this is not yet very clear.

The total signal area A extracted from such 'purple' scheme fittings can be seen in Fig. 49 (magenta dots), rescaled on the x-axis for the factor of 2 in signal due to the double-pump configuration. We compare it to similar signals from 'green', 'red', and 'blue' schemes (respective colour dots), the same as on Fig. 36. The green solid line corresponds to Eq. 121 for 'green' pumping without any technical heating contribution T_{heat}.

While the deviation of the 'green' data (precisely because of T_{heat}) is very clear, the magenta points align extremely well until the very end of the curve. We must conclude that technical heating is somehow shifted towards higher powers in the BAE scheme for an unknown reason. But these results come at some cost: it is extremely demanding experimentally to tune due to the increasing influence of fluctuations as we increase the pumping power. It happens that after some time, the working point of the experiment can suddenly change, and one needs to retune everything back to optimal settings. In some devices, it is even not possible to use BAE at all above the 'blue' threshold. Such fluctuations will be further addressed in Ch. 8.

We are currently trying to describe these features in the framework of the electric circuit theory, including the 'purple' instability. This is work in progress, and not yet conclusive.

8

STATISTICS OF A SINGLE MECHANICAL MODE

8.1 CONTEXT

In recent decades, the laws of thermodynamics have been pushed down to smaller and smaller scales within the theoretical field of stochastic thermodynamics and state-of-art experiments performed on microfabricated mesoscopic systems. But these measurements mostly concern thermal properties of electrons and photons. Here we will demonstrate the measurements of the thermal fluctuations of a single mechanical mode in-equilibrium with a heat reservoir.

Statistical physics, and by induction thermodynamics, are the basis of our understanding of macroscopic properties from the microscopic entities and laws that structure matter. One of the key results is the second law of thermodynamics, which explains the arrow of time from purely reversible microscopic processes [105]. Fluctuations δX of a quantity X are then Gaussian and vanishingly small leading to a well-defined mean value $\langle X \rangle$.

But many of our intuitive understandings break down at small scales: fluctuations can become as large as mean values, and a specific class of theories known as fluctuation theorems have been developed to describe them [27, 121]. With today's technologies, these concepts (and their related paradoxes) can even be probed experimentally using mesoscale and nanoscale devices. For instance, a Maxwell demon has been realised by monitoring the charge in a Single Electron Box (SEB), and feeding back this information through a gate voltage controlled by a computer; work is thus extracted [28]. Such electronic systems are extremely promising, since one can cool them down low enough (tens of milli-Kelvin) so that they behave according to the laws of quantum mechanics. It should then (at least in principle) be possible to probe the impact of quantum coherence on thermodynamic concepts, which is the new exciting field of quantum thermodynamics [30, 122].

Beyond electric circuits, thermodynamics is conveying concepts which are at the intersection of physics, chemistry, and biology; after all, motion is a key ingredient there. Indeed, the Landauer erasure principle has for instance been tested using soft cantilevers and trapped colloids [34, 123] demonstrating that erasing one bit of information produces a minimum $k_B T \cdot \ln 2$ amount of heat. Similar stochastic thermodynamics implementations have been realised on DNA molecules, e.g. monitoring their folding/unfolding and extracting work from it [124]. Motion is thus at the core of the definition of heat; after all, phonons are

elementary (quasi-)particles constructed from the (quantized) collective motion of atoms [39]. The quantum limit of heat fluctuations [125] and phonon thermal conductance [126, 127] are still a subject of debate today [20, 29], with very few experiments available in the literature [128, 129]. Besides, centre-of-mass motion of mesoscopic objects is thought to be sensitive to quantum aspects of gravity (or any other fluctuating fields that might be at the source of wave-function collapse) [36]. Such mechanisms predict an imprint on mechanical fluctuations that might be measurable [130, 131]. But of course, having a large mechanical object cold enough to host very few thermal excitations (population $n_{th} < 1$) while being in-equilibrium with a heat reservoir is a technological challenge. This has been recently demonstrated with a 10 μm aluminium drumhead device cooled down to 500 μK [24].

Studying quantum fluctuations at equilibrium in a macroscopic mechanical object down to the single quantum might thus be within reach in the near future [20]. We have developed and implemented a specific scheme enabling such kinds of measurements based on microwave optomechanics. We focus here on a strict classical description of the experiment which is a mandatory preliminary step towards the quantum realisation [42]. The generic measuring scheme we use is presented on Fig.9, in Sec. 2.2. For the purpose of this Chapter, we use the optomechanical system fabricated by Xin Zhou (Sec. 1.2). The mechanical mode is the first flexure of a beam resonator (Ch. 4) coupled capacitively to a microwave cavity. The experiment requires extreme sensitivity, down to the Standard Quantum Limit (SQL), which is reached by means of two parametric amplification stages in series: a Travelling Wave Parametric Amplifier (TWPA) provided by Nicolas Roch (from Néel), and the use of a 'blue' detuned pumping scheme (Ch. 6). The optomechanical parametric amplifier directly amplifies the mechanical motion (the phonon population) with a gain defined as $\mathcal{G} = \Gamma_m/\Gamma_{opt}$. The sample was measured in reflection. The setup is mounted in a commercial BlueFors® dilution cryostat (Sec. 3.5), and experiments are performed while regulating the mixing chamber base plate temperature from 100 mK to 400 mK. At higher temperatures, the TWPA amplifier (Sec. 2.7) stops working properly, while at lower temperatures an internal optomechanical instability known in the community as 'spikes' corrupts the results [40, 44].

The TWPA plays a crucial role in this experiment, as it significantly improves the signal to noise ratio allowing us to perform time-resolved measurements with high enough data acquisition rate, which is the core of fluctuations characterisation. We separate what is directly the expression of expected properties of a single phononic mode in contact with a heat bath from features (certainly material-dependent) which are not expected. The former is an energy power spectrum typical of an Ornstein-Uhlenbeck process [105, 106] with exponentially distributed fluctuations (see Sec. 6.6). The latter are visible as $1/f$-type contributions to the spectra and out-of-equilibrium signatures (the 'technical heating' introduced in Ch. 7), which will be discussed in the framework of the Two Level Systems (TLSs) theory [132, 133].

To track fluctuations of the phononic population of the mechanical mode, we have to be able to measure this population itself directly with time-resolved accuracy. This is what is hard to perform while obtaining mean values is quite standard with optomechanical systems: the signal is usually acquired during reasonably long time spans (Fig. 50 and discussion below).

The main difference between what we present here and standard optomechanical measurements, as described in Sec. 6.5, is that the acquisition has a duration in time δt which is not long anymore. Usually, optomechanical probing is not considered to be time-resolved: the signal is acquired for a 'long enough' time and the resulting spectrum is treated as the one obtained after infinite time averaging. This supposedly leads to the well-known Lorentzian peak which represents the mean thermodynamic population. On the other hand, if the acquisition time becomes infinitely small, the expected signal (mathematically) should evolve into a Dirac peak. As one can guess, both cases are not really possible from the experimental point of view. Very slow measurements always suffer from noises of $1/f$ type, while very fast ones are limited by the fact that the frequency resolution is inversely proportional to the acquisition rate (Nyquist-Shannon Theorem [134]). Indeed, each measured power spectral density of the photon flux on the lock-in $S_{\dot{\varphi}}(\omega)$ in photons, from which we extract the value of our signal (area of Lorentzian peak), is actually acquired over a finite time period δt around time t: $\langle S_{\dot{\varphi}}(\omega)\rangle_{\delta t}(t)$. This

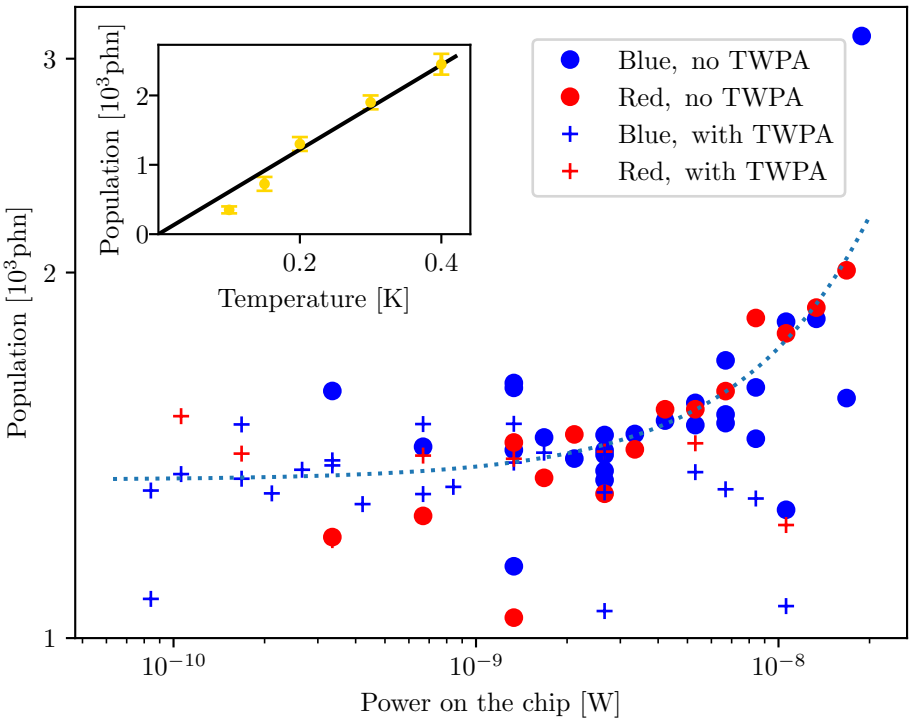

Figure 50: Phonon population as a function of power at 200 mK (main) and temperature (inset)

is simply proportional to the mechanical energy spectrum $\langle S_n(\omega)\rangle_{\delta t}(t)$ expressed in phonons/(Rad/s) within a coefficient $(\kappa_{ext}/(2\kappa_{tot}))\,|\Gamma_{opt}| \propto P_{in}$ (according to Eq. 120). We can construct a mean energy observed over $\Delta T = 1000\delta t$ (1000 is just chosen for convenience and will be kept for all data sets):

$$\langle \dot{E}_\varphi \rangle = \langle \langle \dot{E}_\varphi \rangle_{\delta t}(t) \rangle_{\Delta T} = \langle \frac{1}{2\pi} \int_{-\infty}^{+\infty} \langle S_{\dot{\varphi}}(\omega) \rangle_{\delta t}(t)\, d\omega \rangle_{\Delta T}. \tag{171}$$

Similar expressions hold for the mechanical energy (in phonons) with $\langle E_n \rangle$ and spectrum $\langle S_n(\omega)\rangle_{\delta t}(t)$.

Results of very slow measurements of the phononic population, used to define the mean energy stored in the mode are shown on Fig. 50 as a function of applied power on chip P_{in} (main part) and as a function of temperature T (inset). The former was measured at fixed temperature (200 mK) with different powers, with different measuring schemes ('red' and 'blue'), and with/without TWPA. How to recalculate the mechanical population (in phonons, 'phn' in the graph) shall be explained later on. From these measurements, the intrinsic and undisturbed by applied power value of $\langle E_n \rangle$ was defined as an extrapolation at zero power (see dotted blue line on Fig. 50). Similar measurements were repeated at different temperatures to produce the inset of Fig. 50 which is the temperature dependence of the phonon population. The solid black line is a linear law $k_B T/(\hbar\Omega_m)$ with no fit parameters. Note the small deviation from it at temperatures below 150 mK which is of unknown origin. From the figure it is clear that there is no difference between 'red' and 'blue' pumping when defining the population. Besides, there is a clear increase of effective (observed) population at high pump powers without

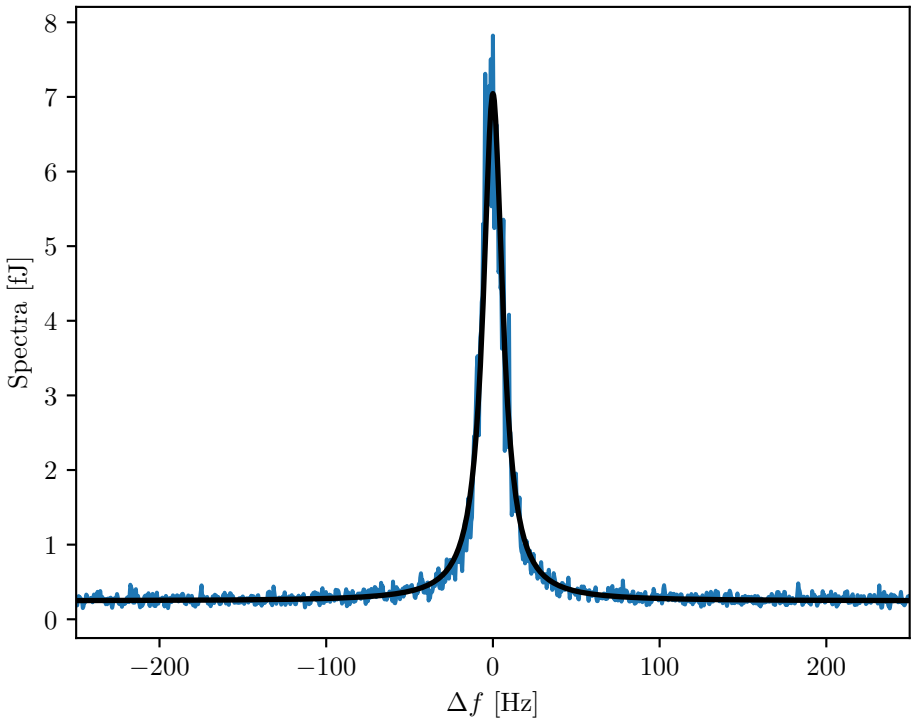

Figure 51: Example of a phononic population measurement

TWPA: this is 'technical heating', already discussed in Ch. 7. With the TWPA on, we cannot measure at high powers, as it becomes impossible to cancel the pump tone with our opposition line (see Sec. 2.5). Therefore the TWPA saturates and 'eats' the signal. This also explains the small deviation at the highest powers between measurements with and without TWPA. However, the scatter in this graph comes from intrinsic properties and not our measurement resolution. The unexpected features observed in Fig. 50 will be commented further in the text below.

An example of single power spectral density of photon flux (optomechanical response) measured during $t_1 = 85$ s with a 'blue' pumping of power $P_{in} = 10$ nW at a cryostat temperature of $T_{cryo} = 200$ mK is demonstrated in Fig. 51. By fitting this response with a Lorentzian function (black solid line in Fig. 51) and taking into account all losses and gains of our detection scheme, we can find the signal on chip in photons which corresponds to the energy stored in this sideband peak. This acquired signal corresponds to a mechanical population (which is easily recalculated), but for the sake of introducing our physical discussion, we will keep it for now in units of photons on the chip (we write: 'ph' in graphs); the corresponding raw data will be simply given in Joules.

By repeating successively the measurement shown in Fig. 51, we can construct a time-trace which is the time resolved evolution of the acquired signal with this specific time-step t_1. Of course, all parameters should stay fixed during this repetition period, e.g. the temperature in the cryostat T_{cryo}, the pump power P_{in}, the level of cancellation of the opposition line, and even the room temperature,

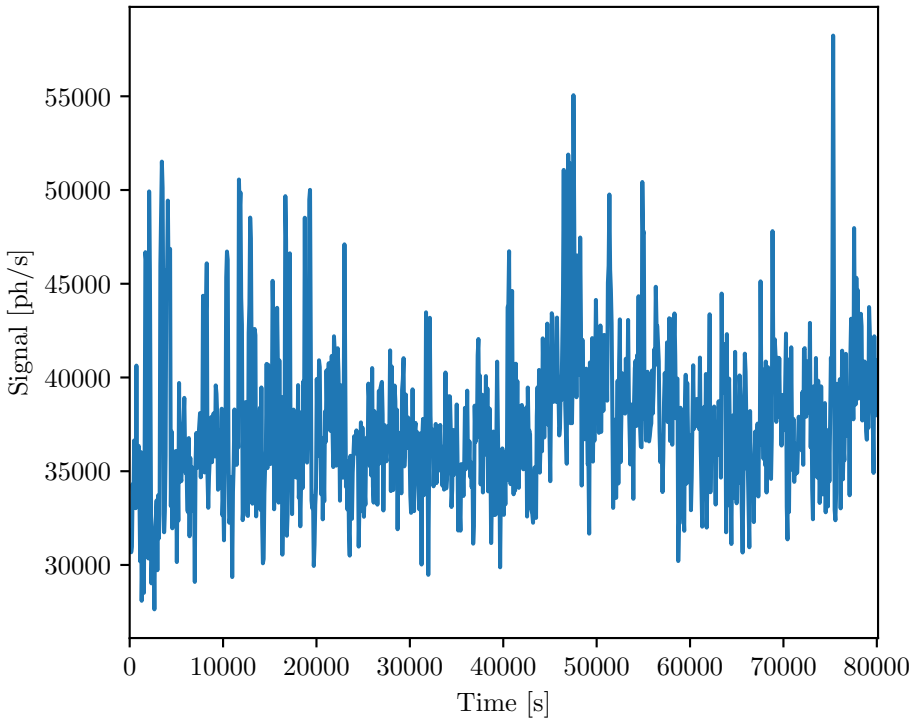

Figure 52: Time-trace of signal acquired during 22 hours with a time step of 85 s

as the gain of the 300 K HEMT drifts slightly with its changes. Such a time-trace, made of 1000 measurements, is demonstrated in Fig. 52 by plotting the area A of the fit Lorentzian. Note the relatively large fluctuations of the signal with respect to the quality of the data and its fit in a single measurement: they all look like the one in Fig. 51.

Such a time-trace can be analysed statistically, as fluctuations are deviations from the mean value already reported. The simplest way is to look at the Probability Distribution Function (PDF) which is just the histogram of our data-set divided by its mean value (to make it unitless on the x-axis) with the y-axis in units of probability density (amount of events in the bin divided by the total amount of events and the size of the bin). The PDF of the time trace shown in Fig. 52 can be seen in Fig. 53.

This probability distribution cannot be fit with a Gaussian function: it is too wide at the mid-height part and the top is too spiky. The reason for this can be understood by looking at the Power Spectral Density (PSD) of the same time-trace. This PSD is the product of a Fast Fourier Transform (FFT) applied to the auto-correlation function of the given data. The corresponding auto-correlation function is defined as:

$$C_{\dot{E}_\varphi}(\tau) = \langle \langle \dot{E}_\varphi \rangle_{\delta t}(t) \, \langle \dot{E}_\varphi \rangle_{\delta t}(t-\tau) \rangle_{\Delta T}. \tag{172}$$

In Eq. (172), τ takes discrete values from $-1000\,\delta t$ to $+1000\,\delta t$. As always, taking the experimental averaging over ΔT for an ensemble average is based on a fundamental hypothesis: Ergodicity. This assumption is not that straightforward here

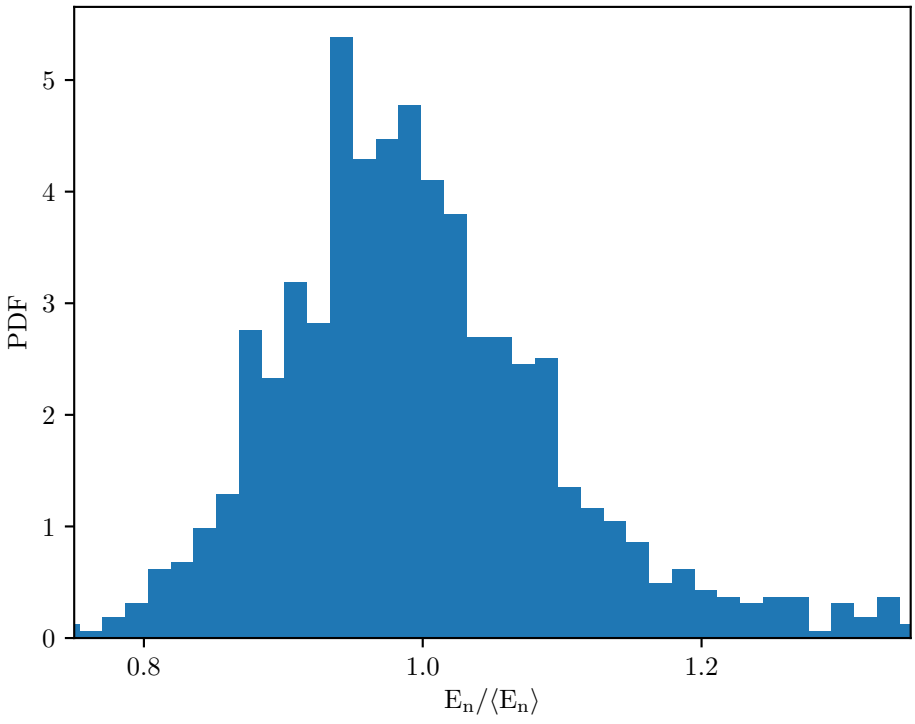

Figure 53: PDF of the time trace from Fig. 52

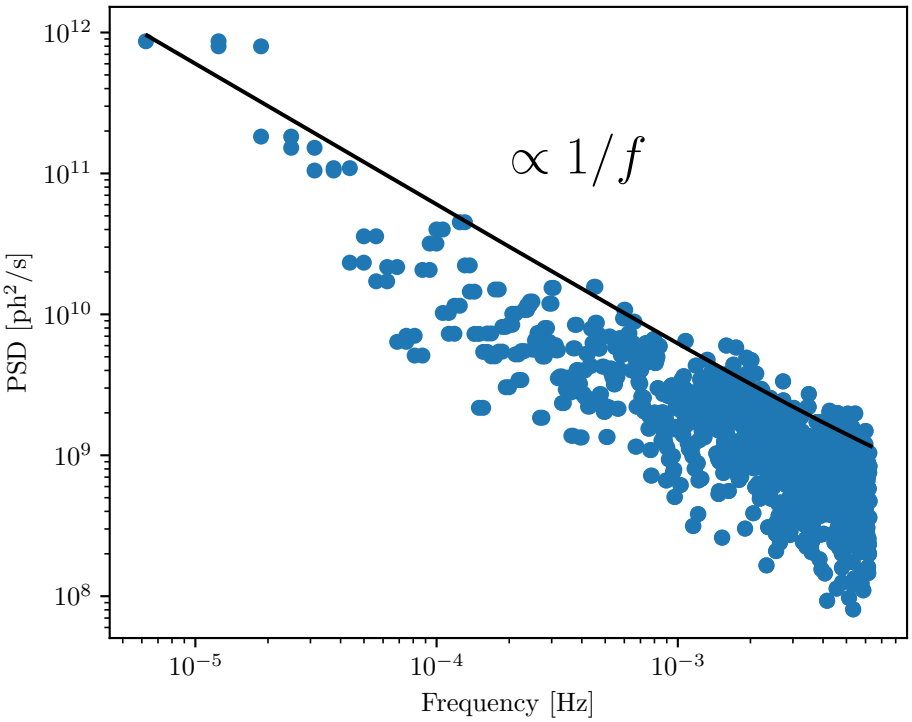

Figure 54: PSD of the time trace from Fig. 52

precisely because of the $1/f$ detected features mentioned above. We shall come back to this point below.

The Discrete Fourier Transform (DFT) for the data-set $\{x_k\}$ of size N is defined as:

$$X_k = \sum_{n=0}^{N-1} x_n e^{-i2\pi kn/N}, \quad k = 0, 1, \ldots, N-1. \tag{173}$$

However, it is very demanding for computing power as it has a complexity of $O(N^2)$ and is therefore rarely used. FFT is the general name for algorithms that compute the same result with a complexity of $O(N \log N)$. In our case, we used the one from the NumPy package for Python [135]. To bring the results of FFT into proper units, the following treatment was applied:

$$\mathrm{FFT}_{final} = |\mathrm{FFT}_{NumPy}| \cdot \frac{\Delta T}{N^2} \,. \tag{174}$$

As well, the x-axis for the PSD was manually constructed as follows:

$$f_k = \frac{k\,N}{2\Delta T}, \quad k = 1, \ldots, N+1, \ldots, 1. \tag{175}$$

The PSD of the time trace from Fig. 52 can be seen on Fig. 54. The power spectral density of our time trace has a strong $1/f$ dependence, as illustrated by the black solid line on top of it. This explains the non-Gaussian shape of its PDF and the unexpectedly big fluctuations in the signal on the (rather long) scale of 22 hours.

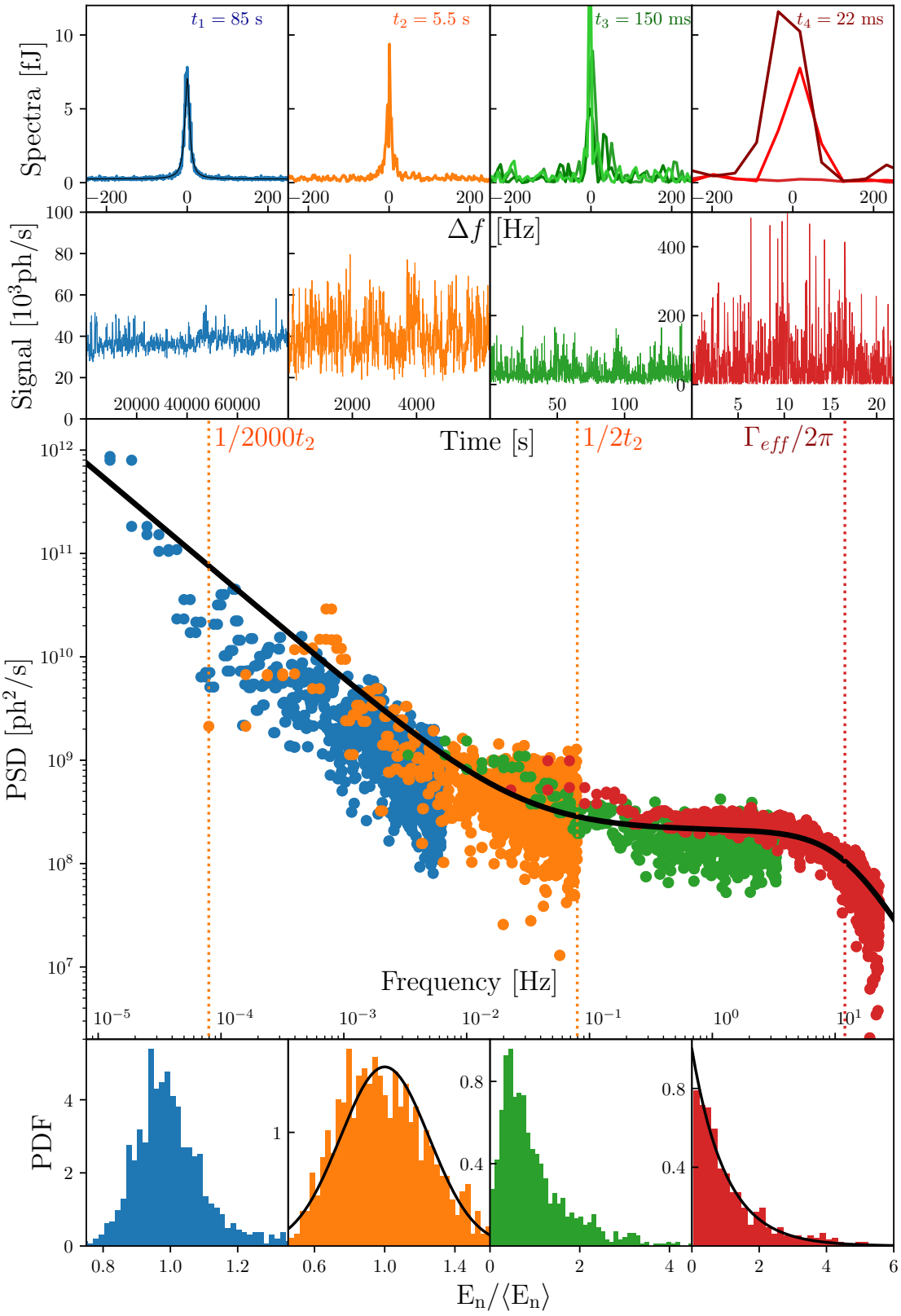

Figure 55: Fluctuations of the signal at 200 mK with 10 nW pump

Similar measurements were performed for different time steps t_x (duration of a single measurement); precisely for $t_2 = 5.5$ s, $t_3 = 150$ ms and $t_4 = 22$ ms at fixed pump power P_{in} and temperature T_{cryo}. The total result is plotted on Fig. 55; all illustrative graphs are taken at 200 mK and 10 nW input pump power. Note that the top four insets share the same y-axis, while the four below them share their y-axis in couples (two on the left and two on the right). Each t_x set has its own corresponding colour of data for the whole figure.

The top insets of Fig. 55 show single measurements acquired during a time span t_x. Only for t_3 and t_4, we have shown three examples of them, in order to demonstrate how much the signal actually fluctuates between acquisitions, and can even disappear (see one of the red traces). They all were fitted with Lorentzians to produce the area time-traces shown on the insets below; the case of the specific normalisation of the red ones (the fastest) is discussed explicitly below. Clearly, the fluctuations are growing significantly when increasing the data acquisition rate.

The bottom insets of Fig. 55 show how the PDF evolve from the 'blurred' Gaussian, already demonstrated on Fig. 53, through an almost perfect Gaussian distribution (orange one, corresponding to t_2, with solid black line Gaussian fit on top), into a clear exponential distribution (right bottom inset). The solid black line on top of the red PDF is not a fit, it is just the normalised (mean value set to 1) exponential distribution defined as:

$$P(x) = e^{-x}. \tag{176}$$

The green PDF is a transition distribution, neither Gaussian nor exponential. Naively speaking, one could have expected a Gaussian distribution for any time-trace acquisition rate $1/\delta t$ and we even got one for $\delta t = t_2$. But in reality, the fastest acquisition should reproduce the exponential distribution which is theoretically expected for a single mode (Sec. 6.6). Slowing down the measurement acts as a low-pass filtering which transforms the distribution into a Gaussian, as expected from the Central Limit Theorem [136]. In this sense, the slowest tracks should be ideally Gaussian, but they are corrupted by $1/f$ excursions which can produce essentially any shape: they are, in principle, non-stationary.

The important feature of the exponential distribution is that its variance is equal to its mean value. When acquiring a measurement, this leads to two very distinguishable cases: one can get either an enormous peak, which is much larger than the mean one, or one can observe the complete absence of signal (see red lines in the top right inset of Fig. 55 which demonstrates both cases). The observation of the exponential distribution is one of the proofs that the fluctuations we observe are indeed the ones of the population of a single mechanical mode: it is just the well-known Boltzmann distribution of energy. Actually, the introduction of a Gaussian-distributed Langevin force representing the mechanical bath (as is done in the framework of the Fluctuation Dissipation Theorem - FDT), is strictly equivalent to the Boltzmann energy distribution; this is demonstrated in Sec. 6.6.

The main part of Fig. 55 shows the power spectral density of all four time traces on top of each other. One can see how with the increase of the acquisition rate

$1/\delta t$ the $1/f$ contribution gets overtaken by the flat ('white') part, which then drops as a 'low-pass' filter around the frequency $\Gamma_{eff}/2\pi$. Note that the acquired spectra are each focused on their own range of frequencies, but they present an overlapping part with each other. Indeed, they overlap rather well in these ranges; we call it 'stitching' of the full spectrum. This tells us that the produced data does not depend on the measurement scheme: as we take ensemble averages over finite periods of time and knowing that the experiment is impacted by $1/f$ drifts, this was not straightforward in the first place. We therefore conclude that Ergodicity is well verified even at the slowest speeds, where these $1/f$ drifts are non-negligible. However, the fastest tracks (only red data) should be re-scaled because of the acquisition finite bandwidth. This scaling will be discussed below together with all the tests and calibrations performed to validate the method.

The full spectrum displayed in Fig. 55 is fit by the expression (black full line):

$$2S_{\dot{E}_\varphi}(f) = \frac{A_f}{f} + \frac{S_0}{1+\left(\frac{f}{\Gamma_{eff}/(2\pi)}\right)^2}, \tag{177}$$

with the factor 2 on the left-hand-side due to the experimental convention $f > 0$ (and here in Hz). The parameter Γ_{eff} is actually not fitted but obtained from the known power dependence of the measured peak width (obtained independently, see below), demonstrating very good agreement with data. It basically means that the mode cannot exchange energy with its environment at speeds exceeding its relaxation rate. This feature, as the exponential distribution, is strong proof that we measure mechanical fluctuations. S_0 then gives us the level of energy fluctuations, while A_f/f corresponds to an unexpected contribution responsible for the slow drifts and the finite error bar in Fig. 50. These two variables shall be discussed in Sec. 8.3. We shall now focus on experimental details of the fast-tracking procedure.

FAST-TRACKS PROPERTIES AND OTHER EXPERIMENTAL CALIBRATIONS

The most difficult measurements are obviously the ones realised at the fastest acquisition speed. When opening the bandwidth, the background noise increases as well, and we can resolve the sideband peak only at the highest powers P_{in} with the largest gains $\mathcal{G}$ due to blue pumping. Besides, with an acquisition bandwidth $1/\delta t$ larger than the peak width Γ_{eff}, we lose information on the shape of the sideband: the imprint of the motion is visible as only 1-3 points higher than the background, see right top inset in Fig. 55.

The fitting procedure has to be adapted and is then as follows: we first average together all the data sets taken over the period $\Delta T = 1000\delta t$. This produces a sideband peak which looks reasonably Lorentzian with a width essentially given by the acquisition bandwidth. Then in the fitting routine that infers the sideband parameters of each data-file, we fix the Lorentz peak width to its mean value and constrain the peak position to be around 0 Hz (in the lock-in demodulated frame) within only a few frequency-steps $1/\delta t$. As such, the fit peak frequency position distribution looks like a (centred) truncated Gaussian, and our main

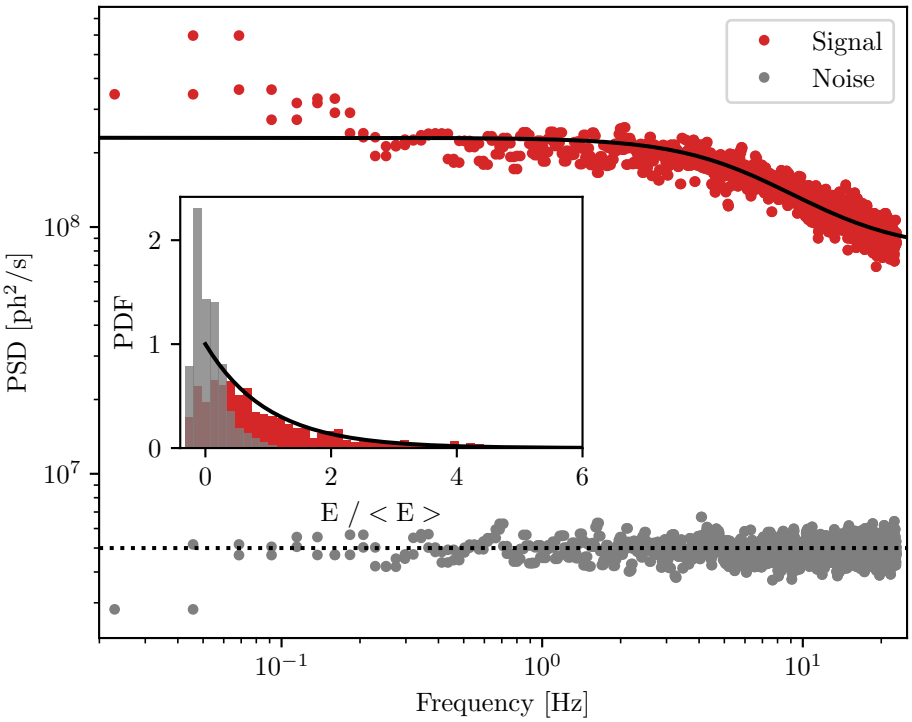

Figure 56: Spectrum of the fastest acquisition rate

fitting parameter is the height of the peak or equivalently its area, the parameter we are looking for. Obviously, acquiring data faster than Γ_{eff} should impact quantitatively the extracted area value; this point is explicitly discussed next. The optomechanical gain $\mathcal{G}$ is then computed from the known power (and temperature) dependence of Γ_{eff}; note that at these acquisition speeds, the $1/f$ noise in damping Γ_m is irrelevant. The properties of Γ_{eff} are explicitly discussed within the present Section.

The great capability of this technique is that we can easily separate what is genuinely characteristic of the sideband from what is simply due to the noise background. This is illustrated in Fig. 56, where we compare the Power Spectral Density calculated from the previous fitting (red) and the one obtained when constraining the fit position of the Lorentz peak far from the central value of 0 Hz (grey). In the latter case, the obtained spectrum is white and more than one order of magnitude smaller than what is obtained when fitting on the sideband (main graph, dashed line). The Probability Distribution Function is centred on 0 and clearly distinct from the exponential tail obtained with the sideband peak data (inset). Finally, only the sideband processed data show the cutoff at Γ_{eff} in the spectrum, but the computed Power Spectral Density does not fall to zero above this value (see fit in Fig. 56). This is presumably due to the fit error which is distinct from the background noise; this has been subtracted in Fig. 55 for clarity.

Since the shape of the peak is lost at high acquisition rates, it leads to a quantitative mistake in our fitting procedures which should obviously be calibrated for. In Fig. 55, we see that the shape of the sideband peak is altered (red data,

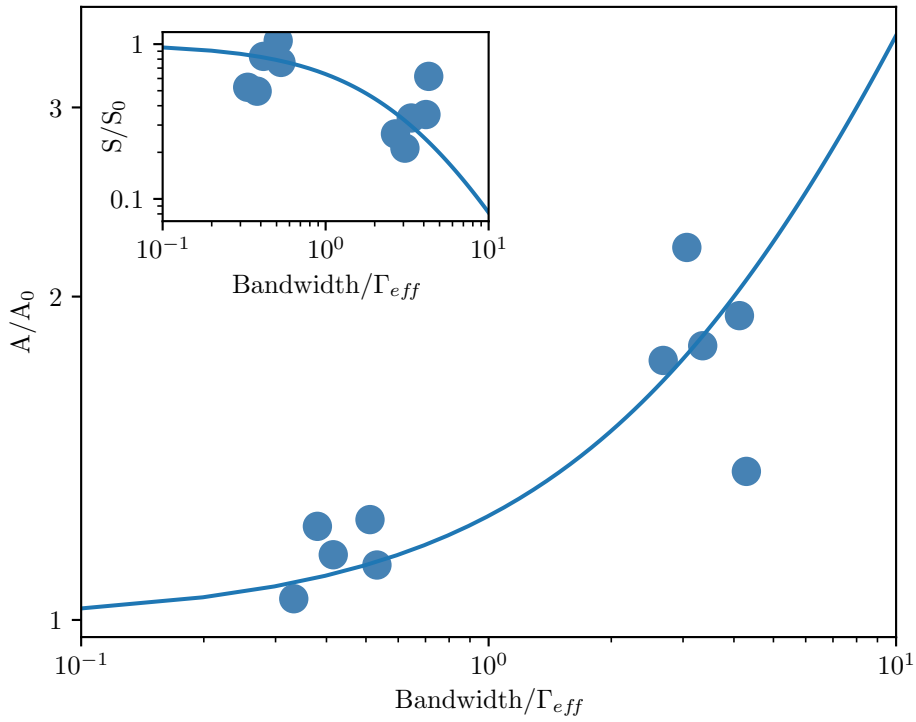

Figure 57: Area and spectrum corrections as a function of acquisition rate

right top inset): it becomes broader as its width is now defined by the sampling rate. This is not the only impact of the fast-tracking: comparing the mean area obtained at different rates $1/\delta t$, we also find out that it is over-estimated. On the contrary, when stitching the fastest spectrum to the others, we realise that we under-estimate fluctuations. This is summarised in Fig. 57, in a universal plot with normalised axes: this plot shall not depend on T and P_{in}. The x-axis corresponds to the sampling bandwidth normalised to Γ_{eff}. The y-axis is the mean area normalised to its value obtained at slow acquisitions A_0 (main), or the fit plateau in the fluctuation spectrum normalised to the value extracted with slower tracking S_0 (inset). These can be fit by very simple empirical laws (lines in Fig. 57): $f(x) = 1 + x/4$ for the area and $1/f(x)^2$ for the power spectrum level. In practice, with our settings only the fastest tracks ($\delta t = 22$ ms, Fig. 55) need re-scaling. Note that it does not impact the fit of the plateau S_0 in the Power Spectral Density, which is very clearly defined by slower acquisition rates. It is only needed for display purposes when plotting the full-range data from the $1/f$ contribution to the fast cutoff Γ_{eff}.

The effective damping Γ_{eff} appearing in Eq. 177 which is used to fit the fastest track spectrum, is independently measured as a function of power for each temperature, similarly to Fig. 37 in Sec. 6.5. The results of all these measurements (shown as points) are summarised on Fig. 58. The graph is obtained from the mean sideband peak characteristics (averaging together all of the data measured during the period ΔT, using the 'blue detuned' pumping). This is done for all acquisition speeds δt except the fastest one which distorts the measured line shape.

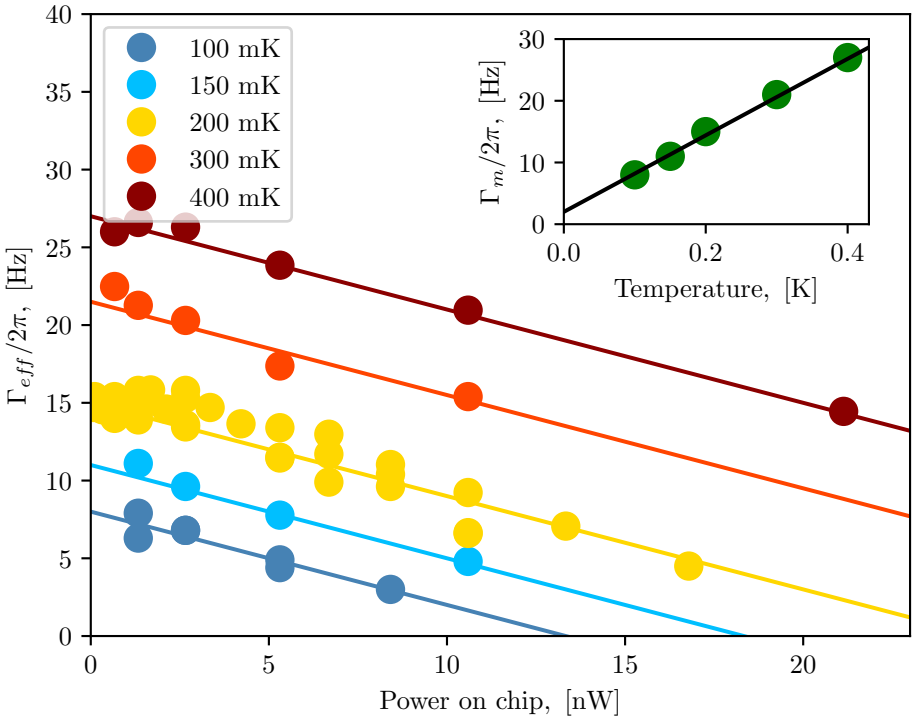

Figure 58: Effective damping measurements at different temperatures (main) and temperature dependence of the extracted intrinsic mechanical damping (inset)

The Lorentzian fit enables to extract area, peak position, and half-height-width $\Gamma_{eff}/2\pi$. The latter can be fit with Eq. 124 as a function of injected power P_{in} for each temperature T. This is shown in Fig. 58 as full lines allowing us to obtain the optomechanical coupling G of this particular device. The slopes of these lines lead to $G/(2\pi) \approx 1.8 \cdot 10^{13}$ Hz/m, and the $P_{in} \to 0$ extrapolation gives us the mechanical damping rate Γ_m. It is found to be linear in temperature in this range (see inset of Fig. 58), in agreement with Ref. [40]. Note that these slopes are independent of T, as they should be since the coupling is a pure geometrical effect. The scatter in Fig. 58 is genuine and comes from the fluctuations of mechanical parameters (see following Sec. 8.3). Finally, the measurement of Γ_{eff} enables us to compute the optomechanical gain $\mathcal{G}$ for any T, P_{in} (and for any of the two schemes, 'red' or 'blue detuned').

In order to validate our analysis in terms of mechanical energy, we compare explicitly the outcomes of the 'red' and 'blue detuned' schemes. For the mean mechanical energy, this has been done in Fig. 50 by recalculating $\langle E_n \rangle$ from the proper corresponding gain $\mathcal{G}$. This energy (in Joules) is also plotted in phonons ('phn' in graphs) by simply dividing by $\hbar\Omega_m$. We see that indeed the recalculated populations in phonons correspond to the same result (dashed line in Fig. 50). Now, let us produce the same recalculated graphs for fluctuations. The principle of the gain scaling for fluctuations is based on the description of the mechanical mode as being connected to two uncorrelated heat reservoirs: the mechanical bath

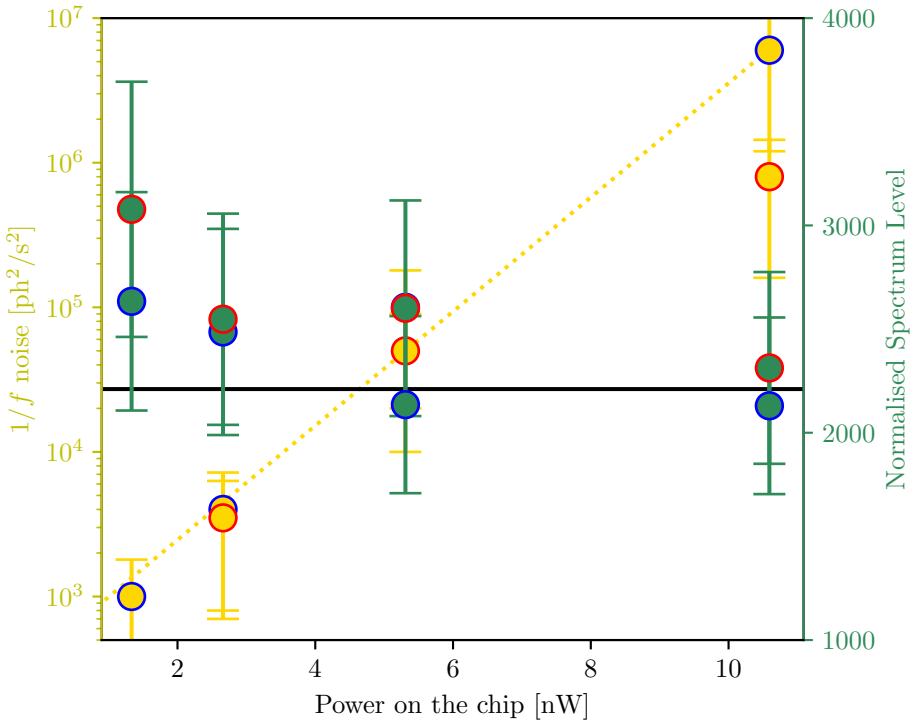

Figure 59: Comparison of 'blue' and 'red' pumping schemes fluctuations

(at cryostat temperature T), and the optical bath (at effective temperature T_{opt}). The mechanical fluctuation spectrum then writes (in Joules, adapted from Sec. 6.6):

$$S_{\Delta E}(\omega) = \frac{2\left[\Gamma_m (k_B T)^2 + |\Gamma_{opt}|(k_B T_{opt})^2\right]}{(\Gamma_m + \Gamma_{opt})^2 + \omega^2}. \tag{178}$$

The point is that the effective bath temperature can be taken to be $T_{opt} \to 0$: the cavity is essentially empty. It follows then that the flat region of the spectrum satisfies:

$$S_{\Delta E}(|\omega| \ll \Gamma_{eff}) \approx \mathcal{G}^2 \frac{2(k_B T)^2}{\Gamma_m}, \tag{179}$$

where $2(k_B T)^2/\Gamma_m$ is precisely the flat fluctuation level of an unpumped mechanical spectrum: reversing the equation, one can thus calculate the thermodynamic fluctuations (at equilibrium with the bath at temperature T). In Fig. 59 we therefore plot the normalised phonon spectrum level $\sqrt{\frac{\Gamma_m S_0}{\mathcal{G}^2}} \Big/ \left(\frac{\kappa_{ext}/2}{\kappa_{tot}}|\Gamma_{opt}|\right)$, recalculated from the photon flux spectrum fit S_0 (right green axis and circles, 200 mK data). We present both 'blue detuned' data (which will be discussed more in the following Sec. 8.3), and 'red detuned' (blue and red borders of circles respectively). As for the mean mechanical energy, the agreement between the two pumping methods is very good (full black line); the difference being obviously that it is not possible to follow the fastest tracks with a 'red detuned' scheme, since we need the optomechanical gain $\mathcal{G} > 1$ to be able to resolve the signal. This is again strong proof that what is measured are indeed phonon fluctuations.

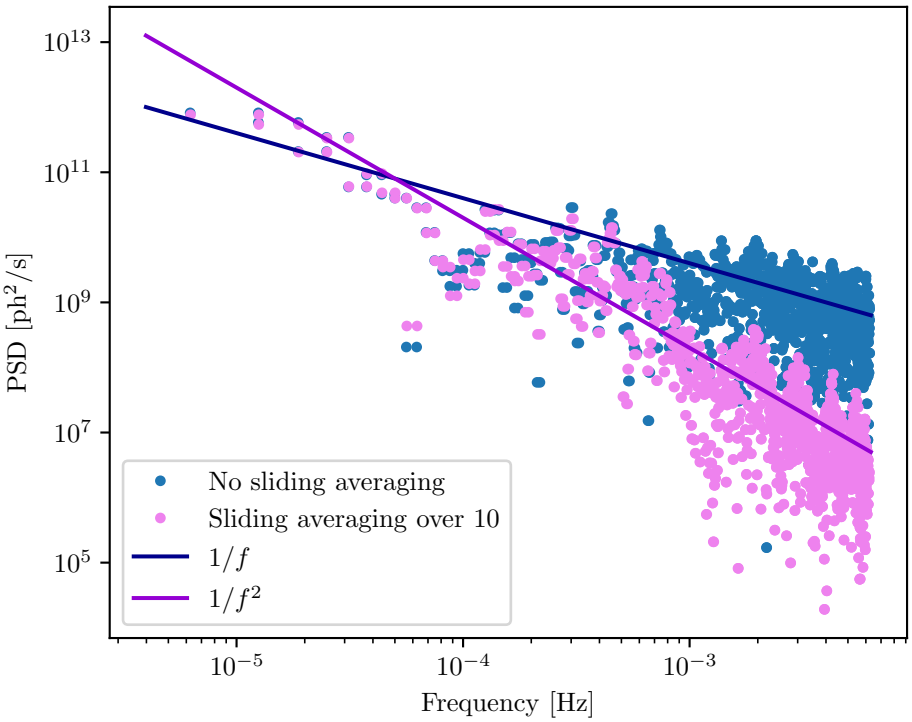

Figure 60: Filtering by sliding averaging of PSD

In the same Fig. 59, we also show the corresponding $1/f$ components (left yellow axis and circles). However, we kept them in units of photons because transforming the graph into phonons following the same procedure as for the flat spectrum S_0 does not produce a much better plot (the fit of A_f in Eq. 177 is not that good). Determining whether the origin of this effect is in the mechanics or the optics remains thus an open question. However, we clearly see that 'red' and 'blue detuned' pumping data follow the same trend as a function of P_{in}; the $1/f$ term grows very quickly with increasing power (dashed line).

A first attempt to produce energy fluctuations spectra had been made in Ref. [24] with measurements performed down to the quantum regime. While the idea was clearly defined, the resolution of the experiment was very far from the requirements needed to produce the results we describe here. To obtain fittable data, the Authors had to process a 'sliding averaging' on the acquired measurements (averaging together $\#n$ neighbouring files while shifting this window through the whole set of data). In that case the extracted spectral characteristics did not represent the expected thermodynamic behaviour. Here we study the effect of 'sliding averaging' on our own data. In Fig. 60, we plot the Power Spectral Density obtained with our raw slow data measured at 200 mK (same as the one on the Fig. 54) together with the one obtained when processing a 'sliding averaging' (with a $\#n = 10$ file averaging window). We clearly see that the averaging acts as a low pass filter which transforms the initial $1/f$ component of our data into something which could be mistaken for a $1/f^2$ law (see fit lines). Besides, it completely suppresses the thermodynamic plateau S_0. We therefore conclude that 'sliding

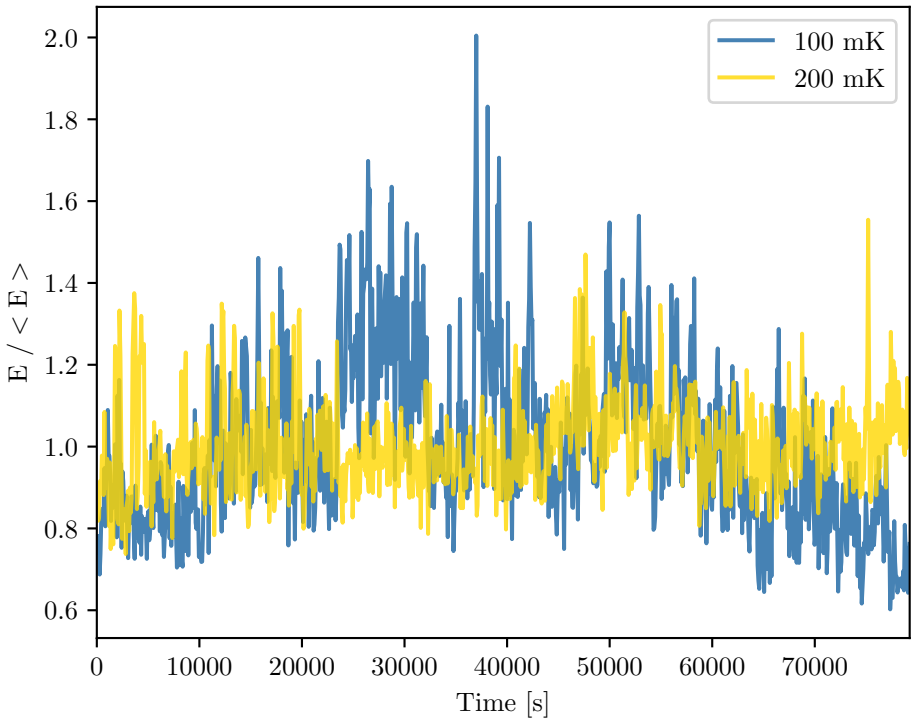

Figure 61: Demonstration of fluctuations increase at lower temperature

averaging' essentially preserves only the $1/f$ component of energy fluctuations. There is also no particular information in the shape of the spectra obtained this way, since they are characteristic only of the filtering method. Especially, what looked like a very low frequency cutoff with a plateau is nothing but an artefact of filtering plus FFT method. However, the $\sigma_E \propto \sqrt{T}$ law observed in Ref. [24] contains genuine information which is characteristic of the (unknown) mechanism causing these slow fluctuations. We discuss the physics of it in Sec. 8.3.

In Ref. [40], an instability in the dynamics of the beam was reported for temperatures lower than about 150 mK. It is visible as large amplitude peaks appearing in the sideband spectrum, which were nicknamed 'spikes'. The origin of this phenomenon is still unknown, and we presume that it should also impact our measurements. Therefore in Fig. 61, we plot two slow time-tracks, similar to the one shown on Fig. 52, taken at different temperatures: 100 mK and 200 mK with 10 nW input power. Strikingly, we see that the amplitude of fluctuations is much larger on the colder data set which is a clear signature of the mentioned 'spikes'.

Let us comment in more details the data. When computing the mean energy $\langle E_n \rangle$, we see that the value extrapolated at zero injected power is actually smaller than expected, see inset of Fig. 50. On the other hand, the relative importance of technical heating grows as we cool down; if this is not taken into account properly (which is particularly difficult at low temperatures without TWPA), the inferred mode energy at a finite power P_{in} would then be much larger than the thermodynamic value. It is very tempting to suggest that 'spikes' are inherently linked to the $1/f$ type fluctuations whatever might be the microscopic mechanism behind

this. How to understand a smaller mean energy compared to the thermodynamic temperature T also remains an open question, especially in the light of increasing slow fluctuations.

The measurements demonstrated on Fig. 55 were repeated for different pump powers P_{in} and temperatures T_{cryo}. They all showed a similar behaviour and their spectra were fitted with Eq. 177. The extracted fit parameters S_0 and A_f will now be analysed in the next Section.

8.3 DISCUSSION

The fit parameter S_0 should correspond to the flat level of fluctuations of the mechanical resonator's population. However, on Fig. 55 our spectrum corresponds to fluctuations in the optical field's sideband, therefore it should be properly recalculated into units of phonons (denoted 'phn', no units). This is properly done following the procedure illustrated by Fig. 59 in the previous Section. The coefficient we should discuss here therefore writes:

$$S_m = \sqrt{\frac{\Gamma_m S_0}{\mathcal{G}^2}} \Big/ \left(\frac{\kappa_{ext}/2}{\kappa_{tot}} |\Gamma_{opt}| \right). \tag{180}$$

Normalised this way, the parameter S_m measured at different powers is shown on Fig. 62 as a function of temperature T_{cryo}. The size of dots corresponds to the pump power P_{in}, from small/low to big/high. The black solid line in Fig. 62 is

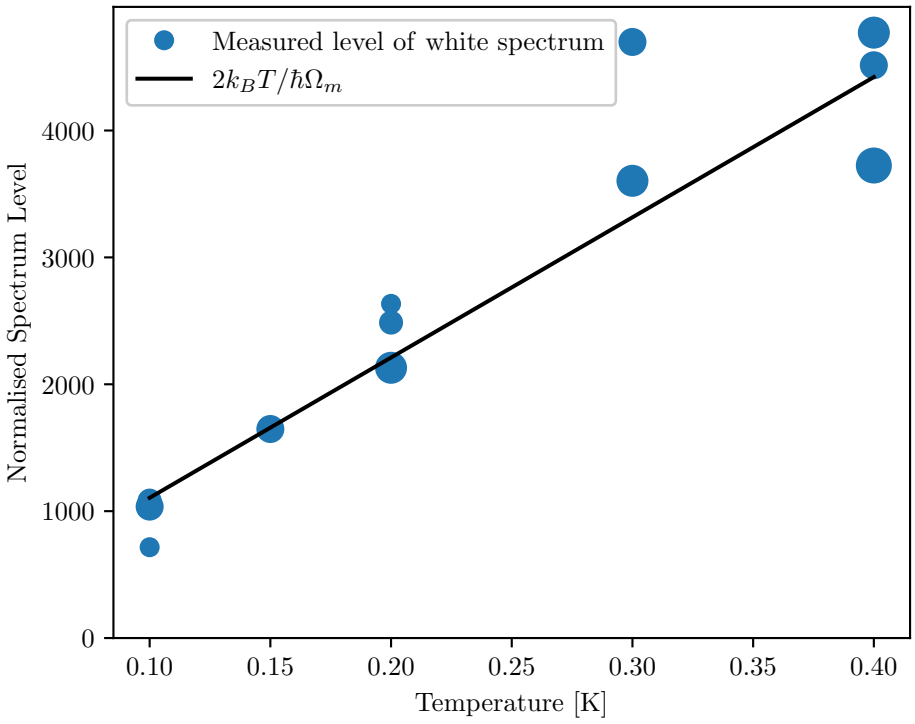

Figure 62: Normalised spectrum flat level as a function of temperature

not a fit but just the theoretical calculation with no free parameters:

$$S_m = \frac{2k_B T}{\hbar \Omega_m}. \tag{181}$$

The scatter seems to be due to our reproducibility and fitting capability with no specific link to the microwave power P_{in}. It confirms the magnitude of the variance $\langle \Delta E^2 \rangle = 1/(2\pi) \int_{-\infty}^{+\infty} S_{\Delta E}(\omega) d\omega = (k_B T)^2$ in this canonical ensemble; the subtlety being that the specific heat associated with the single-mode is precisely k_B [137].

Despite the $1/f$ term, we reach here at the fastest tracks a resolution of about 100 phonons (corresponding to real-time red data trace in inset Fig. 55) being limited mainly by our relatively poor optomechanical coupling G. In quantum mechanics terms with the zero point fluctuation $x_{zpf} \approx 27$ fm, we have $g_0 = G\, x_{zpf} \approx 2\pi \cdot 0.5$ Rad/s. Using one of our drumhead aluminum devices in the future, one can reach couplings as high as $g_0 \approx 2\pi \cdot 250$ Rad/s, therefore we gain about a factor $\sim 10^5$ on the detected signal (all other parameters being kept equivalent) [46]. This potentially could lead to a single phonon resolution even in the vicinity of the ground state which is reachable with brute-force cooling as was demonstrated on a drum device with our DN1 cryostat (Sec. 3.6) in Ref. [24]. This opens up exciting possibilities, as the measurement of the impact of a single phonon tunneling event on the sideband dynamics. To conclude about the S_0 measurements, the very good agreement reached in Fig. 62 is again strong proof that the measured fluctuations are the ones of a single mesoscopic mechanical mode.

But our data demonstrates also a striking unexpected feature: the observed $1/f$ type component at low frequencies. The dependence of the fit parameter A_f to pump power P_{in} and temperature T_{cryo} is shown on the main plot of Fig. 63, using semi-log axes. With this display, we observe that this coefficient can be fit by an exponential power dependence with a smooth temperature dependence. We thus fit A_f as:

$$A_f = A_0(T) e^{\frac{P_{in}}{P_0(T)}}. \tag{182}$$

The fit parameter P_0 temperature dependence is plotted in the inset of Fig. 63. The other parameter A_0 has a similar temperature behaviour but is less important because it affects the exponential law only as a prefactor. From this equation, P_0 can be understood as some kind of effective activation power meaning that these $1/f$ fluctuations are getting easier to activate with pump power P_{in} as the temperature T_{cryo} is decreased. Besides, since the optomechanical signal of Brownian motion decreases with temperature, the decrease of the activation power P_0 could lead to a situation where at any reasonable pump power P_{in} there is nothing to observe but $1/f$ noise. Potentially, that could be part of the mechanics behind the 'spikes' issue [40, 44] which was already mentioned a few times in this manuscript. The origin of this effect remains unknown. It is not even clear if it originates in the phonon or in the photon field which is why we characterise it in terms of photons. Besides, since $1/f$ drifts are responsible for very slow (close to $\omega \to 0$) dynamics, one could wonder whether this signature has to be linked to

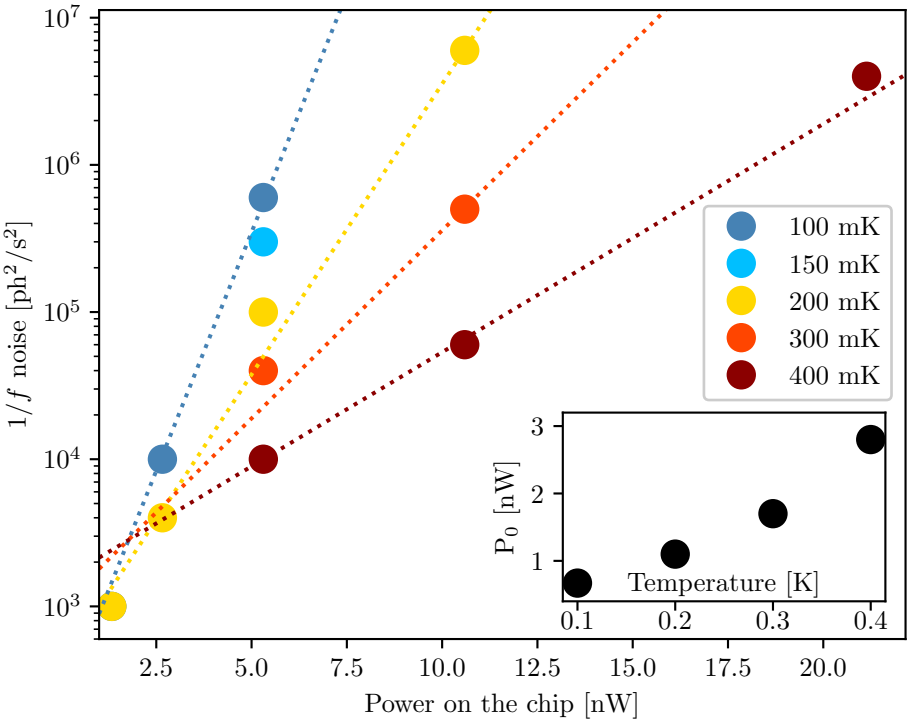

Figure 63: $1/f$ noise prefactor as a function of power and temperature

the technical heating of Fig. 50 (a supposedly true D.C. effect). Again, this remains an open question.

Besides, one should also keep in mind that the mechanical parameters Ω_m and Γ_m are also fluctuating; this had been already reported in Ref. [24] in the framework of low-temperature optomechanics but also in more conventional experiments [138, 139]. Since we fit the mechanical response (on not-too-fast tracks), we can extract these parameters and compute their statistical properties. This is summarised in Fig. 64 where Allan variances of mechanical frequency $\Omega_m/2\pi$ (blue) and of mechanical damping $\Gamma_m/2\pi$ (green) are plotted as a function of temperature. Tracks are acquired with our slowest acquisition speed for 22 h, while the Allan variance is calculated arbitrarily over about 14 h. The size of dots corresponds to different microwave powers (same as in Fig. 62). The dashed lines are guides for the eyes. A typical Power Spectral Density, here computed for frequency fluctuations (at 200 mK, with drive power 10 nW), is shown in the inset of Fig. 64. The black solid line is a $1/f$ fit which shows a good agreement with data. Note that no white contribution could be identified at higher frequencies which justifies why the mechanical parameters of the oscillator are very stable on fast-tracks. The Power Spectral Density of the damping parameter Γ_m looks very similar. The probability distributions are reasonably Gaussian but more potato-like because of the reproducibility of the slow drifts. We find out that the damping noise is essentially constant in temperature T which is consistent with findings from Ref. [139] taken at slightly higher temperatures. On the other hand, the frequency noise grows as we cool down which is a feature also seen in Ref. [24]

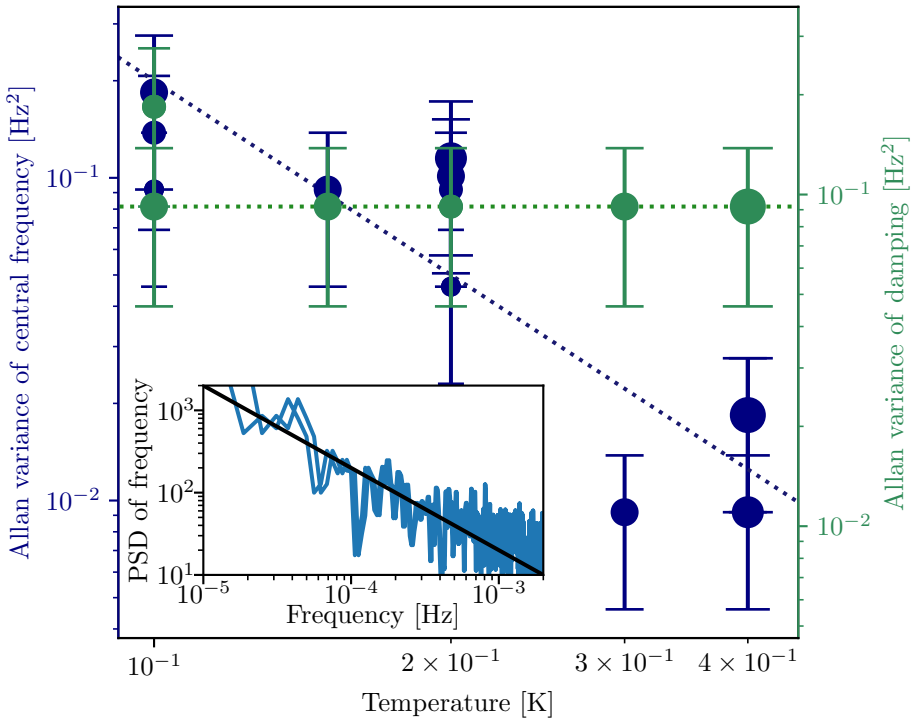

Figure 64: Allan variance of $1/f$ noise in resonance frequency and damping temperature dependence

down to much lower temperatures. Both damping and frequency fluctuations are of the same order as reported values for SiN beam devices cooled at cryogenic temperatures [139]. The scatter in Fig. 64 is rather large (as is usually the case when measuring $1/f$), but no specific drive power dependence can be seen. Again, the mechanism behind these features might be linked to the previous properties impacting energy fluctuations, but no microscopic theory has been formulated yet.

To summarise, we report on a technology that enables us to measure in real-time the energy fluctuations of a single mesoscopic mechanical mode. The setup is constructed around a state-of-art microwave optomechanical cryogenic platform and possesses a background noise of about 3 SQL (3 photons at 6 GHz). The resolution is then about 100 phonons at our fastest acquisition rates (about 20 ms) by using a 4 MHz mode in a weakly coupled beam device. The limiting parameters are the intrinsic losses of the TWPA [52] and mostly this weak optomechanical coupling [40]. We believe that both aspects can be greatly improved and will lead to an effective resolution on the detected sideband spectrum equivalent to a single mechanical quantum. This means not only that these experimental capabilities surpass the best microfabricated calorimetric setups to date (zepto-Joule calorimetry [140]), but also that the phonons themselves become the quantum bath being probed which allows for performing quantum calorimetry with phonons thus opening a new experimental field [141, 142].

The next experimental step is therefore to mount this measurement setup onto a cryostat to enable us a 'brute-force' cool down to the quantum regime such

MHz mechanical modes, as demonstrated in Ref. [24]. Quantum stochastic thermodynamics experiments would be within reach [20], but this requires us to further analyse the setup in quantum mechanics terms (the theoretical treatment we use stayed purely classical). Let us finally point out that the measurement is constructed around the observable $\hat{x} \propto \hat{a} + \hat{a}^\dagger$ (motion amplitude), not energy $\hbar\Omega_m \hat{n} \propto \hat{a}^\dagger\hat{a}$, which means that we shall not detect single-phonon tunnellings per se but their (dispersive) imprint onto the optical field. This should nonetheless enable us to study single phonon events, transposing to mechanics what has been beautifully achieved for electrons. As an example, one should be able to demonstrate, at extremely low temperatures where the mechanical thermal population $n_{th} < 1$, how the system can be absolutely free of excitations over macroscopic timescales (similarly to electrons in a superconductor) [143]: a rather counter-intuitive possibility which essentially means that the system could be said to be a $T = 0$ K exactly for a short period of time, while obviously on average $T > 0$ K would always be recovered. Besides, beyond the conventional thermodynamic baths that one intuitively imagines (phonons, electrons, or gas particles, see following Ch. 9), one could imagine detecting signatures of unexpected contributions: 'spikes' being one of them. This would make our setup also valuable for the study of the grounds of quantum mechanics, as described by recent collapse theories [36], which postulate such kinds of interactions with new fluctuating fields of Nature.

9

KNUDSEN LAYER

9.1 CONTEXT

Quantum fluids, such as ^{4}He and ^{3}He, are unique model systems for tackling complex fundamental questions of many-body physics: from quantum turbulence [144] to topological superfluidity (with the detection of elusive Majorana fermions or other exotic quasi-particles) [145], with even applications to other fields of fundamental research like dark matter detection [146]. Many emergent phenomena can be studied in almost ideal conditions, see e.g. Ref. [147]. However, physical outcomes of experiments are limited by the quality of the probes in use which rely on many drastic requirements concerning sensitivity, non-invasivity and response-time among the most obvious ones.

Currently, a broad variety of devices has already been implemented to probe quantum liquids down to ultra-low temperatures. Restricting the discussion to mechanical objects immersed in the fluids, one can cite: microspheres [148], vibrating wires [149, 150], quartz tuning forks [151, 152, 153], microelectromechanical (MEMS) [154], and nanoelectromechanical (NEMS) [10, 155, 156, 157] systems. All of these tools have their advantages and disadvantages. The beam-like NEMS realised today in the clean room can be considered to be the most convenient and the least invasive probes: in particular due to their cross-sections which are orders of magnitude smaller than all other mentioned options (240 μm for microspheres, down to 5 μm for NbTi vibrating wires). The mechanical resonances reach high quality factors, with very small masses, a very broad range of working frequencies (especially reasonably high ones, enabling fast response), and finally high stability. Besides, these systems are used not only for probing quantum liquids but also in a variety of other fields like single-particle mass spectrometry [158] or quantum detection based on optomechanics [159].

When making a suspended beam NEMS device on a chip, there is in practice a finite distance to the underlying substrate [10, 155, 156, 157]. This means that the moving sensor can couple to the chip surface through the fluid it is probing: a finite size effect that can be relevant (or even dominant) depending on the fluid characteristics. Such a phenomenon had been demonstrated with ^{4}He gas at 4 K in the very low pressure limit in recent papers [47, 160]. What is reported is a decrease of the gas damping onto the beam NEMS. This is understood in terms of a rarefaction phenomenon occurring next to a wall within a distance of the order of the particle's mean-free-path: the so-called boundary (or Knudsen) layer.

If one wishes to completely avoid this effect, it requires creating and using fully suspended systems where the distance to any surface can be effectively taken as infinite. This was our first Motivation for creating a new type of probes, presented in Sec. 1.4.

Besides, to avoid as much as possible any disturbance of the fluid by the probe itself, there is a need to decrease its cross-section down to below the smallest relevant lengthscale characterising the quantum liquid; for superfluids, this shall be the coherence length ξ_0. For ^{4}He, this is a very strong constraint since ξ_0 is on the scale of an atom. However for ^{3}He, it varies from about 15 nm to 80 nm depending on pressure [161] which is of the order of the smallest NEMS beams cross-sections achievable by modern nanofabrication technologies. Thus, creating unique probes for the study of superfluid-^{3}He is our Motivation II.

The design and fabrication of such NEMS devices was demonstrated in Sec. 1.4 and Sec. 1.5. The cryogenic characterisation in vacuum was described and demonstrated in Ch. 5. The particularity of the design lies also in multiplexing: by connecting many NEMS beams in series, we are able to measure up to 5 resonators in a single cool-down. This ability is obviously scalable to much larger numbers and is a mandatory capability in some of the modern quantum fluid research [162].

In this chapter, we will discuss magnetomotive measurements (Sec. 5.2) of our NEMS fully suspended beams in a rarefied gas, namely ^{4}He gas at 4.2 K. Such measurements are a mandatory step before immersing them in superfluids, but it is also a subject of study on its own. The influence of the probe on the measured properties will be demonstrated. ^{4}He in this case is chosen as a benchmark gas, as it is particularly simple: monoatomic, inert and can be considered ideal if not too close to the condensation line in the (P, T) phase diagram. Its thermodynamic properties are well known and tabulated (see [47, 160] and references therein). The point of our study is to show how the invasivity of the probe can be linked to the same boundary layer physics as the one studied with an infinite wall underneath the resonator. We present a unified formalism that describes both effects and fully characterises experimentally the Knudsen region.

9.2 RESULTS

We measured the extra damping on our devices caused by the presence of gas in the chamber $\Delta\Gamma = \Gamma_{gas} - \Gamma_m$ (with Γ_m the vacuum damping rate), and furthermore we compared the result with measurements performed on similar devices [47] (see Fig. 65). The main difference is that devices in Ref. [47] had a finite gap to the silicon substrate of about $g \approx 4$ μm, while ours are fully suspended. The mechanical damping Γ_m was carefully measured prior to gas introduction using the same magnetic field for all data taking. All measurements were performed at low enough velocities to ensure that the system stays in a linear response regime. The results presented here are published in Ref. [86].

The effect of gas damping is well known and documented at room temperature. At high pressures P, the fluid is described by the Navier-Stokes theory: the

mean-free-path λ_{mfp} between atomic collisions is very small and the gas can be considered as a continuum with a given viscosity. The resulting friction, originally computed by Stokes for a cylinder [163], can be computed for a rectangular cross section object of any aspect ratio [164]. At low pressures, the gas medium is in the molecular (or ballistic) regime: the mean-free-path is very long, and the friction is described by individual collisions of atoms onto the probe [165]. The cross-over happens when the mean-free-path of gas particles λ_{mfp} is of the order of the width w of our devices, which is around 1 Torr at 4.2 K for $w \approx 250$ nm [47, 160] (see vertical black dotted lines on Fig. 65, 66 and 67). This is a flow finite-size effect, as opposed to a flow finite-time effect: for us, the relevant adimensional Weissenberg parameter $f_0/\Delta\Gamma$ remains always much larger than 1, which means that the probe is always fast enough to 'feel' gas damping [166].

The molecular damping is linear in pressure P and well documented for room temperature experiments [167]. However, at cryogenic temperatures a deviation had been reported: the measured gas damping is smaller than expected [47, 160] (blue data in Fig. 65). This has been attributed to a rarefaction phenomenon occurring in the boundary Knudsen layer of the gas [47]. Physically, when λ_{mfp}/g grows above 1, the atoms in the gas thermalise not only through collisions among themselves but also with the nearby wall (at distance g below the device). In the limit $\lambda_{mfp}/g \gg 1$, the scattering from the boundary surface dominates the damping mechanism and thus the atom's thermalisation. The apparent signature of this effect is a local decrease in the gas density, as shall be discussed further in this Chapter. The difference between room temperature and low temperature

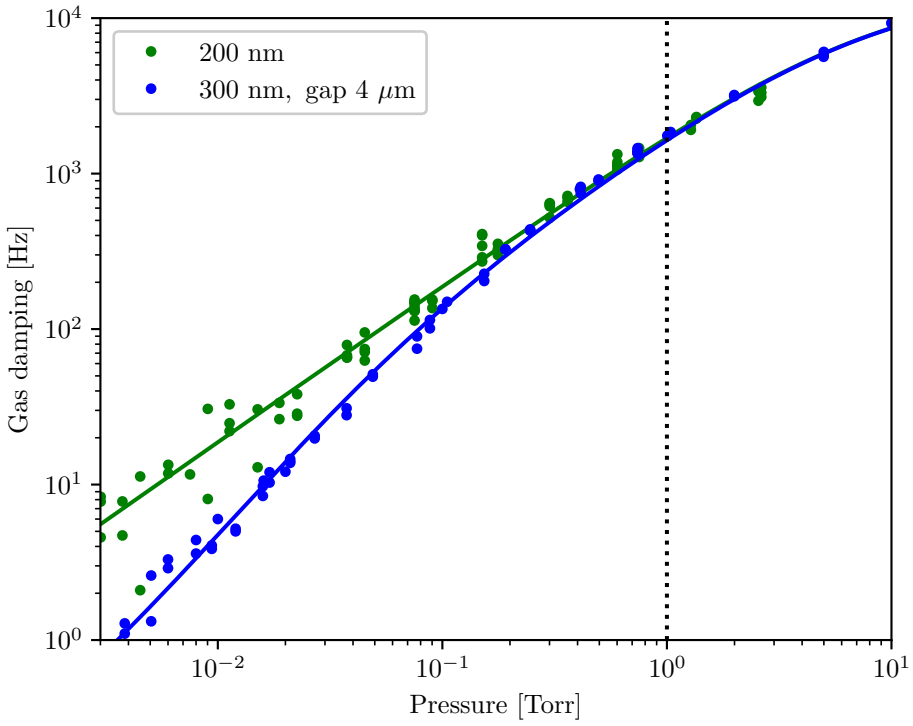

Figure 65: Comparison of similar devices with and without a gap to substrate

results is presumably linked to physical properties of adsorbed atoms (forming from $1-3$ disordered layers on the surfaces) [47, 168].

Therefore, with our devices which are fully suspended (i.e. $g \to \infty$), this effect should not exist and we should recover the linear in P law. This is indeed demonstrated in Fig. 65, where we show the comparison of gas damping $\Delta\Gamma$ between a fully suspended 200 nm wide beam (green data, the most similar device we have to the ones used in [47]) with data from Ref. [47] on a 300 nm wide device, where the gap to the substrate was about 4 μm (blue data). Both devices were 100 μm long. The lines are theoretical fits discussed below. Indeed, the damping $\Delta\Gamma$ experienced by our fully-suspended beams is linear at low P which confirms the conclusions reached in Refs. [47, 160].

The natural extension of this work was to study the spatial invasivity of the beam probe. We therefore made the same measurements for devices of different widths w: 100, 200, 500 and 1000 nm. The measurements of these four devices are plotted together on Fig. 66. On this plot, gas damping $\Delta\Gamma$ is normalised to the linear molecular law aP. The constant a is chosen such that the result is equal to ≈ 1 at a pressure of 1 Torr. Curves for different devices were shifted manually by factors of 4 for clarity. Dots correspond to the actual measured data and lines are fits discussed thereafter. The dotted blue line resembles the blue line of Fig. 65 corresponding to the $g \approx 4$ μm device [47]. As can be seen, the 100 and 200 nm width devices behave according to expectations: the normalised damping is flat at low pressures which means $\Delta\Gamma \propto P$. Note however that for the smallest w device (100 nm, magenta colour in Fig. 66), an addendum contribution of about $+20$ Hz (on top of the initial vacuum 250 Hz) had to be taken into account: an extra damping (above the standard molecular expectation) was visible at the smallest pressures. This effect was only noticeable at the lowest pressures and was reproducible in multiple runs. We do not know the nature of that extra damping for the narrowest devices, but it stayed below 10 % of the total damping in the studied range, and was therefore simply subtracted. This could be linked to some rearrangements in the adsorbed layers, which will be discussed in the following. For 500 and 1000 nm wide devices, a deviation from linear gas damping is observed at low pressures. The dotted red and magenta lines indicate the theoretical asymptotic tendencies at high pressure calculated for beams with aspect-ratio width over thickness equal to 10 and 1 respectively [164].

To fit the data of all samples in a universal way, the following phenomenological equation is used (a, h, l, b positive real numbers):

$$\frac{\Delta\Gamma}{a\,P} = \frac{1}{1 + h \cdot P + \frac{l}{1+b\cdot P}}. \tag{183}$$

The constant a is the proportionality coefficient of molecular damping in the limit $\Delta\Gamma \propto P$ (meaning $h, l \approx 0$). In principle, a does not depend on device width w. For the pragmatic purpose of fitting, it can be obtained from the value at which the above ratio is maximum, $max(\Delta\Gamma/aP) \approx 1$. The constant h is mostly relevant at high pressure values and defines phenomenologically the transition from the molecular damping regime into the Navier-Stokes limit (the dashed asymptotes

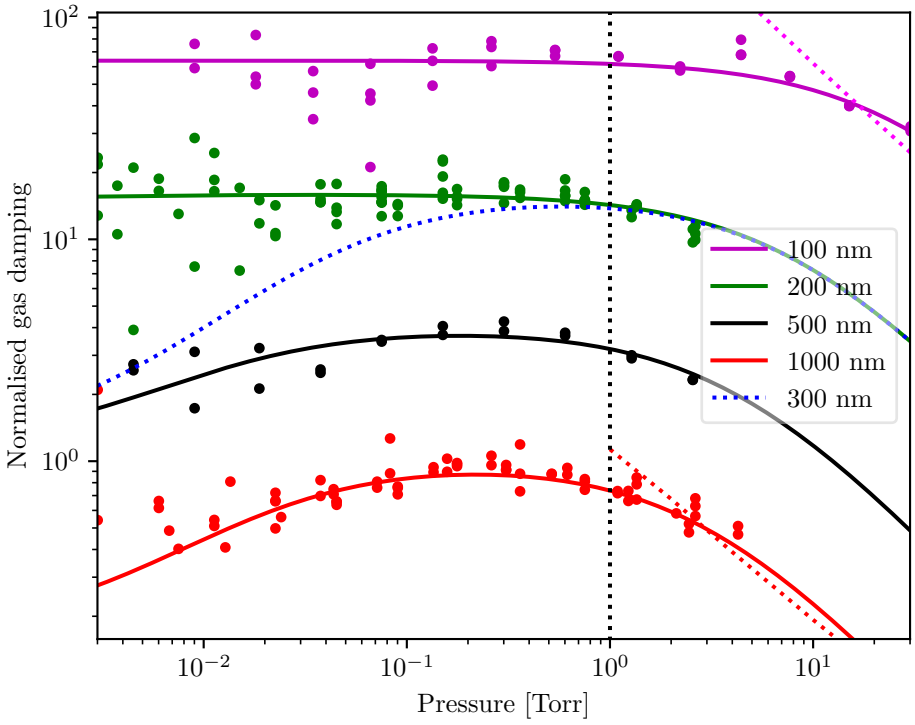

Figure 66: Normalised gas damping measured on beams with different widths

in Fig. 66). As such, the parameter h depends on the aspect ratio and therefore on w. Finally, the two parameters b and l are both important in the low pressure limit and define the deviations from the linear law in P. In order to minimise the amount of fitted constants, we decided to fix one of these two for all of the samples: $b = 300$ Torr^{-1}. That allows us to investigate the dependence of the second one l to device width w. Note that inversely, it was not possible to fix the variable l for all the samples and build our analysis on an width-dependent parameter b.

To conclude the Section, we should point out that adding gas to the chamber generates a frequency shift of the resonance. It is associated with adsorbed atoms on the beam's surface which means that the frequency shift $\delta f / f_0$ can be recalculated in terms of adsorbed mass $\delta m / m_0$ of ^{4}He atoms as follows:

$$\frac{\delta m}{m_0} = -2\frac{\delta f}{f_0}. \tag{184}$$

This recalculated relative added mass is plotted on Fig. 67. The dotted line on top of the data is just a guide for the eyes underlining that all samples behave identically within error-bars; similar results were obtained in Refs. [47, 160]. The dashed vertical marks the transition to the Navier-Stokes regime, where an extra shift occurs because of the fluid mass dragged by the device.

All these experiments were performed at a fixed temperature of 4.2 K. We also did some measurements at different T (in the range from 4 K to 30 K), but the effect due to the temperature change is relatively small for our samples and shows the same trend as previous results on similar devices [47]. However, the

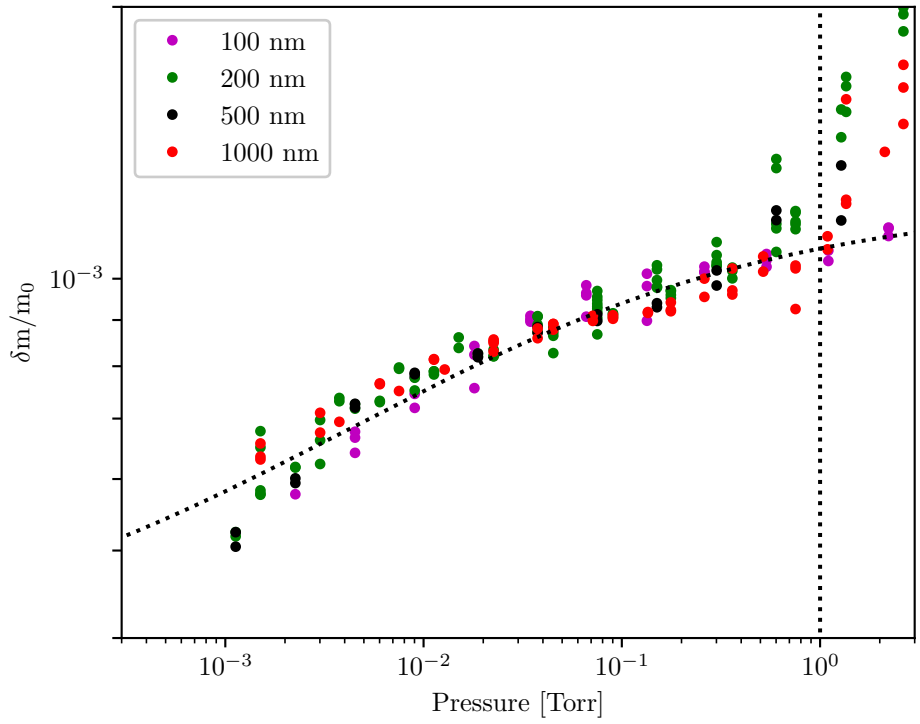

Figure 67: Added mass due to adsorbed gas on the NEMS surface

T-dependence is certainly specific to the underlying mechanisms, which shall be discussed in the following Section.

9.3 DISCUSSION

As already mentioned, we demonstrated in the first place the validity of the conclusions achieved in Ref. [47] using similar but fully-suspended devices. Furthermore, with experiments based on wider beams, some deviations from the linear molecular law at low pressure were observed. These are reminiscent of the signatures observed with devices having a finite gap g to the substrate: a decrease in gas damping below the $\propto P$ law. This width-dependent effect is smaller than the one which is gap-dependent, even for the widest sample, but it is clearly visible and reproducible. Here, we will comment these deviations by analysing the coefficients of Eq. 183 used to fit the data of Fig. 66 as a function of the only parameter which is different for all our samples: their width w. The fit parameters from Eq. 183 are plotted in Fig. 68 as a function of width w. Since the thickness e is the same for all devices (about 130 nm), these graphs can also be interpreted as a dependence to aspect ratio w/e (ranging from about 1 to 10). The empty circles correspond to the device of Ref. [47].

First of all, note the inset of Fig. 67 which demonstrates that the coefficient a is almost width-independent, as expected. The small decrease noticed for the widest beam could be explained by the largest low-pressure deviation which blurs

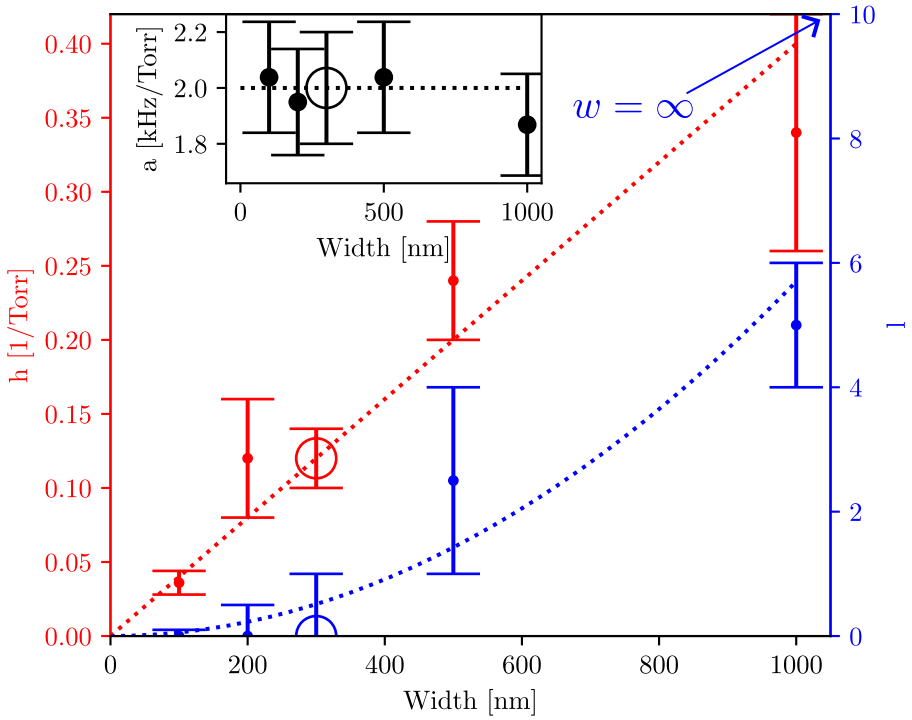

Figure 68: Fit parameters from Eq. 183 as a function of w

the transition from Navier-Stokes to molecular (there is no obvious flat part for $w = 1000$ nm on Fig. 66, making the definition of a more difficult).

Secondarily, the h parameter (left y-axis, in red) captures the molecular-to-laminar crossover at high pressures. Eq. 183 creates a simple interpolation from $\Delta\Gamma \approx a\,P$ to $\Delta\Gamma \approx a/h$ as P increases which enables us to link (at lowest order) the molecular law with the proper high-pressure Navier-Stokes solution [164] (represented in Fig. 66 by dashed lines for aspect ratios $w/e = 1$ and 10). As a result, h seems to be essentially linear with width w (dotted red line in Fig. 68, guide for the eyes), a feature reminiscent of the discussion presented at the beginning of this Section about the finite size nature of the cross-over. This empirical procedure is rather different from published works [166, 167]. Although it is very practical, the fits performed here are not very accurate because of the reduced high pressure range explored in our work (see error bars in Fig. 68).

Finally, the l parameter (right y-axis, blue) describes the small device-dependent decrease seen at low pressures (along with the fixed parameter $b = 300$ Torr^{-1}). This is the new finite-size result that extends earlier works [86]. The analytic expression we use here is slightly different from the one of Ref. [47] which was focused on explaining a $\Delta\Gamma \propto P^2$ dependence when deeply in the Knudsen boundary layer, when $P \ll 1$ Torr. Here instead, we propose that gas damping gradually drops from $\Delta\Gamma \approx aP$ to $\Delta\Gamma \approx aP[1/(1+l) + (bl-h)/(1+l)^2 P]$ as P is decreased towards zero pressure. The fit function has been chosen on purely empirical grounds. However, the drawback of our expression is that l and b coefficients are quite correlated within the fitting routine. Error bars are quite

large from the fit (note that b can also be chosen ± 100 Torr^{-1} producing a similar outcome). However, the tendency is the relevant result here: for small devices (i.e. $w < 300$ nm typically) there is no fittable correction, while for larger ones it is clearly growing with increasing of the characteristic size which is the width w of the beam in our case (dashed guide for the eyes in Fig. 68). From this guide in Fig. 68, we infer that l cannot be much larger than 0.75 for a 300 nm wide beam. This implies about 15 % maximum damping reduction at 10^{-2} Torr which is within the error bars of the measurements, and demonstrates that this effect does not impact the conclusions of Ref. [47], where the beam was of that size. In this sense, it seems (luckily) that $w = 300$ nm is about the limit defining non-invasivity in space. Note that non-invasivity can also be understood in terms of the absence of disturbance of the momentum distribution of gas properties. Such disturbances are excluded here, since experiments are conducted at low enough nano-beam velocities such that no nonlinear damping effects can be noticed [47, 160].

The presence of a wall at a distance g from a non-invasive probe had been interpreted in the framework of the boundary layer effect: as $\lambda_{mfp}(P)/g \gg 1$ with $P \to 0$, the device enters into this so-called Knudsen layer and the gas damping drops (Fig. 65). This drop is understood as a rarefaction phenomenon, see Ref. [47]. We will give here only a short overview of the formalism at stake. Mathematically, this result is obtained by first expanding at lowest orders the Maxwell-Boltzmann (MB) velocity distribution of gas particles $f_0(\vec{v})$ in terms of velocities. Defining the volumic gas density as $n(\vec{x})$, the density of particles per unit volume and unit velocity in the phase space $\{\vec{x}, \vec{v}\}$ writes:

$$n\,f = n(\vec{x}) f_0(\vec{v})\,[1 + Pl(\vec{v})]\,, \tag{185}$$

with $Pl(\vec{v})$ a polynomial deviation function: this is the Grad approach [169, 170, 171, 172]. The next step is to apply the Chapman-Enskog [169, 170] method to the coefficients of this polynomial. This assumes that if we are not too close to the wall, the corrections to the MB equilibrium function can be developed in power series of λ_{mfp}/x, here $x \approx g$. Solving mathematically the problem is thus performed by writing explicitly the collision integral entering into the Boltzmann equation with a given similar expansion. Applying also all conservation rules and symmetries, we will eventually end up with a system of equations that will link all of these coefficients and define the thermodynamic properties as a function of the initial Taylor coefficients introduced for the kernel of the collision integral. This is all very tedious and can be found in the Supplementary Material of Ref. [47]. In particular, the force acting onto the device is deduced and one can demonstrate that the effect can be recast into a density drop near the wall. Note that in this case, the wall is assumed to have an infinite width and therefore all deviations coefficients are independent of setup dimensions. Obviously, if the width of the surface at distance g would be much smaller than the width of the probe itself, the effect would disappear. This is the starting point for the understanding of our new results.

We interpret our width-dependent phenomenon as being the signature of the Knudsen boundary layer rarefaction effect occurring onto the device itself.

Mathematically, the idea lies in taking the Taylor expansion of the polynomial form (and of the collision kernel) in the reverse limit, as x/λ_{mfp}. The idea is that now the transition at low pressures will occur for $\varepsilon/\lambda_{mfp}(P) \ll 1$, with $x \approx \varepsilon$. This new lengthscale is in principle directly related to physical properties of the adsorbed layers on the surface of the probe; we shall comment it in the following paragraph. A similar mathematical development to the one performed for the Grad-Chapman-Enskog method presented above should lead to the definition of all properties as a function of the kernel's expansion coefficients. But there is now a big difference: these coefficients are size-dependent, since the probe width w is finite (which was not the case for the infinite wall addressed in Ref. [47]). Fitting the data of Ref. [47] leads to $l \approx 10$, as shown on the graph of Fig. 68 with an arrow and label $w = \infty$. Our measurements and the previous published results are thus compatible and assuming a (quite reasonable) monotonic change of l with w, this tells us that the probe would behave as a 'fully invasive' wall around about $w \approx 2$ μm. The demonstration that the fit parameter l does not vary anymore with width above this limit would require it to be tested experimentally. As well, we have not performed the full theoretical calculation and leave it for future work on this topic.

Consider now the case $w \to \infty$. Our expansion can then be written as $\Delta\Gamma \approx aP[o(1) + c \cdot \varepsilon(T)/\lambda_{mfp}]$, with c a positive number. From the fits, we can give a quantitative estimate for the parameter $\varepsilon(T)$; according to data published in Ref. [47], this is a temperature-dependent coefficient which proves indeed its material-dependent nature. Note that the fit realised in the opposite limit, when entering into the boundary layer, was given in the same reference by $\Delta\Gamma \approx aP[1 - 0.3 \cdot \lambda_{mfp}/g]$. The coefficient -0.3 is approximate but is geometry-and-temperature independent. Its equivalent in the $P \ll 1$ Torr limit is the parameter c introduced just above. Both parameters should thus tend to zero when the width of the object tends to zero: the limit where the wall invasivity disappears. However, we have no means in the low pressure limit to separate the numerical coefficient c from the lengthscale ε; we shall thus take arbitrarily $c = 1$. In this case it turns out that at 4.2 K, $\varepsilon \approx 60$ μm. This is a strikingly large lengthscale for an atomically thin adsorbed layer. We speculate that this could be a correlation length between atoms in the layer and atoms in the gas. It may tell us on what distance both entities are coupled together which is the distance over which the gas density will be affected (and shall drop, according to the theoretical approach). The mechanism would be the competition between adsorption on one side, driven by the nature of the surface and by the chemical potential in the vapour on the other side which is characteristic of the gas.

To conclude, let us come back to the fact that the adsorbed layers seem to play a key role in this phenomenon: this was pointed out with the temperature dependence of the fit coefficients measured in Ref. [47]. It is clear from Fig. 67 that in the whole pressure range of our experiments all our devices are covered with at least a layer of Helium. Clearly, the nature and structure of the layers influences the way gas particles are reflected in a collision process. As such, future experimental work could be performed on how the nature of the gas changes the

measured properties: using ^{3}He (which is lighter), or N_2 (heavier and diatomic). Furthermore, one could imagine coating the surfaces of the beam device with one type of molecules (say, N_2), and study the impact of this on another type of gas (e.g. ^{4}He or ^{3}He).

CONCLUSION

In this PhD manuscript, we summarised the developed technologies and important aspects of the experiments which we carried out over about three years spent at Institut Néel, CNRS. The element at the core of our work is a mesoscopic mechanical object, a beam-like or drum-like device. The main measuring scheme we have been building on is microwave optomechanics, which was implemented down to the Standard Quantum Limit (SQL). The focus has been put on in-equilibrium thermodynamic properties of mesoscopic mechanical modes and tackling fundamental aspects of physics.

Modern technologies in nanofabrication, microwaves, and cryogenics were introduced in corresponding chapters of the first part. We presented the fully suspended nanobeams that have been developed with the specific aim of probing quantum fluids in the future. The microwave chapter described our quantum limited measurement scheme built around a Travelling Wave Parametric Amplifier (TWPA). The functioning of the latter, which is prone to saturation, needed the development of a 'self-tuning microwave opposition line' which enabled us to cancel the optomechanical pumping tones. One motivation of our work is to mount our experiments on a nuclear demagnetisation stage to reach temperatures below one milli-Kelvin. We participated in some developments aiming at building cryogen-free and continuous demagnetisation cryostats. Such equipment requires very low resistance superconducting heat switches [70].

In the theoretical part, we gave a brief introduction to the dynamics of nano-mechanical resonators, including the basic magnetomotive technique for their simple experimental characterisation. A clear theoretical description of optomechanical systems is also presented. Specifically, in Ch. 4 the generic theory of nano-mechanical resonators was discussed and updated by including a new model of clamps [74]. Also, the fundamental link between thermal transport and mechanics has been introduced and discussed [90]. In Ch. 5, the magnetomotive technique has been described and examples of its application to nano-mechanical beams characterisation was given, in both the linear and non-linear regime. Finally in Ch. 6, the quantum and classical formalisms used to describe optomechanical systems were introduced and compared. The specific state of self sustained oscillations, which exists beyond the parametric instability created by the optomechanical coupling, has been described. This state has been applied to the characterisation of non-linearities in the optomechanical coupling [45].

Our main results were presented in the last part of this manuscript, where we used nano-mechanical and optomechanical systems to probe thermodynamical concepts of various origin. All of which are linked to nano-mechanics and/or optomechanics and concern steady-state properties of a mechanical mode in contact with a specific bath. In Ch. 7, we demonstrated experimentally the validity of the classical description of the optomechanical interaction. In these experiments

performed below one Kelvin, both the mechanical mode and the optical mode are in their classical limit: the optical mode being driven by an effective bath mimicking a temperature of 300 K [46]. There, only a single microwave tone was applied to the system which leaves a lot of room for further investigations of optomechanics in the classical limit. This includes Back Action Evading schemes (BAE), with first attempts made during this work. In Ch. 8, thermal fluctuations of the population of a single mesoscopic mechanical mode were observed, along with a $1/f$-noise of unknown nature [42]. We demonstrate for the first time that its energy fluctuations have exponential statistics, as expected for a Boltzmann distribution, and that the power spectral density matches the Ornstein-Uhlenbeck law with a high frequency cutoff (at the relaxation rate). This method has a great potential to probe single mechanical modes of macroscopic resonators cooled passively in their ground state [24] with potentially a resolution down to a single phonon transition. This may lead to a new understanding of quantum thermodynamics and phonon transport and revealing single-phonon tunnelling. As well, studying sideband asymmetry in real-time may bring new insight in the nature of quantum fluctuations. In Ch. 9, we characterised the influence of the Knudsen boundary layer in rarefied ^{4}He gas at 4.2 K on a nano-mechanical beam device [86]. We discovered that the probe itself can suffer from the Knudsen layer and therefore change the outcome of the damping measurements. These results are in agreement with the previous ones interpreted as a rarefaction phenomenon near the walls, and we extend them as a function of the size of the probe. It turns out that the analysis introduces a new lengthscale, characteristic of the pair gas-adsorbed layers, that we interpret as its correlation length. This quantity happens to be quite large, of the order of tens of microns. Those experiments could be expanded in the future by introducing different gases, new samples probing different scales and even different geometries.

Starting from nanofabrication, microwave technologies, and cryogenics, we have ended up with extremely sensitive measurements of different thermodynamic properties. Even though all our measurements, yet very sensitive, were completely classical so far, they demonstrated our primary understanding of these unique setups and also showed what is not completely understood to date. The shift to the pure quantum regime does not look unreachable anymore and shows great promise for fundamental physics.

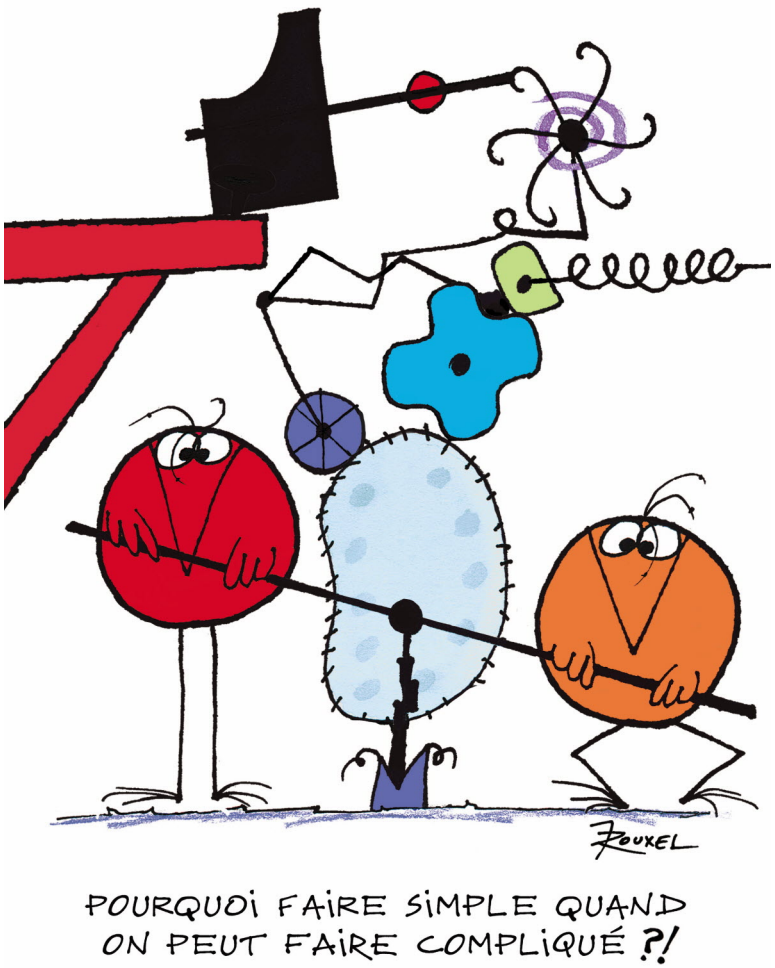

Figure 69: Illustration from 'Les Shadoks' by Jacques Rouxel

BIBLIOGRAPHY

1. Feynman, R. There's plenty of room at the bottom. *The talk presented to the American Physical Society in Pasadena* (Dec. 1959) (cit. on p. 15).
2. Pashkin, Y. A. *et al.* Quantum oscillations in two coupled charge qubits. *Nature* **421,** 823–826 (2003) (cit. on p. 15).
3. Guthrie, A. *et al.* Cooper-Pair Box Coupled to Two Resonators: An Architecture for a Quantum Refrigerator. *Phys. Rev. Applied* **17,** 064022 (6 June 2022) (cit. on p. 16).
4. Tavakoli, A. *et al.* Specific heat of thin phonon cavities at low temperature: Very high values revealed by zeptojoule calorimetry. *Phys. Rev. B* **105,** 224313 (22 June 2022) (cit. on p. 16).
5. Maillet, O. *et al.* Optimal Probabilistic Work Extraction beyond the Free Energy Difference with a Single-Electron Device. *Phys. Rev. Lett.* **122,** 150604 (15 Apr. 2019) (cit. on pp. 16, 19).
6. Schwab, K. C. & Roukes, M. L. Putting Mechanics into Quantum Mechanics. *Phys. Today* **58,** 36–42 (2005) (cit. on p. 16).
7. Coulomb, C.-A. Premier mémoire sur l'électricité et le magnétisme. *Histoire de l'Academie royale des sciences,* 569–577 (1785) (cit. on p. 16).
8. Cavendish, H. Experiments to determine the density of the earth. *Philosophical Transactions of the Royal Society* **88,** 469–526 (Dec. 1798) (cit. on p. 16).
9. Friedsam, C., Wehle, A. K., Kühner, F. & Gaub, H. E. Dynamic single-molecule force spectroscopy: bond rupture analysis with variable spacer length. *J. Phys.: Condensed Matter* **15,** S1709 (2003) (cit. on p. 16).
10. Guthrie, A. *et al.* Nanoscale real-time detection of quantum vortices at millikelvin temperatures. *Nat. Commun.* **12,** 2645 (2021) (cit. on pp. 16, 145).
11. Mercier de Lépinay, L., Ockeloen-Korppi, C. F., Woolley, M. J. & Sillanpää, M. A. Quantum mechanics–free subsystem with mechanical oscillatorse. *Science* **372,** 625–629 (6542 May 2021) (cit. on pp. 16, 120).
12. Leggett, A. J. Testing the limits of quantum mechanics: motivation, state of play, prospects. *J. Phys.: Condensed Matter* **14,** R415 (Apr. 2002) (cit. on p. 16).
13. Maillet, O., Vavrek, F., Fefferman, A. D., Bourgeois, O. & Collin, E. Classical decoherence in a nanomechanical resonator. *New J. Phys.* **18,** 073022 (2016) (cit. on p. 16).
14. Motte, J.-F. *et al.* Microscale Crystalline Rare-Earth Doped Resonators for Strain-Coupled Optomechanics. *J. Mod. Phys.* **10,** 1342–1352 (2019) (cit. on p. 16).

15. Braginsky, V., Khalili, F. & Thorne, K. *Quantum Measurement* (Cambridge University Press, 1992) (cit. on pp. 17, 81, 87).

16. Dorsel, A., McCullen, J. D., Meystre, P., Vignes, E. & Walther, H. Optical Bistability and Mirror Confinement Induced by Radiation Pressure. *Phys. Rev. Lett.* **51,** 1550–1553 (17 Oct. 1983) (cit. on p. 17).

17. Caves, C. M. Quantum-Mechanical Radiation-Pressure Fluctuations in an Interferometer. *Phys. Rev. Lett.* **45,** 75–79 (2 July 1980) (cit. on pp. 17, 81, 87).

18. Clerk, A. A. Quantum-limited position detection and amplification: A linear response perspective. *Phys. Rev. B* **70,** 245306 (24 Dec. 2004) (cit. on p. 17).

19. Abbott, B. P. *et al.* Observation of Gravitational Waves from a Binary Black Hole Merger. *Phys. Rev. Lett.* **116,** 061102 (6 Feb. 2016) (cit. on pp. 17, 82).

20. Collin, E. Mesoscopic quantum thermo-mechanics: A new frontier of experimental physics. *AVS Quantum Science* **4,** 020501 (2022) (cit. on pp. 17, 19, 124, 143).

21. Rimberg, A. J., Blencowe, M. P., Armour, A. D. & Nation, P. D. A cavity-Cooper pair transistor scheme for investigating quantum optomechanics in the ultra-strong coupling regime. *New J. Phys.* **16,** 055008 (May 2014) (cit. on p. 18).

22. Maccabe, G. S. *et al.* Nano-acoustic resonator with ultralong phonon lifetime. *Science* **370,** 840–843 (6518 Nov. 2020) (cit. on p. 18).

23. Regal, C., Teufel, J. & Lehnert, K. Measuring nanomechanical motion with a microwave cavity interferometer. *Nat. Phys.* **4,** 555–560 (2008) (cit. on pp. 18, 86).

24. Cattiaux, D. *et al.* A macroscopic object passively cooled into its quantum ground state of motion beyond single-mode cooling. *Nat. Commun.* **12,** 6182 (2021) (cit. on pp. 18, 29, 124, 137, 138, 140, 141, 143, 156).

25. Armani, D. K., Kippenberg, T. J., Spillane, S. M. & Vahala, K. J. Ultra-high-Q toroid microcavity on a chip. *Nature* **421,** 925–928 (2003) (cit. on p. 18).

26. Youssefi, A., Kono, S., Chegnizadeh, M. & Kippenberg, T. J. A squeezed mechanical oscillator with milli-second quantum decoherence. *arXiv:2208.13082* (2022) (cit. on p. 18).

27. Jarzynski, C. Nonequilibrium Equality for Free Energy Differences. *Phys. Rev. Lett.* **78,** 2690 (1997) (cit. on pp. 19, 123).

28. Koski, J. V., Maisi, V. F., Pekola, J. P. & Averin, D. V. Experimental realization of a Szilard engine with a single electron. *Proceedings of the National Academy of Sciences* **111,** 13786–13789 (2014) (cit. on pp. 19, 123).

29. Pekola, J. P. & Karimi, B. Colloquium: Quantum heat transport in condensed matter systems. *Rev. Mod. Phys.* **93,** 041001 (4 Oct. 2021) (cit. on pp. 19, 124).

30. Pekola, J. P. Towards quantum thermodynamics in electronic circuits. *Nat. Phys.* **11,** 118–123 (2015) (cit. on pp. 19, 123).

31. Manzano, G. *et al.* Thermodynamics of Gambling Demons. *Phys. Rev. Lett.* **126,** 080603 (8 Feb. 2021) (cit. on p. 19).

32. Harris, N. C., Song, Y. & Kiang, C.-H. Experimental Free Energy Surface Reconstruction from Single-Molecule Force Spectroscopy using Jarzynski's Equality. *Phys. Rev. Lett.* **99,** 068101 (6 Aug. 2007) (cit. on p. 19).

33. Dago, S., Pereda, J., Ciliberto, S. & Bellon, L. Virtual double-well potential for an underdamped oscillator created by a feedback loop. *J. Stat. Mech.: Theory Exp.* **2022,** 053209 (May 2022) (cit. on p. 19).

34. Bérut, A. *et al.* Experimental verification of Landauers principle linking. *Nature* **483,** 187–189 (2012) (cit. on pp. 19, 123).

35. Dago, S., Pereda, J., Barros, N., Ciliberto, S. & Bellon, L. Information and Thermodynamics: Fast and Precise Approach to Landauer's Bound in an Underdamped Micromechanical Oscillator. *Phys. Rev. Lett.* **126,** 170601 (17 Apr. 2021) (cit. on p. 19).

36. Bassi, A., Lochan, K., Satin, S., Singh, T. P. & Ulbricht, H. Models of wave-function collapse, underlying theories, and experimental tests. *Rev. Mod. Phys.* **85,** 471–527 (2 Apr. 2013) (cit. on pp. 19, 124, 143).

37. Monsel, J. *Quantum thermodynamics and optomechanics* PhD thesis (Université Grenoble Alpes, 2019) (cit. on p. 19).

38. Stepanova, M. & Dew, S. *Nanofabrication: Techniques and Principles* (Springer Vienna, 2011) (cit. on p. 27).

39. Cleland, A. N. *Foundations of Nanomechanics: From Solid-State Theory to Device Applications* (Springer Science & Business Media, 2013) (cit. on pp. 27, 57, 59, 69, 124).

40. Zhou, X. *et al.* On-chip Thermometry for Microwave Optomechanics Implemented in a Nuclear Demagnetization Cryostat. *Phys. Rev. Applied* **12,** 044066 (4 Oct. 2019) (cit. on pp. 28, 29, 42, 46, 47, 114, 124, 135, 138, 140, 142).

41. Kumar, S., Cattiaux, D., Collin, E., Fefferman, A. & Zhou, X. Microwave Optomechanically Induced Transparency and Absorption Between 250 and 450 mK. *J. Low Temp. Phys.* (2022) (cit. on p. 28).

42. Golokolenov, I. *et al.* Thermodynamics of a single mesoscopic phononic mode. *Phys. Rev. Res.* **5,** 013046 (1 Jan. 2023) (cit. on pp. 28, 98, 124, 156).

43. Rocheleau, T. *et al.* Preparation and detection of a mechanical resonator near the ground state of motion. *Nature* **463,** 72–75 (2010) (cit. on p. 29).

44. Kumar, S. *Low temperature microwave optomechanics : anomalous force noise and optomechanically induced transparency* PhD thesis (Université Grenoble Alpes, 2021) (cit. on pp. 29, 124, 140).

45. Cattiaux, D. *et al.* Beyond linear coupling in microwave optomechanics. *Phys. Rev. Research* **2,** 033480 (3 Sept. 2020) (cit. on pp. 29, 104, 105, 155).

46. Golokolenov, I. *et al.* Microwave single-tone optomechanics in the classical regime. *New J. Phys.* **23,** 053008 (May 2021) (cit. on pp. 29, 140, 156).

47. Gazizulin, R. R. *et al.* Surface-Induced Near-Field Scaling in the Knudsen Layer of a Rarefied Gas. *Phys. Rev. Lett.* **120,** 036802 (3 Jan. 2018) (cit. on pp. 30, 145–153).

48. Pozar, D. M. *Microwave engineering; 3rd ed.* (Wiley, Hoboken, NJ, 2005) (cit. on p. 35).

49. Mutus, J. Y. *et al.* Design and characterization of a lumped element single-ended superconducting microwave parametric amplifier with on-chip flux bias line. *Appl. Phys. Lett.* **103,** 122602 (2013) (cit. on p. 41).

50. Planat, L. *et al.* Understanding the Saturation Power of Josephson Parametric Amplifiers Made from SQUID Arrays. *Phys. Rev. Applied* **11,** 034014 (3 Mar. 2019) (cit. on p. 41).

51. Agrawal, G. *Nonlinear Fiber Optics; 5th ed.* (Elsevier, Burlington, MA, 2012) (cit. on p. 41).

52. Planat, L. *et al.* Photonic-Crystal Josephson Traveling-Wave Parametric Amplifier. *Phys. Rev. X* **10,** 021021 (2 Apr. 2020) (cit. on pp. 41, 42, 142).

53. Pobell, F. *Matter and Methods at Low Temperature* (Springer, Third Edition, 2007) (cit. on pp. 43, 49, 50).

54. Lounasmaa, O. V. *Experimental Principles and Methods Below 1K* (Academic Press, 1974) (cit. on pp. 43, 50).

55. Schmoranzer, D., Gazizulin, R., Triqueneaux, S., Collin, E. & Fefferman, A. Development of a Sub-mK Continuous Nuclear Demagnetization Refrigerator. *J. Low Temp. Phys.* **196,** 261–267 (2019) (cit. on pp. 43, 50, 51).

56. Chernyak, V. G., Porodnov, B. T. & Suetin, P. E. Application of the variation method to the problem of thermomolecular pressure difference in a cylindrical channel. *J. Eng. Phys.* **26,** 309–312 (Mar. 1974) (cit. on p. 45).

57. Rusby, R. *et al.* European Dissemination of the Ultra-low Temperature Scale, PLTS-2000. *AIP Conference Proceedings* **684,** 89 (2003) (cit. on p. 46).

58. Leachman, J. W., Jacobsen, R. T., Lemmon, E. W. & Penoncello, S. G. *Thermodynamic Properties of Cryogenic Fluids* (Springer, Second Edition, 2017) (cit. on p. 46).

59. Herzfeld, C. *et al. Temperature: Its Measurement and Control in Science and Industry* (Reinhold, 1941) (cit. on p. 46).

60. Winkelmann, C. B., Collin, E., Bunkov, Y. M. & Godfrin, H. Vibrating Wire Thermometry in Superfluid ^{3}He. *J. Low Temp. Phys.* **135,** 3–14 (2004) (cit. on p. 46).

61. Meschke, M., Pekola, J. P., Gay, F., Rapp, R. E. & Godfrin, H. Electron Thermalization in Metallic Islands Probed by Coulomb Blockade Thermometry. *J. Low Temp. Phys.* **134,** 1119–1143 (Mar. 2004) (cit. on p. 47).

62. Bäuerle, C. *et al.* The new Grenoble 100 μK refrigerator. *Czechoslovak J. Phys.* **46,** 2791–2792 (1996) (cit. on p. 49).

63. Korringa, J. Nuclear magnetic relaxation and resonnance line shift in metals. *Physica* **16,** 601–610 (7-8 1950) (cit. on p. 50).

64. Batey, G. *et al.* A microkelvin cryogen-free experimental platform with integrated noise thermometry. *New J. Phys.* **15,** 113034 (2013) (cit. on p. 50).

65. Todoshchenko, I., Kaikkonen, J.-P., Blaauwgeers, R., Hakonen, P. J. & Savin, A. Dry demagnetization cryostat for sub-millikelvin helium experiments: Refrigeration and thermometry. *Rev. Sci. Instrum.* **85,** 085106 (2014) (cit. on p. 50).

66. Palma, M. *et al.* Magnetic cooling for microkelvin nanoelectronics on a cryofree platform. *Rev. Sci. Instrum.* **88,** 043902 (2017) (cit. on p. 50).

67. Yan, J., Yao, J., Shvarts, V., Du, R.-R. & Lin, X. Cryogen-free one hundred microkelvin refrigerator. *Rev. Sci. Instrum.* **92,** 025120 (2021) (cit. on p. 50).

68. Takimoto, S., Toda, R., Murakawa, S. & Fukuyama, H. Construction of Continuous Magnetic Cooling Apparatus with Zinc-Soldered $PrNi_5$ Nuclear Stages. *J. Low Temp. Phys.* **208,** 492–500 (Sept. 2022) (cit. on p. 51).

69. Schmoranzer, D., Butterworth, J., Triqueneaux, S., Collin, E. & Fefferman, A. Design evaluation of serial and parallel sub-mK continuous nuclear demagnetization refrigerators. *Cryogenics* **110,** 103119 (Sept. 2020) (cit. on p. 51).

70. Butterworth, J. *et al.* Superconducting aluminum heat switch with 3 nΩ equivalent resistance. *Rev. Sci. Instrum.* **93,** 034901 (2022) (cit. on pp. 51, 155).

71. Kittel, C. *Introduction to Solid State Physics; 8th ed.* (John Wiley & Sons, New York, 2004) (cit. on p. 57).

72. Unterreithmeier, Q. P., Faust, T. & Kotthaus, J. P. Damping of Nanomechanical Resonators. *Phys. Rev. Lett.* **105,** 027205 (2 July 2010) (cit. on pp. 59–62).

73. Lifshitz, R. & Roukes, M. L. Thermoelastic damping in micro- and nanomechanical systems. *Phys. Rev. B* **61,** 5600–5609 (8 Feb. 2000) (cit. on p. 59).

74. Golokolenov, I. *et al.* Nano-beam clamping revisited. *arXiv:2211.01617* (2022) (cit. on pp. 59, 62, 64–66, 155).

75. Zener, C. *Elasticity and Anelasticity of Metals* (University of Chicago Press, 1948) (cit. on p. 60).

76. Timoshenko, S., Young, D. & Weaver, W. *Vibrations problems in engineering* 4th ed. (John Wiley and Sons, 1974) (cit. on p. 60).

77. Photiadis, D. M. & Judge, J. A. Attachment losses of high Q oscillators. *Appl. Phys. Lett.* **85,** 482 (2004) (cit. on p. 62).

78. Judge, J. A., Photiadis, D. M., Vignola, J. F., Houston, B. H. & Jarzynski, J. Attachment loss of micromechanical and nanomechanical resonators in the limits of thick and thin support structures. *J. Appl. Phys.* **101,** 013521 (2007) (cit. on p. 62).

79. Cross, M. C. & Lifshitz, R. Elastic wave transmission at an abrupt junction in a thin plate with application to heat transport and vibrations in mesoscopic systems. *Phys. Rev. B* **64,** 085324 (2001) (cit. on p. 62).

80. Wilson-Rae, I. Intrinsic dissipation in nanomechanical resonators due to phonon tunneling. *Phys. Rev. B* **77,** 245418 (2008) (cit. on p. 62).

81. Schmid, S., Jensen, K. D., Nielsen, K. H. & Boisen, A. Damping mechanisms in high-Q micro and nanomechanical string resonators. *Phys. Rev. B* **84,** 165307 (2011) (cit. on p. 62).

82. Suhel, A., Hauer, B. D., Biswas, T. S., Beach, K. S. D. & Davis, J. P. Dissipation mechanisms in thermomechanically driven silicon nitride nanostrings. *Appl. Phys. Lett.* **100,** 173111 (2012) (cit. on p. 62).

83. Tsaturyan, Y., Barg, A., Polzik, E. S. & Schliesser, A. Ultracoherent nanomechanical resonators via soft clamping and dissipation dilution. *Nat. Nanotechnol.* **12,** 776 (2017) (cit. on p. 62).

84. Ghadimi, A. H. *et al.* Elastic strain engineering for ultralow mechanical dissipation. *Science* **360,** 764 (2018) (cit. on p. 62).

85. Sadeghi, P., Tanzer, M., Christensen, S. L. & Schmid, S. Influence of clamp-widening on the quality factor of nanomechanical silicon nitride resonators. *J. Appl. Phys.* **126,** 165108 (2019) (cit. on p. 62).

86. Golokolenov, I., Alperin, B., Fernandez, B., Fefferman, A. & Collin, E. Fully suspended nano-beams for quantum fluids. *J. Low Temp. Phys.* (2022) (cit. on pp. 62, 76, 146, 151, 156).

87. Babaei Gavan, K., van der Drift, E. W. J. M., Venstra, W. J., Zuiddam, M. R. & van der Zant, H. S. J. Effect of undercut on the resonant behaviour of silicon nitride cantilevers. *J. Micromech. Microeng.* **19,** 035003 (2009) (cit. on p. 66).

88. Yu, P.-L., Purdy, T. P. & Regal, C. A. Control of Material Damping in High-Q Membrane Microresonators. *Phys. Rev. Lett.* **108,** 083603 (8 Feb. 2012) (cit. on p. 67).

89. Cattiaux, D., Kumar, S., Zhou, X., Fefferman, A. & Collin, E. Geometrical nonlinearity of circular plates and membranes: An alternative method. *J. Appl. Phys.* **128,** 104501 (2020) (cit. on p. 67).

90. Collin, E., Golokolenov, I., Maillet, O., Saminadayar, L. & Bourgeois, O. On the link between mechanics and thermal properties: mechanothermics. *arXiv:2211.15106* (2022) (cit. on pp. 68, 70, 71, 155).

91. Thurston, R. Elastic waves in rods and optical fibers. *J. Sound Vib.* **159,** 441–467 (1992) (cit. on p. 70).

92. Cleland, A. & Roukes, M. External control of dissipation in a nanometer-scale radiofrequency mechanical resonator. *Sens. Actuator A Phys.* **72,** 256–261 (1999) (cit. on p. 73).

93. Lifshitz, R. & Cross, M. C. *Nonlinear Dynamics of Nanomechanical and Micromechanical Resonators* in *Reviews of Nonlinear Dynamics and Complexity* 1–52 (John Wiley & Sons Ltd, Weinheim, 2008) (cit. on p. 78).

94. Aspelmeyer, M., Kippenberg, T. J. & Marquardt, F. Cavity optomechanics. *Rev. Mod. Phys.* **86,** 1391–1452 (4 Dec. 2014) (cit. on pp. 81, 82, 95).

95. Harris, G. I. *et al.* Laser cooling and control of excitations in superfluid helium. *Nat. Phys.* **12,** 788–793 (Aug. 2016) (cit. on p. 82).

96. Cattiaux, D. *Ultra-low temperatures microwave optomechanics for quantum sensing* PhD thesis (Université Grenoble Alpes, 2021) (cit. on pp. 82, 88).

97. Clerk, A. A., Devoret, M. H., Girvin, S. M., Marquardt, F. & Schoelkopf, R. J. Introduction to quantum noise, measurement, and amplification. *Rev. Mod. Phys.* **82,** 1155–1208 (2 Apr. 2010) (cit. on p. 82).

98. Barzanjeh, S. *et al.* Mechanical on-chip microwave circulator. *Nat. Commun.* **8,** 953 (Oct. 2017) (cit. on pp. 87, 111).

99. Weinstein, A. J. *et al.* Observation and Interpretation of Motional Sideband Asymmetry in a Quantum Electromechanical Device. *Phys. Rev. X* **4,** 041003 (4 Oct. 2014) (cit. on pp. 87, 118).

100. Shevchuk, O., Steele, G. A. & Blanter, Y. M. Strong and tunable couplings in flux-mediated optomechanics. *Phys. Rev. B* **96,** 014508 (1 July 2017) (cit. on p. 87).

101. Faust, T., Krenn, P., Manus, S., Kotthaus, J. & Weig, E. Microwave cavity-enhanced transduction for plug and play nanomechanics at room temperature. *Nat. Commun.* **3,** 728 (Mar. 2012) (cit. on pp. 89, 111).

102. Zhou, X., Cattiaux, D., Theron, D. & Collin, E. Electric circuit model of microwave optomechanics. *J. Appl. Phys.* **129,** 114502 (2021) (cit. on pp. 89, 92, 95, 111, 118, 119).

103. Aspelmeyer, M., Kippenberg, T. & Marquardt, M. *Cavity optomechanics: Nano- and Micromechanical resonators interacting with light* (Springer Berlin, Heidelberg, 2014) (cit. on p. 97).

104. Mishin, Y. & Hickman, J. Energy spectrum of a Langevin oscillator. *Phys. Rev. E* **94,** 062151 (6 Dec. 2016) (cit. on p. 100).

105. Landau, L. & Lifshits, E. *Statisticheskaya physica; Teoreticheskaya fizika (Tom 5)* (Nauka, 1964) (cit. on pp. 101, 123, 124).

106. Uhlenbeck, G. E. & Ornstein, L. S. On the Theory of the Brownian Motion. *Phys. Rev.* **36,** 823–841 (5 Sept. 1930) (cit. on pp. 101, 124).

107. Armour, A. D. & Rodrigues, D. A. Quantum dynamics of a mechanical resonator driven by a cavity. *Comptes Rendus Physique* **13,** 440–453 (2012) (cit. on p. 103).

108. Druge, J., Jean, C., Laurent, O., Méasson, M.-A. & Favero, I. Damping and non-linearity of a levitating magnet in rotation above a superconductor. *New J. Phys.* **16,** 075011 (2014) (cit. on p. 104).

109. Devoret, M. H. & Martinis, J. M. Implementing Qubits with Superconducting Integrated Circuits. *Quantum Inf. Process.* **3,** 163–203 (Oct. 2004) (cit. on p. 111).

110. Mallet, F. *et al.* Single-shot qubit readout in circuit quantum electrodynamics. *Nat. Phys.* **5,** 791–795 (Aug. 2009) (cit. on p. 111).

111. Ockeloen-Korppi, C. F. *et al.* Single-shot qubit readout in circuit quantum electrodynamics. *Nature* **556,** 478–482 (Apr. 2018) (cit. on p. 111).

112. O'Connell, A. D. *et al.* Quantum ground state and single-phonon control of a mechanical resonator. *Nature* **464,** 697–703 (Apr. 2010) (cit. on p. 111).

113. Regal, C. A., Teufel, J. D. & Lehnert, K. W. Measuring nanomechanical motion with a microwave cavity interferometer. *Nat. Phys.* **4,** 555–560 (July 2008) (cit. on p. 111).

114. Higginbotham, A. P. *et al.* Harnessing electro-optic correlations in an efficient mechanical converter. *Nat. Phys.* **14,** 1038–1042 (Oct. 2018) (cit. on p. 111).

115. Wollman, E. E. *et al.* Quantum squeezing of motion in a mechanical resonator. *Science* **349,** 952–955 (2015) (cit. on p. 118).

116. Hertzberg, J. *et al.* Back-action-evading measurements of nanomechanical motion. *Nat. Phys.* **6,** 213–217 (2010) (cit. on pp. 118, 120).

117. Teufel, J. D. *et al.* Sideband cooling of micromechanical motion to the quantum ground state. *Nature* **475,** 359–363 (2011) (cit. on p. 120).

118. Chan, J. *et al.* Laser cooling of a nanomechanical oscillator into its quantum ground state. *Nature* **478,** 89–92 (Oct. 2011) (cit. on p. 120).

119. Liu, Y., Zhou, J., Mercier de Lépinay, L. & Sillanpää, M. A. Quantum backaction evading measurements of a silicon nitride membrane resonator. *New J. Phys.* **24,** 083043 (Aug. 2022) (cit. on p. 120).

120. Shomroni, I. *et al.* Two-Tone Optomechanical Instability and Its Fundamental Implications for Backaction-Evading Measurements. *Phys. Rev. X* **9,** 041022 (4 Oct. 2019) (cit. on p. 120).

121. Jarzynski, C. Equalities and Inequalities: Irreversibility and the Second Law of Thermodynamics at the Nanoscale. *Annu. Rev. Condens. Matter Phys.* **2,** 329–351 (2011) (cit. on p. 123).

122. Campisi, M., Hänggi, P. & Talkner, P. Colloquium: Quantum fluctuation relations: Foundations and applications. *Rev. Mod. Phys.* **83,** 771–791 (3 July 2011) (cit. on p. 123).

123. Dago, S., Pereda, J., Barros, N., Ciliberto, S. & Bellon, L. Information and Thermodynamics: Fast and Precise Approach to Landauer's Bound in an Underdamped Micromechanical Oscillator. *Phys. Rev. Lett.* **126,** 170601 (17 Apr. 2021) (cit. on p. 123).

124. Ribezzi-Crivellari, M. & Ritort, F. Large work extraction and the Landauer limit in a continuous Maxwell demon. *Nat. Phys.* **15,** 660–664 (2019) (cit. on p. 123).

125. Averin, D. V. & Pekola, J. P. Violation of the Fluctuation-Dissipation Theorem in Time-Dependent Mesoscopic Heat Transport. *Phys. Rev. Lett.* **104,** 220601 (22 June 2010) (cit. on p. 124).

126. Rego, L. G. C. & Kirczenow, G. Quantized Thermal Conductance of Dielectric Quantum Wires. *Phys. Rev. Lett.* **81,** 232–235 (1 July 1998) (cit. on p. 124).

127. Blencowe, M. P. & Vitelli, V. Universal quantum limits on single-channel information, entropy, and heat flow. *Phys. Rev. A* **62,** 052104 (5 Oct. 2000) (cit. on p. 124).

128. Schwab, K., Henriksen, E., Worlock, J. & Roukes, M. Measurement of the quantum of thermal conductance. *Nature* **404,** 974–977 (2000) (cit. on p. 124).

129. Tavakoli, A. *et al.* Heat conduction measurements in ballistic 1D phonon waveguides indicate breakdown of the thermal conductance quantization. *Nat. Commun.* **9,** 4287 (2018) (cit. on p. 124).

130. Diósi, L. Testing Spontaneous Wave-Function Collapse Models on Classical Mechanical Oscillators. *Phys. Rev. Lett.* **114,** 050403 (5 Feb. 2015) (cit. on p. 124).

131. Vinante, A. & Ulbricht, H. Gravity-related collapse of the wave function and spontaneous heating: Revisiting the experimental bounds. *AVS Quantum Science* **3,** 045602 (2021) (cit. on p. 124).

132. Phillips, W. A. Tunneling states in amorphous solids. *J. Low Temp. Phys.* **7,** 1573–7357 (1972) (cit. on p. 124).

133. Anderson, P. W., Halperin, B. I. & Varma, C. M. Anomalous low-temperature thermal properties of glasses and spin glasses. *Philos. Mag.: A Journal of Theoretical Experimental and Applied Physics* **25,** 1–9 (1972) (cit. on p. 124).

134. Shannon, C. Communication in the Presence of Noise. *Proceedings of the IRE* **37,** 10–21 (1949) (cit. on p. 125).

135. Harris, C. R. *et al.* Array programming with NumPy. *Nature* **585,** 357–362 (2020) (cit. on p. 129).

136. Gnedenko, B. V. & Kolmogorov, A. N. *Predelnye raspredelniya dlya summ nezavisimykh sluchainykh velichin* 1st ed. (Moskva–Leningrad, 1949) (cit. on p. 131).

137. Chui, T. C. P., Swanson, D. R., Adriaans, M. J., Nissen, J. A. & Lipa, J. A. Temperature fluctuations in the canonical ensemble. *Phys. Rev. Lett.* **69,** 3005–3008 (21 Nov. 1992) (cit. on p. 140).

138. Sansa, M. *et al.* Frequency fluctuations in silicon nanoresonators. *Nat. Nanotechnol.* **11,** 552–558 (2016) (cit. on p. 141).

139. Maillet, O. *et al.* Measuring Frequency Fluctuations in Nonlinear Nanomechanical Resonators. *ACS Nano* **12,** 5753–5760 (6 2018) (cit. on pp. 141, 142).

140. Tavakoli, A. *et al.* Specific heat of thin phonon cavities at low temperature: Very high values revealed by zeptojoule calorimetry. *Phys. Rev. B* **105,** 224313 (22 June 2022) (cit. on p. 142).

141. Stahle, C. K., McCammon, D. & Irwin, K. D. Quantum Calorimetry. *Phys. Today* **52,** 32–37 (8 1999) (cit. on p. 142).

142. Karimi, B., Brange, F., Samuelsson, P. & Pekola, J. P. Reaching the ultimate energy resolution of a quantum detector. *Nat. Commun.* **11,** 367 (1 2020) (cit. on p. 142).

143. Mannila, E. T. *et al.* A superconductor free of quasiparticles for seconds. *Nat. Phys.* **18,** 145–148 (2 2022) (cit. on p. 143).

144. Stalp, S. R., Skrbek, L. & Donnelly, R. J. Decay of Grid Turbulence in a Finite Channel. *Phys. Rev. Lett.* **82,** 4831–4834 (24 June 1999) (cit. on p. 145).

145. Qi, X.-L., Hughes, T. L., Raghu, S. & Zhang, S.-C. Time-Reversal-Invariant Topological Superconductors and Superfluids in Two and Three Dimensions. *Phys. Rev. Lett.* **102,** 187001 (18 May 2009) (cit. on p. 145).

146. Bradley, D. I. *et al.* Potential Dark Matter Detector? The Detection of Low Energy Neutrons by Superfluid ^{3}He. *Phys. Rev. Lett.* **75,** 1887–1890 (10 Sept. 1995) (cit. on p. 145).

147. Volovik, G. *The Universe in a Helium Droplet* (Jan. 2003) (cit. on p. 145).

148. Niemetz, M., Hänninen, R. & Schoepe, W. On the Transition from Potential Flow to Turbulence Around a Microsphere Oscillating in Superfluid ^{4}He. *J. Low Temp. Phys.* **187,** 195–220 (2017) (cit. on p. 145).

149. Guénault, A., Keith, V., Kennedy, C., Mussett, S. G. & Pickett, G. The mechanical behavior of a vibrating wire in superfluid ^{3}He-B in the ballistic limit. *J. Low Temp. Phys.* **62,** 511–523 (1986) (cit. on p. 145).

150. Bradley, D. *et al.* Breaking the superfluid speed limit in a fermionic condensate. *Nat. Phys.* **12,** 1017–1021 (2016) (cit. on p. 145).

151. Clubb, D., Buu, O., Bowley, R., Nyman, R. & Owers-Bradley, J. R. Quartz Tuning Fork Viscometers for Helium Liquids. *J. Low Temp. Phys.* **136,** 1–13 (2004) (cit. on p. 145).

152. Schmoranzer, D. *et al.* Acoustic Emission by Quartz Tuning Forks and Other Oscillating Structures in Cryogenic ^{4}He Fluids. *J. Low Temp. Phys.* **163,** 317–344 (2011) (cit. on p. 145).

153. Guthrie, A. *et al.* Multimode probing of superfluid ^{4}He by tuning forks. *Appl. Phys. Lett.* **115,** 113103 (2019) (cit. on p. 145).

154. Defoort, M. *et al.* Probing Bogoliubov Quasiparticles in Superfluid ^{3}He with a 'Vibrating-Wire Like' MEMS Device. *J. Low Temp. Phys.* **183,** 284–291 (2016) (cit. on p. 145).

155. Guénault, A. M. *et al.* Probing superfluid ^{4}He with high-frequency nanomechanical resonators down to millikelvin temperatures. *Phys. Rev. B* **100,** 020506 (2 July 2019) (cit. on p. 145).

156. Guénault, A. M. *et al.* Detecting a phonon flux in superfluid ^{4}He by a nanomechanical resonator. *Phys. Rev. B* **101,** 060503 (6 Feb. 2020) (cit. on p. 145).

157. Bradley, D. *et al.* Operating Nanobeams in a Quantum Fluid. *Sci. Rep.* **7,** 4876 (2017) (cit. on p. 145).

158. Sage, E. *et al.* Single-particle mass spectrometry with arrays of frequency-addressed nanomechanical resonators. *Nat. Commun.* **9,** 3283 (2018) (cit. on p. 145).

159. Pikovski, I., Vanner, M. R., Aspelmeyer, M., Kim, M. S. & Brukner, Č. Probing Planck-scale physics with quantum optics. *Nat. Phys.* **8,** 393–397 (2012) (cit. on p. 145).

160. Defoort, M. *et al.* Slippage and Boundary Layer Probed in an Almost Ideal Gas by a Nanomechanical Oscillator. *Phys. Rev. Lett.* **113,** 136101 (13 Sept. 2014) (cit. on pp. 145–149, 152).

161. Vollhardt, D. & Woelfle, P. *The Superfluid Phases Of Helium 3* (July 1990) (cit. on p. 146).

162. Baggaley, A. W. *et al.* Visualizing Pure Quantum Turbulence in Superfluid ^{3}He: Andreev Reflection and its Spectral Properties. *Phys. Rev. Lett.* **115,** 015302 (1 July 2015) (cit. on p. 146).

163. Stokes, G. G. *Mathematical and physical papers* (Cambridge University Press, London, 1901) (cit. on p. 147).

164. Brumley, D. R., Willcox, M. & Sader, J. E. Oscillation of cylinders of rectangular cross section immersed in fluid. *Phys. Fluids* **22,** 052001 (2010) (cit. on pp. 147, 148, 151).

165. Bhiladvala, R. B. & Wang, Z. J. Effect of fluids on the Q factor and resonance frequency of oscillating micrometer and nanometer scale beams. *Phys. Rev. E* **69,** 036307 (3 Mar. 2004) (cit. on p. 147).

166. Kara, V., Yakhot, V. & Ekinci, K. L. Generalized Knudsen Number for Unsteady Fluid Flow. *Phys. Rev. Lett.* **118,** 074505 (7 Feb. 2017) (cit. on pp. 147, 151).

167. Kara, V. *et al.* Nanofluidics of Single-Crystal Diamond Nanomechanical Resonators. *Nano Lett.* **15,** 8070–8076 (12 2015) (cit. on pp. 147, 151).

168. Noury, A. *et al.* Layering Transition in Superfluid Helium Adsorbed on a Carbon Nanotube Mechanical Resonator. *Phys. Rev. Lett.* **122,** 165301 (16 Apr. 2019) (cit. on p. 148).

169. Cercignani, C. *Mathematical Methods in Kinetic Theory* (Springer New York, NY, 1969) (cit. on p. 152).

170. Chapman, S. & Cowling, T. G. *The Mathematical Theory of Non-Uniform Gases* (Cambridge University Press, 1970) (cit. on p. 152).

171. Grad, H. On the kinetic theory of rarefied gases. *Commun. Pure Appl. Math.* **2,** 331–407 (4 1949) (cit. on p. 152).

172. Patterson, G. N. *Molecular Flow of Gases* (John Wiley & Sons inc., New York, 1956) (cit. on p. 152).

ABSTRACT

Nano-Electro-Mechanical Systems (NEMS) are unique sensing devices, with record breaking sensitivity in force/mass detection. They can also be thought of as model systems for physicists, implementing given concepts into engineered, artifical devices. To do so, they can be interfaced with the most sensitive detection scheme: optomechanics, which has already been demonstrated in the microwave domain, in cryogenic conditions.

In this Thesis, we probe concepts linked to thermodynamics at small scales. In the first place, we investigate the optomechanics platform with one optical and one mechanical degree of freedom. Classical back-action concepts are studied with an artificial bath. Using a quantum-limited detection scheme, we demonstrated our ability to measure classical thermal fluctuations for a single phononic mode. In the second place, we use nanomechanical resonators as sensors for low temperature investigations: namely here, we probed the specific properties of a rarefied ideal gas. We demonstrate that we can resolve the signature of the boundary (Knudsen) layer of the gas onto the probe element itself.

ABSTRACT EN FRANÇAIS

Les systèmes nano-électro-mécaniques (NEMS) sont des dispositifs de détection uniques, avec une sensibilité record en matière de détection de force/masse. Ils peuvent également être considérés comme des systèmes modèles pour les physiciens, mettant en œuvre des concepts donnés dans des dispositifs artificiels. Pour cela, ils peuvent être interfacés avec l'un des systèmes de détection le plus sensible : l'optomécanique, qui a déjà fait ses preuves dans le domaine des micro-ondes, en conditions cryogéniques.

Dans cette thèse, nous sondons des concepts liés à la thermodynamique à petite échelle. En premier lieu, nous étudions la plate-forme optomécanique avec un degré de liberté optique et un degré de liberté mécanique. Les concepts classiques d'action-en-retour sont étudiés avec un bain artificiel. En utilisant un schéma de détection à la limite quantique, nous avons démontré notre capacité à mesurer les fluctuations thermiques classiques pour un seul mode phononique. En second lieu, nous utilisons des résonateurs nanomécaniques comme capteurs pour des investigations à basse température : à savoir ici, nous avons sondé les propriétés spécifiques d'un gaz parfait raréfié. Nous démontrons que nous pouvons résoudre la signature de la couche limite (Knudsen) du gaz sur l'élément de sonde lui-même.